Developing MAX Phases for Nuclear Fusion

A thesis submitted to the University of Manchester
for the degree of
Doctor of Philosophy
in the Faculty of Science and Engineering

2022

Maxwell T. P. Rigby–Bell

Department of Materials
School of Natural Sciences

Contents

Word count: 60,142

List of Figures

List of Abbreviations

ABF	Annular bright field
AFM	Anti–ferromagnetic
BB	Breeder blanket
BCC	Body–centred cubic
BSE	Backscattered electron
CCFE	Culham Centre for Fusion Energy
C_{FP}	Carbon Frenkel pair
COP26	United Nations Climate Change Conference
DBTT	Ductile–brittle transition temperature
DCF	Dalton Cumbrian Facility
DEMO	Demonstration fusion power plant (future)
DFT	Density functional theory
dpa	Displacements per atom
DT	Deuterium–tritium
EDS	Energy dispersive X–ray spectroscopy
EFDA	European Fusion Development Agreement
EIA	Energy Information Administration
F/M	Ferritic/martensitic
FCC	Face–centred cubic
FIB	Focussed ion beam
FiM	Ferrimagnetic
FM	Ferromagnetic
FWHM	Full–width half–maximum
Gen II	Generation II
Gen III	Generation III
Gen IV	Generation IV
GFR	Gas–cooled fast reactor
GGA	Generalised gradient approach
GIS	Gas injection system
GOF	Goodness of fit
HAADF	High angle annular dark field
HCP	Hexagonal close–packed
HHF	High heat flux materials
HRDIC	High–resolution digital image correlation
IEA	International Energy Agency
IFMIF	International Fusion Materials Irradiation Facility
i–MAX	In–plane ordered MAX
IPCC	International Panel on Climate Change
ITER	*‘The way’* – international experimental fusion reactor
JET	Joint European Torus

LFR	Lead–cooled fast reactor
LOCA	Loss–of–coolant accident
LWR	Light water reactor
MAX	$M_{n+1}AX_n$
MCF	Magnetic confinement fusion
MSR	Molten salt reactor
NM	Non–magnetic
ODS	Oxide dispersion strengthened
o–MAX	Out–of–plane ordered MAX
PAW	Projector augmented wave
PBE	Perdew–Burke–Ernzerhof
PCTF	Phase contrast transfer function
PFM	Plasma facing material
PKA	Primary knock–on atom
PWR	Pressurised water reactor
Q	Fusion power efficiency
RMM	Risk mitigation materials
SAED	Selected area electron diffraction
SCWR	Super–critical water reactor
SEM	Scanning electron microscopy
SFR	Sodium–cooled fast reactor
SNR	Signal–to–noise ratio
SS	Stainless steel
S–S	Solid solution
STEM	Scanning transmission electron microscopy
TEM	Transmission electron microscopy
TPB	Tritium permeation barrier
TRL	Technology readiness level
TZM	Titanium–zirconium–molybdenum
VASP	Vienna Ab–initio Simulation Package
VHTR	Very high temperature reactor
XRD	X–ray diffraction

Abstract

The search for high heat flux and radiation resistant component materials remains one of the most stubborn obstacles to the realisation of nuclear fusion as a terrestrial power source. A group of promising materials is the $M_{n+1}AX_n$ (MAX) phases, where 'M' is generally an early transition metal or lanthanide, 'A' is a group 13–15 element, 'X' is carbon or nitrogen, and 'n' is a positive integer. Their interesting mix of properties has led to their consideration as candidates for extreme environment applications, such as in fusion devices. However, whilst some MAX phases have shown promise in certain areas like irradiation–induced amorphisation resistance, others have shown susceptibility to issues such as corrosion and mechanical failure. Nevertheless, given the vast elemental parameter space in which MAX phases exist and the relatively sparse data available in the literature on their tolerance to fusion–relevant environments, there is great potential in the field for development towards fusion–relevant applications.

This thesis demonstrates the initial stages of a rapid MAX phase development workflow for nuclear fusion applications. This is achieved *via* a combination of high–throughput computational predictions, high–temperature powder synthesis, advanced X–ray and electron microscopy characterisation techniques, and high energy ion radiation damage assessments. The relative thermodynamic stabilities of hundreds of potential MAX phases have been calculated using density functional theory (DFT), with the results used to guide high temperature pressure–less sintering trials of promising candidates. As such, a series of novel $(Ta,Ti)_3AlC_2$ MAX phases have been synthesised, with crystallographic and elemental characterisations from the atomic to the macroscale performed using X–ray diffraction (XRD) and a suite of high–resolution electron microscopy techniques, such as energy dispersive X–ray spectroscopy (EDS). Finally, the response of Ti_3AlC_2 and the newly synthesised $(Ta_{0.25}Ti_{0.75})_3Al_{0.77}C_2$ and $(Ta_{0.38}Ti_{0.62})Al_{0.81}C_2$ MAX phases to extreme nuclear environments has been assessed using high–energy proton irradiations at a range of temperatures up to ~650 °C, with subsequent crystallographic and microstructural evolution quantified in unprecedented detail using XRD, high–resolution digital image correlation (HRDIC) and scanning electron microscopy (SEM). A comparison of the radiation damage tolerance of the three materials is given, with implications for the applicability of Ti–Ta–alloy MAX phases in future nuclear environments, as well as the suitability of proton irradiation in simulating reactor–relevant neutron radiation damage.

Declaration

No portion of the work referred to in this thesis has been submitted in support of an application for another degree or qualification of this or any other university or other institute of learning.

Copyright

i. The author of this thesis (including any appendices and/or schedules to this thesis) owns certain copyright or related rights in it (the "Copyright") and he has given The University of Manchester certain rights to use such Copyright, including for administrative purposes.

ii. Copies of this thesis, either in full or in extracts and whether in hard or electronic copy, may be made only in accordance with the Copyright, Designs and Patents Act 1988 (as amended) and regulations issued under it or, where appropriate, in accordance with licensing agreements which the University has from time to time. This page must form part of any such copies made.

iii. The ownership of certain Copyright, patents, designs, trademarks, and other intellectual property (the "Intellectual Property") and any reproductions of copyright works in the thesis, for example graphs and tables ("Reproductions"), which may be described in this thesis, may not be owned by the author and may be owned by third parties. Such Intellectual Property and Reproductions cannot and must not be made available for use without the prior written permission of the owner(s) of the relevant Intellectual Property and/or Reproductions.

iv. Further information on the conditions under which disclosure, publication and commercialisation of this thesis, the Copyright and any Intellectual Property and/or Reproductions described in it may take place is available in the University IP Policy (see http://documents.manchester.ac.uk/DocuInfo.aspx?DocID=487), in any relevant Thesis restriction declarations deposited in the University Library, The University Library's regulations (see http://www.manchester.ac.uk/library/aboutus/regulations) and in The University's policy on Presentation of Theses.

Acknowledgements

First and foremost, I want to thank my supervisor and veritable force of nature, Sarah, for her relentless inspiration, invaluable criticism, guidance, and apparently interminable energy. Without her support, I would never have made it this far.

Secondly, Philipp, my co–supervisor, for his insight and instruction on all things radiation damage. I am also hugely grateful for the introduction into the Manchester Zr group community, which was absolutely vital for collaborations and in helping me solve even the most stubborn of PhD–based problems.

To Michel and the LSG team across the pond – I can't thank you enough for welcoming me to your lab, showing me the fascinating world of MAX phase and MXene discovery, and giving me the tools needed to perform my research.

To Jo and Dave for showing me the ropes in the rabbit–hole–filled field of MAX phases; Dan for providing answers to pretty much anything and for his brilliant HyperSpy work; Dave Lunt, for putting up with my constant pestering, powering through mountains of HRDIC data, and essentially carrying my irradiation studies; Paul and Alex for their essential alliances, meme–making, sample prep and indentations; and of course to Paddy, Matt, Duc–The, Gary, Andy, Samir, Ken and all the other technical heroes in the department for their wisdom and support.

To all the wonderful people in the Haigh/Eggeman, Zr and Fusion groups who made PhD life endurable even at the most challenging of times – especially Nick, Evan, Ercin, Angus, Ollie, James, Emre, Aneeqa, Eu–Pin and Matt.

Finally, and most importantly, to my awesome wife, Florence. Thank you for your limitless patience, advice, love, laughter, understanding and encouragement. Here's to a stress–free future.

Chapter 1: Introduction

The quest for fusion energy as a viable terrestrial power source poses unprecedented challenges for materials scientists. The extreme operational environments found in fusion devices necessitate the continued development of advanced materials to meet these challenges. Promising candidate materials for high heat flux and radiation resistant applications exist, such as tungsten carbide and oxide–dispersion strengthened steel, but all carry significant drawbacks. Considering the strict nuclear site licensing criteria, a lack of suitable fusion–spectrum neutron materials test facilities, and extensive research timelines, the challenges are great. As such, research into the development of new and existing materials is on–going in the fusion materials community, with a wealth of potential candidates being considered at various stages of technology–readiness.

1.1 Project Overview

This thesis demonstrates a practical example of the initial development of new MAX phases for nuclear fusion, *via* a workflow of design (elemental down–selection and stability prediction), synthesis and characterisation (including response to fusion relevant conditions), with reference to both the 'bottom up' and 'top down' approaches performed in the nuclear fusion materials community. Arguments are made for the benefits of the continued development of new and/or advanced materials such as MAX phases, in addition to the development of more conventional (and better understood) materials, despite the potentially impractical timelines involved.

Consequently, a further understanding of the chemical diversity and properties of the MAX phases and their 2–dimensional derivatives, the MXenes, is demonstrated through the prediction, synthesis, and characterisation of new MAX phase materials in the quaternary $(Ta_{1-x}Ti_x)_3AlC_2$ system.

In Chapters 2 and 3 of this thesis, the background and motivation of the subsequent work is explained through a comprehensive review of the relevant literature. A focus is placed on MAX phases and their potential application to extreme environments, against a backdrop of nuclear fusion energy and the materials challenges the community faces.

The key experimental and computational methods employed in this work are detailed in Chapter 4, with practical examples from the literature regarding the application of each method to the MAX phase field, in terms of prediction, synthesis, and characterisation.

The ensuing three chapters concentrate on the exemplar first three stages of the development of new MAX phases, from concept to empirical testing. These are:

- Chapter 5: Design *via* elemental down–selection, followed by high–throughput computational structural optimisation using DFT.
- Chapter 6: Synthesis of novel MAX phases and their 2–dimensional derivatives – MXenes, supported by DFT calculations, *via* high temperature pressure–less powder sintering, followed by crystallographic and compositional analysis using XRD, SEM, EDS, and transmission electron microscopy (TEM).
- Chapter 7: Characterisation of response to proton irradiation over a temperature range relevant to nuclear fusion environments, using a combination of HRDIC, SEM, EDS, XRD, micro–indentation, and dilatometry.

The thesis is then summarised in Chapter 8, with critical considerations of the workflow and results obtained, as well as suggestions for improvements, alternatives, and further work.

1.2 List of Publications

In addition to the work detailed in this thesis, which represents a significant proportion of the project as a whole, the author has contributed to a number of other scientific publications. Whether within a field relevant to this project, such as nuclear materials, or not, these contributions have supported the development of skills essential to the delivery of this thesis. All publications, including those representing Chapters 5, 6 and 7, are listed here:

1. **'High throughput relative stability predictions of 211 and 312 $M^IM^{II}AX$ phases'**

Rigby–Bell, M. T. P., Evitts, L., Middleburgh, S., Race, C. P., Frankel, P., and Haigh, S. J., (not submitted, Chapter 5)

The author performed the density functional theory calculations, processed the data, analysed the results, and wrote the manuscript.

2. **'Irradiation tolerance of novel $(Ta_xTi_{1-x})_3AlC_2$ ($x = 0, 0.25$ or 0.32) MAX phases'**

Rigby–Bell, M. T. P., Lunt, D., Wylie, A. P., Barron, P. J. Shubeita, S. M., Harrison, G., Barsoum, M. W., Frankel, P., and Haigh, S. J., Acta Materialia (not submitted, Chapter 7).

The author planned the irradiation and characterisation experiments, synthesised, and prepared the $(Ta,Ti)_3AlC_2$ samples, performed the SEM EDS characterisations, processed all the data except for the HRDIC, analysed the results, and wrote the manuscript.

3. **'Phase stability of V–based multi–principal element alloys'**

Barron, P. J., Carruthers, A., Dawson, H., Rigby, M. T. P., Haigh, S., Jones, N. G., and Pickering, E. J., Materials Science and Technology (2021) doi: 10.1080/02670836.2022.2067645 (published).

The author created some of the TEM samples and contributed to the writing of the manuscript.

4. **‘Doped graphene/carbon black hybrid catalyst giving enhanced oxygen reduction reaction activity with high resistance to corrosion in proton exchange membrane fuel cells’**

Ji, Z., Chen, J., Perez–Page, M., Guo, Z., Zhao, Z., Cai, R., Rigby, M. T. P., Haigh, S., and Holmes, S., (2022) Journal of Energy Chemistry, 68, pp. 143–153, doi: 10.1016/j.jechem.2021.09.031 (published).

The author performed part of the SEM characterisations and contributed to the writing of the manuscript.

5. **‘Synthesis of new M–layer solid–solution 312 MAX phases $(Ta_{1-x}Ti_x)_3AlC_2$ (x = 0.05, 0.1, 0.2, 0.33 or 0.5), and their corresponding MXenes’**

Rigby–Bell, M. T. P., Natu, V., Sokol, M., Kelly, D., Hopkinson, D., Zou, Y., Bird, J. R. T., Evitts, L. J., Smith, M., Race, C., Frankel, P., Haigh, S., and Barsoum, M. W., RSC Advances (2021) 11(5), pp. 3110–3114, doi: 10.1039/d0ra09761f (published, Chapter 6).

The author planned the synthesis and characterisation experiments, performed the density functional theory calculations, synthesised the MAX phase samples, performed most of the XRD, all the SEM, and most of the TEM characterisations, processed the data, analysed the results, and wrote the manuscript.

6. **‘Novel Reduced–Activation TiVCrFe Based High Entropy Alloys’**

Carruthers, A., Li, B. S., Rigby, M., Raquet, L. C., Mythili, R., Ghosh, C., Dasgupta, A., Armstrong, D. E. J., Gandy, A. S., and Pickering, E., Journal of Alloys and Compounds (2021) 856, doi: 10.1016/j.jallcom.2020.157399 (published).

The author created the TEM samples and contributed to the writing of the manuscript.

Chapter 2: Background & Motivation

2.1 Overview

The dawn of the computer revolution ushered in an age defined by exponential developments, bringing to light humanity's insatiable appetite for technology and growth. Explosions in everything from microchip transistor density to worldwide population represent an international hyper–development which demands ever–increasing quantities of energy. Without this energy, the persistent gears of progress would grind to a halt [1].

According to the 2020 bp plc. Energy Outlook, projections for the global primary energy demand by 2050 involve a 25% increase in consumption on our current trajectory [2]. This considers averaged 2019 data from nine major energy organisations, including the International Energy Agency (IEA) and the U.S. Energy Information Administration (EIA), amongst others. Whilst this figure has been revised down significantly from, for example, the IEA 2015 projection of a 70% increase in global energy demand by 2040 [3], it still represents a vast acceleration in energy expenditure over the next 25 years. In fact, it is estimated energy generation will need to increase by at least the current combined energy capacity of China and India to meet the demand.

Unfortunately, as a recent Intergovernmental Panel on Climate Change (IPCC) report explained, we are fast approaching a long–term climate destabilisation tipping–point [4]. Beyond this, global average temperatures are expected to continue to rise to levels higher than seen during any interglacial period for the last 1.2 million years, with potentially devastating effects. To curb the rapidly accelerating climate–change inducing carbon emissions, over 170 countries have signed the United Nations Paris Agreement 2015, which signifies a pledge to immediately reduce emissions in an attempt to prevent the global average temperature from increasing more than 1.5 °C above pre–industrial levels [5]. More recently, following the 2021 United Nations Climate Change Conference, also known as COP26, many nations renewed their pledges, but fell somewhat short of commitments to the drastic global systems decarbonisation many climate scientists agree are necessary to prevent disaster.

In recent years, the energy industry has accounted for up to 75% of global greenhouse gas emissions [6]. Despite significant advances and increasing adoption of low–carbon, renewable energy technologies such as solar [7], wind [8], wave [9], and hydroelectric [10], their reliability and locationality are forecast to continue to hinder their full–scale implementation as baseline energy generation solutions. This leaves a requirement for an alternative, more reliable solution such as nuclear energy [11], [12]. Of course, the solution to the sustainable energy issue is not likely to be just one technology – an approach incorporating various technologies such as renewable energy, nuclear fission, nuclear fusion, and carbon capture and sequestration is required in the long term.

2.2 Nuclear Fusion

Nuclear energy has been widely used as an efficient, low carbon emissions source of power since its debut in the 1950s. Last year, over 70% of France's total energy demand was met by domestic nuclear fission power [13]. Compared to other mature electrical energy production methods, nuclear fission has by far the highest energy density – often by several orders of magnitude [14], [15].

However, the environmental, economic, and public safety impacts due to long–lived radioactive waste produced by fission power plants remain a serious issue. Emphasised by a few notable catastrophic plant failures, two of which – the Chernobyl and Fukushima Daiichi accidents [16], [17] – have led to genuine ecological disasters, the nuclear community is scrambling to guarantee the future safety of devices.

An alternative route being pursued by a dedicated international community is nuclear fusion. Fusion has the potential to act as a safe complimentary technology to fission. Not only is part of the fuel mix practically limitless – even if nuclear fusion was the sole means of energy production by tomorrow, oceanic deuterium reserves will take over 8.6 billion years to deplete – but it can, with a suitable selection of in–vessel materials, produce significantly lower quantities of high level radioactive waste [18], [19]. On the other hand, the more scarce part of the fuel mix – tritium, may be readily produced in a suitable fission device or produced *in–situ* in a fusion reactor [20].

However, substantial research, in addition to device iteration, is required over the coming decades before commercial scale nuclear fusion energy production can be realised. A comprehensive understanding of irradiated materials is arguably the most important step to be taken in the short term. The conditions that a material may encounter in a DEMO–style reactor – a demonstration fusion power plant design [21] – are expected to be more far more hostile than any seen before on earth [22].

2.2.1 Fusion – The Basics

There are various fusion reactions which can provide a net energy return [23], however the most notable and well–studied pathway is the deuterium–tritium (DT) cycle:

$$\mathrm{D} + \mathrm{T} \rightarrow \mathrm{n}\ (14.1\ \mathrm{MeV}) + \alpha\ (3.5\ \mathrm{MeV}) \tag{2.1}$$

where D and T are ^{2}H and ^{3}H particles, respectively, n is a neutron and α is a ^{4}He nucleus. Whilst deuterium is abundant, tritium is extremely rare. Not only is it produced in negligible quantities naturally, but it has a relatively short half–life of 12.3 years [24]. It is both expensive and laborious to produce, *via* a one–way process; the fission of lithium–6 *via* the $\mathrm{n}(^{6}\mathrm{Li},\mathrm{T})\alpha$ reaction:

$$n + {}^{6}Li \rightarrow {}^{3}H + \alpha$$

– in which a ^{6}Li nucleus captures a neutron, producing a triton and an α–particle [25]. As a result, this is utilised *in–situ* for many fusion reactor designs. In fusion

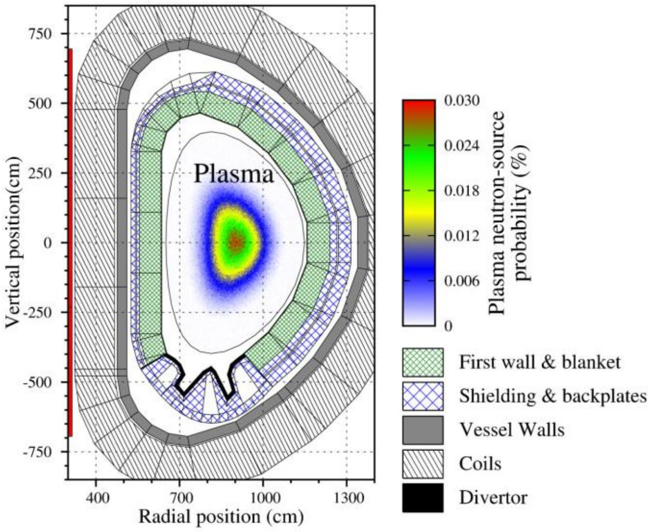

Fig. 2.1 – The tokamak: A simulation of a slice through an ITER–like tokamak. A neutron production probability distribution from the HERCULES code is overlaid, with a peak at 9 m from the central solenoid on the left (major radius) [462]. Reproduced from *Fusion Science and Technology*, 66, 1, M. R. Gilbert *et al.*, *Comparative Assessment of Material Performance in DEMO Fusion Reactors*, p. 9–17, Copyright (2014), with permission from Taylor & Francis [463].

environments, where there is an abundant supply of neutrons, ^{6}Li–rich components – known as tritium breeder blankets (BBs), surround the plasma and provide the necessary tritium for a sustained reaction [26].

At the time of writing, over 130 working fusion reactors have been built, with the leading and most mature technology implanted in the 'tokamak' design [27], [28]. A tokamak is a toroidal vacuum chamber holding a plasma, contained with both a toroidal and poloidal magnetic field at temperatures up to 150 million degrees, in a process known as magnetic confinement fusion (MCF). However, a tokamak which achieves a break–even ratio, Q, of thermal power output from the plasma to thermal power input (to start and maintain the reaction) of at least 1 has yet to be constructed. The current world record of Q = 0.67 was set by the Joint European Torus (JET) device at CCFE in Culham, UK in 1997 [29] and has yet to be improved upon.

The largest fusion reactor in the world, known as 'ITER' (referring to the Latin for 'the way'), is currently under construction in Cadarache, France. As the next step on the road to fusion, ITER is expected to achieve a minimum of plasma Q = 10

[30]. Following this, a demonstration fusion reactor known as DEMO will be built and connected to the grid – incorporating a thermal–to–electrical energy conversion process [21]. This will be the final step before industrial prototype reactors.

2.2.2 The Road to Fusion

With over 50 years of international research on fusion technology, the scientific community has encountered a seemingly endless array of obstacles on the pathway to commercial fusion generated electricity. In 2012, the European fusion development agreement (EFDA) published what is now known as the EUROfusion Roadmap – detailing the issues faced in MCF and the necessary missions to provide solutions [31]. Seven major challenges were identified that must be overcome for the realisation of nuclear fusion electricity:

1. Plasma regimes of operation – for fusion to occur efficiently, a DT plasma must be confined at extreme temperatures and pressures, with energy losses due to turbulence and instabilities minimised. In order to meet the requirements of DEMO (see Table 2.1 and [21] for details), stable steady–state plasma confinement regimes must be developed, using the ITER configurations as a baseline.

2. Heat exhaust – the exhaust system for much of the heat in a tokamak, known as the divertor, lies at the bottom of the chamber. High heat flux components which have not yet been fully licensed, must be developed to build a divertor capable of withstanding the conditions expected in DEMO.

3. Neutron resistant materials – in addition to thermal fluxes of the order of MW m^{-2}, components in the vacuum vessel must contend with an extremely high flux of 14.1 MeV neutrons, whilst maintaining their structural integrity, thermal conductivity, and minimising activation to avoid permanent radioactive waste disposal issues. Structural and high–heat flux materials to qualify for these requirements with regards to a DEMO environment still need to be fully developed.

4. Tritium self–sufficiency – to maintain fusion, deuterium and tritium must be pumped into the plasma continuously – roughly 0.4 kg of tritium will be burned per day in DEMO. As tritium reserves are practically non–existent, it must be produced on–site using the fission of ^{6}Li in tritium breeding blankets surrounding the plasma. To make this possible, an efficient blanket design incorporating materials adequate in neutron and tritium breeding, as well as in thermal conduction to coolant cycles, must be developed.

5. Intrinsic safety – one of the most heavily advertised aspects of fusion energy is its potential as a safe means of electricity production compared with fission. For this to be realised in DEMO and beyond, an intrinsic resistance to accident scenarios must be designed in future reactors. Additionally, adequate material selection is required for the reactor components to minimise activation and waste disposal – with emphasis on tritium retention – as well as ensuring proliferation resistance.

6. Integrated DEMO design – whilst the next stage in the road to fusion is undoubtedly the completion and operation of ITER, the ultimate connection between research and commercialisation will be DEMO. Using the knowledge and expertise gained from ITER, highly reliable remote maintenance and component technologies, as well as efficient heat transfer systems, must be exploited.

7. Competitive cost of electricity – the final hurdle to the realisation of commercial fusion energy is ensuring its market competitiveness. High availability, realistic capital costs and minimised maintenance and accident scenarios are essential for DEMO to serve as a credible example of fusion electricity.

This thesis focuses on challenge 3, the development of neutron resistant and high heat flux materials for DEMO.

2.2.3 Resistant Materials

The alpha particle (He nucleus) and neutron by–products of the DT reaction, typically at energies of 3.5 and 14.1 MeV respectively, are responsible for much of the radiation–induced issues in fusion devices and are therefore a major focus in the fusion Roadmap [31].

Table 2.1 – The expected DEMO environment: Operational parameters from a recent DEMO design, using data from Brooks *et al.* [32]. Abbreviations are ‘full power year’ (fpy) and ‘DT’ (deuterium, tritium).

First wall & blanket			Divertor		
Operational temperatures	Neutron flux (peak)	Neutron fluence	Peak neutron damage	Particle flux (peak)	Peak neutron damage
300–680 °C	8.25×10^{18} $m^{-2}\ s^{-1}$	1–5 MW year m^{-2}	~50 dpa fpy^{-1} (steel) ~20 dpa fpy^{-1} (W)	Neutrons: ~10^{18} $m^{-2}\ s^{-1}$ DT ions: ~10^{23} $m^{-2}\ s^{-1}$	W armour: 5.5 dpa fpy^{-1} Cu heat sink: 10 dpa fpy^{-1}

The divertor (black area in Fig. 2.1) absorbs much of the charged particle flux due to the guiding magnetic fields in the tokamak, potentially leading to retention, clustering, and bubble formation, which results in swelling and embrittlement of the component. However, the neutron, unaffected by fields, will be incident on either the first–wall – the armour between the blanket and the plasma; shown as a green band in Fig. 2.1, or the divertor. High energy neutrons are known to cause significant damage to reactor components, especially the plasma facing material (PFM) – seen in previous fusion experiments such as JET [33]–[36]. At the fluences expected for a DEMO style reactor (a far larger design than JET) over its operational lifetime, the radiation induced damages are expected to be proportionally larger [21] (see Table 2.1). Materials will be exposed to an extremely high heat flux of energetic particles depending on their positioning (0.1–20 MW m^{-2}), high temperatures (especially during disruptive transient plasma events) of 300–3200 °C, gamma radiation, sputtering and erosion, high energy neutron damage (3–30 dpa[1]/year), and H and He trapping.

---

[1] The most fundamental quantity when reporting irradiation damage in materials is displacements per atom (dpa) – a measure which considers the energy and species of irradiation, the total fluence

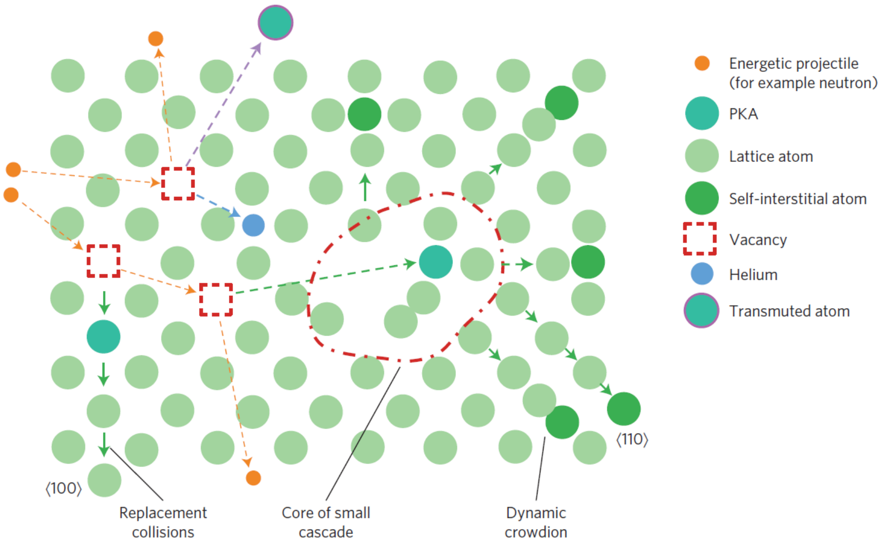

Fig. 2.2 – Radiation damage in materials: A schematic of a variety of fundamental radiation damage mechanisms at play in nuclear environments. 'PKA' is a primary knock–on atom – the atom to which an incoming particle transfers most of its energy. Reproduced from *Nature Physics*, 12, 5, J. Knaster *et al.*, *Materials research for fusion*, p. 424–434, Copyright (2016), with permission from Springer Nature [464].

Material damage will likely include the copious production and accumulation of point–defects [19]; precipitation of alloying elements and impurities [37]–[39]; and bubbles, voids and cavities [40]–[42]. A visual representation of these can be seen in Fig. 2.2. These mechanisms lead to lattice deformation, swelling, embrittlement, cracking and enhanced fuel retention [43]–[46] (a serious concern when tritium is involved, as discussed later in this section [47]). Additionally, material neutron absorption inevitably causes transmutation, resulting in further damage in addition to material activation [22], [48], [49]. The resulting microstructure of irradiated materials will be a combination of primary radiation damage and thermal annealing. This consists of small defect clusters, stacking faults, interstitial and vacancy dislocation loops, precipitates (in the case of alloys), voids and/or helium bubbles

---

and the displacement threshold energies of the target material atoms. Theoretically, this allows the quantitative comparison of the radiation dose received by materials for various irradiation conditions and species. The dose, in dpa, of an irradiation is estimated using cascade models such as that implemented in the software package SRIM [366], [368]. However, dpa represents a highly simplified scenario in which radiation is incident in an amorphous 'sample' which contains no information on local chemistry, dislocations, defect clusters, precipitates, crystallographic orientations, or microstructural features such as grain boundaries.

(some of which are tritium–rich). A diagram with examples of the various radiation–induced events is shown in Fig. 2.2.

Tritium, apart from being extremely rare owing to its ~12–year half–life, offers further problems. The levels of tritium permeation and retention in the wall materials are of paramount importance to both the safety of the site – due to the radiotoxicity of tritium – and the stability of the fusion plasma with regards to the loss of fuel from the core. It is expected that a fully functional DEMO device will incur losses of several kilograms of tritium per year, if no tritium permeation barrier (TPB) is applied to the first–wall [50]. With this in mind, it has been suggested that the permeation rates of tritium must be reduced by at least two orders of magnitude (e.g. [51]–[54]).

So far, several materials have been proposed as TPB candidates. Al_2O_3, Er_2O_3, SiC, and TiN–TiC have demonstrated hydrogen permeation reduction factors of over 1000 in recent studies [55]–[60]. However, a comprehensive assessment of both the compatibility of these candidates with nearby reactor materials and their manufacturability into practical TPB components has yet to be performed.

There is an added safety concern presented by the radiotoxicity of trapped tritium – a loss–of–coolant accident (LOCA). In this scenario, a lack of sufficient flowing coolant (apart from causing an immediate shutdown of the plasma) allows energy released by neutron activated wall materials, especially PFM, to heat vessel materials unchecked. This could lead to an explosive event, in which structural blanket or divertor material is compromised, exposing the inside of the vessel to coolants, with the resulting gas production eventually causing the vacuum vessel to rupture, releasing activated and potentially tritiated materials into the environment.

Several studies have reported enhanced H trapping in irradiated materials [61]–[64]. Added to the likelihood of transmutant He–induced cavity formation providing further sites for H (or T) trapping [62], [65]–[67], indicating that H trapping must be understood fully in candidate fusion materials [68]. A roughly linear relationship is expected between the radiation induced atomic displacement damage and the

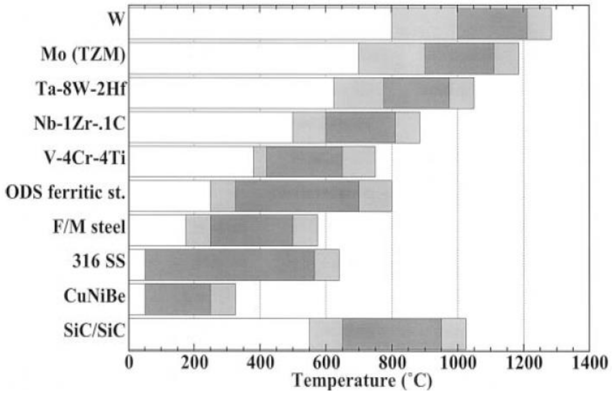

Fig. 2.3 – Operating temperature windows for fusion materials: The suitable operational temperature ranges of a selection of materials suggested as candidates for first–wall, divertor and/or structural component materials in future fusion devices. The abbreviations are titanium–zirconium–molybdenum (TZM), oxide dispersion strengthened (ODS), ferritic/martensitic (F/M) and stainless–steel (SS). Reproduced from *Fusion Engineering and Design*, 51–52, S. Zinkle and N. Ghoniem, *Operating temperature windows for fusion reactor structural materials*, p. 55–71, Copyright (2000), with permission from Elsevier [465].

helium concentration (in atomic parts per million, appm) in fusion reactors, based on current experience with nuclear fission materials, as shown in Fig. 2.6 [69]–[71]. This allows a loose prediction of the fuel retention, as well as the expected embrittlement due to helium bubble formation [71]–[75], to be made for fusion materials.

Additionally, dust caused by erosion, sputtering and evaporation of PFM by plasma radiation can present safety issues. Not only will the neutron induced radiotoxicity of first–wall dust make it unsafe during reactor decommissioning, but the potential related hazards in a LOCA situation could be detrimental to life nearby.

To summarise, plasma facing and high heat flux materials must:

1. limit neutron activation
2. limit helium agglomeration
3. limit tritium retention
4. have a high melting point
5. have a high sputtering energy (PFM only)

6. have good thermal conductivity and shock resistance
7. be resistant to at least 15 × 10^3 fatigue cycles and 12 × 10^3 hours at maximum stress (~100 MPa) at normal operational temperatures (300–800 °C), and far higher temperatures for short periods of time during off–normal events, such as edge localised modes (ELMs).

2.2.4 Developing Fusion Materials

As noted in the EUROFusion Roadmap, around 10–15 years of research is required to develop a nuclear–grade material from a 'proof–of–principle' stage [31]. For this to happen, testing with 14.1 MeV neutrons is essential. As a reliable, high flux fusion neutron materials testing facility is yet to be built (the International Fusion Materials Irradiation Facility (IFMIF) is currently in the engineering validation stage), the minimum 14.1 MeV testing requirements must be attained using fission neutrons, ions and either isotopically or chemically doped materials. This data is needed for fulfilment of the EUROfusion Roadmap by 2026 [68].

The selection of fusion materials is limited by several factors. The main three are: thermal conductivity; plasma contamination minimisation (from sputtering and

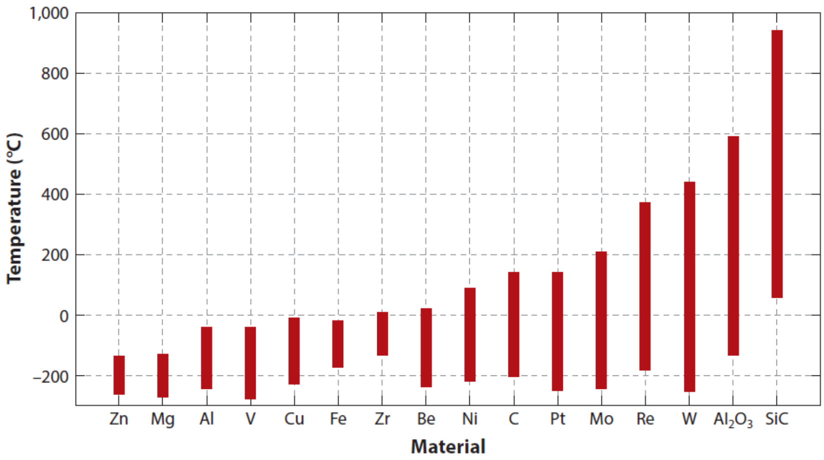

Fig. 2.4 – Interstitial mobility thresholds: The temperature regimes associated with the onset of interstitial mobility and before the activation of vacancy migration in various single component metals, in addition to Al_2O_3 and SiC, proposed as candidates for components in fusion devices. Reproduced from *Annual Review of Materials Research*, 44, 1, S. Zinkle and L. Snead, *Designing radiation resistance in materials for fusion energy*, p. 241–267, Copyright (2014), with permission from Annual Reviews, Inc. [464].

erosion); and neutron cross–section leading to the production of active transmutants. Regarding the reduction of activation of structural materials, thereby enhancing safety following decommissioning, Gilbert *et al.* have identified Fe, Cr, Ti, V, W, Si and C as suitable candidate alloying elements [76], [77].

The current DEMO designs incorporate either a helium– or water–cooled lithium–beryllium pebble bed BB, EUROFER97 (a bespoke reduced–activation ferritic/martensitic (RAFM) steel developed for fusion applications [78]) as structural material, and a tungsten first–wall armour plated on the front face of the EUROFER97 BB, with copper alloy cooling channels. As this configuration of materials has been developed primarily for the operation of ITER, it is expected that significant optimisations will be required before incorporation into DEMO. In the case that specific materials prove unsuitable for the DEMO requirements, a set of ‘risk mitigation materials’ (RMM) were identified in the Roadmap. These are newer, more advanced materials that have shown promise as candidates for structural, high heat flux (HHF) or PFM, but are still at an early stage on the technology readiness level (TRL) scale (TRL 1–2). Since the publishing of the Roadmap, several of these materials have undergone advancements up to and beyond the ‘proof–of–concept’ stage (TRL 3), with research and testing underway [79]–[83]. However, there still exists a need for further RMMs to ensure the safe and reliable operation of future fusion plants, especially those beyond DEMO.

For the first–wall materials in ITER, a high–purity Be armour will be used (although not suitable for DEMO) brazed to a Cu alloy (to act as the heat sink) which is, in turn, plated to a 316–stainless steel (likely to be replaced by EUROFER97 in DEMO). Other considered options are carbon fibre composites or W–based materials.

The current choice for the divertor armour is pure tungsten plated onto a copper alloy. However, its derivative alloys and composites are also being considered. Pure W is known to have excellent high temperature (> 700 °C) properties such as a high melting point, thermal conductivity, creep resistance, erosion resistance, strength and a low vapour pressure [84]. However, like many body–centred cubic (BCC)

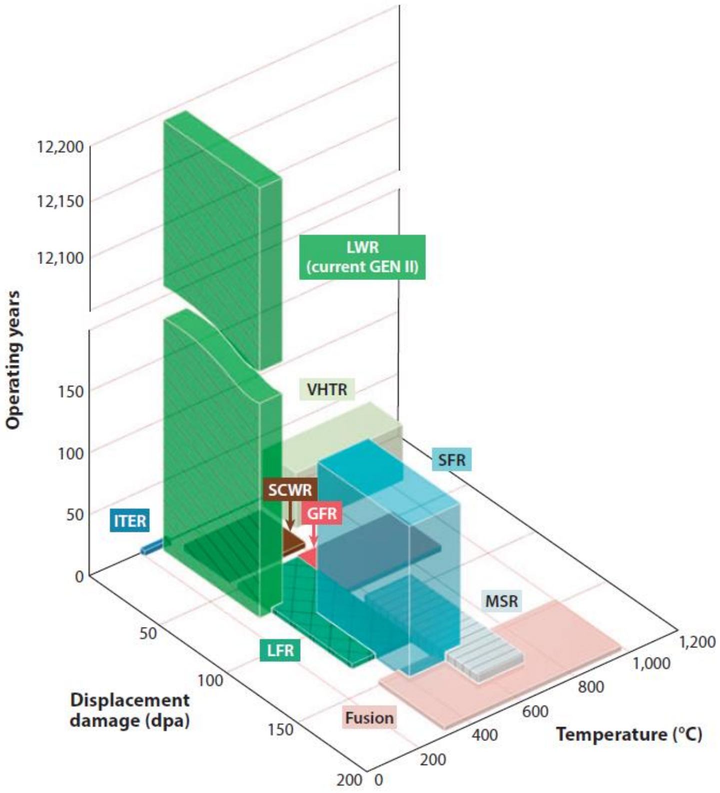

Fig. 2.5 – Experience, as of 2001, of radiation damage in nuclear materials: A comparison of normal operating conditions, in terms of displacement damage (dpa) and operational temperature (°C), for structural materials in a variety of fission reactors and proposed fusion reactor designs). The data is plotted as a function of operating years – a measure of the combined operational time of all relevant devices across the world. The pink 'Fusion' plot refers to the estimated environment in DEMO. Abbreviations are as follows: light water reactor (LWR), very high temperature reactor (VHTR), gas–cooled fast reactor (GFR), sodium fast reactor (SFR), molten salt reactor (MSR), lead–cooled fast reactor (LFR), supercritical water reactor (SCWR), Generation II (GEN II), and Generation IV (GEN IV) [466]. Reproduced from *Annual Review of Materials Research*, 44, 1, S. Zinkle and L. Snead, *Designing radiation resistance in materials for fusion energy*, p. 241–267, Copyright (2001), with permission from Annual Reviews, Inc. [464].

materials, the rather high characteristic ductile–to–brittle transition temperature (DBTT) of W (300–400 °C) makes it brittle at the standard operating temperatures of some leading reactor designs [85], [86]. It has been found that the addition of Re, due to the formation of solid solutions, can improve the ductility and toughness of W, leading to a lower DBTT, as well as inhibiting He–induced formation of unique surface nanostructures [87]–[91]. That said, irradiation has been shown to embrittle W–Re alloys to a greater extent than pure W variants. Equally, the low availability of Re severely limits its use as an alloying element in W [92]. Additionally, the elements Ir and Os (the next two elements in the periodic table after Re), which have been considered as ductility enhancing alloying elements for tungsten, have not been studied in much depth and early results have not been entirely encouraging [93].

EUROFER97 is the current choice of structural material for beyond ITER, but does not lack in drawbacks: above the 500–550 °C range, its strength and creep–rupture failure time declines rapidly [78]. Additionally, due to serious low temperature embrittlement problems, the EUROFER97 operational temperature window is restricted to 350–550 °C [94]. This presents a serious issue for DEMO, as it is expected that the thermodynamic efficiency of Rankine or Brayton cycles operated at a limit of 500 °C will not meet the minimum electrical generation requirement [95]. Equally, at this temperature limit, radiation damage annealing cycles are impossible.

ODS ferritic steels, SiC/SiC composites and V alloys have all been proposed as alternatives to the current ITER structural material choices [96], due to their operational and defect recovery temperature windows (see Fig. 2.3 and Fig. 2.4,

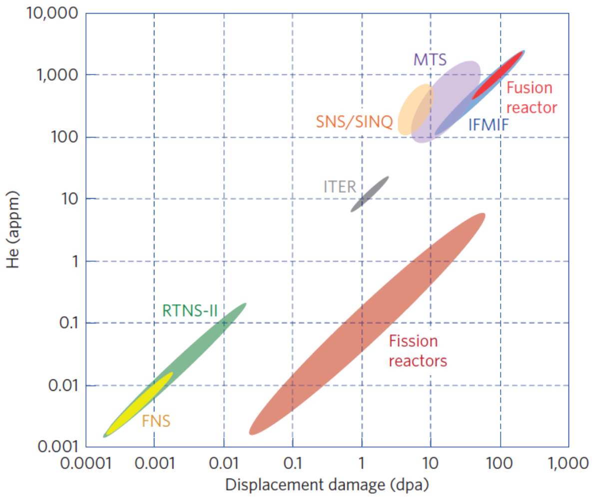

Fig. 2.6 – Helium and displacement damage: The correlation between the displacement damage (dpa) and helium concentration (in appm) in operational fission environments (both existing and simulated) and fusion reactor designs (simulated). Reproduced from *Annual Review of Materials Research*, 44, 1, S. Zinkle and L. Snead, *Designing radiation resistance in materials for fusion energy*, p. 241–267, Copyright (2001), with permission from Annual Reviews, Inc. [464]

respectively, for comparisons). However, these materials are far from being nuclear grade. For example, SiC/SiC composites have significant problems within nuclear environments. Their low ductility make them prone to cracking. Equally, it has been reported that the thermal conductivity – essential for heat removal – of SiC/SiC composites degrades rapidly during irradiation (by at least an order of magnitude, even during irradiation at 800 °C to 2–3 dpa [97], [98]). It has also been reported that SiC/SiC undergoes > 1% volumetric swelling at irradiation temperatures below 600 °C. This is expected to be increased by the significant amounts of transmutant helium produced in fusion neutron irradiation simulations, > 10000 appm after 5 years, if the material is in the blanket first–wall [99], [68] [73], [100].

Chapter 3: MAX Phases in Fusion

3.1 Overview

Discovered in the 1960s by Hans Nowotny *et al.* [101], the $M_{n+1}AX_n$ (MAX) phases are a group of over 155 materials proposed as candidates for nuclear applications. The defining features of MAX phases are distorted edge sharing XM_6 octahedra layers, locally arranged in a rock salt structure, interleaved by single atom thick metallic 'A'–layers (see Fig. 3.1 for examples). Part of the $P6_3/mmc$ (194) hexagonal space group, MAX phases have the general formula $M_{n+1}AX_n$, where M is generally an early transition metal, A is a group III or IVA element, X is either carbon or nitrogen, and n = 1, 2, 3, etc. (see Fig. 3.1) [102].

The MAX phase nomenclature refers to stoichiometry, where '211' means M_2AX and '312' refers to M_3AX_2, and so on. So far, the vast majority of stable phases synthesised are 211, 312 or 413, but higher order MAX phases are known to exist [102]. Using the example of Ti_3SiC_2, the Ti_6C octahedra are similar in structure to that of TiC, where the (111) plane is coherent with the (0001) face of Ti_3SiC_2.

Very little research existed on MAX phases until the 1990s, when Barsoum & El–Raghy synthesised largely phase pure, bulk Ti_3SiC_2 and demonstrated its thermal shock resistance, machinability and high temperature strength [103]. This paper ignited a period of significant international research interest in MAX phases which continues to grow today. Since then, various interesting properties of MAX phases have been reported, including impact damage tolerance (through crack propagation resistance) [104]; good thermal conductivity (for ceramics – up to 60 $W\ m^{-1}\ K^{-1}$) [105]; good thermal shock resistance (e.g. retention of flexural strength following quenching from 1400 °C) [102]; oxidation resistance (in select scenarios, such as an activation energy of 325 $kJ\ mol^{-1}$ at 1400 °C) [106]; elastic rigidity (Young's modulus, $E > 300$ GPa) [107]; low densities ($< 4.5\ g\ cm^{-3}$, as with other ceramics) [102]; and good wear properties ($< 1.34 \times 10^{-3}\ mm^3\ N^{-1}\ m^{-1}$ wear rate) [108]. For example, early work on the damage tolerance of MAX phases recognised specifically Ti_2AlC and Ti_2AlN as having outstanding abrasive properties, to the same degree even as SiC [109].

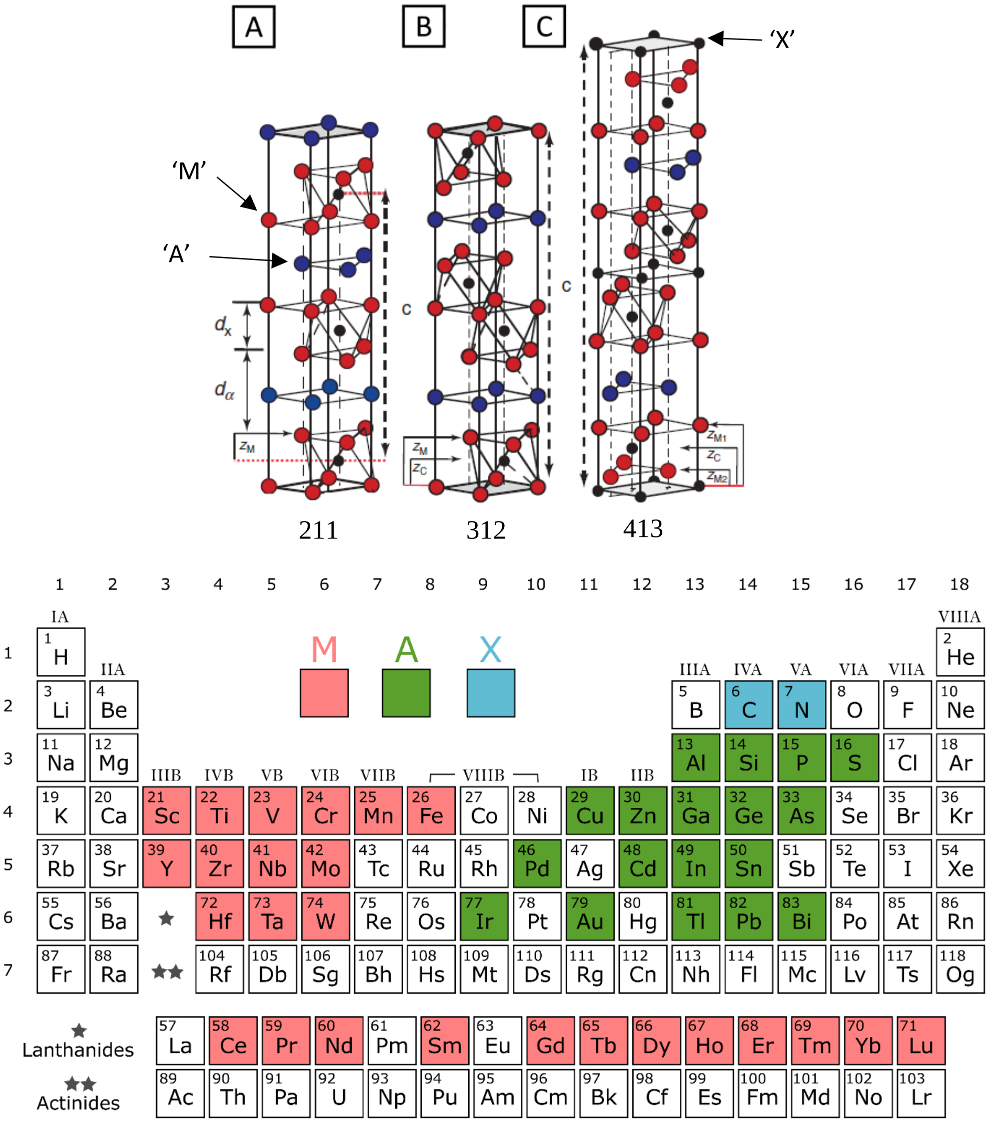

Fig. 3.1 – The MAX phase unit cell (top): Conventional '211' (A), '312' (B), and '413' (C) MAX phase unit cells, showing the hexagonal layered structure, interleaved by the A–layer element. Also shown are the *c*–lattice parameters as vertical dashed lines; the thickness, d_x of the $M_{n+1}X_n$ layers; the thickness, d_α of the A–layers; and the various '*z*' values (refer to Table 2.2 in reference [102] for further explanation). Reproduced from *MAX Phases: Properties of Machinable Ternary Carbides and Nitrides*, M. W. Barsoum, p. 14, Copyright (2013), with permission from John Wiley & Sons [102]. Elements of the MAX phases (bottom): a simplified periodic table highlighting the various elements which can be used to synthesise the currently known MAX phases [110].

3.2 Solid Solutions

In addition to the conventional ternary MAX phases, solid solutions of one or more elements in the M, A or X layers are possible. This greatly increases the size of the compositional parameter space and allows for a high degree of variation in the chemistry of MAX phases [110].

Dahlqvist *et al.* predicted the thermodynamic stability of phases in the 211 Ti–M–Al–C system, where M = V, Cr, Nb, Mo, Ta or W [111]. They found that for many of the compositions the order–disorder transition temperature of M–layer elements is significantly lower than the usual synthesis temperatures of MAX phases (> 1200 °C), indicating a preference for solid solution formation in the M–layer of many compositions with more than one M–element. To an extent, this has been verified by experimental reports of $(Nb_{0.5}V_{0.5})_2AlC$, $(Nb_{0.8}Zr_{0.2})_2AlC$, $(Cr_{0.5}V_{0.5})_3AlC_2$ and $(TaTi_2)_3AlC_2$ [112]–[114], although many predicted compositions have yet to be synthesised. For higher order MAX phases ($n \geq 3$), relatively few M–layer solid solutions have been investigated experimentally [110].

Table 3.1 – Partial occupancies in quaternary MAX phases: A selection of solid solution or ordered M–layer MAX phases, with relative M–site occupancies shown for comparison. The second two phases are o–MAX phases (see main text), with full occupancy M–layer sites.

	Relative occupancy			
Phase	2a	4f	4e	Ref.
$(V_{0.5}Cr_{0.5})_3AlC_2$	V 100%, Cr 0%	V 27%, Cr 73%	–	[115]
$(Ti_{1/3}Cr_{2/3})_3AlC_2$	Ti 100%, Cr 0%	Ti 0%, Cr 100%	–	[116]
$(Ti_{1/3}Mo_{2/3})_3AlC_2$	Ti 100%, Mo 0%	Ti 0%, Mo 100%	–	[117]
$(V_{0.5}Cr_{0.5})_4AlC_3$	–	V 84%, Cr 16%	V 32%, Cr 68%	[118]
$(Ti_{1/2}Mo_{1/2})_4AlC_3$	–	Ti 86%, Mo 14%	Ti 23%, Mo 77%	[119]

That said, the addition of a second transition M–element to a starting mixture can stabilise the MAX phase structure, where otherwise a pure $M_{n+1}AX_n$ will not form. For example, V_3AlC_2, Cr_3AlC_2, Cr_4AlC_3, Mo_3AlC_2 and Mo_4AlC_3 do not form under normal synthesis conditions and all except V_3AlC_2 are not expected to be stable, based on DFT calculations [110], [120]. However, related M–layer solid solutions

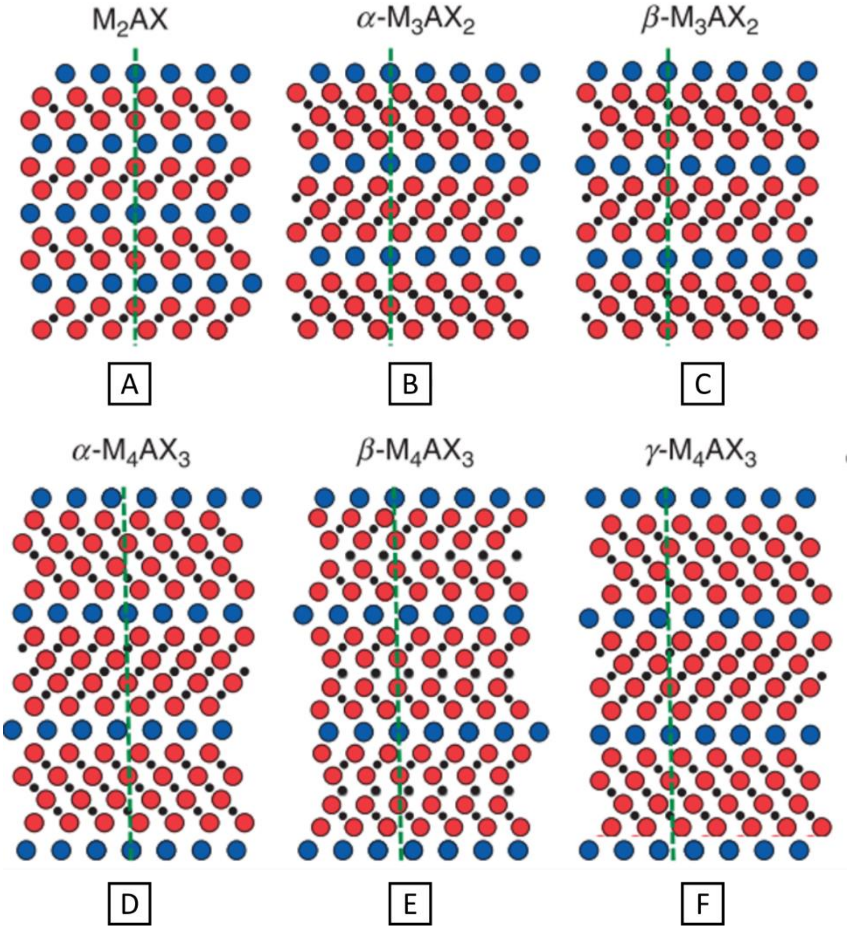

Fig. 3.2 – MAX phase polymorphs: The only known 211 MAX phase structure (A), along with structural variations of the 312 (B, C) and 413 (D–F) MAX phases. The ‘M’, ‘A’ and ‘X’ atoms are shown in red, blue, and black, respectively and dashed green lines are included as visual aids. Reproduced from *MAX Phases: Properties of Machinable Ternary Carbides and Nitrides*, M. W. Barsoum, p. 14, Copyright (2013), with permission from John Wiley & Sons [102].

have been realised experimentally, such as $(V_{0.5}Cr_{0.5})_3AlC_2$, $(Ti_{3/8},Cr_{5/8})_4AlC_3$, $(Ti_{1/3}Mo_{2/3})_3AlC_2$, and $(Ti_{0.5}Mo_{0.5})_4AlC_3$ [117]–[119], [121]. The formation of double solid solutions has been used to improve the phase purity of sintered MAX phases in select cases, such as $(Zr_{0.8},Nb_{0.2})_2(Al_{0.5},Sn_{0.5})C$. Here, the addition of Nb and Sn to the starting mixture suppresses the formation of ZrC impurities, resulting in a phase pure MAX phase [122], [123].

Additionally, some multi–element sites do not consist of entirely random distributions. Several authors have noted a preferential occupation of certain sites in solid solution MAX phases of $n \geq 2$, with a higher concentration of the heavier, and higher electronegativity M–element in the central M^{II} layers. A summary of these reports is shown in Table 3.1, with two ordered 'o–MAX' phases – compositions with full out–of–plane M–layer ordering, also included. Recently, the discovery of o–MAX and in–plane ordered 'i–MAX' quaternary phases, rare–earth i–MAX phases and even high–entropy MAX phases (with 3 or more elements on the same site) have expanded the diversity of MAX phases further still, with a wealth of interesting properties in tow [116], [124]–[127].

Solid solution and ordered multi–M–element MAX phases have garnered increasing attention in recent years due to the potential for tuning mechanical and physical properties, such as strength, hardness, thermal expansion, electrical resistivity and magnetism, to name a few [128]–[136]. As in many metallic systems, a solid solution strengthening effect has been observed in certain MAX phases. An early example is the addition of 15 at.% V to the M–layer of Ti_2AlC, which was reported by Meng *et al.* to increase the Vickers hardness, flexural and shear strengths by 29%, 36% and 45% in turn [137]. Likewise, the x–site of the MAX phases can be interchanged between C and N, as reported initially by Barsoum *et al.* in 2000 [138]. $Ti_2AlC_{0.5}N_{0.5}$ was found to possess a considerably higher hardness and stiffness than both Ti_2AlC and Ti_2AlN. C and N atoms form similar bonds with transition metals, as in their parent MX phase counterparts (TiC and TiN). As such, a range of C:N ratios may be possible for many MAX phases.

3.3 Polymorphs

MAX phase polymorphs, representing a variation in stacking configuration of the A or MX layers, have been observed or predicted for several compositions. Ti_3SiC_2, Ti_3AlC_2, Ta_4AlC_3, as well as the more recent $(Ta,Ti)_3AlC_2$ phases all display polymorphic variation [105], [114], [139]–[141]. For 312 phases, the polymorphs are A–layer based and most likely shear strain driven. The α and β polymorphs represent a basal plane shearing of the A–layers relative to each other, with the A–elements occupying the 2*b* and 2*d* Wyckoff positions, respectively. Evidence of this has been observed following diamond anvil testing as well as during transmission electron microscopy (TEM) sample preparation using focussed ion beam (FIB) milling.

On the other hand, the (somewhat confusingly) synonymous α and β polymorphs for Ta_4AlC_3 exist solely in the MX layers. An MX–layer 'zig–zag' stacking configuration has been observed in the β configuration, where the positions of the Ta(2) and C(2) atoms are shifted compared to the α variant. It is suspected that the transformation from α to β in this case is thermodynamically driven, following DFT Gibbs free energy predictions of such a transformation at 1875 K [142]. Additionally, the 413 γ–phase is formed upon the shearing of the A–layer, as in the 312 structures – see Fig. 3.2 for a representation.

3.4 Dislocations

As with many crystalline materials, dislocations in MAX phases underpin their strength and ability to accommodate strain. The hexagonal close–packed structure, large c/a ratio and relatively weak M–A bonds in MAX phases result in the vast majority of dislocations being confined to the basal plane and often of screw, 30°, 60° or edge type [105], [143]–[146]. As such, they tend to align along the $\langle 11\bar{2}0\rangle$ and $\langle 10\bar{1}0\rangle$ directions. During plastic deformation, dislocations have been observed to pileup at grain boundaries, form walls and kink bands, and even interact to form entangled networks, all on the basal plane [147]–[150]. Production of basal dislocations in MAX phases can be due to the shearing of M–A bonds or radiation damage.

3.5 Grain Boundaries

As–sintered MAX phases generally contain high angle (> 10°) grain boundary misorientations, with both twist and tilt components [151]. However, upon compression, copious small angle grain boundaries have been reported to form, increasing the number of grains by over 300%. This is in–line with the commonly observed kink–bands and delaminations of MAX phases during mechanical deformation, which results in sub–grain formation. Farber *et al.* proposed a dislocation model for kink–bands in MAX phases, comprising mixed dislocations of opposite sign forming a dislocation wall [149]. If this wall contains an imperfect arrangement of dislocations, a small twist angle is expected, resulting in a grain boundary. Hexagonal screw dislocation networks have been observed to form in Ti_3AlC_2 under compression, which resulted in small–angle twist sub–grain boundaries [152]. In many ceramics, such as Al_2O_3, high temperature bulk mechanical performance is often deleteriously affected by thin (< 10 nm) amorphous regions in grain–boundaries, which flow into incipient microcracks during deformation [153]. Fortunately, observations of similar amorphous layers have not been reported for MAX phases to date.

A grain size effect is also evident in MAX phases, in which both bulk mechanical properties and grain morphology are a function of grain size. For Ti_3SiC_2, Ti_2AlC and Ti_2AlN, smaller grains (< 5 μm) are generally equiaxed and contribute to higher strength, whilst courser grains are more platelike and are present in samples with higher fracture toughness, thermal shock resistance and damping performance [138], [154], [155].

3.6 Mechanical Properties

The binary MX carbides and nitride precursors to the MAX phases are notoriously hard materials. For example, TiC and WC have Vickers hardness values of 30 GPa and 22 GPa, respectively [156]. The MAX phases, however, are surprisingly soft, often falling within the 2–8 GPa range for bulk indents [102]. However, if individual grains are sampled by a small indenter tip, i.e., nanoindentation, there is a strong hardness anisotropy relative to grain orientation. Grains with the basal plane perpendicular to the loading direction (*c*–axis) are considerably softer than for parallel (*a*–axis) indents. This is due to the increase in plastic deformation driven by delamination crack, ripplocation and kink band formation on unconstrained surfaces, in which dislocation nucleation accommodates a significant amount of the energy *via* in–plane to out–of–plane bond strain redistribution [102], [145], [157], [158]. This deformation mechanism, unique to layered crystalline solids, is also responsible for the limited *in–situ* crack healing ability of MAX phases. This has been demonstrated in single crystalline Cr_2AlC by Rathod *et al.*, in which basal plane crack growth is suppressed and even partially healed during in–plane

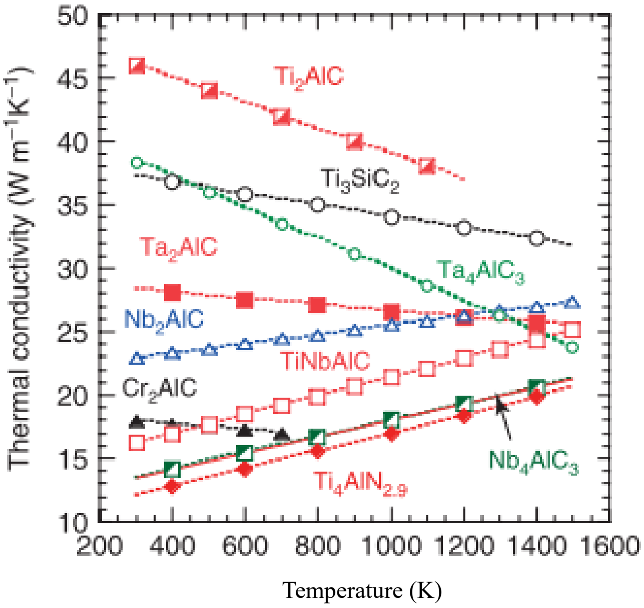

Fig. 3.3 – High temperature thermal conductivities of the MAX phases: A comparison of the thermal conductivities of Ti_3SiC_2, Ti_2AlC, Ta_4AlC_3, Ta_2AlC, Nb_2AlC, Nb_4AlC_3, Cr_2AlC, TiNbAlC and $Ti_4AlN_{2.9}$ at temperatures up to 1550 K. Reproduced from *MAX Phases: Properties of Machinable Ternary Carbides and Nitrides*, M. W. Barsoum, p. 112, Copyright (2013), with permission from John Wiley & Sons [102].

indentation of deformation constrained samples (normal to the basal plane) [159]. Additionally, indentation of MAX phases produces an increase in hardness both with decreasing indentation load and grain size, known as the indentation size effect [144], [160], [161].

The nanolaminated structure and relatively weak bonding between M– and A–layers result in a preferred slip system in the basal plane [162]. This explains MAX phases' relatively low hardness compared with parent ceramics such as TiC (~31 GPa), as well as their machinability, like metals [156]. This is a unique and useful property for ceramic materials, where the stiffness and brittleness of binary carbides and nitrides often result in difficulty machining. That said, the softness of the MAX phases is coupled with elastic stiffness ($E > 300$ GPa) and high fracture toughness (> 10 MPa $m^{1/2}$) – a unique combination in ceramics [102], [107], [163].

Foratirad *et al.* reported that an increase in impurity TiC content in Ti_3SiC_2 samples results in a proportional increase in Vickers hardness (up to 12.9 GPa for 39 wt.% TiC compared with 2–5 GPa reported by Barsoum *et al.*) [150], [164]. This is unsurprising given the hardness of the binary carbides in pure form – 28–35 GPa for TiC and 24–28 GPa for SiC [165]–[167]. Additionally, an increase in flexural strength was observed (750 MPa compared with 300 MPa reported by Barsoum), likely due to the increased microstructural resistance to deformation as a result of the presence of harder TiC grains.

3.7 Thermal Properties

Due to their reported high temperature stability, MAX phases have been proposed for use in high temperature applications, such as heating elements [168], electrical contacts [169], jet engine nozzle vanes [170] and high–temperature foil bearings [171].

Some MAX phases have shown unusual responses to high temperature environments, with an increase in thermal conductivity and yield strength with increasing temperature – often put down to their unique metallo–ceramic bonds and incipient kink band formation during mechanical deformation [102]. MAX phases display good thermal conductivities compared with their pure transition metal constituents over a range of temperatures – e.g. > 38 W m^{-1} K^{-1} for Ti_3SiC_2 compared with ~20 W m^{-1} K^{-1} for Ti [165], [172], [173]. At temperatures up to 300 K, MAX phases generally show a non–linear increase in thermal conductivity, κ_{th}, with a higher phonon conductivity, κ_{ph}, contribution than electronic conductivity, κ_e, contribution for S– and Al– based phases, and a higher electronic contribution ($\kappa_e > \kappa_{ph}$) for other phases.

A multitude of factors affect the thermal conductivity of solids, including the stiffness of covalent bonds, which scales with phonon conductivity; the density of free electrons, which controls the electronic conductivity; the presence and concentration of point defects, which limits conductivity; and the aptly named *rattler* effect, in which especially high vibrational displacements about atomic sites efficiently scatter phonons, thus reducing conductivity. As expected, the relative atomic sizes in solid solution MAX phases reduces the thermal conductivity. For example, the thermal conductivity of TiNbAlC is 50% lower than Ti_2AlC, and TiHfInC sees a 25% decrease compared to Ti_2InC [174], [175].

Above room temperature, κ_{th} is generally a linear function of temperature, with some MAX phases displaying an increasing κ_{th} and others a decrease. As shown in Fig. 3.3, the phases with low κ_{th} values at room temperature often see an increase with temperature, whilst for phases with relatively high κ_{th} values, the opposite is true. The thermal conductivities of MAX phases generally range from 26 to 60 W/m K, placing them between ceramics and metals [102].

A major drawback of conventional ceramics, despite their often excellent high temperature stability, is their characteristic susceptibility to brittle failure following thermal shock [176]–[180]. Several MAX phases, on the other hand, such as Ti_3SiC_2, Ti_3AlC_2 and Ti_4AlN_3 (to name a few), display unique behaviour under quenching above a critical temperature – their flexural strength increases with increasing quench temperature [103], [181]–[183]. This is highly unusual amongst ceramics and represents an essential property for in–chamber components in

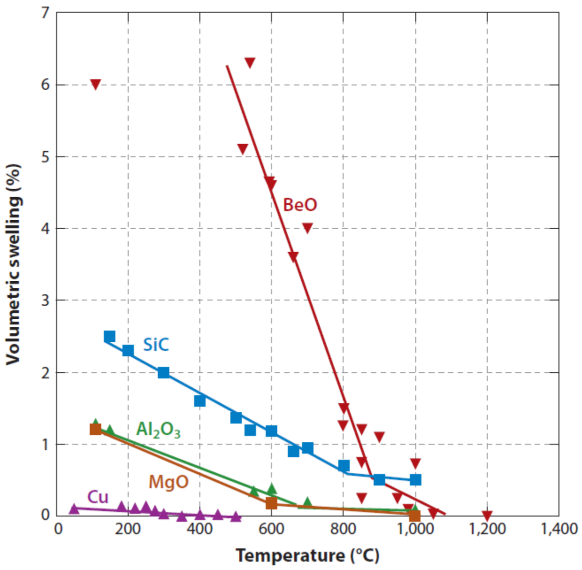

Fig. 3.4 – Radiation–induced swelling in ceramics: A comparison of the volumetric radiation damage induced swelling in some common ceramics over a range of temperatures up to 1200 °C. Reproduced from *Annual Review of Materials Research*, 44, 1, S. Zinkle and L. Snead, *Designing radiation resistance in materials for fusion energy*, p. 241–267, Copyright (2014), with permission from Annual Reviews, Inc. [464].

magnetic fusion devices, in which extreme thermal shocks resulting from plasma disruptions are expected to be common.

MAX phases have been repeatedly hailed in the literature as possessing remarkable high temperature resistance. Depending on the composition and environment, some MAX phases, notably Ti_3SiC_2, live up to this [102], [182], [184]–[186]. Other compositions, such as Cr_2GaN, are less stable at high temperatures [105]. MAX phases are known to thermally decompose peritectically into a combination of constituent binary carbides/nitrides and the A–layer element. Often, especially in Al–based phases, oxidation of the A–layer element can lead to the formation of stable and, at times, protective oxide scales, thus increasing resistance to further oxidation. Additionally, Low *et al.* studied the response of Ti_3SiC_2, Cr_2AlC, Ti_2AlC and Ti_3AlC_2 to a 1550°C vacuum, finding the higher order, 312 phases are less resistant to phase decomposition into binary carbide constituents [185]. The 312 phases readily dissociated into derivative 211 phases and TiC (e.g., $Ti_3AlC_2 \rightarrow Ti_2AlC + TiC$).

3.8 Chemical Stability

Ti_2AlC and Ti_3AlC_2 have shown resistance to chemical attack in water and air, *via* the formation of a passivating Al_2O_3 scale on surfaces, which prevents runaway oxidation [187], [188]. Cr_2AlC has displayed an excellent oxidation resistance, even at temperatures up to 1200 °C [189]. These phases, along with Nb_4AlC_3, Zr_3AlC_3, $Zr_2AlCTi_3SiC_2$ (amongst others) have also shown a resistance to corrosion in molten metals such as Na, Pb, Pb–Bi and molten salts such as FLiNaK, up to 750 °C and exposures up to 3500 h [190]–[193].

Oxidation–induced crack healing in other ceramics has been reported extensively in the literature [194]–[200]. Often this occurs due to either thermal diffusion or oxidation of free surfaces, with the surface oxidation route resulting more efficient filling of crack volumes. The ability of MAX phases to undergo this process was first reported by Song *et al.* in 2008 [201]. A Ti_3AlC_2 micro–crack of length ~7 mm and 5 μm average thickness was shown to heal completely following oxidation treatment at 1100 °C for 2 hours, *via* oxidation of Al–rich free surfaces to form α–Al_2O_3 and small quantities of TiO_2. This heralded a key advancement towards the potential application of MAX phases in extreme environments, such as nuclear reactors. A MAX phase coating that cracks due to anisotropic cyclic thermal expansion of its structural substrate may not portend its failure as a protective layer, at least not for long at high temperatures. An important aspect of this process was not investigated, however – the threshold temperature at which oxidative healing will reliably occur. Understanding the relationship between temperature and healing rate is key for nuclear fusion environments where thermal cycling to high temperatures occurs regularly.

3.9 Nuclear Applications

MAX phases have been proposed for use as coatings in current nuclear fission environments and even in structural applications for nuclear fusion devices [184], [202], [203].

SiC/SiC composites have gained much attention since their proposal as cladding materials for nuclear fission reactors [204]. Whilst they have demonstrated good in–core performance in test reactor environments, the joining of SiC/SiC component interfaces has proven an obstacle to further development. Initial studies showed Ti_3SiC_2/SiC composite joints display good mechanical performance ([205], [206]), with Katoh *et al.* later describing the effects of neutron irradiation at 800 °C on shear strength and microstructure as ‘minor or insignificant’ [207]. More recently, high purity (98.6%) ceramic matrix composites consisting of Cr_2AlC and a small amount (5–10 wt.%) of SiC fibres, were reported by Gonzalez–Julian *et al.* to improve mechanical performance compared with monolithic Cr_2AlC [208]. This could potentially pave the way to MAX phase composites with nuclear relevant properties. The first reported consideration of MAX phases for nuclear applications was in 2006, by Audubert *et al.* in CEA, France [209]. Initial thermal characterisations of Ti_3SiC_2 were performed, including a differential scanning calorimetry analysis of powdered Ti_3SiC_2 and liquid Na, showing no reactivity, with Na–cooled fast reactor environments in mind. At the point of publishing, two in–

reactor fast neutron irradiations of Ti_3SiC_2 were either in progress or planned – the first of their kind.

For future advanced reactors, such as Gen IV [210], material operational temperatures and radiation fluxes and fluences are considerably higher than current fission (Gen III) reactors and much closer to the expected conditions in a fusion PFM environment (see Fig. 2.5 for a visual comparison). Ti_3SiC_2 has been proposed in many Gen IV areas: as a fuel coating in GFRs (designed to operate at above 800 °C) [211]; as a candidate material for use in cladding and core applications in LFRs [212]; for pump impellers in the MYRRHA reactor project [213]; and in Pb–Bi eutectic environments [214], amongst others [184].

Table 3.2 – Bound defect energies for antisite and Frenkel–pairs in select MAX phases. The defects listed are the M–, A– and X–site Frenkel pairs (M_{FP}, A_{FP}, and X_{FP}, respectively), and the M–X, A–X and M–A antisite pairs (M_X–X_M, A_X–X_A, and M_A–A_M, respectively).

	Middleburgh *et al.* [215]		Zhao *et al.* [216]		Xiao *et al.* [217]			
Defect	Ti_3AlC_2	Ti_3SiC_2	Ti_3AlC_2	Ti_3SiC_2	Ti_3AlC_2	Ti_3SiC_2	Cr_2AlC	Ti_2AlC
M_{FP}	7.87	6.46	7.40	7.38	7.41	7.08	7.05	7.57
A_{FP}	4.00	2.59	3.42	3.30	3.60	3.20	7.26	3.67
X_{FP}	2.95	2.93	3.67	3.85	3.23	3.28	3.14	4.01
M_X–X_M	16.44	17.27	13.58	13.36	11.40	11.67	7.53	11.78
A_X–X_A	9.25	6.11	8.54	6.41	8.41	6.05	8.86	9.41
M_A–A_M	3.41	4.07	3.36	4.49	3.13	3.52	2.40	2.96

So, could MAX phases be suitable in a fusion environment? To qualify a MAX phase for operation, its expected behaviour under fusion relevant neutron irradiation at a variety of fluxes, fluences and temperatures must be fully understood. As this is not possible until the completion of a suitable fusion materials test facility, such as IFMIF, both computational and experimental simulation methods must be utilised. There exist plenty of examples in the literature of heavy ions, light ions, protons, fission spectrum neutrons and even electrons being used to impart lasting damage on materials to simulate their response under reactor–relevant neutron spectra, supported with respective modelling – both for fission and fusion applications. However, the literature is incomplete – especially with regards to nuclear fusion applications.

3.10 Ion vs Neutron Irradiation

To reliably test and validate materials for use in the fission industry, samples are exposed to similar environments in operational or test reactors, with periodic removal and characterisation [218]. However, the low availability, high cost, stringent sample requirements, at times unclear temperatures and neutron irradiation parameters, and target activation following irradiation can make this prohibitive [219]. Equally, these sorts of irradiations often take years to reach desired damage levels and are, therefore, not practical for many studies [220]. As such, even if test fusion reactors existed, materials irradiation studies would still not be efficient. The development of new and existing materials for fusion requires accelerated radiation damage testing at a range of temperatures to provide sufficient operational predictions.

A cost and time effective solution to this is the irradiation of specimens with charged particles, such as protons or heavy ions. These can be efficiently generated at sufficient energies and fluxes to emulate the primary knock–on atoms produced by high energy neutrons, with doses up to 100s of dpa attainable in a matter of days, rather than years. The sputtering and subsequent acceleration of ions from a variety of sources, producing species from H to U, allows the damage structures found in neutron irradiated material to be reproduced, albeit in a thin subsurface region (< 250 um) in the specimen.

Protons can be produced by spallation sources at energies of > 100 MeV, allowing the irradiation of larger volumes of material and at similar regimes to neutrons [62], [72], [205], [221]–[224]. However, the residual activation produced at such high energies is just as prohibitive as that from fission test reactor exposure. As such, lower energies of the order of 1–10 MeV are often utilised instead. This has the added benefit of increased displacement damage production at the same flux, due to the lower penetration of the ions. The issue, therefore, is that the damage is confined to a thin (< 250 µm) region, limiting the possible characterisation techniques to those sampling a near–surface area [225]–[227].

Over the years, a multitude of studies have attempted to rationalise the relationship between neutron and ion irradiations (e.g. [227]–[232] and references therein). In 300 series stainless steels, zirconium alloys and nuclear grade tungsten, proton irradiations in the literature have shown similarities to neutron damage in terms of segregation, microstructural changes and precipitate formation [227], [228], [232], [233].

3.11 Radiation Damage in MAX phases

In the past two decades, dozens of reports have been published on the response of MAX phases to irradiation, both with neutrons and ions – a summary of key results from many of these is displayed in Table 3.3. However, there has been notable contention over the exact mechanisms at play [234]. This is perhaps unsurprising given the chemical and structural diversity of the MAX phases, coupled with the multitude of irradiation species, temperatures, fluxes, fluences and environments employed in radiation damage studies. The result of this convoluted parameter space is increased difficulty in comparing the responses of different compositions to irradiation.

Table 3.3 – Irradiations of MAX phases: A summary of MAX phase irradiation studies in the literature, sorted by composition. Abbreviations are given for 'hexagonal close–packed' (HCP), 'solid solution' (S–S), and face–centred cubic (FCC).

Phase	Species	*E* (MeV)	*f* (cm^{-2})	Dose (dpa)	*T* (°C)	Key observations	Ref.
$(Ti_{0.95}Zr_{0.05})_3(Si_{0.9}Al_{0.1})C_2$	Xe^{23+}	92	2.5×10^{13}	8	20	Irradiation hardening to 22 GPa; saturation after 3.2 dpa	[203]
$(Zr_{0.5}Ti_{0.5})_3AlC_2$	H^+	2		0.01 –0.79	400 –600	Defect recovery above 400 °C	[235]
Cr_2AlC	Xe^{2+}	0.34	6×10^{14}	2.7	20	Full phase decomposition to MX	[236]
	Au	1	1×10^{16}	94	20	Full phase decomposition to MX	[237]

Phase	Species	E (MeV)	f (cm^{-2})	Dose (dpa)	T (°C)	Key observations	Ref.
Cr_2GeC	Xe^{2+}	0.34	1.5×10^{14}	0.81	20	Full amorphisation	[236]
Nb_4AlC_3	H^+	2		0.01 –0.79	400 –600	Defect recovery above 600 °C	[235]
Ti_2AlC	n	LWR	3.4×10^{20}	0.1	360(25)	Dislocation loops; black spots; electrical resistivity increase	[238]
	n	LWR	3.4×10^{20}	0.1	695(25)	Dislocation loops; electrical resistivity increase	[238]
	Au	1	2×10^{16}	165	20	Stacking faults; nano–TiC formation; β–transformation	[239]
	Au	1	2×10^{16}	83		MAX to HCP–γ (S–S) to FCC (SS) phase transformation	[240]
Ti_2AlN	n	LWR	3.4×10^{20}	0.1	360(25)–695(25)	Electrical resistivity increase, 36wt.% Ti_4AlN_3 formation	[238]
	Au	1	2×10^{16}	89		MAX to HCP–γ (S–S) to FCC (S–S) phase transformation	[240]
	He	70	1×10^{18}	7.5	20	Phase transformation begins below 1.1 dpa	[241]
Ti_2AlN_x–(Ti,Al)N film	Ar^{2+}	0.1		12		Slight anisotropic lattice parameter changes	[242]
$Ti_3(Al_{0.5}Si_{0.5})C_2$	Xe	2		0.15		Atomic disorder	[243]
$Ti_3(Si_{0.95}Al_{0.05})C_2$	Xe^{23+}	92	4.5×10^{13}	14.6	20	Irradiation hardening to 20 GPa; saturation after 3.2 dpa	[203]
Ti_3AlC_2	n	LWR	3.4×10^{20}	0.1	360(25)–695(25)	Dislocation loops; electrical resistivity increase	[238]
	He	0.5	1×10^{18}	52		He bubbles; dislocation loops	[244]
	Kr^{2+}, Xe^{2+}	1	6.25×10^{15}	25	20	Minor amorphisation	[245]
	Xe^{26+}	7	$2–4 \times 10^{15}$	6	20, 600	β–transformation at 2×10^{15}	[246]
	Ar^{2+}	0.24	1.5×10^{15}	1.7		A–layer disorder, annealing from 600 °C	[236]
	He	0.05		31	20	Antisite basal defects destroy nanolamellar structure; Frank loops, stacking faults; β–transition at 2.61 dpa	[247]
	Au	1	4×10^{16}	300	20	Full phase transformation to FCC (S–S)	[248]

Phase	Species	E (MeV)	f (cm^{-2})	Dose (dpa)	T (°C)	Key observations	Ref.
	He	0.05	1×10^{18}	52		Spherical and elongated bubbles, faulting zone, atomic disorder	[249]
	He	0.2		5.5	500	A–layer disorder	[250]
	H^+	1.5	1.44×10^{18}	0.1	350	*c*–axis expansion, *a*–axis contraction	[251]
$Ti_3Si_{0.9}Al_{0.1}C_2$	Kr^{20+}	74	1×10^{15}	3.25	20, 500	Hardness increase, annealed at 800 °C; β–transformation	[243]
	Xe^{23+}	92	1×10^{15}	4	20, 300, 500	Hardness increase, annealed at 800 °C; β–transformation	[243]
Ti_3SiC_2	Xe	930	1×10^{18}	0.01	20	*c*–axis expansion, *a*–axis contraction, minor amorphisation, black spots	[252]
	Au	4	1×10^{18}	0.05, 4.3	20	*c*–axis expansion, *a*–axis contraction, black spots	[252]
	Kr	74	1×10^{18}	0.08	20, 500	*c*–axis expansion, *a*–axis contraction, black spots	[252]
	Xe	92	1×10^{18}	0.22	20, 300	*c*–axis expansion, *a*–axis contraction, minor amorphisation, black spots	[252]
	Kr^{2+}, Xe^{2+}	1	6.25×10^{15}	25	20	Black spots	[245]
	Xe^{26+}	7	$2–4 \times 10^{15}$	6	20, 600	Minor amorphisation	[246]
	I^{2+}	2	3×10^{15}	10.3	200	Phase decomposition (partial); microcracks at grain boundaries; annealing of strain at 500–800 °C	[253]
	Xe	90				Grain boundary sputtering	[211]
	H^+	1.5	1.44×10^{18}	0.1	350	*c*–axis expansion, *a*–axis contraction	[251]
Ti_3SiC_2 (CG)	n	LWR	3.4×10^{20}	0.1	360(25)–695(25)	Electrical resistivity increase	[238]
Ti_3SiC_2 (FG)	n	LWR	3.4×10^{20}	0.1	360(25)–695(25)	Electrical resistivity increase	[238]
Ti_4AlN_3	Au	1	2×10^{16}	80		MAX to HCP–γ (S–S) to FCC (S–S) phase transformation	[240]
	He	70	1×10^{18}	7.5	20	Phase transformation begins below 1.1 dpa	[241]
V_2AlC	Au	1	1×10^{16}	80	20	FCC (S–S) transformation	[237]
Zr_3AlC_2	H^+	2		0.01–0.79	400–600	Defect recovery above 400 °C	[235]

As an approximation, dpa is used to compare radiation damage levels and response in ceramics such as MAX phases, as in other materials. However, the dpa value depends on a knowledge of the individual threshold displacement energies of atoms in a lattice. Accurate calculations for ceramics under neutron irradiation require in depth molecular dynamics simulations, like experimental data on neutron damage in ceramics such as MAX phases are limited. As a workaround, many neutron irradiation studies on MAX phases have used the silicon carbide damage cross–sections reported by Heinisch *et al.* in 2004 [254] – assumed to be a reasonable analogue due to the bonding similarities to MAX phase TiC – in conjunction with relevant neutron spectra to calculate dpa values in SiC. However, this analogy is not perfect and is therefore not entirely respective of the cross–sections in a Ti–based MAX phase.

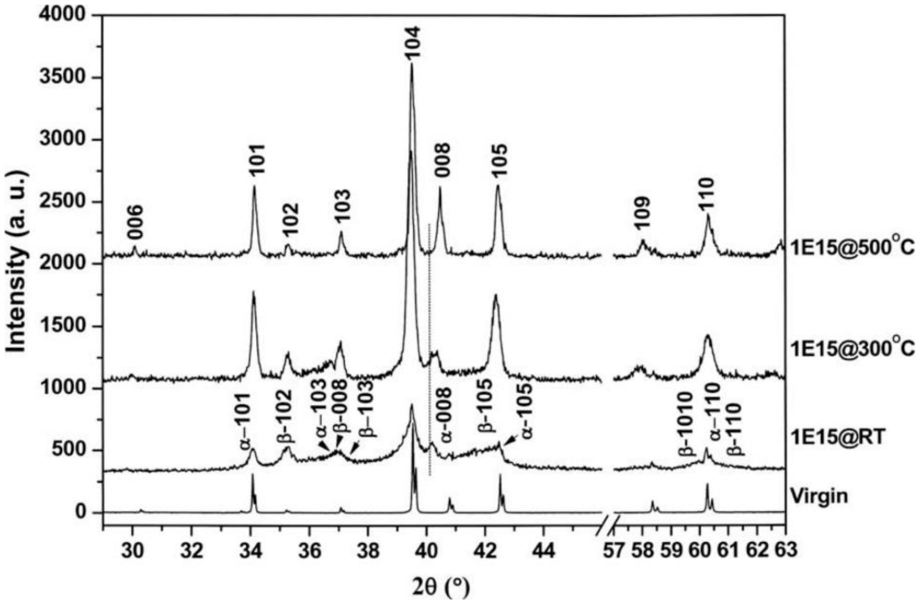

Fig. 3.5 – Irradiation induced phase transformation: X–ray diffraction (XRD) scans of $Ti_3Si_{0.9}Al_{0.1}C_2$ irradiated with 92 MeV Xe^{+23} ions to 1×10^{15} ions cm^{-2} at room temperature (RT), 300 °C and 500 °C. Peaks due to the original α–MAX phase and end–state β–polymorph are identified on the RT scan. Note the increasing basal peak shift to lower 2θ values at decreasing temperatures, indicated for the 0008 peak by a vertical line, which corresponds to an increase in *c*–lattice parameter. Reproduced from *Nuclear Instruments and Methods in Physics Research, Section B: Beam Interactions with Materials and Atoms*, 268, 5, X. Liu *et al.*, *XRD investigation of ion irradiated* $Ti_3Si_{0.90}Al_{0.10}C_2$, p. 506–512, Copyright (2010), with permission from Elsevier [270].

In ceramics, where covalent bonds often dominate physical property contributions, irradiation induced structural modifications, such as point–defect formation, phase transformation, amorphisation and decomposition, are common. For light ions, or heavier ions with low energies (< 1 MeV/u), electronic interactions in a target material are responsible for much of the energy transfer, resulting in many of these structural changes. Crystalline materials exposed to energetic particle radiation will generally undergo atomic disorder and, eventually, amorphisation. This is down to a combination of knock–on damage, radiolysis and, in the case of neutron bombardment, activation. Many MAX phases studied under irradiation have shown remarkable resistance to amorphisation, even at extremely high damage levels [234].

3.11.1 Modelling

The onset of radiation damage in MAX phases involves the production copious point defects [247]. Middleburgh *et al.* and Zhao *et al.* have calculated the isolated point defect formation energies (E_F) in Ti_3AlC_2 and Ti_3SiC_2 using DFT.

However, the results differed greatly as Middleburgh *et al.*'s work did not consider chemical potential elemental variations [215]. Xiao *et al.* then proceeded to investigate bound defects, so the stoichiometry remains constant during the simulation [217]. Their results were correlated with previous modelling work by including isolated defect values Table 3.2. It was found that the $M_A - A_M$ antisite and the C–Frenkel pair (C_{FP}) interstitial in select 211 phases have the lowest formation energies and are therefore the most likely to form.

Zhang *et al.* later confirmed that the $M_A - A_M$ antisite had the lowest E_F in Ti_3SiC_2 [255]. Xiao *et al.* suggested (seconded by Zhao *et al.* [256]) that a higher irradiation tolerance of Ti_3AlC_2 compared with Ti_3SiC_2 was likely due to the lower migration barrier energy of the $M_X - X_M$ antisite (despite being the antisite with the highest formation energy in all MAX phases, thereby being unlikely to remain post–irradiation) [217]. However, the neutron irradiation work by Tallman *et al.*, showing higher lattice instabilities in Ti_3AlC_2 than Ti_3SiC_2 at 350 °C and below, as well as

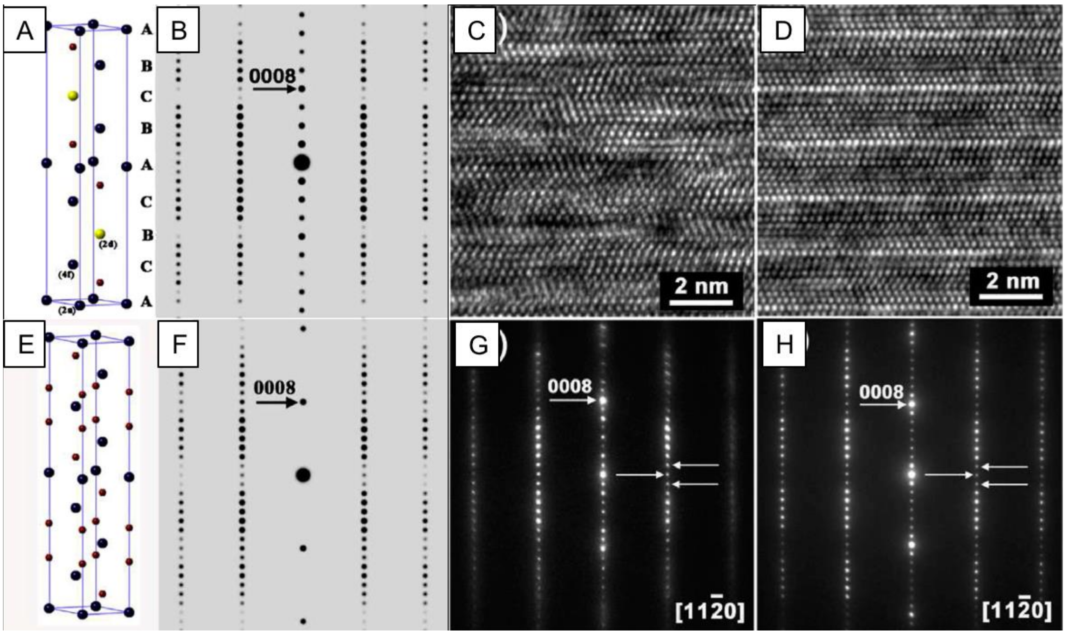

Fig. 3.6 – Evidence of the 'modified β–phase': Unit cell schematics of the conventional β–polymorph (A) and Huang *et al.*'s modified β–phase (E), in which A–atoms have been replaced with M–atoms. Corresponding electron diffraction patterns are shown in B and F, respectively. These are compared with high–resolution TEM (HRTEM) micrographs and corresponding SAED patterns of Ti_3SiC_2 (C, G) and Ti_3AlC_2 (D, H), respectively, following 7 MeV Xe ion irradiation at room temperature to a fluence of 2×10^{15} ions cm^{-2}. Reproduced from *Journal of Nuclear Materials*, 465, X. Liu *et al.*, *Irradiation resistance of MAX phases Ti_3SiC_2 and Ti_3AlC_2: Characterization and comparison*, p. 640–647, Copyright (2015), with permission from Elsevier [246]

the heavy ion irradiations performed by Huang *et al.* at 600 °C, are in direct contrast with these claims [238], [246], [257].

Middleburgh *et al.* claimed that the C and Ti interstitials will have the most impact following irradiation of Ti_3SiC_2, due to the defects' low energy state and mobility [215]. However, the migration and recombination of Si interstitials are, theoretically, energetically inexpensive. For Ti_3AlC_2, Ti interstitial defects are thought to be dominant due to enhanced migration – although no experimental data exists to confirm this.

Nonetheless, the underlying indication is that the majority of point defects in the MAX phases studied are likely to be A– or X–based. DFT investigations by Wang *et al.* have indicated that Ti_2AlC is stable up to an Al deficiency of 50%, as a result of copious A–site vacancies, with similar reports for Ti_3SiC_2 and Ta_4AlC_3 by other authors [258], [259]. Combined with the low migration energy barrier (< 1 eV) of

A–vacancies in the basal plane, this could be instrumental in enabling the diffusion of A–layer elements at high temperatures to potentially form protective Al_2O_3 scales on either free surfaces or in microcracks [260], [261]. It should be emphasised that defect calculations have only been reported for a select number of compositions, including Ti_3SiC_2, Ti_3AlC_2, Cr_2AlC, Cr_2GeC, Ti_2AlC and Ti_2AlN [262]. Investigations into the defect production and mobility in other compositions are notably absent from the literature.

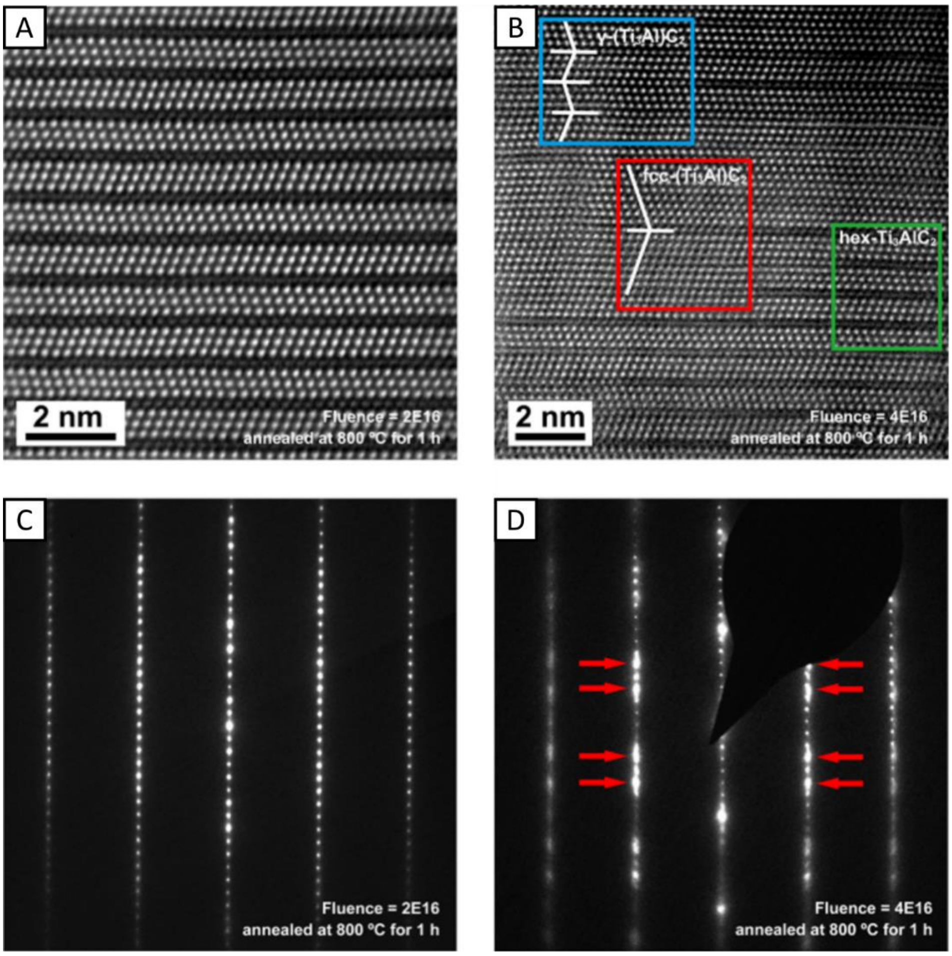

Fig. 3.7 – Direct observation of ion irradiation–induced phase transformations in Ti_3AlC_2: HAADF–STEM micrographs (A, B) and corresponding SAED patterns (C, D) of Ti_3AlC_2 irradiated with Au ions at room temperature to fluences of (A) 2×10^{16} cm^{-2} and (B) 4×10^{16} cm^{-2}. The latter contains local examples of all three stages of the Ti_3AlC_2 – γ–$(Ti_3Al)C_2$ – FCC–$(Ti_3Al)C_2$ phase transformation, indicated by coloured boxes. Reproduced from *Applied Physics Reviews*, 7, 4, C. Wang *et al.*, *Radiation effects in* $M_{n+1}AX_n$ *phases*, p. 1–28, Copyright (2020), with permission from AIP Publishing [265].

3.11.2 Experimental Observations

Like many industrial ceramics, such as SiC and metal oxides, MAX phases undergo anisotropic unit cell expansion during irradiation [96], [97], [263], [264]. The vast majority of studies report a decrease in *a*–lattice parameter and increase in *c*–lattice parameter, regardless of flux, fluence, temperature or irradiation specie [265]. These instabilities, observed even at doses as low as 50 mdpa, are thought to be a result of the formation of a combination of defects. These are X–site Frenkel defects, leading to an increase in both *a*– and *c*–lattice parameters, and M_A–A_M antisites, which lead to a decrease in *a*– and increase in *c*–lattice parameter [235], [251]. Both neutron and ion irradiation studies report similar qualitative anisotropic lattice changes [211], [238], [269], [270], [243], [246], [250], [252], [257], [266]–[268].

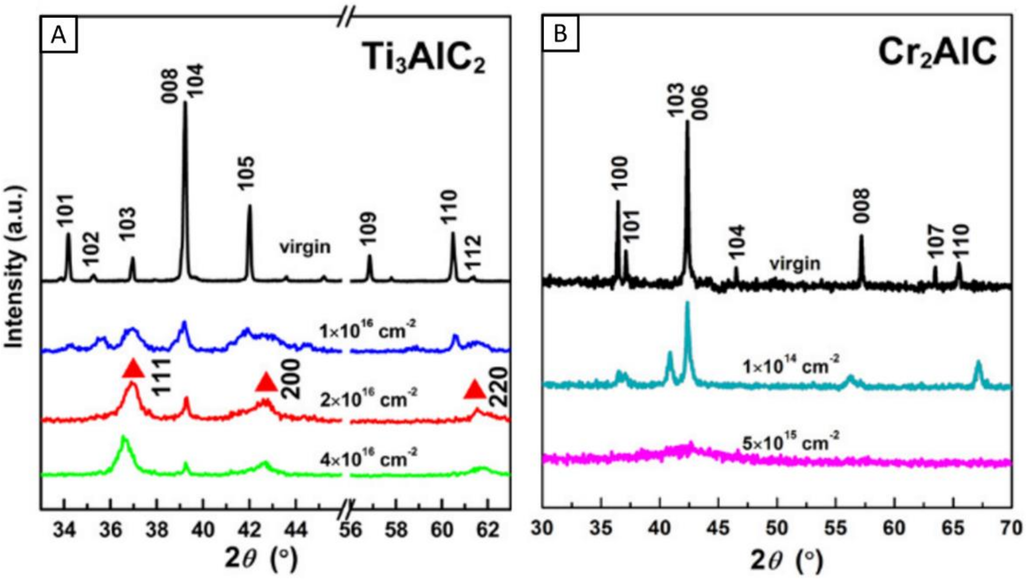

Fig. 3.8 – Amorphisation resistance in Ti$_3$AlC$_2$ and Cr$_2$AlC: XRD diffractograms of (A) Ti$_3$AlC$_2$ at fluences from 0 (virgin) to 4 × 10^{16} Au ions cm^{-2} and (B) Cr$_2$AlC at fluences ranging from 0 to 5 × 10^{15} Au ions cm^{-2}. Peaks identified as the FCC–$(M_{n+1}A)X_n$ phase have been indicated by triangles. Note the almost total loss of crystallinity, indicated by a disappearance of all well–defined peaks, in Cr$_2$AlC at an order of magnitude lower fluence than Ti$_3$AlC$_2$, which is still partially crystalline. Reproduced from *Applied Physics Reviews*, 7, 4, C. Wang *et al.*, *Radiation effects in* $M_{n+1}AX_n$ *phases*, p. 1–28, Copyright (2020), with permission from AIP Publishing [265].

These lattice evolutions cause anisotropic microstrain which leads to cracks, especially at grain boundaries, and is particularly evident at low temperatures, where defect migration and recombination is supressed. This has been reported following neutron irradiation by Tallman *et al.* [257], heavy ion irradiation by Clark *et al.* [271], proton irradiation by Ward *et al.* [251] and others [252], [271]–[273]. At higher temperatures (> 700 °C), where irradiation–induced lattice strains are reduced, microcracks are also supressed to an extent. In addition to lattice parameter instabilities, the formation of defects reduces the mobility of dislocations, both pre–existing and irradiation–induced, which causes hardening of the microstructure, as observed in several studies [271], [272], [274], [275].

3.11.3 Heavy Ions

The first irradiation resistance assessment of MAX phases was performed by Nappe *et al.* in 2009, with heavy ion irradiations of Ti_3SiC_2 at room temperature to various fluences [211]. 4 MeV Au ions led to amorphisation at high fluences (10^{15} cm^{-2}), whilst 90 MeV Xe^{23+} ions led to the characteristic anisotropic lattice parameter changes (*c*–axis expansion; *a*–axis contraction) at low fluence, evolving into grain boundary cracking and amorphisation at higher fluence. The same authors then studied the effect of increasing temperature on heavy ion radiation damage in Ti_3SiC_2, at 200 °C and 500 °C. The lattice parameter changes were found to be less severe at higher temperatures [252], [269]. It was also concluded that nuclear interactions (rather than electronic as previously thought) were responsible for the changes.

Liu *et al.* irradiated $Ti_3Si_{0.9}Al_{0.1}C_2$ with 92 MeV Xe^{+2} ions to 1×10^{15} ions cm^{-2}, resulting in 3.25 dpa at a depth of 7.5 µm, at room temperature, 300 °C, and 500 °C [270]. XRD showed significant peak shifts in all irradiated sample patterns, relating to an expansion of the *c*–parameter. It was speculated that an α– to β–phase transformation – i.e. a lateral shift of the A–layer stacking (see Fig. 3.2), may have occurred during irradiation, potentially seen in an 0008 XRD reflection shift at room temperature post–irradiation (Fig. 3.5). However, the lattice parameter shift this would relate to (9.3% increase) is so severe that cracking of the MAX phase

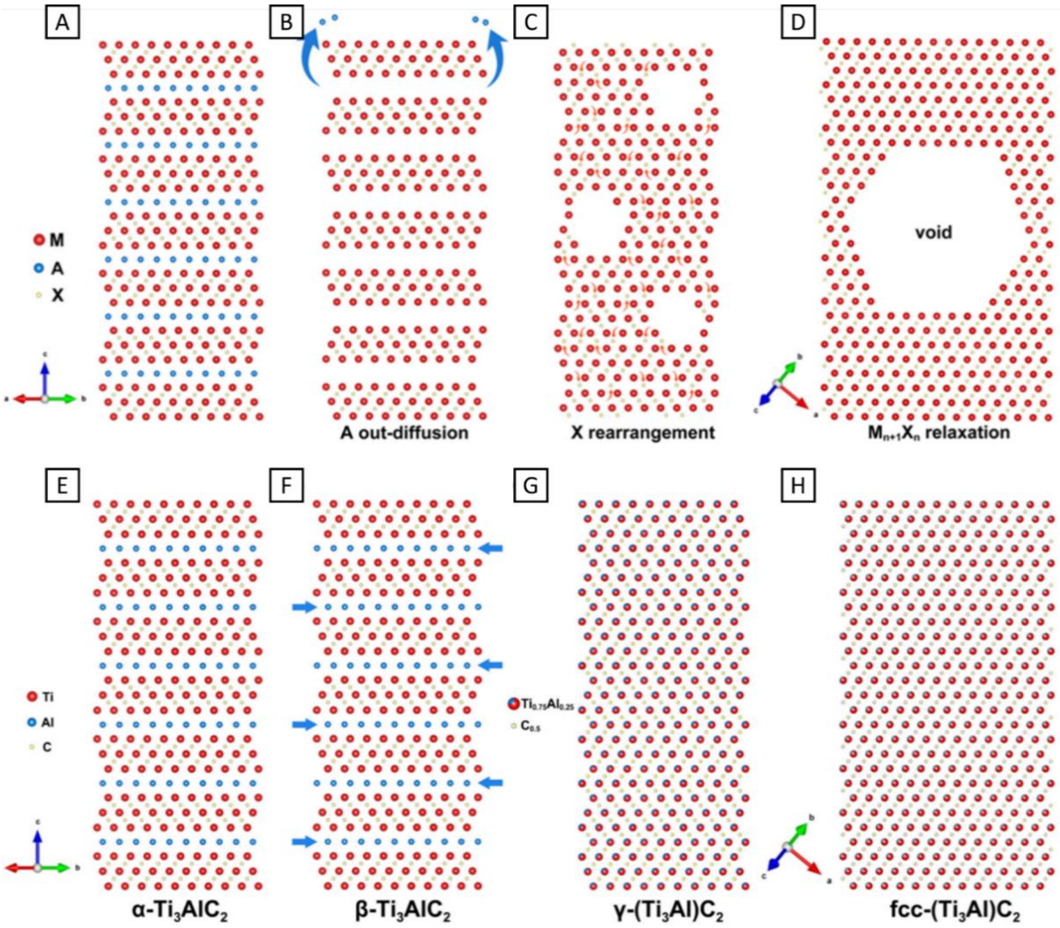

Fig. 3.9 – Decomposition and transformations in irradiated MAX phases: The proposed mechanisms for high temperature phase decomposition (A), showing diffusion and loss of the A–layer (B), X–site rearrangement, and void formation (C), resulting in the formation of FCC–$M_{n+1}X_n$ (D); and proposed ion irradiation induced transformations from α–$M_{n+1}AX_n$ – β–$M_{n+1}AX_n$ – γ–$(M_{n+1}A)X_n$ – FCC–$(M_{n+1}A)X_n$ (E – H, respectively). Reproduced from *Applied Physics Reviews*, 7, 4, C. Wang *et al.*, *Radiation effects in $M_{n+1}AX_n$ phases*, p. 1–28, Copyright (2020), with permission from AIP Publishing [265].

would likely have been extensive. As no cracking was observed, this shift is uncertain.

Huang *et al.* reported the formation of β–phase at room temperature, following irradiation of Ti_3SiC_2 and Ti_3AlC_2 with 7 MeV Xe^+ ions, using a combination of XRD, selected area electron diffraction (SAED) and simulated electron diffraction patterns for analysis [246]. They modified the β–phase unit cell to include Ti atoms in the A atom site (suggested by Yang *et al.* to cause the phase transformation [247]). The similarities between the SAED patterns of the modified β–phase and the irradiated Ti_3SiC_2 and Ti_3AlC_2 suggest the formation did indeed occur, as seen in Fig. 3.6.

However, the β–phase was not identified in all XRD refinements, including at room temperature. As the β–phase was absent from all higher temperature irradiations (300 and 500 °C) – suggested to be due to the higher Si mobility causing migration from the 2d to the 2b Wyckoff position (see Fig. 3.6), no distinct correlation between the phase transformation and irradiation temperature can be made. To take this further, it was speculated that Huang *et al.* may have misidentified the β–phase – more recent irradiations, performed by Liu *et al.* with 1.1 MeV C^+ on Ti_2AlC at room temperature and 600 °C (to various fluences), produced similar SAED patterns as those of irradiated Ti_3AlC_2. Additionally, the layered structure, post–irradiation, is similar.

Ward *et al.* also pointed out that the accumulation of point defects in 312 MAX phases will cause a shift in structure factors, leading to a change in XRD reflection intensities – subsequently providing a better fitting for the observed intensity changes in previous XRD spectra of irradiated MAX phases [238], [246], [257],

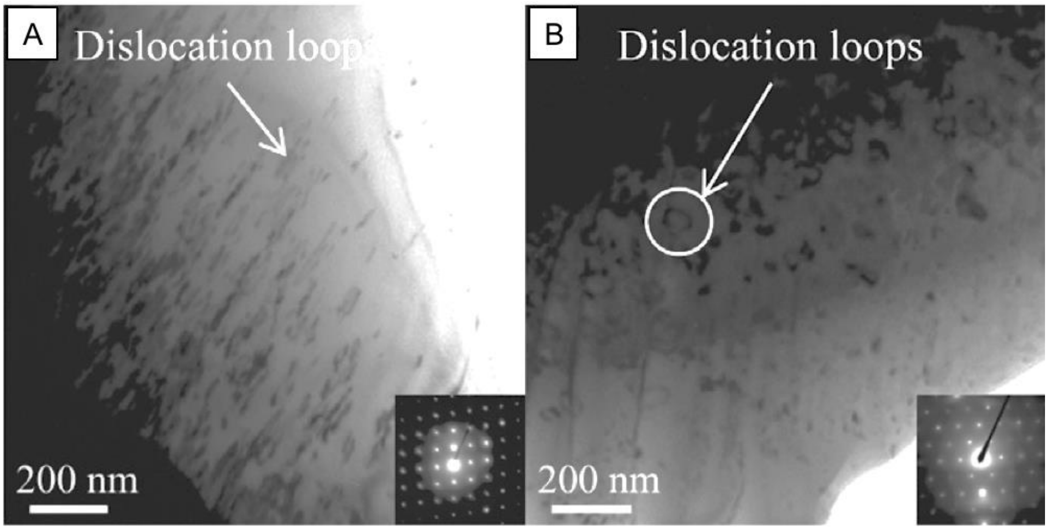

Fig. 3.10 – Dislocation loops in irradiated MAX phases: Ti_3AlC_2 following neutron irradiation to 0.1 dpa at 360 °C, with basal dislocation loops visible in TEM micrographs as viewed down the $(11\bar{2}0)$ (A) and (0001) (B) zone axes. Reproduced from *Acta Materialia*, 85, D. Tallman *et al.*, *Effect of neutron irradiation on select MAX phases*, p. 132–143, Copyright (2015), with permission from Elsevier [238].

[271]. Further evidence that point defects are likely responsible for lattice parameter changes in 211 phases was provided by Wang *et al.* and Huang *et al.*, who showed that the Cr_{Al} antisite provides the necessary characteristic lattice parameter changes in Cr_2AlC under irradiation [237], [267].

Wang *et al.* attempted to address this issue and resolve the contention over the radiation damage mechanisms responsible. The authors used annular bright field (ABF) and high–angle annular dark field scanning TEM (HAADF–STEM) to observe direct evidence for M_A–A_M antisite clusters – as predicted by theoretical reports in the literature [234]. Ti_3AlC_2 was irradiated up to 300 dpa at room temperature using 1 MeV Au ions. No evidence of amorphisation was observed, confirming an extremely high resistance to irradiation. However, rather than the phase decomposition to a face–centred cubic (FCC) TiC phase, as reported by several prior authors, Wang *et al.* observed a full transformation of the Ti_3AlC_2 matrix to a solid–solution FCC–$(Ti_3Al)C_2$ rock salt–like phase, *via* an intermediary solid solution hexagonal close–packed (HCP) $(Ti_3Al)C_2$ phase after < 2.3 dpa. Some of their observations can be seen in Fig. 3.7.

The authors proposed that the accumulation of M_A–A_M antisites and radiation induced redistribution of X–atoms forms the solid–solution γ–$(M_{n+1}A)X_n$ phase, from the initial $M_{n+1}AX_n$. This structure remains HCP, albeit with an increase in *a*– and *c*–lattice parameters. Observations in the literature of an expansion in the *c*–axis and contraction in the *a*–axis, with an overall volume expansion, can then be explained by the formation of C_{FP} defects and A vacancies, or otherwise out–diffusion of Al from the MAX structure during irradiation, leading to an overall decrease in the *a*–lattice parameter. Interestingly, a similar γ–$(M_{n+1}A)X_n$ structure was first observed during the crystallisation of Cr_2AlC from Cr–Al–C amorphous coatings in 2011, by Abdulkadhim *et al.* [276], suggesting the initial phase transformation may be reversible.

As the irradiation fluence was increased, bringing the Ti_3AlC_2 irradiation dose to $>$ 150 dpa, Wang. *et al.* observed a further phase transformation to an FCC–$(M_{n+1}A)X_n$ structure, with lattice parameters smaller than those of the precursor MX carbides or nitrides. Evidence of this transformation was reported by the same authors in an earlier study, using XRD scans to identify FCC phase, as shown in Fig. 3.8. This was explained through dislocation dissociations introducing copious stacking faults, resulting in a phase transformation to the FCC symmetry above a threshold fault density. The authors concluded that, because no evidence of Al out–diffusion was observed, even to very high damage levels (in fact, the Ti:Al ratio at 300 dpa was identical to the virgin Ti_3AlC_2), and the irradiations were all performed at room temperature, the phase transformation could only be irradiation–induced. Incidentally, it was proposed that previous reports of irradiation–induced phase decomposition are erroneous.

However, this was perhaps premature, as the effect of temperature was excluded from Wang *et al.*'s discussion. It is likely, after all, that synergistic relations between temperature and radiation damage affect the rate or extent of atomic disordering and even phase decomposition and will, therefore, affect the $M_{n+1}AX_n \rightarrow \gamma$–$(M_{n+1}A)X_n \rightarrow$ FCC–$(M_{n+1}A)X_n$ transformation. Equally, whilst the author's irradiations were performed with no external heating, local beam heating due to damage cascades will likely encourage defect mobility, especially at high dose rates. Of course, short of fully characterising the end–point FCC phases reported by previous authors, this matter can only be settled by extending similar observations to high temperature irradiations. It must be emphasised at this point that the phase transformation described begins at < 2.3 dpa, at which point the nanolaminar MAX structure has already transformed to the γ–$(M_{n+1}A)X_n$. Then, it isn't until ~150 dpa that the γ–$(M_{n+1}A)X_n \rightarrow$ FCC–$(M_{n+1}A)X_n$ transformation occurs. As such, strictly speaking it is γ–$(Ti_3Al)C_2$ and FCC–$(Ti_3Al)C_2$, rather than the Ti_3AlC_2, that display excellent resistance to amorphisation.

According to theoretical predictions and experimental characterisation by Bugnet *et al.*, the end structure after the irradiation–induced phase transformation of Ti_3AlC_2 at a dose of 2 dpa is FCC–$Ti(Al_{0.33}C_{0.67})$, rather than FCC–$(Ti_3Al)C_2$ [136]. However, without direct observational evidence of this and in light of the report of the intermediary γ–$(M_{n+1}A)X_n$ structure at low fluences, not to mention the similar lattice parameters of both phases, it is possible that the authors' model was incorrect. Nonetheless, their research provided one of the first reliable analysis on antisite formation in MAX phases.

Based on these observations, the proposed irradiation–induced transformation pathway for MAX phases at room temperature is:

1. Point defects, primarily Frenkel pairs, are produced in large quantities by radiation damage cascades.
2. Defect migration and copious M_A–A_M antisite formation triggers a shearing of the relatively loosely bound A–layer to form a β–$M_{n+1}AX_n$ phase – a polymorph of the conventional α–$M_{n+1}AX_n$. This assumes the target material begins in the α–phase.
3. Atoms in the X–site are redistributed during irradiation due to changes in local bonding structure and a low threshold migration energy.
4. A solid–solution HCP γ–$(M_{n+1}A)X_n$ phase is formed due to the accumulation of sufficient antisites and full redistribution of X–atoms into a metastable configuration.
5. Further radiation damage–induced dislocations in the basal plane dissociate to form basal stacking faults.
6. Above a critical density of stacking faults, a transition to a solid–solution FCC–$(M_{n+1}A)X_n$ phase is triggered.

A schematic of this transformation pathway, alongside an often–proposed decomposition mechanism, is displayed in Fig. 3.9. Ample evidence for the $M_{n+1}AX_n \rightarrow$ γ–$(M_{n+1}A)X_n \rightarrow$ FCC–$(M_{n+1}A)X_n$ transformation exists elsewhere in the literature in the form of XRD, SAED and HRTEM observations for Ti_2AlC, Cr_2AlC, Ti_2AlN, V_2AlC, Ti_3AlC_2, Ti_3SiC_2 and Ti_4AlC_3 [236], [237], [239], [240], [246], [247], however the effect of temperature has not been addressed in detail.

Evidence of an α–β phase transformation has been observed by Liu *et al.* for $Ti_3Si_{0.9}Al_{0.1}C_2$ irradiated with 92 MeV Xe ions, as well as by Deng *et al.* in Ti_3AlC_2 after 1 MeV C^{4+} irradiation [270], [277]. Whether this is a result of an increase in A–vacancies or an effect of radiolysis, is unknown. However, these reports are unique in the literature on irradiated MAX phases. Due to the low formation energy

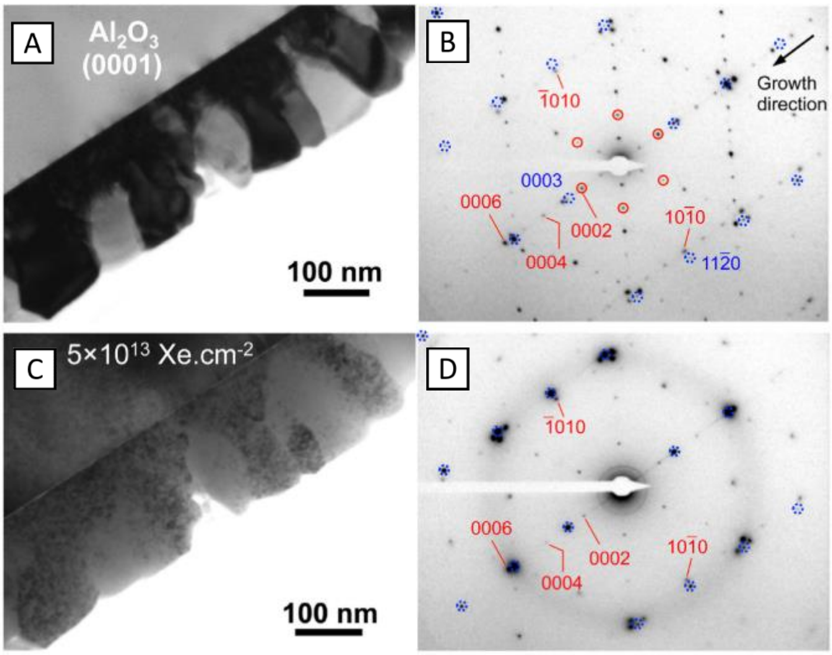

Fig. 3.11 – Phase transformations in Cr_2AlC and Cr_2GeC: TEM micrographs and associated SAED patterns of (A) Cr_2AlC and (B) Cr_2GeC, after irradiation with Xe ions to fluences of 1×10^{14} cm^{-2} and 5×10^{13} cm^{-2}, respectively. Note the variation in the diffuse amorphous ring appearing in both figures, as well as the difference in fluence, indicating a considerably lower amorphisation resistance of Cr_2GeC. Reproduced from *Journal of Nuclear Materials*, 441, 1–3, M. Bugnet *et al.*, *Chemically sensitive amorphization process in the nanolaminated Cr_2AC (A = Al or Ge) system from TEM in–situ irradiation*, p. 133–147, Copyright (2013), with permission from Elsevier [236].

of antisites, coupled with high mobility of A–layer atoms along the basal plane, it is likely that the $\alpha - \beta - \gamma$–$(M_{n+1}A)X_n$ transition occurs concurrently. Therefore, it is possible that the lack of common observation of the β–phase is either because it was missed due to the narrow fluence margin of formation, or that its relative abundance was below detection limits in XRD.

However, an important takeaway from the $\alpha \rightarrow \beta \rightarrow \gamma$–$(M_{n+1}A)X_n$ → FCC–$(M_{n+1}A)X_n$ irradiation–induced transformation model is the current lack of neutron irradiation data to support it. After all, the purpose of ion irradiations of this sort is to emulate nuclear reactor environments which involve high energy neutrons. If this transformation pathway is unique to heavy ion irradiations, then its applicability to the simulation of neutron damage becomes rather limited.

3.11.4 Neutrons

Tallman *et al.* studied neutron irradiation of Ti_3AlC_2, Ti_2AlC, Ti_3SiC_2 and Ti_2AlN to 0.1 dpa at 360 and 695 °C [238]. At the lower temperature, similar anisotropic lattice parameter changes to the literature (observed with XRD), as well as an increase in the intensity of XRD reflections associated with impurity MX binaries observed in the virgin material, were found for all samples. However, Ti_3AlC_2 displayed an unprecedented increase in TiC – far higher than the other samples, (1.9 wt.% to 52.6 wt.% and 44.8 wt.%, for low and high temperature irradiations, respectively). It was suggested that the removal of the A–layer is responsible for this, although it is unknown why the change was so drastic.

Using TEM, the presence of dislocation loops and anisotropic lattice parameter changes have been confirmed at low temperature for high fluence neutron and heavy ion irradiations by Ang *et al.*, Zhang *et al.*, Huang *et al.*, Liu *et al.* and Whittle *et al.* [245], [253], [266], [267], [270]. Nappe *et al.* reported 'black dots' in images of the layered structure of heavy ion irradiated Ti_3SiC_2 (3 dpa, 950 °C) [252], [269]. It was suggested that these were evidence of Frenkel pair or loop agglomerations – inspired by Le Flem *et al.*'s work, in which dark region perturbations in the layered structure were observed in room temperature, 92 MeV Xe, 0.15 dpa irradiated $Ti_3(Al, Si)C_2$ (4.5×10^9 ions cm^{-2} s^{-1}) [243]. Equally, both works reported characteristic anisotropic lattice parameter changes. However, the TEM structures observed differed slightly across the studies: the higher damage samples from Nappe displayed stacking changes which are not present in Le Flem's low dose irradiations, in which it was suggested that the features could be clusters of interstitials or loops (< 3 nm in size). Unfortunately, no correlation was possible between fluence and loop density due to the unknown sample thicknesses.

Yang *et al.* irradiated Ti_3AlC_2 with 70 keV He ions to 13.7 dpa at room temperature and reported a structural change from HCP MAX phase ($P6_3/mmc$) to cubic ($Fm3m$) [278]. A change in stacking sequence was observed at 3 dpa, which was not seen in lower dose samples. This correlates well with the reports by Le Flem *et al.* and suggests that a stacking change occurs at high damage levels. Incidentally, this indicates that stacking changes are not responsible for the anisotropic lattice parameter changes.

Tallman *et al.* reported similar defect structures as Le Flem *et al.*, although considerably larger, in TEM investigations of neutron irradiated Ti_3AlC_2 (Fig. 3.10) [238]. The increased size of the structures could be due to the longer irradiation time, allowing increased diffusion of point defects into clusters and dislocation loops. Further TEM investigations by Tallman *et al.* revealed a burgers vector of the loops to be $b = ½[0001]$ [279].

TEM analysis of Ti_2AlC irradiated with pressurised water reactor (PWR) neutrons up to 10 dpa at 1000 °C revealed needle like precipitates, suggesting a level of phase decomposition not seen in other irradiations [280]. Whether this was due to radiation damage, thermal effects at high temperature or a combination of the two is unclear. In more recent irradiations, Tallman *et al.* reported significantly less decomposition (to TiC) at ~0.14 dpa (114 and 735 °C), ~1.6 dpa and ~3.4 dpa at ~735 °C [279]. These irradiations showed negligible lattice parameter changes at temperatures above 700 °C.

3.11.5 Light Ions

In addition to heavy ions, such as Au, Kr and Xe, MAX phases such as Ti_3AlC_2 have also shown excellent amorphisation resistance to light ion (such as H or He) irradiation.

The first proton irradiations of MAX phases were performed by Ward *et al.* in 2018. Ti_3SiC_2 and Ti_3AlC_2 were irradiated with 1.5 MeV protons at 350 °C to 0.1 dpa (1.438×10^{18} protons cm^{-2}), at a dose rate of 4.57×10^{-6} dpa s^{-1}. Both materials developed characteristic expansions of the *c*–lattice parameter and slight contractions in the *a*–parameter, as shown in Fig. 3.12, along with extensive microcracking at grain boundaries. Additionally, an increase in FCC phase, presumed to be either TiC or a solid solution FCC–$(Ti_3Al/Si)C_2$ phase, was observed with XRD. The effects were more pronounced for Ti_3AlC_2, indicating a lower resistance to damage. That said, HAADF–STEM analysis showed no loss in

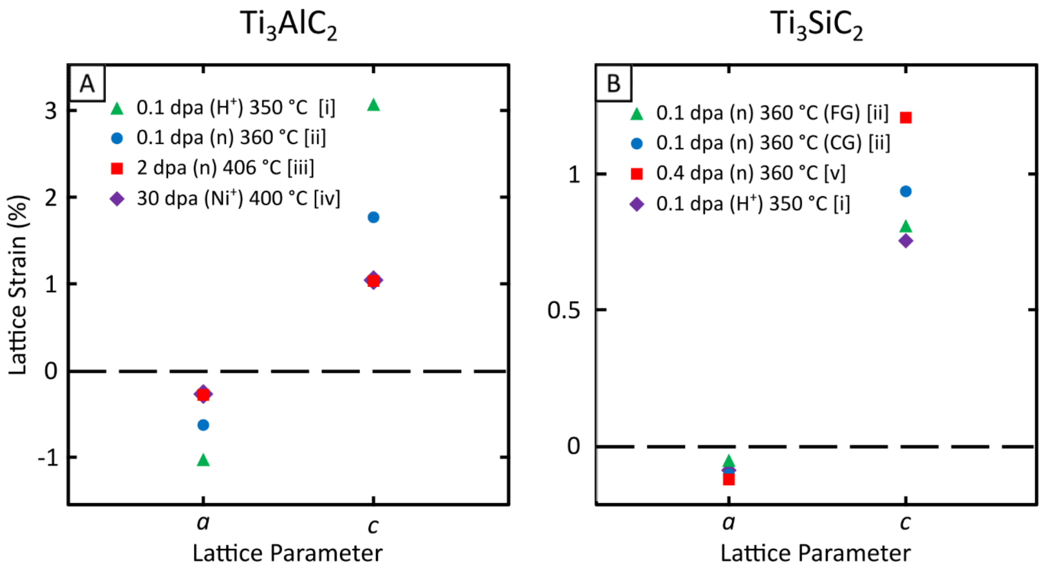

Fig. 3.12 – Comparisons of lattice instabilities in Ti_3SiC_2 and Ti_3AlC_2 following various irradiation conditions. The references [i–v] are [238], [251], [257], [266], [467], respectively.

the nanolaminated structure following irradiation, representing a resistance to amorphisation. As with heavy ion irradiation, it is assumed that M_A–A_M antisite formation was responsible for the observed lattice instabilities, supported by defect formation and mobility DFT calculations [251].

In a later study of the same materials, but with 2 MeV protons and at 350–600 °C, Ward *et al.* reported lattice strain following an inverse linear trend with irradiation temperature, indicating lattice defect mobility induced recovery [281]. As well as undergoing higher lattice strain, Ti_3AlC_2 showed a significantly weaker lattice recovery response with irradiation temperature, compared to Ti_3SiC_2. The authors extrapolated the temperature *versus* *c*–parameter strain relation, estimating threshold recovery temperatures of ~685 °C and ~1050 °C for Ti_3SiC_2 and Ti_3AlC_2, respectively. Additionally, at 350 °C and 5.4×10^{-6} dpa s^{-1} the Ti_3AlC_2 samples underwent bulk mechanical exfoliation of the target region during irradiation – with failure occurring the Bragg peak. It is possible that the trapping and accumulation of hydrogen caused the exfoliation, due to a more sluggish diffusion of protons in the Ti_3AlC_2 lattice. However, more investigation is required for this to be confirmed.

As discussed in section 2.2.3 (Chapter 2), an understanding of the diffusion, retention, and agglomeration of He in MAX phases and the effects of these mechanisms on material properties is important for successful utilisation in demanding environments.

Jia *et al.* modelled the effect of He impurities in Ti_3SiC_2, finding that He segregates near Si planes, weakening cohesion between Si–Ti layers and potentially leading to delamination [282]. Additionally, it was found that two He atoms can occupy a single Si vacancy site in a dumbbell formation, resulting in enhanced lattice strain. This was validated by Zhang *et al.* in 2015, who performed similar simulations for Ti_3SiC_2, but over a variety of temperatures, finding a threshold for He impurity mobility and diffusion, leading to damage annealing at temperatures above ~300 °C [283]. Similar results for Ti_3SiC_2 were reported by Song *et al.*, who predicted a preferential agglomeration of He atoms in the Si layer, which is supressed beyond clustering of 7 He atoms above ~500 °C, corresponding to a lattice volume expansion of around 2% [284]. Similar behaviour is expected in Ti_3AlC_2, in which He atoms are reported to prefer to reside in the basal plane, with Al vacancies posing as favourable trapping sites over Ti or C [285]. This supports observations of the formation of He platelet bubbles in Ti_3AlC_2 under irradiation. Additionally, spherical bubbles were predicted to form due to He trapping in C vacancy sites – explaining the various bubble morphologies seen later in experimental He^+ irradiations of MAX phases (e.g. [244], [286]).

Yang *et al.* took this further, showing an anisotropic diffusion preference of H and He impurities in Ti_3AlC_2 – along the c–axis, whilst preferentially occupying octahedral interstitial sites [287]. Liu *et al.* partially confirmed this in similar first–principles calculations, showing that H and He occupied tetrahedral and octahedral interstitial sites respectively, in pristine Ti_3AlC_2 [288]. It was also found that He agglomeration suppresses further aggregation of H atoms, a potentially desirable mechanism for the suppression of tritium fuel retention in fusion materials.

In MAX phases exposed to He^+ ion irradiation at high fluence, the formation of spherical and lenticular bubbles in the basal plane has been observed empirically by several authors in the literature, including during *in–situ* TEM He^+ ion irradiation [244], [273], [274], [289]. In contrast to radiation damage effects discussed previously, in which recovery is promoted at high temperatures, He bubbles grow in size at increasing temperatures due to the enhanced mobility of He atoms [244]. Whilst these bubbles are primarily observed in the basal plane, they also coalesce at grain boundaries, thought to be due to the presence of misfit dislocations acting as nucleation sites [290]. The primary issue with He bubbles is their deleterious effect on bulk mechanical properties which, at high concentrations, can lead to subsurface blistering and even bulk exfoliation near the peak implantation depth [249]. This could be similar to the 2 MeV proton irradiation–induced exfoliation of Ti_3AlC_2 observed by Ward *et al.* [251].

Wang *et al.* reported spherical and string–like He bubble formation at low fluence (8×10^{16} cm^{-2}) 50 keV He^+ irradiation of Ti_3AlC_2 at room temperature, with significant lattice disorder (although no amorphisation) and even surface exfoliation at higher fluence (1×10^{18} cm^{-2}) [249]. Patel *et al.* irradiated Ti_3AlC_2 with 200 keV He ions to 2×10^{17} ions cm^{-2} (14 at.%) at 500 °C, reporting characteristic MAX phase lattice strain [250]. He bubbles (< 1 nm diameter) were also found, whilst XRD observations suggested that the retention of He caused A–layer disorder, as with the previous room temperature study by Wang *et al.* [249]. TEM specimens were prepared using both tripod polishing and FIB from a similar damage region, with both techniques producing the same observations – ruling out preparation induced damage mechanisms.

Similar effects were reported during 400 keV He^+ irradiation of Ti_3AlC_2 at room temperature and 500 °C, up to a fluence of 2×10^{17} cm^{-2} [286]. Lattice disorder, surface cracking, and exfoliation were observed following irradiation, with the cracks found to grow along the $(10\bar{1}0)$ plane – attributed to *a*–parameter contraction. The surfacing blistering is believed to be due to the agglomeration of pressurised He bubbles near the surface, leading to extensive delamination of the lattice. Whilst similar surface effects to those reported by Wang *et al.* were observed, their study used He ions with significantly lower energy (50 compared with 400 keV), at room temperature and an order of magnitude higher fluence (1 ×

10^{18} cm^{-2}). Irradiation energy, temperature and fluence are therefore critical factors in MAX phases under light ion irradiation.

Song *et al.* then irradiated Ti_3AlC_2 with 500 keV He^+ ions at room temperature, 300 and 500 °C to between 5×10^{16} and 1×10^{18} cm^{-2} (~6.4×10^5 appm, ~52 dpa) [244]. As in Wang *et al.*'s study, spherical and string–like He bubbles were observed with TEM, despite the order of magnitude higher ion energy. Zhang *et al.* performed 110 keV He^+ irradiations of Ti_3SiC_2 to between 5×10^{15} and 1×10^{17} cm^{-2}, at room temperature and 450 °C [291], [292]. He bubble–induced displacement of adjacent Si atoms was found to induce a structural transformation to large grain crystalline TiC at annealing temperatures above 900 °C. Despite this, significant damage recovery was found at mid–range temperatures.

3.11.6 Temperature Effects

At higher temperatures (> 700 °C), both neutron and heavy ion irradiation studies have shown significantly reduced lattice parameter changes [238], [271]. Middleburgh *et al.* suggested this is due to higher thermal energies allowing mobility of defects, leading to annihilation or migration to grain boundaries [215]. If the conditions are right, this recovery can be comparable to the defect production rate, leading to an equilibrium in which the fluence is, theoretically, independent of the final damage. Evidence for this over a range of fluence levels and temperatures has been seen in MAX phases in the literature [246], [250], [272], [292]–[296]. For example, Ti_3SiC_2 irradiated by 74 MeV Kr ions to 3.25 dpa showed significantly lower *c*–axis and total unit cell volume expansion at 500 °C, compared to room temperature [270]. Similar results were reported by Ward *et al.* for Ti_3SiC_2 and Ti_3AlC_2 under 2.5 MeV proton irradiation up to 600 °C, in which *c*–axis lattice strain reduced by a factor of five compared with that at 350 °C [281].

Despite the decreased lattice strains at higher irradiation temperatures, larger defect structures, such as basal plane dislocation loops, are reported to remain after medium dose levels (> 1 dpa) [279]. Tallman *et al.* found that average dislocation loop size increases and the loop number density decreases with increasing damage level and temperature (~735 to ~1085 °C; 1.6–3.4 dpa) [257] – effects which have not been seen in proton irradiations.

Interestingly, post–irradiation heat treatments of MAX phases have also been shown to reverse the $M_{n+1}AX_n \rightarrow \gamma\text{–}(M_{n+1}A)X_n \rightarrow \text{FCC–}(M_{n+1}A)X_n$ transformation to a certain degree, as well as reducing lattice parameter strain compared with the virgin material. Wang *et al.* showed that Al atoms in Ti_3AlC_2 return to their original $M_{n+1}AX_n$ positions after annealing of material containing a significant proportion of FCC–$(Ti_3Al)C$ [265]. However, at higher fluence (4×10^{16} cm^{-2} compared with 2×10^{16} cm^{-2}), only a partial recovery was observed, indicating a dose limiting effect. That said, anneals were limited to 1 h and at 800 °C, so a full recovery at either higher temperatures or for longer treatments cannot be ruled out as a possibility.

3.11.7 Compositional Effects

Whilst a relatively limited number of reports exist on radiation damage in MAX phases, it is nonetheless clear that their elemental constituents of play a key role in the underlying mechanisms. The most studied two phases, Ti_3SiC_2 and Ti_3AlC_2, both show excellent resistance to amorphisation, but Ti_3SiC_2 undergoes phase transformations at a lower dose than Ti_3AlC_2. On the other hand, Cr_2AlC and Cr_2GeC both fully amorphise at relatively low (< 2 dpa) doses. Huang *et al.* irradiated Cr_2AlC with 7 MeV Xe and 500 keV He^+ ions at room temperature, reporting anisotropic lattice parameter changes which saturated after 1 dpa. Whilst the layered structure was destroyed quickly, the material's crystallinity was still present up to 5.2 dpa [267].

First–principles calculations have had limited success in explaining compositional trends – Middleburgh *et al.* and Zhao *et al.* suggested that a lower M_A–A_M antisite formation energy in a particular phase would result in a higher resistance to irradiation [215], [256]. However, as Xiao *et al.* observed in subsequent calculations, the Cr/Al antisite formation energy in Cr_2AlC (2.4 eV) is lower than that of the Ti/Al defect in Ti_2AlC (2.52 eV), whilst Cr_2AlC displays a significantly lower irradiation resistance [217]. Perhaps an interplay between other defects is responsible for this discrepancy –requires further investigation to verify.

The bonding state of each atom in a phase is also an important factor in the material's resistance to radiation damage, as explored by Xiao *et al.* [217]. The authors, based on theoretical calculations, suggested that the covalency of M–A and M–X bonds can be related to amorphisation resistance due to its effect on the accommodation of lattice distortion. Weaker bonds indicate an increased susceptibility to lattice distortion and, as such, an enhanced ability to accommodate defects. The authors concluded that, of the compositions studied – Ti_2AlC, V_2AlC and Cr_2AlC, Ti_2AlC should display the highest degree of resistance to irradiation – something which has since been experimentally verified [237], [239]. Further evidence for this relationship has been provided by Bugnet *et al.*, who have compared the irradiation–induced amorphisation resistance of Cr_2AlC, Cr_2GeC, Ti_3SiC_2 and Ti_3AlC_2. Ti_3AlC_2 and Cr_2AlC show enhanced amorphisation resistance compared with Ti_3SiC_2 and Cr_2GeC, respectively, with the latter containing higher covalency M–A and M–X bonds [236]. However, this still only represents initial work – validation using further compositions is required for this criterion to become a reliable predictor of irradiation resistance.

In general, the higher order MAX phases, i.e., those with high values of n, show better structural irradiation resistance. This is exemplified by Ti_2AlN, which undergoes a full transition to FCC whilst Ti_4AlN_3 only changes slightly at a fluence of 2×10^{16} cm^{-2} of 1 MeV Au^+ ions at room temperature [240]. This has also been observed for Ti_3AlC_2 compared with Ti_2AlC, under the same conditions [241]. If the $M_{n+1}AX_n \rightarrow \gamma \rightarrow$ FCC transformation is indeed driven by M_A–A_M antisite formation, then it follows that a lower concentration of Al in higher order $M_{n+1}AX_n$ phases would result in a reduced rate of M_A–A_M antisite formation and, therefore, a slower phase transition. Structurally, the γ and FCC phases will also vary according to the order of the parent $M_{n+1}AX_n$ phase, due to the variation in resulting occupancy ratios on the M, A and X sites. A higher concentration of the A–element results in an increased lattice distortion, due to the relative M/A atomic size difference, potentially contributing to the observed decrease in stability under irradiation of lower order phases.

3.11.8 Radiation Hardening

Ion irradiations of MAX phases in the literature have resulted in significant microstructural hardening. In 2010, following irradiation by 92 MeV Xe ions to a dose of 1 × 10^{15} ions cm^{-2}, Ti_3SiC_2 and $Ti_3(Si,Al)C_2$ were reported to have nearly tripled their nanoindentation hardness values (~8 GPa to 18–21 GPa) [202]. Up to this point the relationship between fluence and hardness was observed to follow a power law, as shown in Fig. 3.13. Due to the variance in the indentation values, inherent due to microstructural anisotropies such as voids, impurities and grain orientation, the values were reported as relative, and thus used purely for the purpose of comparison between virgin and irradiated states. Despite this, the indents did not produce cracks, even after irradiation hardening. It should be noted that the difference in nanoindentation values between virgin and irradiated material are similar to the difference between bulk and thin film values, in which thin films appear to have higher hardness values than bulk, reported by Högberg *et al*. [297]. Marion *et al.* later observed a similar rate of hardening in $Ti_3(Si,Al)C_2$ and $(Ti,Zr)_3(Si,Al)C_2$ at the same irradiation conditions, finding a plateau in nano indentation hardness values (at 0.5 N) of ~20.7 GPa [203], even after increasing the dose to 16.6 dpa. This indicates a saturation in radiation damage, presumably due to an increase in resistance to amorphisation above a threshold value as a result of a full phase transformation. Interestingly, this threshold hardness value appeared to be similar for the three compositions studied. It is, therefore, possible that this value represents the threshold for other 312 MAX phases under 92 MeV Xe irradiation, but more data is required to investigate this.

Le Flem *et al.* suggested in a later report, following TEM characterisations of so–called ‘black spot’ defects in the same material following irradiation, that atomic–scale disorder due to dislocation loops or point defect clusters are directly responsible for the hardness increase [243]. An increase in defects of this sort should reduce dislocation and basal slip mobility, therefore increasing resistance to

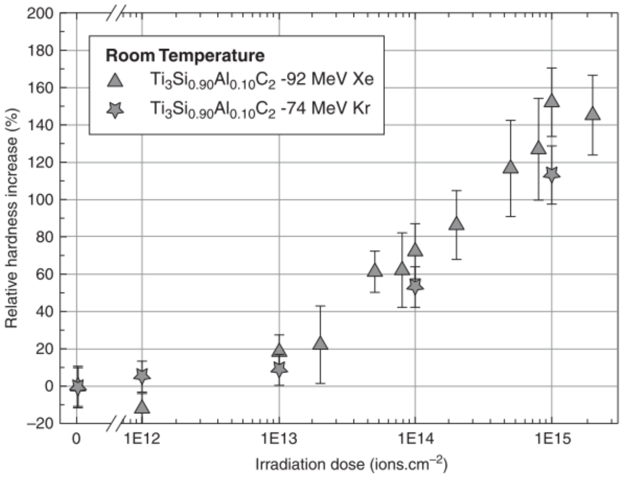

Fig. 3.13 – Irradiation hardening in MAX phases: A comparison of the relative hardness increase as a function of fluence for $Ti_3(Si_{0.9}Al_{0.1})C_2$ exposed to 92 MeV Xe ions (triangles) and 74 MeV Kr ions (stars). Reproduced from *Journal of Nuclear Materials*, 401, 1–3, X. M. Liu *et al.*, *Nanoindentation investigation of heavy ion irradiated $Ti_3(Si,Al)C_2$*, p. 149–153, Copyright (2010), with permission from Elsevier [468].

kink–band formation and other plastic deformation pathways known to accommodate strain in MAX phases.

Current understanding of irradiation damage in ceramics and metals predicts a significant diminution in mechanical properties as a result of irradiation induced hardening. However, analysis of deformation mechanisms in irradiated MAX phases show that kink, ripplocation, and shear band formation, delamination and grain push–out still dominate, as in virgin material, indicating a retained ability to localise damage structures as opposed to crack formation and subsequent bulk failure [102]. This is a particularly favourable property for potential use in cladding or structural components in nuclear environments.

3.11.9 Thermal Property Effects

Due to the limited penetration depth of energetic ions in MAX phases, the effects of irradiation on bulk thermal properties such as conductivity remain elusive – at least until techniques such as transient grating spectroscopy are developed to a practical level [298]. For now, only neutron irradiated samples are suitable for bulk thermal conductivity measurements, due to the volumetric damage profiles produced. Very few studies have been performed on the neutron irradiation effect on thermal properties of MAX phases, with only Ti_3AlC_2, Ti_3SiC_2, Ti_2AlC and Ti_2AlN the subject of analysis. Tallman *et al.* found that the resistivity of these phases was significantly reduced following 0.1 dpa neutron irradiation, thought to be due to the production of point defects which efficiently scatter phonons. Additionally, a strong correlation between resistivity and grain size was observed – larger grains led to a more pronounced resistivity increase, presumably due to the lower defect sink density [238], [257], [279]. Unsurprisingly, at increased temperatures, the resistivity increase was supressed whilst defect annihilation induced recovery increased.

3.12 Summary

Some MAX phases show remarkable tolerance to extreme environments, like the amorphisation resistance of Ti_3AlC_2 under heavy ion irradiation up to 300 dpa [248]. Others, less so. Across the board, irradiation of MAX phases by charged particles or neutrons causes anisotropic lattice instabilities and phase transformations, with instabilities more pronounced at temperatures below ~300 °C [299]. It is highly likely that the production of a combination of defects, primarily M_A–A_M antisites, is responsible for this. These effects are reduced at increasing temperatures, a trend which is seen in other irradiated ceramics and metals (see Fig. 3.4).

Crystallographic instabilities can be detrimental to the structural stability of a MAX phase component due to cracking and subsequent mechanical failure. This limits future nuclear applications of currently studied MAX phases to a temperature range of roughly 600–1300 °C, depending on the composition. The upper operating window region of the first wall in tokamaks, ~800 °C, should be sufficient to promote lattice recovery in MAX phases.

Due to their multiscale anisotropy, one of the most important attributes of MAX phases in nuclear environments is microstructure. The combination of high thermal loads, high energy radiation flux, and corrosion, often result in crack formation and mechanical failure due to differential swelling. There are a few essential microstructural parameters which can be optimised for the mitigation of failure. The first is phase purity – cubic binary carbide impurities are common in MAX phases, and the added anisotropy of such secondary phases, with different crystal symmetry and grain shape can compound differential swelling induced failure [280]. This can be achieved *via* optimisation of synthesis methods, atomic starting ratios, and even solid solution formation [122], [184], [300], [301]. The second is texture – the platelet–like MAX phase grain structure lends itself to void formation during synthesis of untextured samples, which can lead to transmutant gas nucleation and crack formation during irradiation and thermal cycling. Combined with the anisotropic swelling characteristic in MAX phases under irradiation, untextured materials are significantly more vulnerable to cracking than textured variants. Texturing has been achieved *via* magnetron sputtering of thin MAX phase films, which have shown enhanced resistance to mechanical failure under irradiation and thermal loading [302], [303]. Additionally, an increase in fracture toughness has been observed in textured Nb_4AlC_3, compared with its untextured counterpart, due to the suppression of crack propagation [304]. The third is grain size – this is essential to the performance of MAX phases in irradiating environments, as grain boundaries have been shown to act as point defect sinks during irradiation [279]. As such, a finer grain structure may be desirable for MAX phases in nuclear applications for radiation damage resistance.

Despite the wealth of data on the response to extreme environments of some MAX phases, barely 15 of the ~155 currently known phases have been investigated in radiation damage studies, leaving at least 90% with unknown irradiation responses. Even for Ti_3SiC_2 and Ti_3AlC_2 – by far the most extensively studied, there is still significant radiation damage testing required before inclusion in nuclear systems design.

Additionally, the vast majority (~60%) of irradiation investigations have been performed at room temperature, which is not relevant to even low temperature operational nuclear environments, despite being useful for the understanding of underlying radiation damage mechanisms. Equally, the damage levels in many studies are low (< 1 dpa), often limiting the knowledge gathered to radiation damage onset mechanisms, whilst in–vessel components in DEMO are expected to receive up to 200 dpa in the first wall. Further high temperature investigations on promising MAX phases over a range of doses is required, along with the characterisations of as–of–yet unirradiated compositions that are compatible with activation considerations.

Of course, this suggestion is rather idealistic on a practical scale – high dose irradiations are expensive, time consuming and only possible at a handful of facilities across the globe. Nevertheless, they are still considerably faster and cheaper than neutron irradiations of comparable doses, not to mention the significant reduction in activation issues that come as an additional challenge with neutron irradiated material.

The effect of radiation damage on thermal conductivity in MAX phases is also of particular concern if they are to be considered for nuclear fusion applications. If the heat flux is of the order of 10 MW/m^2, as expected in DEMO, a small degradation of thermal conductivity could be detrimental to a MAX phase component, leading to thermally induced decomposition, ablation, or sublimation. The practical difficulty in collecting this data, however, as mentioned previously, highlights the requirement for relevant near–surface property measurement techniques.

Equally, a full understanding of the response of MAX phases to hydrogen, helium, and tritium environments, to study diffusion, retention, and the potentially corrosive nature of these species, is required to fully understand the response of MAX phases to fusion plasma environments.

The mechanical properties of MAX phases under irradiation are currently poorly understood – something that must be remedied to assess their potential infusion. Knowledge is required on the response of MAX phases to external mechanical strain during irradiation, to simulate the effect of anisotropic expansion and contraction during thermal cycling of a tokamak. This is especially relevant if they are to be used as coatings on structural or high heat flux components, as proposed in the literature [305]–[308]. Equally, fatigue behaviour, hardening and embrittlement, crack propagation and mechanical failure mechanisms, as well as extreme thermal shock response must be investigated at high temperature and irradiation dose.

Based on the literature, MAX phases are still very much at the beginning of the development scale and are, therefore, highly unlikely to be at the reactor deployment stage in time for DEMO (assuming they are not ruled out before this). Whilst experiments in this thesis will make reference to the conditions in a DEMO reactor, the foresight is perhaps beyond DEMO–class plants to 2nd or 3rd generation reactors. The aim of this work is to demonstrate an efficient workflow for the development of designer MAX phases for nuclear fusion applications. The hope is for this to inspire and accelerate high–throughput research of MAX phases (or related materials) in the search for suitable candidates for extreme applications, such as in future fusion reactors.

Chapter 4: Experimental Methods

4.1 Synthesis

Despite the discovery of MAX phases in the 1960s (then known as the H–phases) by Jeitschko *et al.* [309], [310], it wasn't until 1996 that the first composition was synthesised in phase pure, bulk form – Ti_3SiC_2. This allowed bulk mechanical, electrical and thermal characterisations to be undertaken, uncovering a trove of interesting properties [103]. The enabling process was an initial uniaxial reactive hot–press, followed by hot isostatic pressing to reduce SiC impurities and achieve 99.9% density. This discovery initiated a torrent of subsequent reports on Ti_3SiC_2 and other MAX phases, a process which continues to this day.

Since then, an arsenal of synthesis methods has been built in the literature, with new routines reported periodically. However, the most common and established techniques, based on the number of reports of phase pure material, are hot pressing; hot isostatic pressing; pressure–less sintering; spark plasma sintering and both chemical and physical vapour deposition [311]. Many MAX phases will form from elemental powders at high temperature under an inert atmosphere, without the need for added pressure. However, the density of these specimens is often lower than

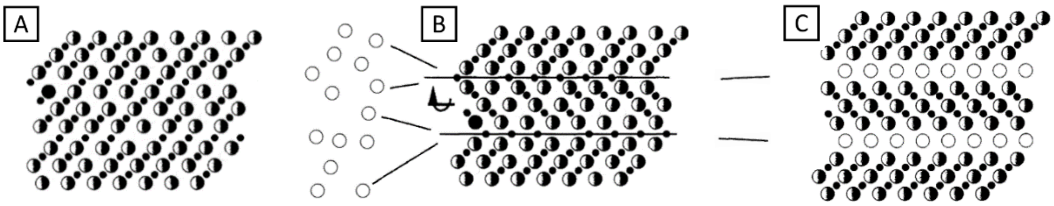

Fig. 4.1 – MAX phase formation on the atomic scale: The proposed 312 MAX phase formation route, according to Barsoum *et al.* [165]: (A) Formation of FCC $M_{n+1}X_n$ phase. Black/white circles are the M–atoms, small black circles are X–atoms. (B) A–atoms (white circles) intercalate into the MX lattice and agglomerate into single atom thick layers. This encourages a rearrangement of the adjoining MX atoms, representing a rotation about the horizontal axis of the region between the black lines. (C) The final $M_{n+1}AX_n$ structure, with A–layer mirror planes.

their pressure–assisted counterparts due to porosity [102], [312]. The choice of synthesis is, therefore, often application based. For the production of MAX phase powders or thin films, pressure–less synthesis methods are a relatively cost–effective and efficient route, whereas for fully dense and/or textured bulk samples, often pressure–assisted synthesis is required [165], [311], [313].

On the atomic scale, MAX phases usually form from individual constituent elements, present in the ratio $M_{n+1}AX_n$, *via* a two–step process. Firstly, the M and X–elements react to form binary carbides and nitrides, along with respective solid solutions if more than one M– and/or X–element is present. It is assumed that these MX compounds are sub–stoichiometric in the X–element, with a ratio approaching $M_{n+1}X_n$, to allow subsequent $M_{n+1}AX_n$ formation. The second step involves the intercalation of the A–layer element (or elements) into the MX structure to form single atom thick layers, which in turn induces a slight rotation of the adjoining MX layers. As such, the binary MX structure undergoes a symmetry transformation from FCC to HCP, with the A–layers acting as basal mirror planes [102]. A schematic of this process is shown in Fig. 4.1.

To reduce the reaction time required compared to a mixture of pure elements, the new materials reported in Manuscript 2 (Chapter 6) were synthesised from powders of TaC, TiC, Ti and Al. The molar ratio was then tuned depending on the desired Ta/Ti concentration and end stoichiometry (i.e., 211, 312, 413, etc.). One of the objectives of this thesis is to present an efficient MAX phase development route,

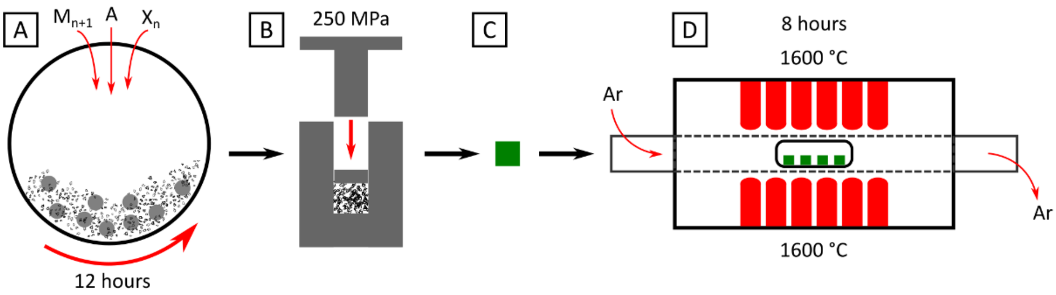

Fig. 4.2 – Pressure–less sintering of $M_{n+1}AX_n$ phases: (A) Starting powders are milled with ZrO_2 balls in the desired $M_{n+1}AX_n$ ratio, with a 10% excess of Al. (B) The mixture is cold pressed at 250 MPa to form a compact pellet (C – green square). (D) Pellets are sintered in a flowing Ar tube furnace at 1600 °C for 8 hours.

from prediction to advanced characterisation. As such, the high temperature pressure–less sintering method was chosen for synthesis trials, in which several, few cm sized samples can be sintered at the same time and using widely available equipment – see Fig. 4.2 for a schematic of the process. This represents a cost– and time–effective route to the production of bulk, relatively dense MAX phases from starting powders.

Starting powders were all obtained from Alpha Aesar (Ward Hill, MA, USA), with mean particle sizes less than 63 μm (see Table 4.1 for details). The powders were then mixed in the desired molar ratios, with a 10% excess of Al to account for vaporisation during heating, before ZrO_2 ball milling in plastic jars for 12 h to provide a homogenous mixture. Compact pellets were produced by uniaxially cold pressing the powders at 250 MPa. The resultant pellets were then pressure–less sintered inside an 82 × 31 × 18 mm Al_2O_3 boat, covered with an Al_2O_3 plate, placed

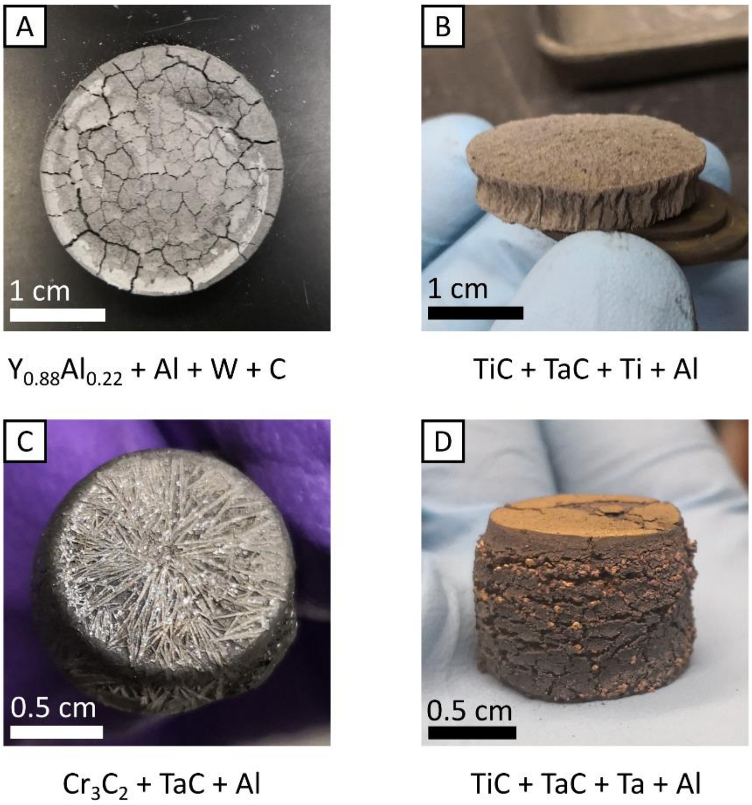

$Y_{0.88}Al_{0.22}$ + Al + W + C

TiC + TaC + Ti + Al

Cr_3C_2 + TaC + Al

TiC + TaC + Ta + Al

Fig. 4.3 – Fresh out of the oven: Examples of starting powder mixtures cold pressed at 250 MPa and sintered for 8 hours at 1600 °C. The resulting primary MAX phases are (A) $(W_{2/3}Y_{1/3})_2AlC_2$, (B) $(Ta_{0.38}Ti_{0.62})_3Al_{0.81}C_2$, (C) $(Cr_{3/4}Ta_{1/4})_4AlC_3$, and (D) $(Ta_{2/3}Ti_{1/3})_3AlC_2$.

inside an Al_2O_3 tube furnace with an inert flowing Ar atmosphere. Pure Ti powder was placed in an adjacent crucible upstream to the pellet, in terms of Ar flow, as a residual oxygen getter. The sintering was performed at 1600 °C, with a heating and cooling rate of 5 °C min^{-1} and an 8–hour dwell at the maximum temperature. After sintering, the densities of the samples were generally > 80% of their theoretical values.

Table 4.1 – Details of source material used for synthesis. *As quoted by the manufacturer.

Material	Purity (wt.%)*	Average particle size* (μm)
TaC	99.5	44
TiC	99.5	2
Ti	99.5	15
Al	99.5	15

For Ti_3AlC_2, used as a reference material in Manuscript 3 (Chapter 7), bulk samples were obtained from Kanthal (Sandvik AB, Hallstahammar, Sweden). The material was synthesised *via* hot–pressing of pre–reacted Ti_2AlC and TiC powders at 1400 °C, with a heating rate of 500 °C h^{-1} for 4 h under a uniaxial pressure of ~40 MPa. The material was 95.1 wt.% Ti_3AlC_2, 4.1 wt.% TiC and 0.8 wt.% Al_2O_3, according to refinements of X–ray diffraction data combined with quantitative SEM–EDS. The mean MAX phase grain size was 15(5) μm as measured *via* inspection of SEM micrographs, using the intercept method:

$$|L| = \frac{1}{\left(\frac{l}{n_i}\right)}$$

Where $|L|$ is the mean grain size (in μm), l is the length of a straight line across the surface (in μm) which intersects a total of n_i grain boundaries. Additionally, the density was measured as 4.242(7) g cm^{-3} using the Archimedes method [314], which is 98.7% of the theoretical value of 4.30(3) g cm^{-3}.

4.2 X–Ray Diffraction

X–ray diffraction is a versatile bulk material analysis technique which exploits the constructive interference of coherent, in phase photons after scattering by atomic planes in ordered structures. For two in phase and parallel photons incident at an angle, θ, to a lattice, in which the photons are reflected by two adjacent atomic planes, the path difference of the reflected photons is $2d \cdot \sin(\theta)$, where d is the separation between the atomic planes. For the case where the path difference is an integer multiple, n, of the wavelength of the incoming photon, λ, the following relation can be written:

$$n\lambda = 2d \cdot \sin(\theta) \tag{4.1}$$

This is known as Bragg's law and allows the inference of the interatomic spacing in materials with repeating atomic structures [315]. X–rays, which are relatively simple to generate and have a wavelength range (0.1–100 Å) well suited to probing interatomic spacings, are widely used in diffraction experiments. In laboratory setups, X–rays of wavelengths 0.5–1.8 Å are typically used, from sources such as Cu, Co, and Mo. These sources are bombarded with electrons to produce a spectrum of X–rays.

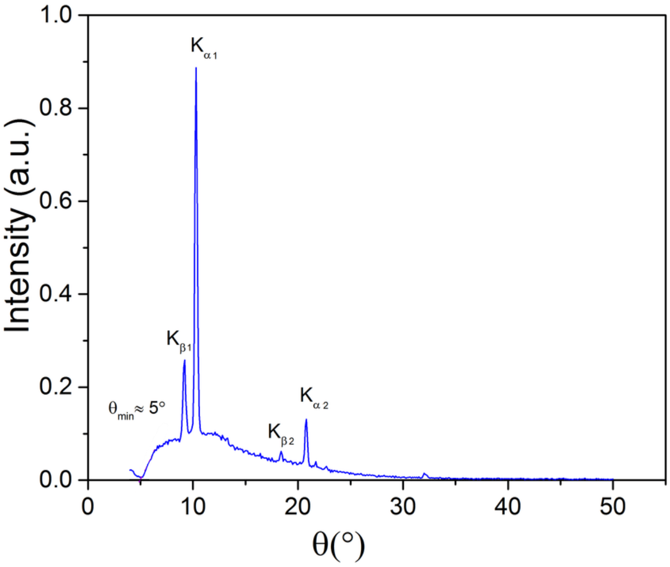

Fig. 4.4 – The production of X–rays: An X–ray spectrum from a Mo target bombarded with 35 keV electrons, showing characteristic K_α and K_β peaks. Reproduced with permissions from Kumar *et al.* [469].

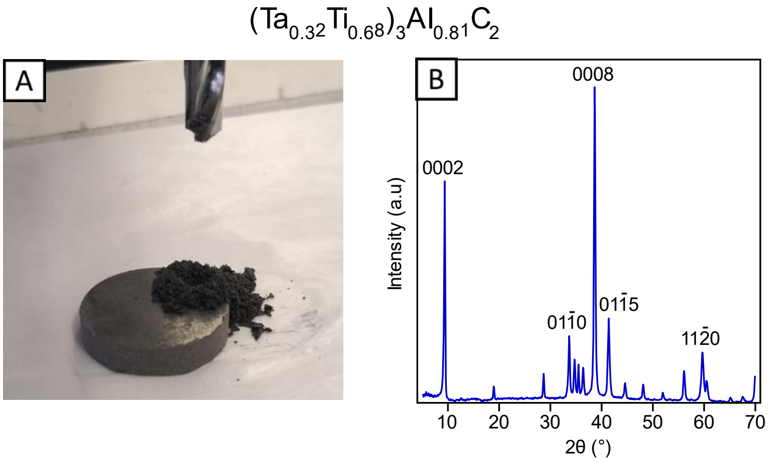

Fig. 4.5 – XRD identification of $(Ta_{0.38}Ti_{0.62})_3Al_{0.81}C_2$: A freshly sintered $(Ta_{0.38}Ti_{0.62})_3Al_{0.81}C_2$ pellet after milling with a TiN coated steel bit, displaying the characteristic machinability of MAX phases (A). The subsequent powder was collected and analysed using XRD, with the spectrum shown in B. The miller indices of the five highest intensity MAX phase peaks are labelled.

Characteristic X–rays are produced when an incoming electron excites an inner–shell bound electron in a source atom. The subsequent hole left by the excited electron is filled by a transitioning electron from a higher energy level. This transition can be from, for example, an L– or M–shell to a K–shell and causes the emission of X–ray photons referred to as K_α and K_β radiation, respectively. Additionally, a continuous spectrum of X–rays known as bremsstrahlung is produced during electron bombardment, due to inelastic scattering as electrons interact with the electric fields of atoms without causing excitation. As such, the X–ray spectrum from a laboratory source consists of a range of wavelengths, as shown in Fig. 4.4.

To derive physical properties of a material using XRD, a sample is exposed to the source X–rays, with a detector placed to receive reflected photons. The incidence angle, θ, of the X–ray beam is then varied, with detected X–rays plotted in counts (or intensity) against θ. For crystalline materials, this results in a series of well–defined peaks in a 1–dimensional diffractogram [316], alongside a background of reflected source X–rays not satisfying the Bragg diffraction condition. The angular positions of the peaks, representing the possible Bragg reflections, correspond to lattice planes in a crystalline unit cell. In this way, every phase will produce a fingerprint XRD pattern from which crystal symmetry, lattice parameters, atomic

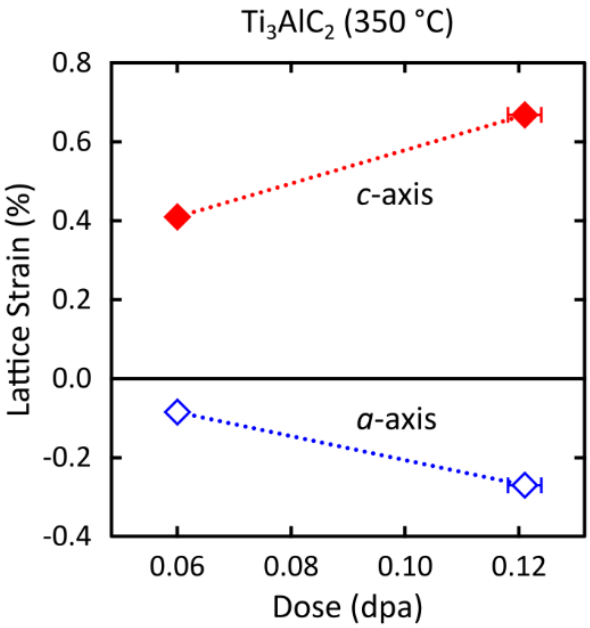

Fig. 4.6 – Irradiation induced lattice instabilities: A comparison of the relative lattice strain exhibited in Ti_3AlC_2, following 2 MeV proton irradiation at ~350 °C to 0.0603(14) dpa and 0.121(3) dpa. The strain was determined using refinements of XRD data in Manuscript 3 (Chapter 7). The expansion in the *c*–axis and contraction in the *a*–axis seen here, which increases with increasing dose, is characteristic of MAX phases under irradiation and is likely due to copious $Ti_{Al} - Al_{Ti}$ antisite production.

positions, occupancies and thermal displacement parameters, texture components, microstructural strain, and even dislocation density can be derived [116], [317]–[321].

It must be emphasised at this point that the attenuation of X–rays in a solid is a function of both incidence angle and the density of the material. As such, XRD only samples atomic planes in a near surface region, which is generally less than 50 μm for MAX phases. Even at an incidence angle of 90°, the intensity of a Cu source X–ray beam will decrease to about a third of its original value at a depth of 62 μm in Ti_3AlC_2 (with a density of 4.26 g cm^{-3}) [182], whilst for $(Ta_{0.38}Ti_{0.62})_3Al_{0.81}C_2$ (with a density of 7.34 g cm^{-3}), it is less than 12 μm [322].

The utilisation of XRD in this thesis is twofold. The first is in the structural and compositional determination of newly synthesised MAX phases and, in the case of $(Ta_{0.38}Ti_{0.62})_3Al_{0.81}C_2$, derivative MXenes. This involves phase identification from peak positions and relative intensities (see Fig. 4.5). Subsequent analytical

Table 4.2 – XRD parameters: A summary of the important machine settings and experimental setup for XRD scans used in Manuscripts 2 and 3 (Chapters 6 and 7).

	Manuscript 1	Manuscript 2
Preparation	Powder	Solid
Diffractometer	Rigaku MiniFlex 300/600	Bruker D8 Discover
Source	Cu–K_α	Cu–K_α
Voltage (kV)	40	40
Current (mA)	15	40
Power (W)	600	1600
Detector	1D	1D
Divergence slit (°)	1.25	N/A
Width (mm)	10	16
Soller slit (incident, °)	5	–
Soller slit (receiving, °)	5	2.5
Receiving slit (°)	1.25	2.339
Width (mm)	0.3	18
2θ range (°)	5–75	5–85
Step (°)	0.02	0.02
Dwell time (s)	0.75	4

refinements using the Rietveld method allow the discernment of unit cell parameters for each detectable phase present in the sample, including an estimation of the relative phase fraction over the scanned region. The second is specifically aimed at ion irradiation induced lattice parameter changes, determined by observing small shifts in the peak positions of MAX phases between virgin and irradiated states (see Fig. 4.6, for example). The effect of ion and neutron irradiation of MAX phases on lattice parameters and subsequent anisotropic unit cell expansion has been widely reported in the literature for a variety of compositions, with a focus on heavy ions and subsequent phase transformations (see [299] and references therein). However, in a recent report by Ward *et al.*, 1.5 MeV proton irradiations of Ti_3SiC_2 and Ti_3AlC_2 to 0.1 dpa at 350 °C resulted in a strain of the *c*– and *a*–lattice parameters of up to 0.72% and –0.43% [251]. Under 2 MeV protons, a similar anisotropic unit cell strain effect is seen in $(Ta,Ti)_3AlC_2$ MAX phases in Manuscript 3 (Chapter 7). At 347(8) °C and 0.112(3) dpa, $(Ta_{0.25}Ti_{0.75})_3Al_{0.77}C_2$ displayed *c*–

and *a*–parameter strains of 1.03% and –0.17%, respectively, representing a unit cell volume increase of 0.68%.

For all XRD characterisations, a Cu–K$_\alpha$ source was used, with X–rays incident on the samples over a 2θ range of either 2–70°, 5–75° or 5–85° for MXene, Manuscript 2 (Chapter 6) MAX phases, and Manuscript 3 (Chapter 7) MAX phases, respectively. The full list of experimental XRD parameters used can be seen in Table 4.2. For the characterisation of new materials in Manuscript 2 (Chapter 6), MAX phase samples were milled to a powder using a TiN–coated steel bit and subsequently crushed using an agate pestle and mortar. For multilayer MXene, as–synthesised powder was scanned after air drying, whilst for delaminated MXene, free standing vacuum filtered films were scanned.

Quantitative phase and unit cell analysis of XRD data was performed using the software package TOPAS [323]. The Rietveld method was employed to refine calculated full profiles to the experimental data, made possible by using the Newton–Raphson nonlinear least–squares minimisation routine [324]. The correlation between the calculated profile intensity I_c and the observed intensity I_o is defined by the objective function, χ^2. This is the sum of the individual squares of the weighted differences between I_o and I_c, written as

$$\chi^2 = \sum \frac{1}{I_o}(I_o - I_c)^2 \qquad (4.2)$$

where I_c is given by

$$I_c = S_f \sum_{i=j}^{N_{phases}} \frac{f_i}{V_j^2} \sum_{i=k}^{N_{peaks}} L_k \left|F_{k,j}\right|^2 S_j\left(2\theta_i - 2\theta_{k,j}\right) P_{k,j} A_j + I_b \qquad (4.3)$$

where S_f is the profile scale factor, N_{phases} is the number of phases present in the sample, f_i and V_j are the phase fraction and volume, respectively, N_{peaks} is the number of refined peaks, L_k is the Lorentz–polarisation factor, $\left|F_{k,j}\right|$ is the structure factor, θ_i is the peak position angle, $P_{k,j}$ is the preferred orientation, A_j is the peak area and I_b is the background profile intensity [320]. After each refinement cycle, the accuracy of the refined profile I_c is given by the 'goodness of fit' (GOF) relation, written as

$$GOF = \frac{R_{wp}}{R_{exp}} = \sqrt{\frac{\sum w_m \left(Y_{o,m} - Y_{c,m}\right)^2}{M - P}} \qquad (4.4)$$

where R_{wp} is the 'R–weighted' pattern, R_{exp} is the expected R–pattern, w_m is the weighting given to the data point m, written as $w_m = \frac{1}{\sigma(Y_{o,m})^2}$, $Y_{o,m}$ and $Y_{c,m}$ are the observed and calculated values at data point m, respectively, $\sigma\left(Y_{o,m}\right)$ is the standard uncertainty in $Y_{o,m}$, M is the number of data points and P is the number of refined parameters (for further details see [325]).

4.3 Scanning Electron Microscopy

Scanning electron microscopy (SEM) is built on the principle of interactions between electrons and matter, with the products thereof analysed to build images and spectra from a specimen. Electrons are generated, accelerated, and focussed to a fine point on the surface of a specimen using a series of electromagnetic lenses, coils, and apertures. Typically, the beam in an SEM is operated at a source acceleration voltage of 0.5–30 kV, with the chosen value based on the application.

When the electrons arrive at the surface, they are scattered by atoms in a series of interactions. These interactions generate secondary, Auger and backscattered electrons (BSE), as well as both characteristic and continuous spectrum X–rays (i.e., bremsstrahlung). In some cases, visible wavelength photons are also produced in a process known as cathodoluminescence. An increased accelerating voltage results in higher energy electrons and, therefore, an increased interaction volume in the specimen. As such, images and spectra obtained from SEM contain information from a near–surface region, usually on the order of a few micrometres for a 30 kV beam. Incidentally, the increased interaction volume at higher energies results in more scattering events and secondary emission from a wider area of the specimen, in the form of electrons and X–rays.

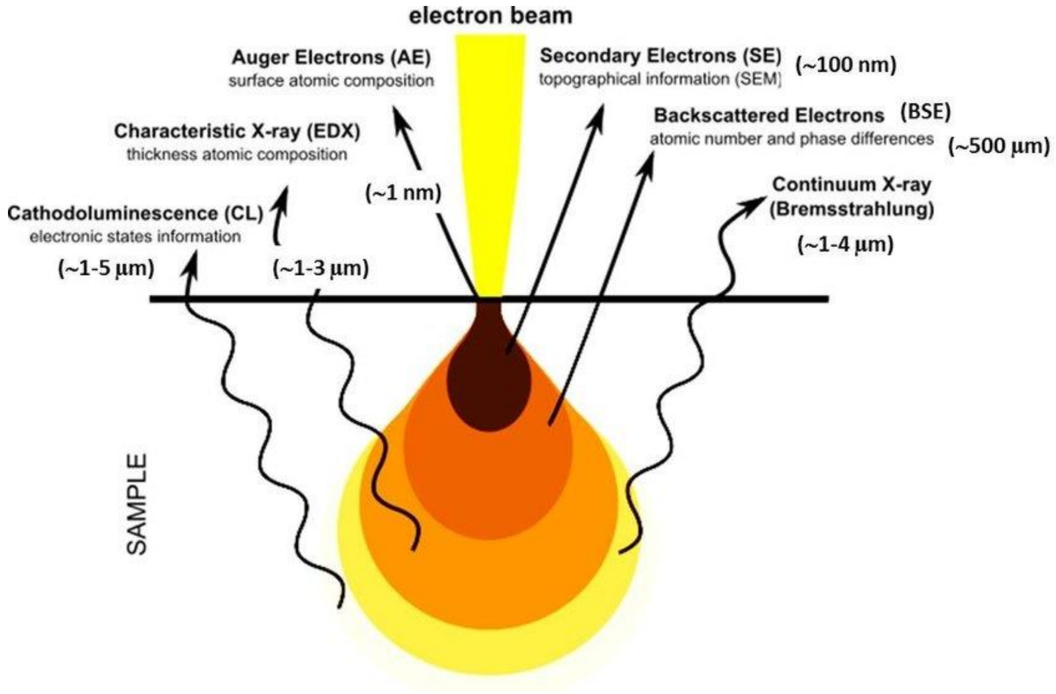

Fig. 4.7 – Electron interactions with matter: A schematic summary of the various interactions an electron beam has with a specimen during SEM. Approximate source depths for each emission have been included.

To build an image or spectra from a region on the surface, the electron beam is rastered over the desired area, pausing periodically for a specified dwell time at points on the surface. An electron or X–ray detector collects beam interaction products from each dwell point and assigns the resulting information to a pixel. The pixels then combine to form a digital image or map of the region of interest. The number of dwell points is dictated by the desired resolution of the resulting image. The resolution is ultimately, however, limited by both the beam size and the fundamental interactions in the specimen. A higher accelerating voltage will lower the spatial resolution, whilst increasing the signal–to–noise ratio (SNR) for X–ray detection. Thus, a compromise in beam parameters is often required. Contrast in an image is generated when a variation in electron or X–ray signal occurs from pixel to pixel, due to beam interactions with different or different numbers of elements or electron shells within an atom. In general, secondary electrons provide increased contrast from to specimen topology, whilst contrast in BSE images is often related to the composition of the specimen.

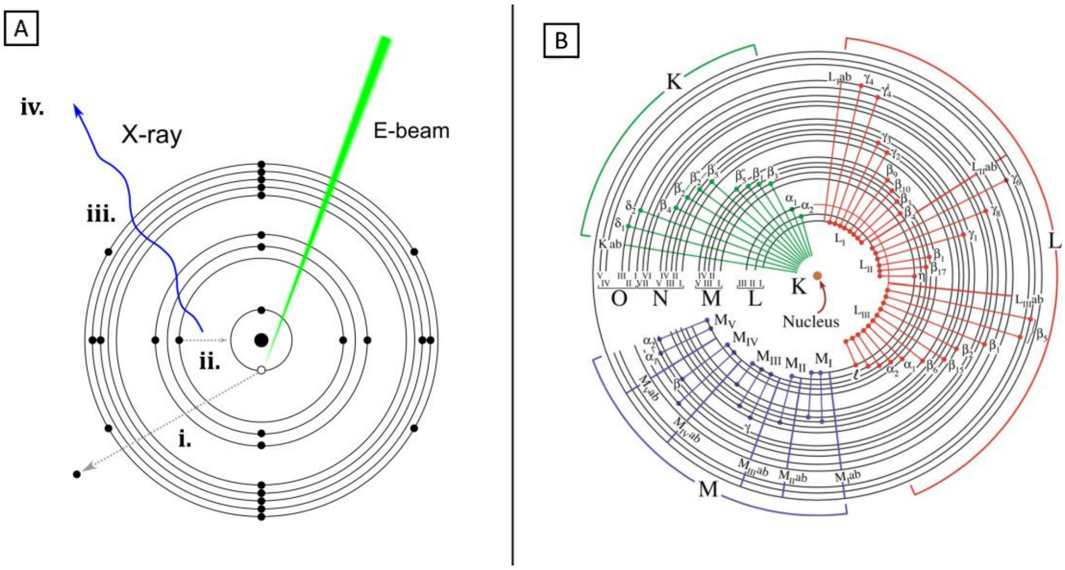

Fig. 4.8 – Atomic energy transitions: (A) A simplified schematic of an incident electron causing the emission of an X–ray *via* excitation and subsequent de–excitation of discrete electronic energy levels within an atom. B) The various energy transitions and respective characteristic X–ray nomenclature. Reproduced from Williams & Carter (2009) [342].

4.3.1 Energy Dispersive X–Ray Spectroscopy

X–rays generated by the beam as it interacts with a specimen can provide rapid qualitative compositional information from the near surface region. As in X–ray generation for XRD, photons are either characteristic or continuous, with the latter forming a background signal. As characteristic X–rays are produced by discrete electronic energy transitions in an atom (see Fig. 4.8), excitation of the electrons responsible is only possible using an incident electron of sufficient energy. As such, incident beam energies of up to 30 kV are often required to generate sufficient high energy characteristic X–rays.

Qualitative analysis of SEM–EDS spectra is relatively simple. Assuming the SNR is sufficiently high, a set of characteristic X–ray peaks will be present in each pixel. The energy of each X–ray peak corresponds to a characteristic energy transition in an atom, for which the transitions are known [316]. Thus, the transition and by derivation the atom responsible for each peak may be deduced.

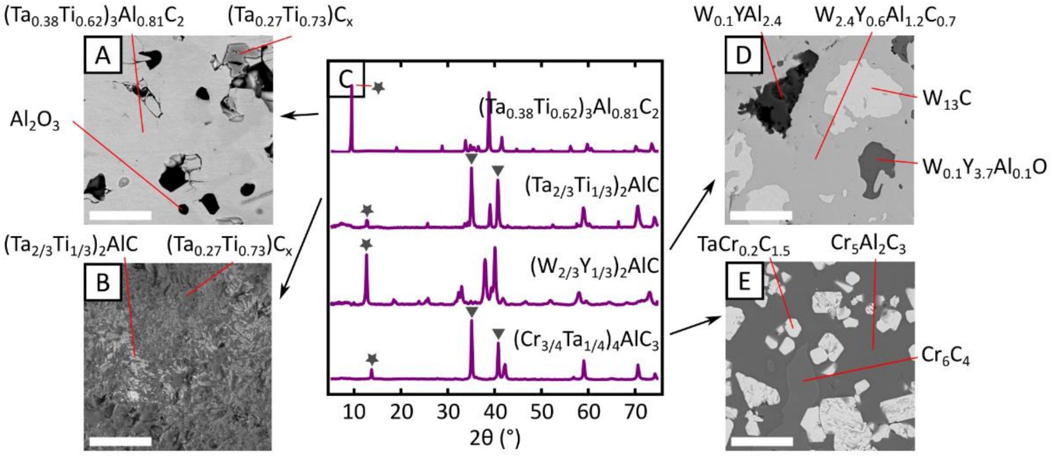

Fig. 4.9 – XRD, SEM + EDS characterisation of new MAX phases: A comparison of correlative data obtained for four trial compositions – $(Ta_{0.38}Ti_{0.62})_3Al_{0.81}C_2$ (A), $(Ta_{2/3}Ti_{1/3})_2AlC$ (B), $(W_{2/3}Y_{1/3})_2AlC$ (C) and $(Cr_{3/4}Ta_{1/4})_4AlC_3$ (D). The micrographs were obtained using BSE–SEM, with the phases identified using EDS labelled on each. The line profiles are XRD scans of the respective compositions, used to determine the crystal symmetry and lattice parameters of the identified phases. The scale bars correspond to 20 μm.

However, to accurately quantify this information requires a reference spectrum from a standard sample with known composition. Modern EDS software often includes a variation of the ‘standardless quantification’ method, involving the comparison of peak intensity ratios in a signal. This is often achieved *via* a mathematical correction of peak intensities known as ZAF. This method takes into account the X–ray source (Z), relative absorption (A) and augmentation of characteristic X–rays (F) to correct the observed peak intensities and thereby provide an estimate for the relative concentrations of elements [326]. Due to practical limitations, however, such as detector efficiency, collection area, X–ray absorption, signal pile–up and sample surface contamination, there are significant uncertainties associated with quantitative SEM–EDS [327]. For light elements, generally up to oxygen, the minimum detectable concentration is > 1000 appm [328].

In Manuscript 2 (Chapter 6), surface SEM and SEM–EDS analyses were performed on newly synthesised MAX phases to investigate the microstructure, impurity content, elemental composition and local phase concentration variations (see Fig. 4.9 for examples). Additionally, phase purity and microstructural damage analysis of proton irradiated samples were performed using SEM and SEM–EDS, in conjunction with high–resolution digital image correlation (see section 4.6) for discussion. These bulk characterisations, along with XRD, build a clear picture of the state and fundamental structure of MAX phases both before and after irradiation and thermal analysis. All SEM characterisations were performed using an FEI Quanta 650 FEG–SEM, equipped with an Oxford Instruments X–Max^N 50 EDS detector. The exception to this is the work pertaining to high–resolution digital image correlation (see section 4.6).

4.3.2 Focussed Ion Beam SEM

In addition to imaging and analytical characterisation, SEM was also used in conjunction with a Ga^+ focussed ion beam (FIB) and Pt gas injection system (GIS) to perform *in–situ* preparation of electron transparent lamellae for TEM analysis (as discussed in the next section).

A FIB–SEM accelerates and focusses Ga^+ ions onto a specimen surface, much in the same way and in addition to the electrons in conventional SEM. The ions sputter near–surface atoms in the specimen at a faster rate than the redeposition of sputtered atoms, resulting in a net removal of specimen material. The beam acceleration voltage (usually 30 kV) and current (usually between 20 pA and 20 nA) is then tuned to increase or decrease the milling rate. Over the last few decades, the application of FIB–SEM to *in–situ* preparation of thin specimens has been well established [329].

Initially, a protective Pt film is deposited using the FIB and an in–chamber GIS, over a region of interest on the specimen surface. This Pt film protects the material in the region of interest during milling and represents the top edge of the subsequent lamella. The lamella is then cross–sectioned by milling surrounding material. A W needle tip is then welded to the Pt layer on the top edge of the lamella using a localised Pt deposit. The perimeter of the lamella is milled to free it from the specimen, before being transferred to a suitable holder using mechanical operation of the tungsten needle. The lamella is then welded to the holder using Pt deposits and subsequent FIB milling to remove the needle from the sample.

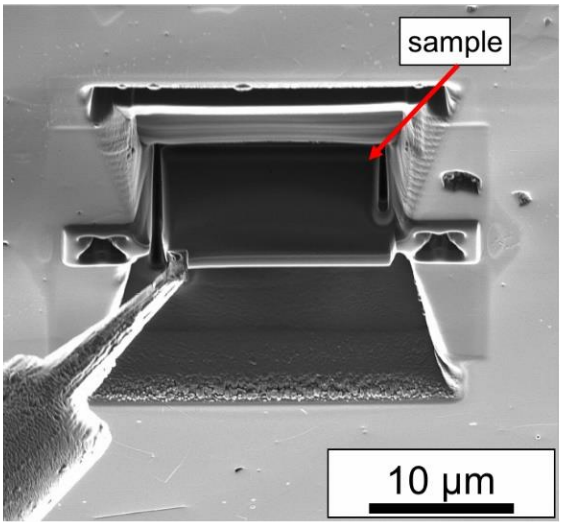

Fig. 4.10 – The *in–situ* FIB–SEM lamella lift–out process: A BSE micrograph of a W needle fixed to a Ti_3SiC_2 lamella, before it is lifted out, welded to a suitable grid and thinned to electron transparency. Reproduced with permission from Ward, J. (2018) [470].

Once attached to the holder, the lamella is thinned to electron transparency using the FIB. This is achieved by repeatedly milling thin sections from either side of the lamella, with decreasing beam currents to systematically reduce the FIB–induced damage to the lamella surfaces. Once the lamella is at the desired thickness, a low voltage, low current milling step is performed to reduce Ga^+ ion beam damage. An example of the lift–out stage of the process is shown in Fig. 4.10.

In this work, electron transparent lamellae were prepared using either an FEI Nova Nanolab 600 or an FEI Helios 660 FIB–SEM (dependent on equipment availability) using the method outlined previously, with more information available from Stevie *et al.* (2001) [329]. Rough milling was performed using a beam current of 7 nA, operated at 30 kV; lamellae were thinned using beam currents from 90 pA to 1.6 nA at 30 kV; and final polishing steps were performed with a 21 pA beam operated at 5 kV, followed by 2 kV.

4.4 Transmission Electron Microscopy

Transmission electron microscopy (TEM) exploits the wave–particle duality and charged state of electrons to achieve sub–Å spatial resolution, allowing the direct imaging of individual atoms under certain conditions [330]–[332]. Combined with

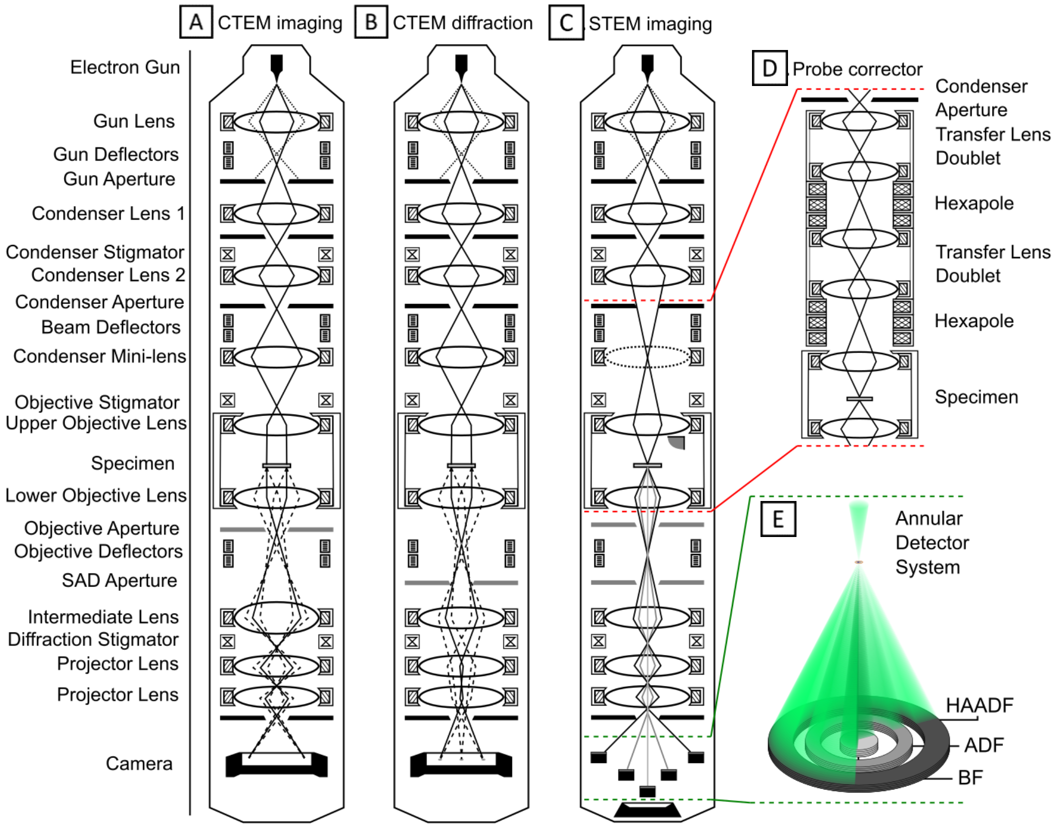

Fig. 4.11 – The transmission electron microscope: A generalised and simplified schematic of the equipment configuration in CTEM: The setup in (A) projects an image onto the camera, whist (B) projects an electron diffraction pattern. A simplified schematic of the STEM configuration (C) with a probe aberration corrector (D). Additionally, the general locations and geometry of three common detectors are identified in (E): HAADF, ADF, and BF. Reproduced from *Transmission Electron Microscopy*, D. B. Williams, B. C. Carter, Copyright (2009), with permission from Springer [342], and from *Developing Imaging and Spectroscopy Capabilities in Liquid–Phase Transmission Electron Microscopy*, D. J. Kelly, Copyright (2019) [471].

powerful analytical techniques like EDS, the atomic structure, local composition, and nature of multiscale–scale defects can be elucidated with high accuracy.

As in SEM, electrons in TEM are generated using either thermionic or electric field emission from a source – often a sharpened W tip. They are accelerated through a high potential difference, often in the 60–300 kV range, before being focussed and shaped *via* a set of apertures and electromagnetic lenses known as the condenser system. They are then incident on a thin (< 200 nm) specimen, where they are mostly transmitted. As the electrons pass through the target specimen, they scatter off atoms and are diffracted, producing an interference pattern in the back focal plane after exiting the specimen. This pattern is then focussed and combined into a highly magnified image using an objective lens and projected onto a screen, camera or spectrometer for analysis or image capture. Both images and diffraction patterns may be obtained in this way, simply by varying the strength of the projector lens system.

Due to the high accelerating voltages involved, the resulting momentum generates electron de Broglie wavelengths on the order of picometers, enabling a higher resolution than is achievable in SEM [333], [334]. However, the relativistic momentum transfers that take place upon the interaction of such electrons with target atoms can induce significant structural changes in a sample, often complicating observations. These effects are encompassed by an understanding of radiation damage, broadly divided into two distinct regimes: knock–on damage – a ballistic process involving atomic displacements, and radiolysis – electronic excitations resulting in changes to local bonding and, therefore, chemistry [335]. In order to generate sufficient signal for high resolution imaging and analytical investigations like EDS, a high flux of incident electrons is usually required. As such, the electron dose received by the specimen and consequential radiation damage effects must be carefully monitored during acquisition [336].

4.4.1 Selected Area Electron Diffraction

When diffracting through a periodic structure with spacing similar to the incident wavelength, electrons will undergo constructive (and destructive) interference. The subsequent interference patterns can be analysed to infer local atomic ordering, grain structure and a range of lattice defects [337]. With a parallel electron beam, a selected area aperture in the image plane of a specimen can be used to specify local regions in the specimen for electrons to pass through, thus allowing only the region of interest to contribute to the diffraction pattern. This is known as selected area electron diffraction (SAED). For a single or few–crystal region, this will produce a diffraction pattern consisting of an array of spots, with polycrystalline and amorphous regions resulting in concentric circles and a diffuse halo ring, respectively. The inverse of the separation of these spots or rings represents the average distance between atomic planes from which the electrons have diffracted.

In this way, electron diffraction is analogous to XRD, albeit on a far smaller scale and, therefore, respective of local crystal structures rather than bulk.

4.4.2 High–Resolution TEM

Close to its resolution limit, TEM can be used to resolve individual atoms or atomic columns in a specimen. As electrons undergo dynamic scattering when passing through a crystal, variations in transmitted phase arise. These differences manifest as phase contrast in TEM images [338]. This contrast, which allows the highest resolution images to be captured, is described by the phase contrast transfer function (PCTF), which oscillates relative to spatial frequency. In conventional TEM (CTEM), the PCTF depends on defocus and objective lens aberrations. As such, artefacts and contrast inversions can appear, which pose challenges in interpreting high resolution micrographs [339].

4.4.3 Scanning TEM

As in the SEM, the beam in TEM can be focussed to a fine point and scanned over the specimen to build up an image on a charge coupled device camera, in a technique called scanning TEM (STEM). With state–of–the–art aberration correction technology, probes as fine as 50 pm can be generated [340]. This probe is then rastered over the specimen region of interest, with a specified dwell time at each point on the surface. The number of points represents the pixel resolution of the subsequent digital image, with the detected electron signal at each point assigned to an individual pixel. As such, the information collected from each point is governed by the size of the probe. Finally, the dwell time denotes how long each point on the specimen receives the total beam current and, therefore, how much damage is imparted [339].

4.4.3.1 *High Angle Annular Dark Field STEM*

High angle annular dark field (HAADF) STEM involves the selection of incoherent high angle scattered electrons (often > 50 mrad) using an annular detector. The coherent, weakly scattered beam then passes through without contributing to the image [341]. The probability of an electron scattering at a high angle is proportional to the square of the atomic number (Z) of the target atom. Thus, the dominant source of image contrast in HAADF is the atomic composition variation of the specimen [342].

4.4.3.2 *Aberrations*

The engineering limitations of electromagnetic lenses, as in many high tolerance applications, result in small physical imperfections. These can cause electrons travelling through the lens bore hole to deviate from the intended path in an effect known as aberration.

There are two aberrations of particular significance in TEM. The first is spherical aberration, which involves electrons far from the optical axis being focussed to a different point than those close to it. This limits the minimum size of a focussed beam, thus reducing the resolution in STEM.

The second notable aberration occurs when electrons of varying wavelengths pass through a lens and are thus focussed to different degrees. This is known as chromatic aberration and is dependent on both the energy spread of the source and variable electron energy losses as the beam interacts with a specimen. It results in the blurring of images, especially at high magnification and with thicker samples.

Lens aberrations can be corrected for in STEM by placing a series of multipole electromagnets before the lenses focussing the probe. This corrector system generates artificial aberrations equal in magnitude and opposite in geometry to those produced by the probe–forming lens, thus counteracting them and resulting in a more finely focussed probe [342], [343].

4.4.3.3 *Energy Dispersive X–Ray Spectroscopy*

A widely utilised analytical technique in STEM in the high–resolution compositional study of MAX phases is EDS. The main practical difference between EDS in SEM and STEM is the resolution achieved. In STEM, the probe can be significantly smaller than in SEM (~50 compared with > 100 pm), allowing for far higher spatial resolution. Equally, the interaction volume is limited by the thin specimens, allowing the vast majority of electrons to scattering inelastically from relatively few atoms and thus generating X–rays from a small spatial cross–section.

When combined with atomic resolution imaging, STEM–EDS can produce X–ray spectra from individual atomic locations, thus allowing atomic resolution elemental mapping to be achieved for certain materials [344]–[346]. This is not to say that the interaction volumes in TEM specimens are negligible– it remains a limiting factor in the practical resolution of EDS. Jones *et al.* [347] approximated the beam spread, b, in metres as

$$b = 8 \times 10^{-12} \frac{Z}{E_0} (N_v)^{0.5} (t)^{1.5} \tag{4.5}$$

where Z is the mean atomic mass number, E_0 is the beam energy in keV, N_v is the specimen atomic number density and t is the specimen thickness. As such, a probe accelerated to 200 kV, travelling through a 50 nm thick Ti_3AlC_2 specimen would experience a broadening of ~1.91 nm, significantly larger than a probe diameter of the order of 0.1 nm. Thus, the spatial resolution suffers whilst the uncertainty is increased.

As with both XRD and SEM, background X–ray emission due to bremsstrahlung reduces the SNR noticeably in TEM. Additionally, the relatively scarce X–ray production as a result of the small volume of specimen material, especially when performing high resolution scans, results in a weak signal. Low energy X–ray absorption and the small collection areas covered by even the largest detectors (at most ~7.2% of the theoretical maximum [348]), further reduces the counts at the detector. Therefore, a useful X–ray spectrum requires an optimised sample tilt, high beam current and/or long exposure times to collect. This is especially important when performing quantitative EDS analysis.

Additionally, due to the crowded nature of TEM sample holders, their associated grids and fixings, as well as the proximity of the EDS detector(s), a significant amount of material exposed to electrons is not based in the specimen. Spurious

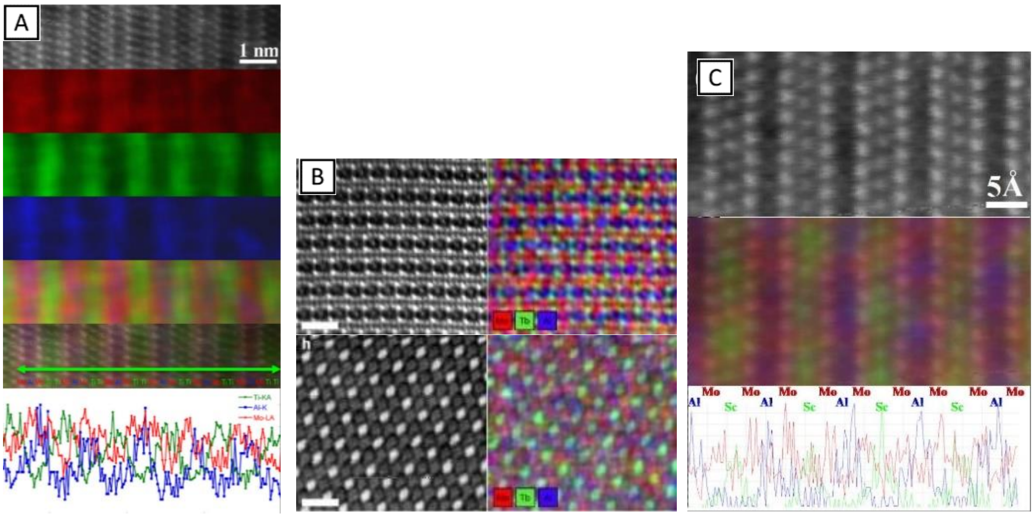

Fig. 4.12 – STEM–EDS of MAX phases: Examples of high–resolution STEM–EDS combined with atomic resolution HAADF STEM imaging of various MAX phases reported in the literature. (A) $Mo_2Ti_2AlC_3$. (B) $(Mo_{2/3}Tb_{1/3})_2AlC$. (C) Mo_2ScAlC_2. Reproduced from: (A) *Journal of Applied Physics*, 118, 9, B. Anasori *et al.*, p. 094304(1–14), Copyright (2015), with permission from AIP Publishing [119]; (B) *Chemistry of Materials*, 31, 7, Q. Tao *et al.*, p. 2476–2485, Copyright (2019), with permission from the American Chemical Society [125]; (C) *Acta Materialia*, 125, R. Meshkian *et al.*, p. 476–480, Copyright (2017), with permission from Elsevier [359].

signals from Cu, Mo and Au from support grids; Ga and Pt from specimens prepared using FIB milling; Fe and Co from the pole piece; or Zr, Si and Pb from the detector itself, are common artefacts in STEM–EDS signals [349]. This increases the likelihood of overlapping peaks. For example, Cu – a common grid and spacer material, has a K_α X–ray emission at 8.04 kV, close to the Ta–L_α emission at 8.145 kV. Due to noise introduced during X–ray detection, the FWHM of STEM–EDS peaks are generally >100 eV. So, specimens containing Ta in a holder containing Cu (or vice versa), will have a combined Ta/Cu peak at ~8.1 keV. This was the case in Manuscript 2 (Chapter 6), which meant quantitative Ta concentration analysis had to be performed using the lower energy M_α emission peak, reducing SNR, and increasing the final uncertainty.

Whilst qualitative EDS is a powerful technique by itself, allowing the identification and mapping of elements at high resolution, a careful quantification procedure is required to produce meaningful concentration values. There are a few methods a user can employ to extract elemental concentrations from EDS signals in TEM, but the most widely utilised is the ‘*k*–factor’ method [350], [351]. The background signal is first subtracted from the X–ray spectrum, often using a simple power law function for fitting. The quantification is then performed using the ratio of relative intensities of a specified peak from each of two elements present in the signal, multiplied by a correction factor, k, using

$$\frac{C_A}{C_B} = k_{A,B}\frac{I_A}{I_B} \tag{4.6}$$

where C_A and C_B are the concentrations of element A and B, respectively, $k_{A,B}$ is the correction factor for elements A and B, with I_A and I_B as the relative intensities of a peak from A and B, respectively. The k–factor for each element is related to fundamental microscope operation parameters such as accelerating voltage. Theoretical values can be calculated, but are less reliable than experimental ones using standard reference materials under the same microscope conditions as used to collect the EDS signal [352]. However, this can be an impossible task for certain samples so, as in Manuscript 3 (Chapter 7), theoretical values are often used instead.

Uncertainties in calculated elemental concentrations can arise from a multitude of sources, including low SNR, convoluted peaks, low energy X–ray absorption, an incomplete element list, background function approximation and, of course, the k–factors themselves. As such, standardless EDS quantifications using theoretical k–factors often result in uncertainties up to ±10%. Despite the inherent uncertainties in STEM–EDS, when combined with high resolution HAADF imaging, as well as complementary bulk characterisations such as XRD, it is an extremely useful tool.

Atomic resolution TEM and STEM has been utilised often in the literature for confirming the layered nature of MAX phases, as well as for investigating stacking configurations [112], [121], [125], [251], [353]–[355]. This has proved especially useful for probing the various A– and MX–layer polymorphs of 312 and 413 MAX phases, which can be difficult to identify using bulk measurements such as XRD. A good example of this is the report by Manoun *et al.* in 2006 on the structure of Ta_4AlC_3 from synchrotron XRD, which was assumed to have a structure similar to the previously studied Ti_4AlN_3 [356]. However, Lin *et al.* showed using atomic resolution TEM and STEM in subsequent work that the structure producing

Manoun *et al.*'s XRD profile was in fact a polymorph of the expected Ta_4AlC_3, with a slightly different intra–MX layer stacking sequence to that of Ti_4AlN_3 [357], [358]. Perhaps partially in response, many subsequent reports on MAX phase structures have included atomically resolved TEM or STEM to bulk measurements, as has been performed in Manuscript 2 (Chapter 6).

Atomic layer spatial resolution has also been achieved using STEM–EDS by a few authors, whilst scanning along the basal plane. Anasori *et al.* were perhaps the first to provide evidence of the power of this technique for MAX phases – in 2015, they used high resolution STEM–EDS with atomically resolved HAADF STEM to confirm the atomic ordering in the quaternary $Mo_2Ti_2AlC_3$ MAX phase, with EDS line profiles showing a close–to atomic spatial resolution [119]. Meshkian *et al.* followed this in 2017 showing similar ordering for the newly discovered Mo_2ScAlC_2 [359], with Tao *et al.* using a similar approach for ordered rare–earth i–MAX phases [125]. More recently, Griseri *et al.* performed lattice resolution STEM–EDS on new Ta–Hf solid solution MAX phases of various stoichiometries [360], finding no evidence for M–layer ordering. Griseri *et al.*'s report leads nicely on to the work in Manuscript 2 (Chapter 6), where partial M–layer ordering was also shown for the newly synthesised Ta–Ti solid solution MAX phases, following combined HAADF STEM and STEM–EDS characterisations. Additionally, quantitative EDS was performed to confirm the Ta/Ti ratio. Quantification of EDS signals was performed using the standardless *k*–factor method, with spectrum images binned by 10 and 4 for the spatial and spectral axes, respectively, for visual clarity and to increase the signal to noise ratio. All STEM–EDS processing was performed in HyperSpy [361], with averaged profiles computed using the NumPy analysis package [362], with uncertainties for all reported values stated in Manuscript 2 (Chapter 6).

As discussed in section 4.3.2, TEM specimens were thinned to electron transparency using a Ga^+ FIB, with final polishing steps performed with a 23 pA beam current at 2 keV. Following this, to reduce Ga^+ ion damage such as curtaining, the samples were irradiated using a Gatan PIPS II broad Ar^+ ion beam for 20 minutes at 500 eV. Additionally, to reduce contamination of the sample during high resolution imaging and EDS mapping, thinned and polished samples were plasma cleaned for 20 s directly before loading for TEM analysis. All SAED patterns were collected using an FEI Tecnai TF–30 FEG–AEM TEM, with an accelerating voltage of 300 kV. STEM images and EDS maps were obtained using a probe C_s corrected FEI Titan G2 with an X–FEG source operated at 200 kV, a probe current of 90 pA, collection semi–angle of 21 mrad and equipped with a ChemiSTEM SuperX system.

4.5 Proton Irradiation

Whilst much of the literature on irradiation of MAX phases focuses on heavy ions [299], there has been growing evidence in recent years that protons can be used as alternatives to simulate neutron damage, despite the significant differences in atomic displacement cascade size. Even at damage rates up to three orders of magnitude higher than fission reactor neutron irradiations, large scale damage structures produced by protons have been shown to be comparable to those produced in fission–relevant spectra, especially in terms of elemental segregation

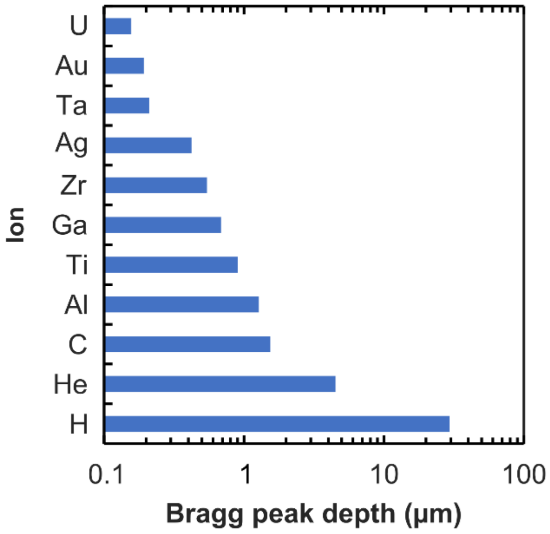

Fig. 4.13 – Bragg peak depths of 2 MeV ions: A comparison of various ions, from H to U (not exhaustive) incident at 2 MeV in Ti_3AlC_2, as calculated using SRIM with displacement energies from Argarwhal *et al.* [368]. Note the almost order of magnitude difference in Bragg peak depth between H (30 μm) and the next element in the periodic table, He (4.5 μm).

and microstructural instabilities. This has been demonstrated in Zr alloys and structural steels [228], [232]. Additionally, the damage profile produced by protons is considerably shallower before the Bragg peak than for heavy ions, with a much higher penetration depth. This can be seen from SRIM simulations represented in Fig. 4.14. In 2018, Ward *et al.* reported on the crystallographic evolution of Ti_3SiC_2 and Ti_3AlC_2 MAX phases following exposure to 1.5 MeV protons at 350 °C, to a dose of 0.1 dpa. Both the characteristic unit cell strain and phase transformation were observed, with a *c*–lattice parameter expansion and *a*–parameter contraction, as in a multitude of previous heavy ion irradiations in the literature [211], [238], [269], [270], [275], [280], [283], [363], [243], [246], [250], [252], [257], [266]–[268].

In this work, 2 MeV proton irradiations were performed at the University of Manchester's Dalton Cumbrian Facility (DCF) using an average beam current of 10.4 µA. A 5 MeV tandem pelletron was used to accelerate protons onto a stationary target containing bulk test samples [364]. As reported in Manuscript 3 (Chapter 7), samples were exposed to damage levels of ~0.06 and ~0.11 dpa, at ~141 °C, ~351 °C and ~658 °C. Bulk 7 × 3 × 1 mm samples were prepared using electrical discharge machining, with the faces subsequently polished to a ¼ µm diamond finish. The rear faces of the samples were mounted to a steel backing plate in direct contact with an inductive heating element using a thin layer of silver paint, with a

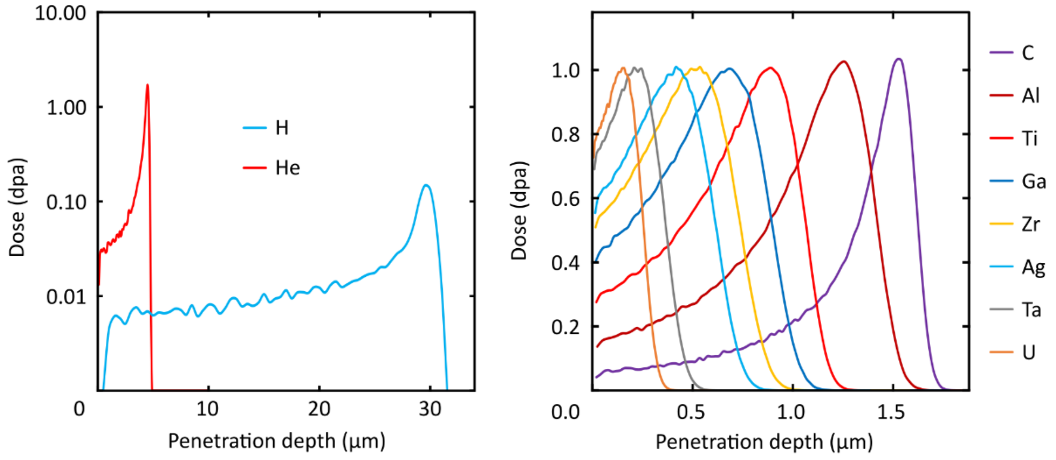

Fig. 4.14 – A comparison of ion damage profiles: Calculated vacancy production, given as dose (dpa) as a function of depth, for a range of ions. Calculations were performed using SRIM–2013 with 1,000,000 ions.

thermocouple soldered to the rear of the central sample. A Ta shim was fixed over the holder edges to prevent stray ions from activating the holder.

For room temperature irradiations, the thermocouple reading was used to track sample temperature variations, which were corrected *via* user beam current adjustments, usually less than 0.5 µA. For irradiations at ~351 °C and ~658 °C, the thermocouple reading was used to calibrate a thermal camera emissivity at the start of the heating. The thermal camera was then used to monitor temperature variations. The difference in process was necessary due to the higher reliability of temperature measurements of the thermal camera, which are generated from the irradiated sample surface, rather than at the rear, next to the heater. The thermal camera, however, only operates reliably above temperatures of ~150 °C and thus could not be used for the lower temperature (~141 °C) setups. As such, thermocouple readings from the room temperature irradiations are likely lower than the surface value, due to beam heating of the irradiated surface and subsequent dissipation of heat as it is conducted through the 1 mm thickness of sample. The emissivities for the three materials were 0.29(3) for Ti_3AlC_2, 0.41(2) for $(Ta_{0.32}Ti_{0.68})_3Al_{0.81}C_2$ and 0.5(3) for $(Ta_{0.25}Ti_{0.75})3Al_{0.77}C_2$.

4.5.1 Calculations

Estimations of both atomic displacement damage and implanted ions were made using the Kinchin–Pease method [365] as implemented in the Monte Carlo software package Stopping and Range of Ions in Matter (SRIM), written by Ziegler and Biersack [366]. The vacancy production method employed was the *Ion Distribution and Quick Calculation of Damage*, which has been benchmarked with experimental data in the literature and shown to not grossly overestimate vacancy production, as with the *Detailed Calculation with full Damage Cascades* method [367], [368]. Whilst SRIM is far from perfect, not in the least due to its consideration of target materials as amorphous blocks, it is nonetheless a widely recognised industry standard in ion radiation damage estimation [369]. As such, values of dpa and appm derived from SRIM simulations should not be considered absolute, but rather a relative measure for comparison across the literature where SRIM has been utilised in a similar fashion. For each material, 100,000 incident ions were simulated. The atomic displacement energies, with associated source references, used for each element and the densities for the materials considered can be seen in Table 4.3 and Table 4.4, respectively.

Table 4.3 – The atomic displacement values (E_d) in eV of the elements used in SRIM calculations.

Element	m_r (amu)	E_d (eV)	Reference
Ta	180.95	90	[369]
Ti	47.867	30	[369]
Al	26.982	25	[369]
C	12.011	30	[368]

Table 4.4 – The theoretical and physical densities of the materials used in this work – using corrected values taking consideration of impurity content, along with their respective Bragg peak depths and damage levels after irradiation to 0.1 dpa by 2 MeV H$^+$ ions. The fluence at this dose is ~2.9 × 10^{18} protons cm^{-2}.

Material	$\rho_{theoretical}$ (g/cm^3)	$\rho_{measured}$ (g/cm^3)	Bragg peak depth (μm)	dpa at Bragg peak	60% Bragg peak depth (μm)	dpa at 60% Bragg peak
Ti_3AlC_2	4.30(3)	4.242(7)	29.6(2)	1.65(4)	17.8(2)	0.113(3)
$(Ta_{0.25}Ti_{0.75})_3Al_{0.77}C_2$	6.12(1)	5.009(12)	27.2(2)	1.41(3)	16.3(2)	0.113(3)
$(Ta_{0.38}Ti_{0.62})_3Al_{0.81}C_2$	7.28(1)	7.092(9)	25.6(2)	1.32(3)	15.4(2)	0.114(3)

By definition, dpa is the average number of times an atom is displaced from its lattice site. The formation of a vacancy, therefore, represents one displacement. So, dpa may written as

$$dpa = \frac{N_{d,vacancies}}{N_d} \tag{4.7}$$

where $N_{d,vacancies}$ is the number density of vacancies, in vacancies per unit volume, and N_d is the atomic number density of the material, in atoms per unit volume.

The ion irradiation simulations performed in SRIM calculate the total number of apparently stable vacancies produced per incident ion at a given depth in the material. This is the sum of the vacancies per ion produced by primary collisions,

$V_{primary}$, and the vacancies per ion due to recoils, V_{recoil}. The total expected vacancies, per unit volume, produced by an irradiation is, therefore, the product of the total number of ions per unit area – i.e., the fluence, f, and the total vacancies per ion per unit length, $V_{primary} + V_{recoil}$. Thus, we can write

$$dpa = \frac{f}{N_d}\left(V_{primary} + V_{recoil}\right) \tag{4.8}$$

As ions have a well–defined charge state, the fluence can be defined as

$$f = \frac{Q}{Aeq} \tag{4.9}$$

where Q is the total charge in coulombs (C) which has passed through an area A, with a charge state q and e as the fundamental electron charge (i.e., $\frac{Q}{eq}$ represents the total number of ions). Using the definition of current, $I = \frac{Q}{t}$ in amps, we can write

$$dpa = \frac{It}{N_d Aeq}\left(V_{primary} + V_{recoil}\right) \tag{4.10}$$

Conversely, given a beam current, ion specie, sample area, material, and the results from the relevant SRIM calculation, the estimated time taken for a desired damage in dpa is

$$t = \frac{dpa \cdot N_d Aeq}{I\left(V_{primary} + V_{recoil}\right)} \tag{4.11}$$

Equation (4.11) was used in Manuscript 3 (Chapter 7) to guide proton irradiations and to estimate the actual damage received during irradiation, which takes into account experimental fluctuations in beam current as well as ramp–up/ramp–down time, which affect the true fluence received. Despite high frequency beam current fluctuations during irradiation of up to 5.7%, the propagated uncertainty of the damage, in dpa, received by the samples was ±2.4% on average.

Another important quantity extracted from the SRIM simulations is the implantation depth of the incident ions. Examples of this for different ion species can be seen in Fig. 4.15. This profile is especially important when considering the potential agglomeration of protons into H bubbles, following neutralisation with delocalised electrons in the target lattice. These bubbles may then grow, creating enough strain in the lattice to cause eventual exfoliation. Evidence of this has been reported in earlier 2 MeV proton irradiations by Ward *et al.* [281], who observed exfoliation of bulk material at a depth close to the Bragg peak for Ti_3AlC_2. The authors also noted a possible link between the exfoliation and the dose rate provided by the proton beam. In Manuscript 3 (Chapter 7), the same effect was observed for both Ti_3AlC_2 and $(Ta_{0.38}Ti_{0.62})_3Al_{0.81}C_2$, also irradiated with 2 MeV protons, but for a slightly lower dose rate of 4.96×10^{-6} dpa s^{-1} compared with Ward's 5.4×10^{-6} dpa s^{-1}. The primary issue with this is the loss of potential data, assuming the exfoliated material can't be recovered, which was the case in Manuscript 3 (Chapter 7), as the damaged region was entirely confined to the exfoliated material.

SRIM automatically calculates the number of implanted ions per unit length, in binned slices of width equal to the depth of the simulation target divided by 100. Once the irradiation fluence and target material number density is known, these values can be converted to a measure of appm, for each binned depth, using the following relation:

$$H^{+}_{appm} = \frac{H^{+}_{SRIM} \cdot f}{N_d} \cdot 1 \times 10^{6} \qquad (4.12)$$

where H^{+}_{appm} is the concentration of implanted H in the target material and H^{+}_{SRIM} is number of H ions per unit length. This allows the elucidation of another benefit of protons over heavy ions for radiation damage studies – the confinement of almost all implanted ions to a narrow region close to the Bragg peak. This is as opposed to a more continuous implantation profile produced by heavier ions, as can be seen in Fig. 4.15.

Interestingly, the ASTM recommended procedure for calculating the implantation profile from SRIM involves a different method to that described previously [369].

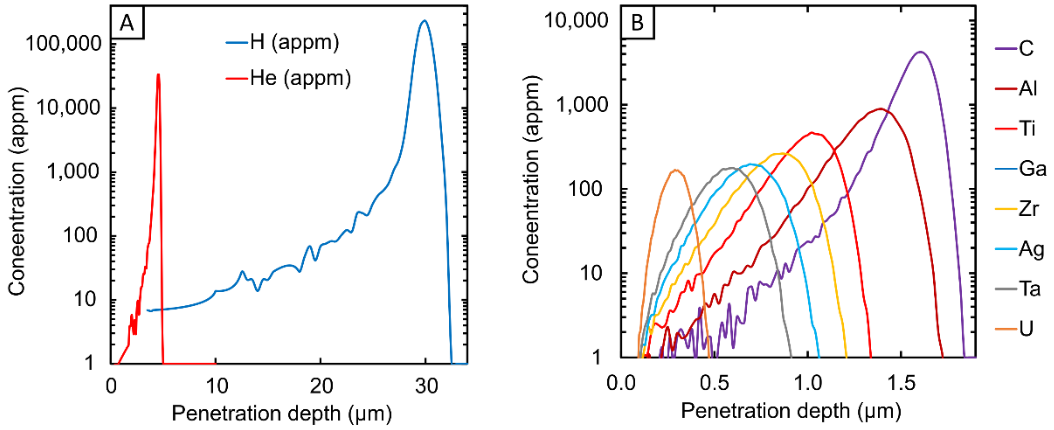

Fig. 4.15 – Implantation profiles: A comparison of the penetration depths of various ions incident at 2 MeV in Ti_3AlC_2, as a function of implanted concentration in the target in appm, after a dose of 1 dpa at the Bragg peak. The profiles for H and He have been placed on a different plot (A) to the heavier ions (B), due to the difference in scale.

Instead, the implantation profile is assumed to be a Gaussian function, with a full–width–half–maximum (FWHM) equal to the SRIM quantity 'straggle' – a measure of the lateral deviation of incident ions from the depth of maximum ion implant. However, the differences in calculated peak concentrations between this method and the previous one are significant. The Gaussian method results in peak concentrations as little as half of those produced by the direct conversion method, presumably due to an overestimation of the FWHM in using the straggle. Incidentally, with the inclusion of the uncertainty due to the finite bin width of the simulation when using the straggle measure, the propagated uncertainties for the Gaussian method are almost an order of magnitude higher than those for the previous method at ~19% compared with ~2.4%. As such, the first method described is used for all implantation profile calculations in this work.

4.6 High–Resolution Digital Image Correlation

The use of digital image correlation (DIC) to monitor large area strain localisations in engineering materials has been well established over the past 20 years [370], [371], [380]–[385], [372]–[379]. The general principle of DIC is to compare the state of a surface of interest before and after deformation of the specimen. A suitable preparation of the specimen surface is applied to allow the displacements of certain

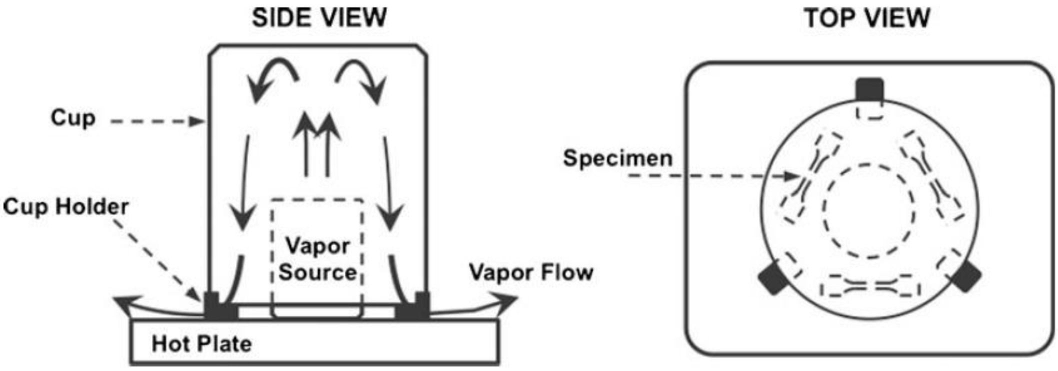

Fig. 4.16 – Remodelling gold: A schematic of the apparatus used for Au layer remodelling to form a speckled surface nanopattern. Reproduced from *Experimental Mechanics*, 53, 5, F. Di Gioacchino *et al.*, *Plastic Strain Mapping with Sub–micron Resolution Using Digital Image Correlation*, p. 743–754, Copyright (2013), with permission from Springer Nature [374].

features to be tracked. Displacement correlations are then used to generate a full field strain map.

Often, surfaces are prepared *via* the deposition of a speckled pattern, in which the displacement of each speckle is digitally tracked as the material it is adhered to deforms. The primary benefits of this method are its resolution and applicability to a large variety of materials. The spatial resolution of the resultant strain maps is ultimately limited by both the size of the speckle features and the pixel size of the digital images used during tracking [374], [386].

Recent advances in deposition and correlation methods have ushered in the field of high–resolution DIC (HRDIC). Di Gioacchino and Quinta da Fonseca developed a technique in which Au nanoparticles are tracked on a specimen surface using high resolution BSE SEM, allowing the observation of individual slip traces in deformed specimens [374]. The Au pattern is formed *via* heat and moisture–induced remodelling of a thin (< 50 nm) sputtered Au layer, resulting in a homogenous speckle pattern of nano–scale Au features with similar spacing. The quantification of strain on this scale allows the true localised strain heterogeneity to be assessed, showing, for some materials, an order of magnitude increase in maximum strain compared to that observed at the microscale [374], [387], [388].

In addition to the high spatial resolution, these patterns have been shown to be stable under proton irradiation and at temperatures up to ~650 °C, allowing for irradiation induced localised strain to be mapped. In 2019, Thomas *et al.* in 2019 reported the first use of HRDIC to quantify the strain localisation in Zircaloy–4 following 2 MeV proton irradiation at ~357 °C to ~0.1 dpa, observing a mean effective shear strain of 2.03% [385]. Following multiple reports in the literature of radiation induced microcracking along grain boundaries in various MAX phases, even at low doses [253], [257], [266], [289], [294], [389], we used the same technique to characterise local irradiation–induced deformation in Ti_3AlC_2 and $(Ta,Ti)_3AlC_2$. In Manuscript 3 (Chapter 7), we observed a maximum average effective shear strain of 1.97(5)% for $(Ta_{0.25}Ti_{0.75})_3Al_{0.77}C_2$, using HRDIC, as well as the characteristic microcracking. This correlates remarkably well with the 2.03(2)% *c*–parameter

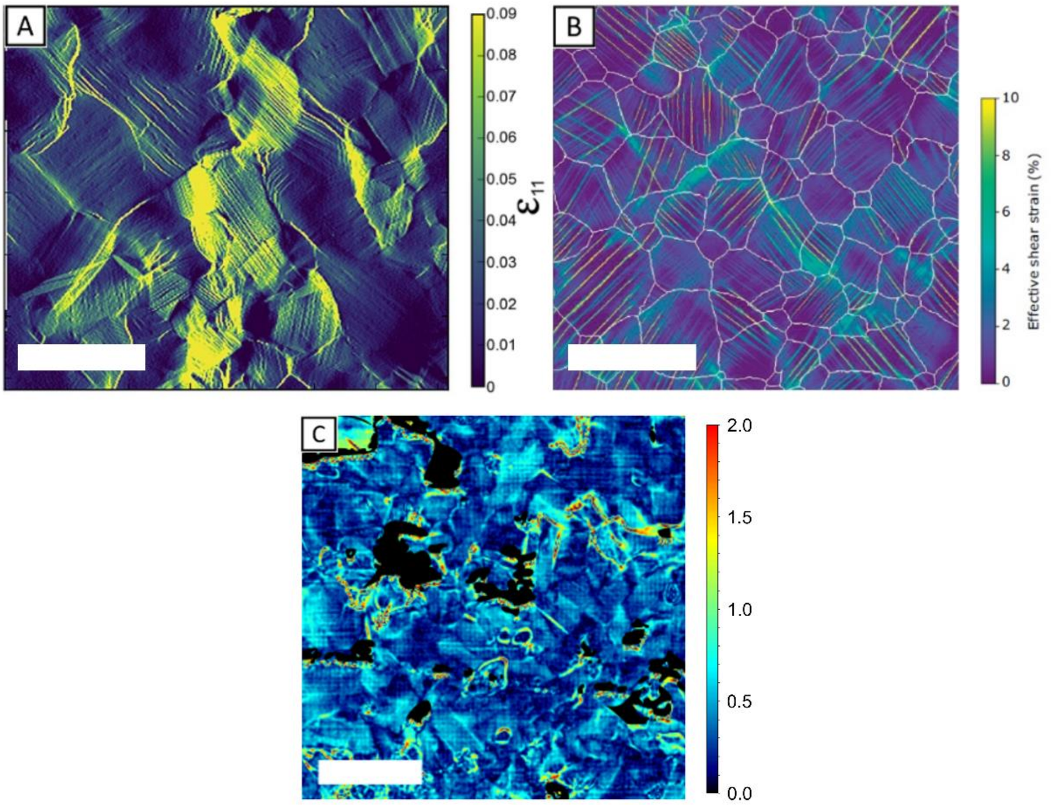

Fig. 4.17 – Full profile strain mapping: The relative strain across a variety of deformed specimens monitored using HRDIC: (A) Mg after 2% uniaxial tensile strain [384]. (B) Zircaloy–4 after 2% uniaxial tensile strain and 2 MeV proton irradiation to ~0.1 dpa at ~357 °C [385]. (C) $(Ta_{0.38}Ti_{0.62})_3Al_{0.81}C_2$ after 2 MeV proton irradiation to 0.06(1) dpa at 354(8) °C. All scale bars represent 30 µm.

strain obtained from XRD data. Whilst this is not currently a well–established method for irradiation investigations, there is growing evidence for the effectiveness of HRDIC in strain mapping for irradiated materials.

To obtain the HRDIC results in Manuscript 3 (Chapter 7), the gold remodelling technique, adapted from [374] was utilised on ¼ µm polished surfaces of Ti_3AlC_2, $(Ta_{0.25}Ti_{0.75})_3Al_{0.77}C_2$ and $(Ta_{0.32}Ti_{0.68})_3Al_{0.81}C_2$. A ~20 nm thick Au layer was deposited using an Edwards S150B sputter coater. Samples were then placed on a steel hot plate at 350 °C and exposed to a partially enclosed steam atmosphere for 180 minutes to reform the Au layer. To prevent further pattern development during irradiations, for the samples intended for ~141 °C and ~351 °C irradiations, a further heat treatment was performed at 350 °C for 6 h in the same environment on the hot plate. For ~658 °C irradiations, the samples were instead heat treated at 600 °C for 9 h in an argon furnace. For the majority of the samples, these heat treatments fully stabilised the speckle pattern, with no development of the speckle sizes seen after irradiation. The subsequent Au nanoscale speckle pattern consisted of a mean particle size of 45(13) nm with a spacing of 32(10) nm, as is shown in Fig. 4.18. However, some of the samples irradiated at ~658 °C underwent further development of the speckle pattern during irradiation, rendering the HRDIC data incomplete. This suggests that a longer heat treatment is required to prevent further development during subsequent irradiations.

The initial Au layer thickness and quality, remodelling time, temperature and humidity all effect the size and structure of the resulting nanopattern [386]. As such, the parameters used in this work are not necessarily optimal for these materials, but nonetheless resulted in a fine, homogenous pattern which allowed a localised strain resolution of ~350 nm to be achieved.

When imaged using BSE SEM, the structure and composition of the pattern contribute to a sufficiently high contrast with the specimen surface to allow digital tracking of the individual Au nanofeatures. Immersion mode BSE images were acquired using an FEI Magellan HR 400L FE–SEM, operated at 10 kV, a beam current of 0.8 nA, a working distance of ~5 mm and images captured using an

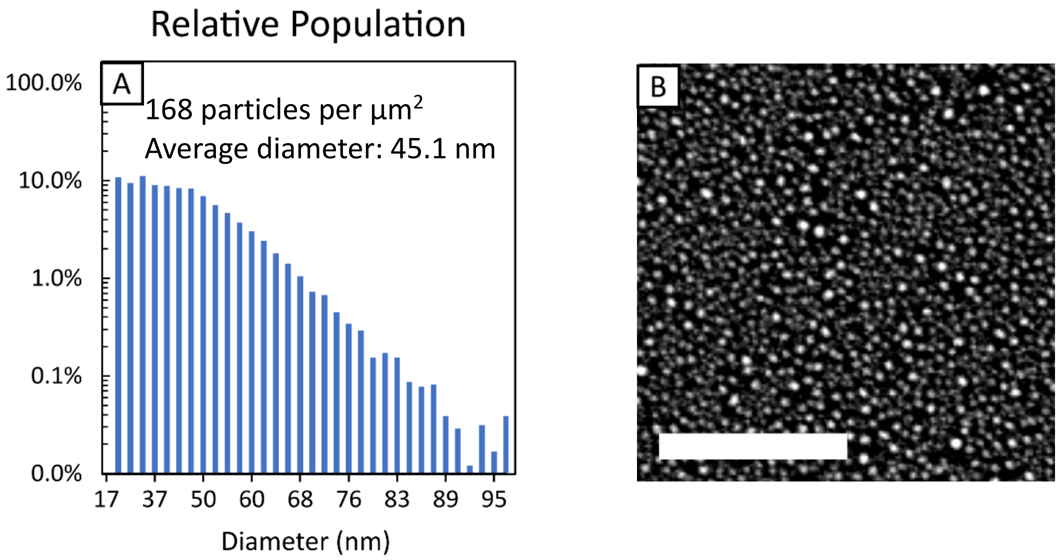

Fig. 4.18 – The speckled nanopattern: (A) The distribution of particle sizes of the pattern used for experiments in Manuscript 3 (Chapter 7), demonstrating the homogeneity and size of the speckles. (B) a region of the nanopattern on $(Ta_{0.38}Ti_{0.62})_3Al_{0.81}C_2$, following 180 minutes of water vapour remodelling at 350 °C. The image is a BSE–SEM micrograph, demonstrating the high contrast between the Au speckles and the substrate surface. The length of the scale bar is 1 µm.

insertable concentric backscattered electron detector. For each sample, both before and after irradiation, an 8 × 8 image array was captured from the specimen centre using the Thermo Fisher Scientific MAPS software [390]. The individual 8–bit images had dimensions of 2048 × 1768 pixels and included a 20% overlap with adjacent regions, resulting in a final stitched map of ~12800 × 11050 pixels or a 187.5 × 161.9 µm field of view. Mosaics consisting of the 64 individual images were stitched using ImageJ by applying a linear blend on overlapping identical regions [391].

The mosaics of virgin and irradiated specimens were correlated using the commercial source software package DaVis 8.4.0 [392]. A sub–window size of 48 × 48 pixels was used with a 50% overlap, equating to a spatial resolution of ~350 × 350 nm^2. The DIC generates a full–field in–plane displacement map for each mosaic pair.

The DIC analysis produces full–field in–plane displacement maps, $u(x_1, x_2, 0)$, on the plane x_1x_2 with normal x_3. The in–plane deformation is then calculated *via* differentiation of the displacement vectors using the displacement gradient tensor:

$$\frac{\partial u_i}{\partial x_j} = \begin{bmatrix} \frac{\partial u_1}{\partial x_1} & \frac{\partial u_2}{\partial x_1} \\ \frac{\partial u_1}{\partial x_2} & \frac{\partial u_1}{\partial x_2} \end{bmatrix} \tag{4.13}$$

To ensure consistency across displacement components and to reduce the impact of displacement uncertainty, second order central differences were used to compute the gradient. The effective shear strain, γ_{eff} – a convenient measure for representing slip shearing, was calculated using [393]:

$$\gamma_{eff} = \sqrt{\left(\frac{\frac{\partial u_1}{\partial x_1} - \frac{\partial u_2}{\partial x_2}}{2}\right)^2 + \left(\frac{\frac{\partial u_1}{\partial x_2} + \frac{\partial u_2}{\partial x_1}}{2}\right)^2} \tag{4.14}$$

When the local strain is large, however, the logarithmic strain, ε_{ii} is a more appropriate measure to plot and is given by

$$\varepsilon_{ii} = \ln\left(\frac{\partial u_i}{\partial x_i} + 1\right) \tag{4.15}$$

Additionally, the magnitude of rigid body rotation about x_3 for small displacements, as described by Dieter [394], is given by:

$$\omega_3 = \frac{1}{2}\left(\frac{\partial u_1}{\partial x_2} - \frac{\partial u_2}{\partial x_1}\right) \tag{4.16}$$

The full HRDIC dataset for the work in Manuscript 3 (Chapter 7) was processed using the DefDAP 0.92.3 Python library [395].

Finally, quantitative microcrack analysis of the samples both before and after irradiation was performed on the BSE micrographs used for HRDIC. A combination of image–based thresholding and particle tracking methods, as implemented in

ImageJ [391], was used to estimate initial crack densities in the virgin material as well as the growth of pre–existing cracks and formation of independent cracks during irradiation.

Chapter 5: Manuscript 1 – 'High throughput relative stability predictions of 211 and 312 $(M^{I}_{2/3},M^{II}_{1/3})_{n+1}(A^{I},A^{II})X_n$ phases for nuclear fusion'

Maxwell T. P. Rigby–Bell,[a] Lee Evitts,[b] Simon Middleburgh,[b] Christopher P. Race,[a] Philipp Frankel,[a] and Sarah J. Haigh[a]

[a] Department of Materials, University of Manchester, Manchester, M1 3BB, UK.

[b] Nuclear Futures Institute, Bangor University, Gwynedd, LL57 2DG, UK.

5.1 Abstract

We report on the consideration of novel MAX phase ceramics in the quaternary $(M^{I}_{2/3},M^{II}_{1/3})_{n+1}(A^{I}_{x}A^{II}_{1-x})C_n$ system (M = Ti, V, Cr, Y, or Ta, W; A = Al or Si; x = 0.5 or 1; and n = 1 or 2), for fast neutron, low activation nuclear applications such as nuclear fusion. Atomic formation enthalpies were obtained from total energy calculations of 180 trial quaternary and quinary MAX phase compositions, with elemental constituents chosen based on their relevance to a future fusion environment.

5.2 Introduction

The development of high heat flux and radiation resistant plasma facing component (PFC) materials for future fusion power plants, such as DEMO, is critical for the delivery of commercial fusion energy [96], and has been identified as one of the seven major challenges outlined by the EFDA Roadmap [31]. First wall PFC

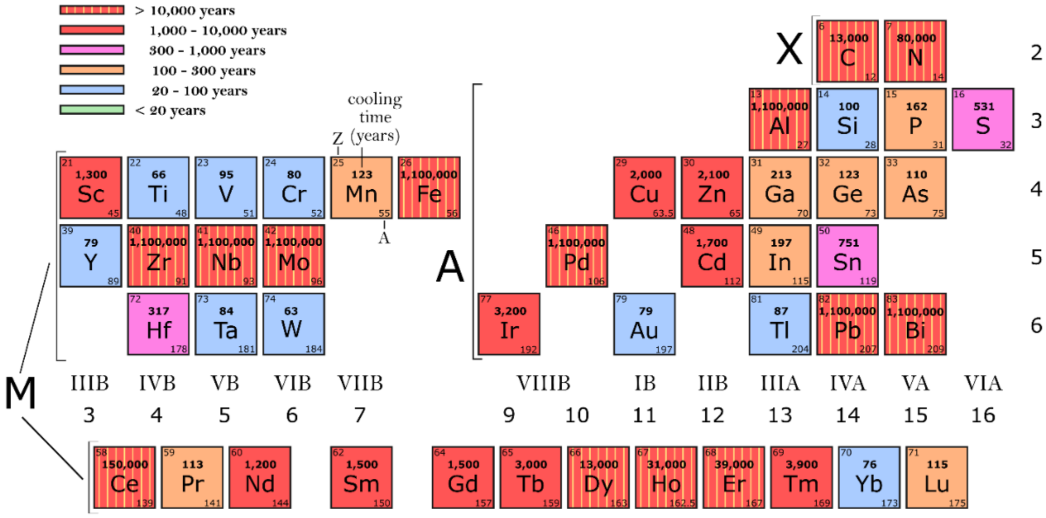

Fig. 5.1 – A reduced periodic table of the MAX phase elements, colour coded with reference to their simulated cooling time to low level waste classification (the number above the element name) following 14 years of pulsed operation in a DEMO–like tokamak. Neutronics data courtesy of Gilbert & Sublet (2015) [77].

materials are required to maintain structural integrity and thermal conductivity, whilst minimising radiation–induced activation, during normal operation and accident scenario conditions, over an expected service lifecycle of at least 5 full power years [396]. Whilst acceptable PFC materials have been developed for use in ITER, such as tungsten for the first wall [68], the conditions in DEMO will be considerably more hostile. These include expected incident particle fluxes of at least an order of magnitude higher at the first wall, reaching 20 MW m^{-2} in select locations [68], high temperatures (especially during transient plasma events) of 300–3200 °C, gamma radiation, plasma induced sputtering and erosion, high energy neutron damage (3–30 dpa yr^{-1}), and hydrogen, tritium, deuterium and helium trapping [397].

Materials able to operate in such conditions simply do not currently exist at a suitable technology readiness level for implementation in a DEMO–like environment in the next decade. As noted in the EFDA Roadmap, around 10–15 years of research is required to fully develop a nuclear–grade material from a ‘proof–of–principle’ stage [31]. It is therefore essential that new materials are continually developed, or we risk severe delays in the realisation of fusion energy if current shielding candidate materials prove unsuitable.

MAX phases are a relatively new class of hexagonal nano–layered carbides and nitrides with a general formula $M_{n+1}AX_n$ where n = 1, 2, 3, etc., M is generally an early transition metal or lanthanide, A is generally a group 13–15 element and X is either carbon or nitrogen (see Fig. 5.1). They have demonstrated a promising mixture of both ceramic and metallic properties, largely attributed to their nano–laminated structure and metallic–like bonding. Like ceramics, some MAX phase materials are elastically rigid (Young's modulus larger than 300 GPa), strong at high temperatures [102], [398], lightweight (< 4.5 g cm^{-3}) and even have good creep and oxidation resistant [168], [184], [201], [399], [400]. On the other hand, like metals, MAX phases have shown excellent electrical and thermal conductivity, machinability [103], [106], thermal shock resistance and even damage tolerance [102].

Whilst various MAX phases, including those containing M– or A–layer solid solutions, have been considered for demanding fission–based environments, such as $(Zr, M^2)_2$–A–C for fuel cladding [401], [402], the compositions are generally not suitable for fusion environments, due to instabilities at high temperature, oxidation, and the presence of 'high activation' elements. In particular Zr, Nb or Al are expected to produce long–lived radioactive isotopes during operation in a fusion environment. The only MAX phase studied in depth to date with an elemental composition of primarily low activation elements is Ti_3SiC_2, which has displayed a tendency towards thermal decomposition at high temperatures (> 1200 K) [403], [404].

5.3 Down–Selection

In Fig. 5.1, the elements are colour coded with reference to their simulated cooling time to low level waste classification after 14 years of DEMO use. Elements like

Ti, V, Cr, and Si, with cooling times less than 100 years, are highly desirable for fusion applications, and cooling times of less than 300 years are still attractive.

Given the vast elemental parameter space of the MAX phases, it would be temporally, not to mention computationally, inefficient to consider every possible combination and stoichiometry when designing a new fusion optimised MAX phase material. The first step, therefore, in the design of a MAX phase for fusion applications is elemental down–selection *via* consideration of limiting factors such as radiation–induced activation, toxicity and availability.

Gilbert & Sublet (2015) simulated the neutron induced activation, amongst other properties, of elements in a pulsed DEMO–like environment [77]. A selection of this data is represented in Fig. 5.1. For each element, the simulated time taken for 1 kg of pure material to cool to low level waste classification is displayed [405]. Elements which are expected to produce long–lived radioisotopes during in–reactor operation must be minimised and, if possible, eliminated. To this end, an arbitrary upper limit of 300 years (the somewhat perceivable future) may be used for down–selection. Notably, Al, C and N are expected to have cooling times of greater than 10,000 years. C, as the lesser of the two X–element evils, as well as an essential alloying element in various structural materials posed for use in fusion, is unavoidable. Al, generally the most stable A–layer element [110], is nonetheless avoidable.

When availability is considered, the list of potential elements is reduced further: Ge, Au, Tl, Yb and Lu are all omitted due to their prohibitive raw material costs [406]. Finally, As is omitted due to its toxicity, P for its astronomical vapour pressure at common synthesis temperatures (1600–1900 K [104]) and Mn for its propensity to form magnetic phases – which may interfere with plasma stability [407]. Thus, the list of suitable elements is reduced to:

M	Ti	V	Cr	Y	Ta	W
A	Si	Ga	In			
X	C					

This leaves 18 ternary compositions per order (211, 312, etc.), 90 elemental combinations for compositions with two independent M–elements (M^I and M^{II}), or 180 combinations for compositions with two M–elements and two A–elements, for a single fixed ratio of both M^{II}:M^{II} and A^I:A^{II} for each elemental combination. It should be noted that for Cr, although it is known to form magnetic phases under certain conditions [408], [409], its innate ability to form passivating oxide scales in extreme environments makes it potentially useful in a nuclear fusion reactor setting [410]–[412].

Although none of the existing MAX phase compositions are ideal for nuclear fusion in terms of activation, the range of viable MAX phase compositions is rapidly expanding. Recently, dozens of novel MAX phases, many with refractory metal M–layers, have been synthesised [110]. In addition, MAX phase materials can have structural variations including M–layer solid solutions and ordered phases, such as the in–plane ordered (i–MAX) phase $(W_{2/3}Y_{1/3})_2AlC$ [413], expanding the elemental parameter space significantly. However, these new materials are all largely Al–based [110] and to date little focus has been applied to non–Al–based refractory MAX phases for demanding environments.

Whilst over 155 MAX phases are known to exist [110], there remain a wealth of compositions and atomic ratios to explore and, with the interesting range of properties exhibited by the currently known phases, such exploration has the potential to bear fruit for PFC material development.

MAX phases are known to form from elemental powders during high temperature solid state reactions [414], [415]. It is suspected that binary MX carbides or nitrides are formed initially, followed by diffusion and intercalation of the A–layer to produce the nanolaminate MAX phase structure [416]. It should, therefore, be possible to substitute Al for another, similar, A–layer element. This has been demonstrated with Ga, a low–activation element, in recent reports [318], [417], but only for a small number of compositions.

In this work, we outline first principles calculations of relative stability and demonstrate the synthesis of new MAX phases, with a focus on elemental relevance to expected fusion environments.

Following elemental down–selection, a suitable template system is chosen. The field of non–ternary MAX phases represents relatively uncharted territory in the literature, especially for fully dense phases of high purity – several reported new phases have either not been synthesised in bulk or are below ~80% phase purity [116], [117], [413], [418], [419]. Furthermore, the recent discovery of a stable W–based i–MAX phase is of interest to the fusion materials community considering the focus on W–based composites for shielding applications [68], [93]. The i–MAX structure consists of a binary in–plane ordered layer of M–elements in the ratio M^I:M^{II} = 2:1 and with the XM_6 octahedra distorted relative to the difference in atomic radius of the M–elements. The interleaving A–layer often forms a Kagome–like 2D lattice as viewed down the [0001] direction. So far, only a 2:1 M^I:M^{II} ratio has been reported to result in the formation of i–MAX and the out–of–plane ordered 'o–MAX' phases. Additionally, these phases appear to exist in only 211 and 312 configurations, respectively [419]. Thus, the M^I:M^{II} = 2:1 ratio presents an interesting starting point for synthesis investigations.

In 2010, Dahlqvist *et al.* developed an efficient and systematic method for the prediction of potentially stable MAX phases, using density functional theory (DFT) [120]. Since then, DFT calculations have shown considerable promise in guiding synthesis trials in the discovery of novel MAX phases [111]. DFT is the approximation of the theoretical interactions in many–body systems. Attempting to solve the many–electron wavefunction to derive properties of a multi–atomic system is a highly expensive and inefficient task. Instead, the overall electronic structure can be approximated as a spatially dependent electron density, expressed by a set of functionals. The first reported *ab initio* calculations using DFT for MAX phases were performed by Medvedeva *et al.* in 1998, who investigated the electronic properties of the Ti_3SiC_2 system. Since then, over 200 relevant reports have been published. Fundamental crystal and electronic structure, bonding, lattice dynamics, phase stability, and elastic properties have been investigated for a swathe of compositions, for both theoretical and experimentally confirmed phases. Due to the inherent chemical diversity of the MAX phases, one of the most useful approximations that DFT can perform is that of thermodynamic stability of a phase, with respect to its competing phases during formation. This allows the prediction and theoretical characterisation of phases, yet to be synthesised but likely to form under the right conditions. In this way, the search for materials to satisfy the requirement for increasingly more complex and demanding technologies may be guided and accelerated.

5.4 Methods

DFT allows the calculation of the electronic ground–state of a group of atoms [420]. The total energy of the system in this state is then used to determine the enthalpy of formation per atom of the material with respect to either its elemental constituents (relative thermodynamic stability) or the sum of its most competing phases (actual thermodynamic stability), using Hess' law – equation (5.1). In this work, to save computational time, the relative thermodynamic stability is calculated to enable a comparison between the compositions studied.

$$\Delta \mathrm{H}_{\mathrm{reaction}} = \sum \Delta \mathrm{H}_{\mathrm{f\,(products)}} - \sum \Delta \mathrm{H}_{\mathrm{f\,(reactants)}} \qquad (5.1)$$

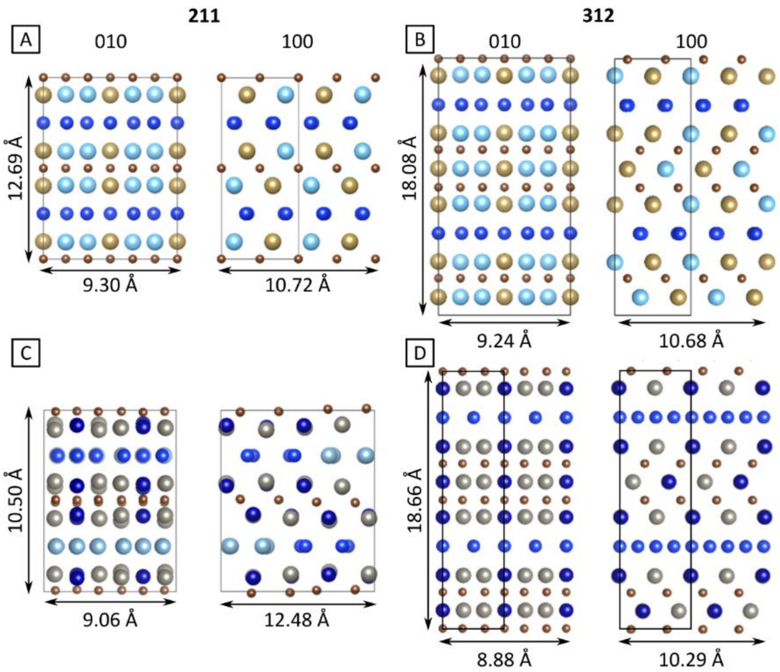

Fig. 5.2 – Relaxed structures clockwise from top left: (A) $(Ti_{2/3}Ta_{1/3})_2SiC$ [C m c m], (B) Ti_2TaSiC_2 [C m c 21], (C) $(W_{2/3}Cr_{1/3})_2(Al_{0.5}Si_{0.5})C$ [P m m n (2)], (D) W_2CrSiC_2 [C m c m]. The first row consists of the most stable 211 (A) and 312 (B) MAX phase structures, with the second row consisting of the least stable 211 (C) and 312 (D) phases. For each structure, the 010 (left) and 100 (right) projections, the order (bold) and comparative distances are labelled.

Total energy calculations were performed on supercells of 2 × 2 × 1 unit cells using DFT as implemented in the Vienna ab initio simulation package (VASP) [420], [421]. A plane–wave basis set cut–off energy of 500 eV was used for all calculations, with electron–ion interactions represented using the projector augmented–wave (PAW) method [422]. The generalized gradient approximation (GGA) [423] was used in the form of the parameterisation proposed by Perdew, Burke, and Ernzerhof (PBE) [424] to represent the electronic exchange–correlation energy. Partial occupancies were set using the tetrahedron method with Blöchl corrections [425]. Brillouin zone *k*–point sampling integrations were applied using a 3 × 3 × 1 gamma–centred grid [426], resulting in a *k*–point spacing of at ~0.5 A^{-1}. Unit cells were relaxed until the forces on ions converged to < 0.1 meV A^{-1}.

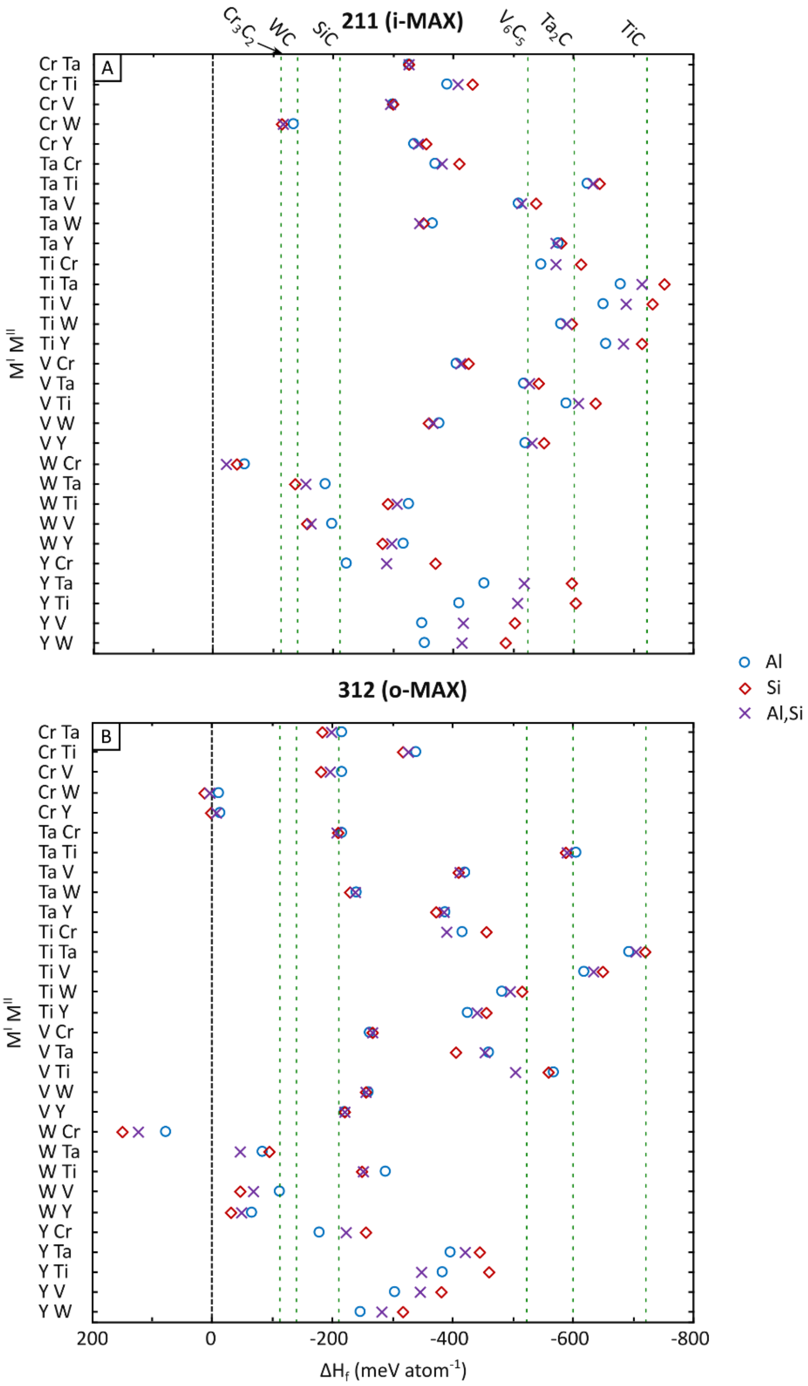

Fig. 5.3 – Elemental formation enthalpies (*x*–axis), in meV, for all MAX phase compositions considered, grouped by their respective (M^I, M^{II}) pair (*y*–axis). The formation enthalpies of common binary carbide competing phases are indicated by dashed green lines for reference. If a competing phase, such as a parent binary carbide, has a lower formation enthalpy than its respective target MAX phase, then it is likely to form instead.

For Cr–containing phases, spin–polarised calculations were performed with the magnetic moment of each element allowed to relax. For each composition, total energy calculations were performed for three initial magnetic configurations: ferromagnetic (FM), anti–ferromagnetic (AFM) and non–magnetic (NM, i.e., net magnetic moment = 0). As such, the formation enthalpy results shown for Cr–based phases represent the most stable final spin configuration – these are detailed in Table 5.1. The computational workload was performed on 16–core Intel Skylake Gold 6130 CPUs at a clock speed of 2.1 GHz, with 6 GB of RAM available on average per core. For each job, 96 cores were utilised, spread over two high performance computers – Supercomputing Wales in Cardiff [427], and the University of Manchester's Computational Shared Facility [428], with 201,598 CPU hours used in total for the calculations.

5.5 Results

The relative enthalpy of formation (ΔH_f) for all considered MAX phase compositions are shown in Fig. 5.3, with the unit cells of the four labelled phases displayed in Fig. 5.2. ΔH_f values range from almost –4 eV to just under 1 eV for Ti_2TaSiC_2 and W_2CrSiC_2 respectively, with no apparent relationship between the A–layer element and the relative stability of the composition. Relaxations indicate a strong correlation between the elemental pairs in the M–layer and the composition's relative stability. The Ti–Ta and Ti–V systems display significantly lower ΔH_f values than the W–Cr systems, regardless of the composition of the A–layer. Comparing the 312 (squares) and 211 (triangles) data in Fig. 5.3 demonstrates that the 312 order phases cover at least a 25% greater ΔH_f range, both higher and lower, than the 211 phases, which are generally found towards the centre of the distribution. Indeed, all seven of the phases which show positive enthalpies of formation are 312 phases – W_2VSiC_2 (+74.41), $Cr_2W(Al_{0.5}Si_{0.5})C_2$ (+79.75), Cr_2WAlC_2 (+83.77), Cr_2WSiC_2 (+157.72), W_2CrAlC_2 (+316.30), $W_2Cr(Al_{0.5}Si_{0.5})C_2$ (+460.37) and W_2CrSiC_2 (+965.00) with values in meV. It is unlikely, therefore, that these phases form in such an ordered structure.

As shown in Fig. 5.2, there is a variation in atomic positioning, especially in the A–layer, depending on the composition. Whilst most stable i–MAX phases synthesised in the literature form a *C 2/c* or *C m c m* unit cell structure [413], [417], [429], the Ti_2TaSiC_2 and $(W_{2/3}Cr_{1/3})_2(Al_{0.5}Si_{0.5})C$ unit cells relax into a *C m c 21* and *P m m n* symmetry respectively. There is no apparent correlation between the relaxed symmetry and either the M^I or M^{II} atomic masses, difference in M–layer atomic masses, or A–layer of the phases. Despite this, Ti_2TaSiC_2 and $(Ti_{2/3}Ta_{1/3})_2SiC$, the most stable 312 and 211 phases respectively, are in–line with the suggestion by Dahlqvist *et al.* that a minimum size difference between M^I and M^{II} is required when $M^I > M^{II}$ for i–MAX stability [419].

Table 5.1 – Atomic formation enthalpies and final magnetic spin configurations of phases containing Cr. 'FiM' means ferrimagnetic.

211			312		
Phase	ΔH_f atom^{-1} (meV)	Final spin state	Phase	ΔH_f atom^{-1} (meV)	Final spin state
$(Cr_{0.66}Ta_{0.33})_2Al_{0.5}Si_{0.5}C$	–324	FM	$Cr_2TaAl_{0.5}Si_{0.5}C_2$	–199	FiM
$(Cr_{0.66}Ta_{0.33})_2AlC$	–322	FM	Cr_2TaAlC_2	–215	FiM
$(Cr_{0.66}Ta_{0.33})_2SiC$	–324	NM	Cr_2TaSiC_2	–184	FM
$(Cr_{0.66}Ti_{0.33})_2Al_{0.5}Si_{0.5}C$	–406	FiM	$Cr_2TiAl_{0.5}Si_{0.5}C_2$	–326	FiM
$(Cr_{0.66}Ti_{0.33})_2AlC$	–386	FM	Cr_2TiAlC_2	–337	FiM
$(Cr_{0.66}Ti_{0.33})_2SiC$	–431	FM	Cr_2TiSiC_2	–317	FiM
$(Cr_{0.66}V_{0.33})_2Al_{0.5}Si_{0.5}C$	–295	FiM	$Cr_2VAl_{0.5}Si_{0.5}C_2$	–196	FiM
$(Cr_{0.66}V_{0.33})_2AlC$	–295	NM	Cr_2VAlC_2	–215	FiM
$(Cr_{0.66}V_{0.33})_2SiC$	–298	FM	Cr_2VSiC_2	–181	FiM
$(Cr_{0.66}W_{0.33})_2Al_{0.5}Si_{0.5}C$	–115	FiM	$Cr_2WAl_{0.5}Si_{0.5}C_2$	4	FM
$(Cr_{0.66}W_{0.33})_2AlC$	–130	NM	Cr_2WAlC_2	–9	FiM
$(Cr_{0.66}W_{0.33})_2SiC$	–112	FiM	Cr_2WSiC_2	13	FiM
$(Cr_{0.66}Y_{0.33})_2Al_{0.5}Si_{0.5}C$	–339	NM	$Cr_2YAl_{0.5}Si_{0.5}C_2$	–8	FiM
$(Cr_{0.66}Y_{0.33})_2AlC$	–330	FM	Cr_2YAlC_2	–11	FiM
$(Cr_{0.66}Y_{0.33})_2SiC$	–354	FM	Cr_2YSiC_2	2	FiM
$(Ta_{0.66}Cr_{0.33})_2Al_{0.5}Si_{0.5}C$	–379	FiM	$Ta_2CrAl_{0.5}Si_{0.5}C_2$	–208	FM
$(Ta_{0.66}Cr_{0.33})_2AlC$	–367	FiM	Ta_2CrAlC_2	–214	FM
$(Ta_{0.66}Cr_{0.33})_2SiC$	–409	NM	Ta_2CrSiC_2	–211	FM

211			312		
Phase	ΔH_f atom^{-1} (meV)	Final spin state	Phase	ΔH_f atom^{-1} (meV)	Final spin state
$(Ti_{0.66}Cr_{0.33})_2Al_{0.5}Si_{0.5}C$	–569	FiM	$Ti_2CrAl_{0.5}Si_{0.5}C_2$	–390	FiM
$(Ti_{0.66}Cr_{0.33})_2AlC$	–544	FM	Ti_2CrAlC_2	–414	FiM
$(Ti_{0.66}Cr_{0.33})_2SiC$	–611	NM	Ti_2CrSiC_2	–456	AFM
$(V_{0.66}Cr_{0.33})_2Al_{0.5}Si_{0.5}C$	–412	FiM	$V_2CrAl_{0.5}Si_{0.5}C_2$	–267	FM
$(V_{0.66}Cr_{0.33})_2AlC$	–403	FiM	V_2CrAlC_2	–262	FiM
$(V_{0.66}Cr_{0.33})_2SiC$	–424	NM	V_2CrSiC_2	–268	FiM
$(W_{0.66}Cr_{0.33})_2Al_{0.5}Si_{0.5}C$	–21	FiM	$W_2CrAl_{0.5}Si_{0.5}C_2$	123	FiM
$(W_{0.66}Cr_{0.33})_2AlC$	–49	FiM	W_2CrAlC_2	79	FM
$(W_{0.66}Cr_{0.33})_2SiC$	–38	AFM	W_2CrSiC_2	148	FM
$(Y_{0.66}Cr_{0.33})_2Al_{0.5}Si_{0.5}C$	–287	NM	$Y_2CrAl_{0.5}Si_{0.5}C_2$	–223	FM
$(Y_{0.66}Cr_{0.33})_2AlC$	–219	FM	Y_2CrAlC_2	–178	FiM
$(Y_{0.66}Cr_{0.33})_2SiC$	–370	FM	Y_2CrSiC_2	–257	FM

Equally, an increasing M^I atomic mass has no apparent overall effect on the relative stability of the phase, although a general increase in relative stability can be seen when increasing the M^I atomic mass within the same period.

The three A–layer compositions per order for each M^I,M^{II} pair – i.e., Al, Si or $Al_{0.5}Si_{0.5}$ – show little variation in formation enthalpy. The exception to this is the 211 M^I = Y systems, for which the Al A–layer phases are generally significantly less stable than either the Si or $Al_{0.5}Si_{0.5}$ phases. Interestingly, the addition of a second element in the A–layer does not seem to affect the formation enthalpy of the phase significantly. For the most part, the formation enthalpy of the $Al_{0.5}Si_{0.5}$ phases sit somewhere between those of the Al and Si based phases for each system of M^I,M^{II} pairs. The sole exception to this is the $Ti_2Cr(Al_{0.5}Si_{0.5})C_2$ phase, which is over 674 meV higher than Ti_2CrAlC_2, the next lowest in the Ti_2Cr system.

It should be emphasised that the calculations of formation enthalpy shown are relative to the elemental constituents of each phase. The values are, therefore, purely relative to each other and are not a prediction of actual thermodynamic or kinetic stability. In further work, the formation enthalpy for each composition should be calculated by considering the respective set of most competing phases. However, as is evident with the W_2Cr and Cr_2W systems, a relatively quick calculation of formation enthalpy, by consideration of elemental competing phases, can save time on a potentially more involved analysis if a positive value is returned.

5.6 Conclusions

The formation enthalpies, relative to elemental constituents, have been calculated for 120 MAX phases in the $(M^{I}_{2/3},M^{II}_{1/3})_{n+1}(A^{I}_{x}A^{II}_{1-x})C_n$ system (M = Ti, V, Cr, Y, Ta, W; A = Al or Si; x = 0.5 or 1; and n = 2 or 3). It was found that the compositions with M^{I},M^{II} = Ti,Ta; Ti,V; and Ti,Y have the lowest formation enthalpies and are the most likely to form stable phases. With the exception of those containing W, compositions with a Si–based A–layer produced lower formation enthalpies than Al–based, indicating an increased stability of Si–based phases. Phases containing both W and Cr generally show the lowest propensity to form, with positive formation enthalpies for $Cr_2W(Al_{0.5}Si_{0.5})C_2$ (+79.75), Cr_2WAlC_2 (+83.77), Cr_2WSiC_2 (+157.72), W_2CrAlC_2 (+316.30), $W_2Cr(Al_{0.5}Si_{0.5})C_2$ (+460.37) and W_2CrSiC_2 (+965.00), with values in meV.

Finally, the addition of a second A–layer element into the lattice doesn't appear to destabilise the unit cell. For the most part, phases containing both Al and Si have formation enthalpies between those of their pure Al and Si counterparts. This could be an indication of thermodynamic stability and, therefore, the potential for partial substitution of Si into the more common but higher–activation Al–layer in MAX phases.

However, it must be emphasised at this point that we have not considered the full equilibrium simplex of competing phases for each composition in this work, as is required to provide an actual thermodynamic stability estimate. Nonetheless, the results presented here can provide guidance for synthesis trials of novel quaternary MAX phases, at a reduced computational cost.

5.7 Conflicts of Interest

There are no conflicts of interest to declare.

5.8 Acknowledgements

This work was supported by the Engineering and Physical Sciences Research Council [EP/L01663X/1, EP/M010619/1, EP/S021531/1, EP/P009050/1].

This work was carried out as part of the Sêr Cymru II programme funded through the Welsh European Funding Office (WEFO) under the European Development Fund (ERDF).

Chapter 6: Manuscript 2 – ‘Synthesis of new M–layer solid–solution 312 MAX phases $(Ta_{1-x}Ti_x)_3AlC_2$ (x = 0.05, 0.1, 0.2, 0.33 or 0.5), and their corresponding MXenes’

Maxwell T. P. Rigby,[a] Varun Natu,[b] Maxim Sokol,[b,c] Daniel J. Kelly,[a] David G. Hopkinson,[a] Yichao Zou,[a] James R. T. Bird,[a] Lee J. Evitts,[d] Matt Smith,[a] Christopher P. Race,[a] Philipp Frankel,[a] Sarah J. Haigh,[a] and Michel W. Barsoum[b]

[a] Department of Materials, University of Manchester, Manchester, M1 3BB, UK.

[b] Department of Materials Science & Engineering, Drexel University, Philadelphia, PA 19104, USA.

[c] Department of Materials Science and Engineering, Tel Aviv University, Ramat Aviv 6997801, Israel.

[d] Nuclear Futures Institute, Bangor University, Gwynedd, LL57 2DG, UK.

Supplementary information available (section 6.6): Computational and experimental details; XRD and electron microscopy characterisations.

6.1 Abstract

Quaternary MAX phases, $(Ta_xTi_{1-x})_3AlC_2$ (x = 0.05, 0.1, 0.2, 0.33 or 0.5), have been synthesised *via* pressure–less sintering of TaC, TiC, Ti and Al powders. *Via* chemical etching of the Al layers, $(Ta_{0.38}Ti_{0.62})_3C_2T_x$ – a new MXene, has also been synthesised. All materials contain an M–layer solid solution of Ta and Ti, with a variable Ta concentration – paving the way for the synthesis of a range of alloyed $(Ta,Ti)_3C_2T_x$ MXenes with tuneable compositions for a wide range of potential applications.

6.2 Introduction

The MAX phases are a class of hexagonal nano–layered carbides and nitrides with general formula $M_{n+1}AX_n$, where n = 1, 2, 3, etc. and referred to by their stoichiometry – for example M_2AX as ‘211’, M_3AX_2 as ‘312’ and so on. Whilst the ‘M’ is generally an early transition metal, ‘A’ an A–group element and ‘X’ either carbon or nitrogen, all three sites may consist of more than one element in either solid solution or ordered form (such as the M^I, M^{II} ordered ‘o–MAX’ phases) [110]. This vast chemical diversity results in a wealth of material structures and properties, with more than 155 phases known to date – a number that likely represents a small proportion of the material possibilities. The MAX phases have attracted attention due to their interesting mix of ceramic and metallic properties. Like ceramics, some MAX phases are elastically rigid (Young’s modulus > 300 GPa) [107], strong at high temperatures [398], lightweight (< 4.5 g cm^{-3}) and creep and oxidation resistant [201], [399]. Like metals, MAX phases have shown excellent electrical and thermal conductivity [162], [172], machinability [103], thermal shock resistance, [103] and even damage tolerance [102]. Recently, the interest in MAX phase materials has increased dramatically because they are the feedstock for their two–dimensional derivatives, MXenes [430]. MXenes are typically obtained *via* etching of the MAX phase ‘A–layer’ and subsequent chemical delamination of the two–dimensional ‘MX–layers’. They have the general formula $M_{n+1}X_nT_x$, where T_x refers to the MX–layer surface terminations – usually –OH, –O, and/or –F [431], [432]. MXenes have shown potential for use in a large range of applications, including photo– and electro–catalysis [433], [434], energy storage and conversion [435], [436], the development of novel hybrid nanocomposites [437], [438], biosensors [439], water purification [440], electromagnetic interference shielding [441], lubrication [442], and conductive inks [443], [444].

The discovery of new MAX phases and, by derivation, new MXenes with different/improved properties can thus be highly valuable. Here we report on the successful synthesis of a range of 312 MAX phase materials, where M is a solid

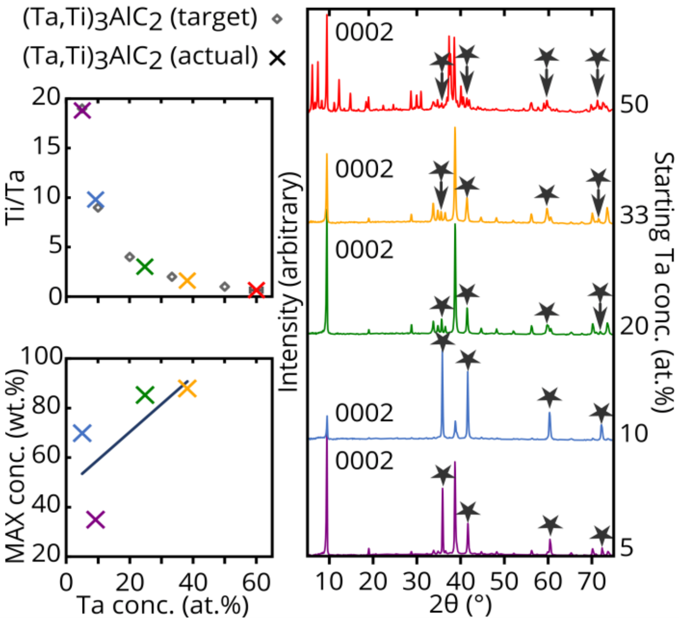

Fig. 6.1 – Ti/Ta fractions for target (diamonds) and actual (crosses) $(Ta,Ti)_3AlC_2$ phases (a). $(Ta,Ti)_3AlC_2$ MAX phase concentrations in wt.% (b). The *x*–axis for (a) and (b) is the Ta concentration in at.%. XRD diffractograms of as–synthesised materials with variable nominal initial Ta concentrations (right *y*–axis) (c). The (0002) basal peaks have been identified for the $(Ta_{1-x}Ti_x)_3AlC_2$ phase in each composition, with the positions of $(Ta,Ti)C_x$ $(x \leq 2)$ impurity peaks labelled with stars. Actual compositions have been colour coded across all plots.

solution of Ta and Ti with variable Ti:Ta ratios, A = Al and X = C. The work builds on previous experimental reports of a 211 MAX phase with similar elemental components – $(Ta_{1-x}Ti_x)_2AlC$ $(0 < x < 1)$ [445], and the pure M–layer 312 MAX phases M_3AlC_2 (M = Ta or Ti) [182], [446]. Our experimental realisation of the $(Ta_{1-x}Ti_x)_3AlC_2$ $(0 < x < 1)$ system was motivated by recent theoretical predictions demonstrating the phase stability of $TaTi_2AlC_2$ and Ta_2TiAlC_2 by Dahlqvist and Rosen [111]. We further demonstrate successful exfoliation of $(Ta_{1-x}Ti_x)_3AlC_2$ $(0 < x < 1)$ to generate a new MXene composition $(Ta_{0.38}Ti_{0.62})_3C_2T_x$.

6.3 Results

Synthesis of the $(Ta_{1-x}Ti_x)_3AlC_2$ quaternary, with nominal compositions of x = 0.05, 0.1, 0.2, 0.33 and 0.5, was investigated starting from TaC, TiC, Ti and Al powders

(Table 6.1, Table 6.2, SI). Powder mixtures were uniaxially cold–pressed at 250 MPa before being heated at a rate of 5 °C min^{-1} to 1600 °C, held for 8 h, and cooled to room temperature at a similar rate to the heating, in a pressure–less flowing Ar tube furnace. Powder X–ray diffraction (XRD) analysis showed each sample contained peaks consistent with a hexagonal P 63/mmc symmetry 312 MAX phase (Fig. 6.1c), with unit cell volumes ranging from 153.29(3) Å^3 to 156.0(1) Å^3 for $(Ta_{0.09}Ti_{0.91})_3AlC_2$ and $(Ta_{0.6}Ti_{0.4})_3AlC_2$ respectively (Table 6.3, SI). A fairly linear increase in cell volume with increasing Ti M– starting Ta at.% is seen, indicating increasing substitution of the site with Ta (atomic radius of 1.45 Å compared to 1.40 Å) [447]. This puts the cell volumes in the expected range between the lowest reported value of 151.8(2) Å^3 for Ti_3AlC_2, and the highest value of 158.73(1) Å^3 reported for Ta_3AlC_2 [446], [448], as expected (Fig. 6.6, SI). The highest phase purity of better than 85 wt.% was obtained for Rietveld refined compositions of $(Ta_{0.25}Ti_{0.75})_3Al_{0.77}C_2$ and $(Ta_{0.38}Ti_{0.62})_3Al_{0.81}C_2$ (Fig. 6.1; Table 6.2, SI).

The best fitting of the XRD data was achieved with the Al layer arranged in the α–312 stacking configuration for $(Ta_{0.25}Ti_{0.75})_3Al_{0.77}C_2$, $(Ta_{0.38}Ti_{0.62})_3Al_{0.81}C_2$ and $(Ta_{0.6}Ti_{0.4})_3AlC_2$, with $(Ta_{0.05}Ti_{2.95})_3AlC_2$ and $(Ta_{0.09}Ti_{0.91})_3AlC_2$ arranged in the β–312 configuration (see Table 6.1, SI). For most of the samples, the major impurity peaks were those belonging to cubic $(Ta,Ti)C_x$ ($x \leq 2$) and small quantities of Al_2O_3 and $TiAl_2$ (for discussion, see section 6.6.3). The sample with the highest starting Ta content (50 at.%), however, produced a multitude of additional phases, including at least two that have not been identified. As such, structural refinement used a combination of the Rietveld and Pawley methods, that indicated the presence of the expected 312 MAX phase as well as up to five further MAX phases (6.6.3 and Fig. 6.7) [449]. The lower purity and presence of these extra phases at the highest Ta concentration suggests a Ta solubility limit in the Ti M–layers.

Energy dispersive X–ray spectroscopy (EDS) implemented within a scanning electron microscope (SEM) was also used for characterisation. EDS provided mean Ti:Ta ratios in the primary phase regions that decreased with increasing Ta

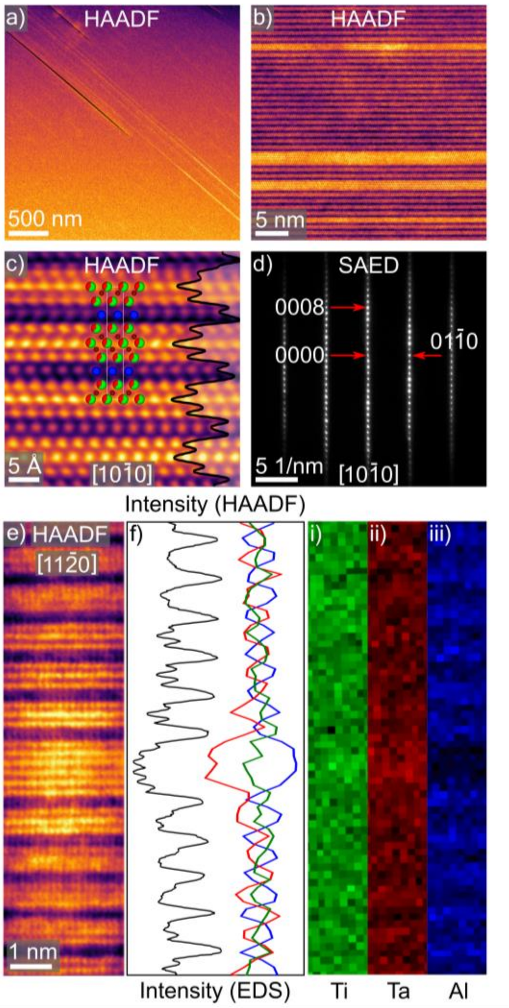

Fig. 6.2 – STEM micrographs at varying magnifications of β–$(Ta_{0.38}Ti_{0.62})_3Al_{0.81}C_2$, viewed along the [10$\bar{1}$0] zone axis (a–c). (c) has been Fourier filtered, with the refined structural model overlaid and the unit cell outlined in white. Ti, Ta, Al and C atoms are represented by green, red, blue and brown spheres respectively. Additionally, an integrated HAADF intensity line profile has been overlaid. SAED micrograph obtained viewing along the same zone axis, with the (0008) and (01$\bar{1}$0) lattice plane reflections identified by red arrows (d). HAADF STEM micrograph of $(Ta_{0.38}Ti_{0.62})_3Al_{0.81}C_2$, with a stacking fault near the centre, as viewed along the [11$\bar{2}$0] zone axis (e). Integrated horizontal line scan profile of (e) (black line), with compositional line profiles obtained from i), ii) and iii), representing EDS scans of Ti, Ta and Al in green, red and blue respectively (f).

concentrations in the starting mixtures (Fig. 6.1a). The sample with intended formula $(Ta_{1/3}Ti_{2/3})_3AlC_2$ produced a Ti:Ta ratio of 1.62:1 compared with the expected 2:1 from the starting mixture (Table 6.2, SI). This is due to the formation of Ti–rich (Ta,Ti)C_x ($x \leq 2$) impurities during synthesis (see section 6.6.3). Both SEM– and scanning transmission electron microscope (STEM) EDS quantitative analysis indicated a sub–stoichiometric Al content in $(Ta_{0.25}Ti_{0.75})_3Al_{0.77}C_2$ and $(Ta_{0.38}Ti_{0.62})_3Al_{0.81}C_2$. Synthesis trials with increased nominal starting Al stoichiometries as high as 1.6 resulted in a decrease in MAX phase purity and increasing quantities of Al_2O_3 and $TiAl_2$. This suggests that the reduced Al occupancy is a thermodynamic effect rather than being due to a deficiency of Al in the starting mixture.

The characteristic 312 MAX phase layered structure of $(Ta_{0.38}Ti_{0.62})_3Al_{0.81}C_2$ can be seen in the high angle annular dark field (HAADF) STEM micrographs in Fig. 6.2c and Fig. 6.2e, aligned with the $[10\bar{1}0]$ and $[11\bar{2}0]$ zone axes, respectively. The configuration, in contrast to the XRD data, is likely the result of an α–β transformation during TEM sample preparation, as reported by one of us previously [102]. The HAADF STEM data also reveals that the central metal layers (M^{II}) have visibly higher positions of Al in Fig. 6.2c are consistent with the β–312 stacking HAADF intensities than the metal layers that sandwich it (M^{I}) (see Fig. 6.4, SI for diagram), indicative of a higher atomic number and hence a higher Ta concentration. This is in–line with the XRD data, in which M^{I} and M^{II} Ta site occupancies converged to 0.340(6) and 0.466(7), respectively (Table 6.2, SI). This preferential elemental enrichment is distinct from the full out–of–plane ordering seen in quaternary 312 o–MAX phases with a 2:1 M–element starting ratio [110]. Nonetheless, similar preferential enrichment of the centre M^{II} layer has been observed in 312 M–layer solid solution MAX phases such as $(Cr,V)_3AlC_2$ [110], [450]. Lattice parameters obtained from selected area electron diffraction (SAED) patterns, like in Fig. 6.2d, of $a = 3.01(2)$ Å and $c = 18.59(2)$ Å, are also in good agreement with bulk lattice parameters from XRD ($a = 3.0981(1)$ Å and $c = 18.6140(7)$ Å (see Table 6.3, SI). It should be stressed at this point that the pristine MAX phase layered structure is occasionally interrupted by stacking faults of varying thickness that, at times, penetrate entire crystallites (Fig. 6.2a, b, e).

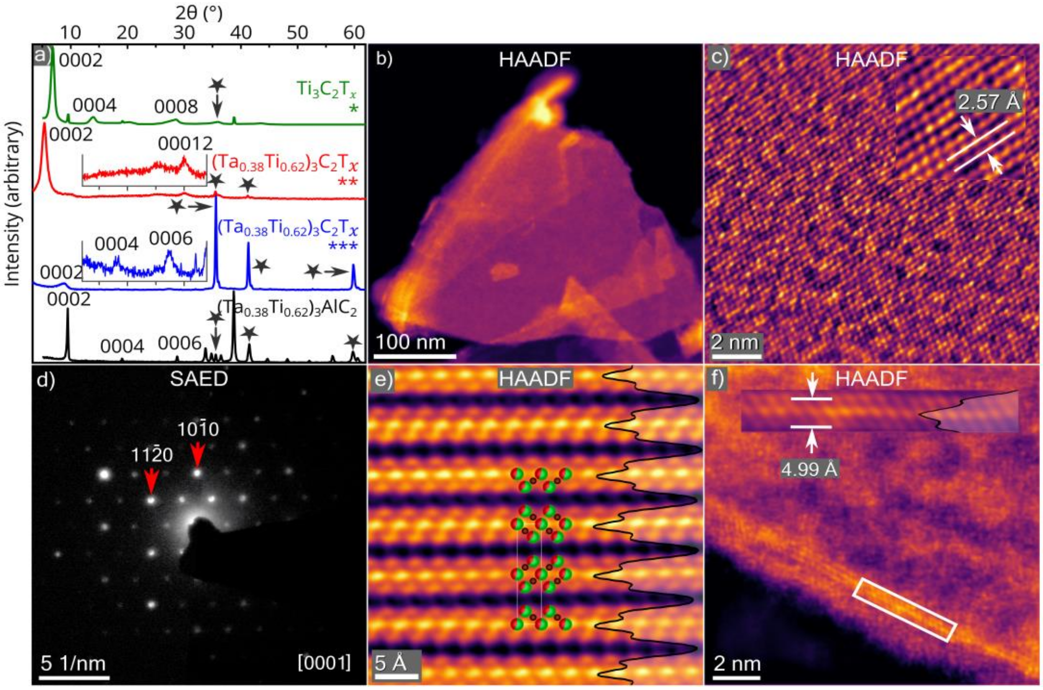

Fig. 6.3 – XRD scans of $Ti_3C_2T_x$ MXene partially intercalated with H_2O (*), delaminated $(Ta_{0.38}Ti_{0.62})_3C_2T_x$ MXene (**), ML $(Ta_{0.38}Ti_{0.62})_3C_2T_x$ MXene (***), and $(Ta_{0.38}Ti_{0.62})_3Al_{0.81}C_2$. A variety of basal plane peaks have been identified, with $(Ta,Ti)C_x$ impurity peaks labelled with stars. Additionally, portions of the central two scans have been rescaled to emphasise basal peaks (insets) (a). STEM micrograph of a $(Ta_{0.38}Ti_{0.62})_3C_2T_x$ MXene flake suspended on a holey C–film (b). Atomic resolution STEM micrograph of the surface of the flake in (b) viewed close to the $[64\bar{1}]$ zone axis, with a magnified and filtered portion (inset) showing the interatomic spacing (c). SAED micrograph of a single flake, as viewed along the [0001] zone axis, with the $(10\bar{1}0)$ and $(11\bar{2}0)$ lattice plane reflections labelled (d). Atomic resolution HAADF STEM micrograph of pristine ML MXene as viewed along the $[10\bar{1}0]$ zone axis, with a proposed structural model overlaid. Ti, Ta and C atoms are represented by green, red and brown spheres, respectively. Additionally, an integrated HAADF intensity line profile has been overlaid in black (e). STEM micrograph of a $(Ta_{0.38}Ti_{0.62})_3C_2T_x$ flake, with a monolayer edge curled up to align along the $[10\bar{1}0]$ viewing axis. Inset: magnified and filtered view of the area in the white box with an integrated vertical line profile overlaid (f).

Structurally, these defects can be thought of as either few–layer ternary carbide impurities, or as MX layers in the MAX phase matrix with an unexpected number of M–layers – such as the 6 shown in Fig. 6.2e, compared with the expected 3.

High resolution EDS scans performed over several regions on $(Ta_{0.38}Ti_{0.62})_3Al_{0.81}C_2$ samples show the expected elemental segregation of Ti, Ta and Al layers, as seen in Fig. 6.2f i, ii, and iii, respectively. Quantitative STEM–EDS analysis provided Ti:Ta ratios, excluding stacking faults, from 1.6–1.9:1, with a mean value of 1.7(1):1, which is close to the 1.62(2):1 obtained from SEM–EDS. Note that electron channelling effects and the limited spatial resolution prevent absolute quantification of the relative Ti:Ta concentrations in M^{II} *versus* M^{I} sites (see section 6.6.4, SI for methods).

To demonstrate the potential to produce solid solution Ta/Ti MXenes, we used an *in–situ* HF etching process at 20 °C for 12 h, similar to that performed by Ghidiu et al. [451] (see section 6.6.2, SI). Etching of the $(Ta_{0.38}Ti_{0.62})_3Al_{0.81}C_2$ sample produced the expected $(Ta_{0.38}Ti_{0.62})_3C_2T_x$ MXene (Fig. 6.3). Characteristic multilayer (ML) flakes were observed following vacuum drying of the MXene solution (Fig. 6.3b), with SEM–EDS analysis producing a 2:1 Ti:Ta ratio over micrometre sized areas –including contributions from Ti–rich $(Ta,Ti)C_x$ impurities (similar to the parent MAX phase sample). The etching resulted in a *c*–lattice parameter increase from 18.6140(7) Å to 19.7(1) Å (Fig. 6.3a). After sonication, this increased dramatically to 34.9(4) Å, indicating full intercalation of the MX–layers. This suggests a similar formation mechanism to that proposed for $Ti_3C_2T_x$ MXene from a parent Ti_3AlC_2 MAX phase, where Al is replaced by terminating species in the etchant such as –OH, –F, or =O, followed by intercalation of the MX–layers by Li^+, allowing for full delamination *via* sonication [430], [435], [452]. The lower intensity of $(Ta,Ti)C_x$ peaks in the XRD of the delaminated MXene compared to the parent MAX phase (Fig. 6.3a) suggests an improvement in the purity of the sample (better than the 87.9(2) at.% of the parent MAX phase) achieved *via* sonication and centrifugation.

STEM imaging and diffraction was further used to investigate the MXene structure. The pre–delamination $(Ta_{0.38}Ti_{0.62})_3C_2T_x$ ML produced lattice parameters of a = 3.14(3) Å and c = 11.8(1) Å, with a being similar to the parent MAX phase and c reduced following the removal of the Al layer. SAED performed on a fully exfoliated monolayer $(Ta_{0.38}Ti_{0.62})_3C_2T_x$ flake was indexed using a hexagonal basis (Fig. 6.3d), and produced an a–lattice parameter of 2.97(3) Å, which is in agreement with the value of 2.98(3) Å obtained from fast Fourier transform of the high resolution STEM data (e.g. Fig. 6.3e), and slightly less than the value of 3.0981(1) Å in the parent phase. The monolayer sheet thickness was estimated from HAADF–STEM analysis of the curled–up edge of a single flake as 4.99(5) Å (Fig. 6.3c) – slightly larger than the MX–layer (4.85(2) Å) in the parent phase. Furthermore, the HAADF contrast suggests Ta enrichment in the M^{II} layer relative to the M^{I} layer, as also observed in the parent MAX phase.

6.4 Conclusions

In summary, a new quaternary $(Ta_{1-x}Ti_x)_3AlC_2$ phase system has been synthesised with a variable Ta:Ti ratio (x = 0.05, 0.1, 0.2, 0.33 and 0.5) and up to 87.9(2) at.% purity. The 'M' sites exist as a solid solution of Ta and Ti, with a higher concentration of Ta in the central M^{II} layers. Experimental results suggest a mean Ta M–layer concentration limit between 38 and 60 at.%, beyond which the formation of several alternative MAX phases is favoured, and thus a significant reduction in phase purity. The $(Ta_{0.38}Ti_{0.62})_3Al_{0.81}C_2$ MAX phase was used to synthesise a new solid solution MXene – $(Ta_{0.38}Ti_{0.62})_3C_2T_x$ – *via* chemical etching, with the synthesis pathway likely to be similar to the unalloyed $Ti_3C_2T_x$ MXene. It is proposed that this approach can be used to synthesise a range of alloyed $(Ta,Ti)_3C_2T_x$ MXenes, with compositions that can be optimised for a wide range of potential applications.

6.5 Conflicts of Interest

There are no conflicts of interest to declare.

6.6 Acknowledgements

This work was supported by funding from the Engineering and Physical Sciences Research Council Fusion CDT programme and grants [EP/L01663X/1, EP/M010619/1, EP/S021531/1, EP/P009050/1]; Henry Royce Institute for Advanced Materials [EP/R00661X/1, EP/S019367/1, EP/P025021/1, EP/P025498/1]; the Graphene NoWNano CDT programme [EP/L01548X/1], H2020 under the European Research Council Starter grant EvoluTEM (715502); the Sêr Cymru II programme funded through the Welsh European Funding Office (WEFO) under the European Development Fund (ERDF), NSF DMR 1740795 and the Department of Materials XRD Facility.

6.7 Supplementary Information

6.7.1 Density Functional Theory

To guide synthesis investigations, the thermodynamic stability relative to atomic constituents of $TaTi_2AlC_2$, for two M–layer ordering and two A–layer stacking configurations (four different unit cells, as shown in Fig. 6.4) was calculated using first principles methods. To achieve this, the total ground state energy at zero Kelvin and zero pressure, E_{MAX}, was calculated along with those for individual elemental

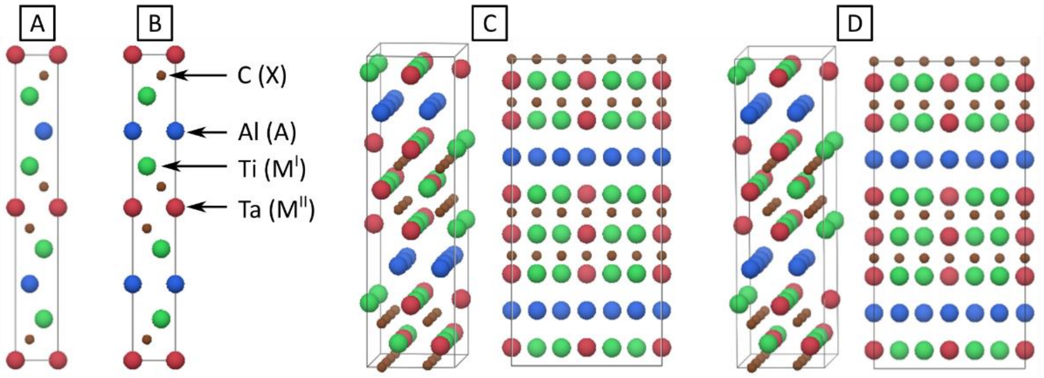

Fig. 6.4 – Structural variations of $TaTi_2AlC_2$ for which total energy calculations were performed: (A) α–$TaTi_2AlC_2$ (o–MAX), (B) β–$TaTi_2AlC_2$ (o–MAX), (C) α–$TaTi_2AlC_2$ (i–MAX–like), and (D) β–$TaTi_2AlC_2$ (i–MAX–like).

constituents, E_{element}, in equilibrium phase under similar conditions. The formation enthalpy of the phase, $\Delta H_{\mathrm{f,MAX}}$ was then obtained using Hess' law:

$$\Delta H_{(\mathrm{f,MAX})} = E_{\mathrm{MAX}} - \sum E_{\mathrm{element}} \qquad (6.1)$$

Total energy calculations were performed for supercells of 2 × 2 × 1 unit cells using density functional theory (DFT) as implemented in the Vienna ab initio simulation package (VASP) [420], [421]. A plane–wave basis set cut–off energy of 500 eV was used for all calculations, with electron–ion interactions represented using the projector augmented–wave (PAW) method [422]. The generalized gradient approximation (GGA) [423] was used in the form of the parameterisation proposed by Perdew, Burke, and Ernzerhof (PBE) [424] to represent the electronic exchange–correlation energy. Brillouin zone *k*–point sampling integrations were applied using a 3 × 3 × 1 Monkhorst–Pack grid [426], resulting in a *k*–point spacing of at most 0.5 A^{-1}. Unit cells were relaxed until the forces on ions converged to < 0.1 meV $Å^{-1}$.

The $TaTi_2AlC_2$ configurations considered are shown in Fig. 6.4. The respective enthalpies of formation, ΔH_f, are shown in Fig. 6.5. A negative ΔH_f value in this

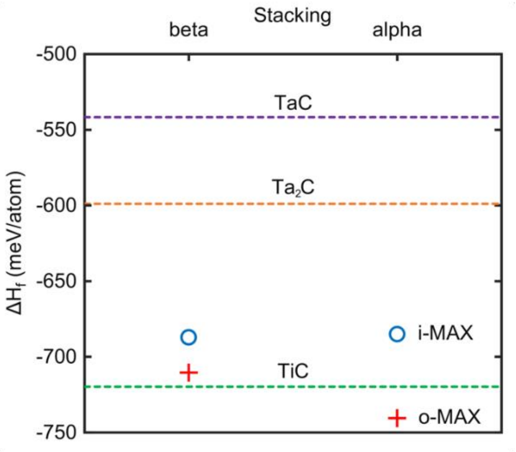

Fig. 6.5 – The formation enthalpies (points), ΔH_f in meV $atom^{-1}$ of the four $TaTi_2AlC_2$ unit cells in Fig. 6.4, with those of common binary carbide impurities (dashed lines) included for reference.

context indicates thermodynamic stability relative to elemental constituents at 0 K and is thus a step towards predicting actual stability. It is important to stress at this point that the aim of these calculations was to provide guidance in the search for new MAX phases, rather than to predict the existence of new stable phases with rigour. As such, the thermodynamic stability at expected synthesis temperatures

(~1600 °C) and in relation to the set of 'most–competing phases' has not been considered as in recent calculations by Dahlqvist and Rosen [111]. For reference, ΔH_f values of common binary carbide impurities TaC, Ta_2C and TiC have been included in Fig. 6.5, as indicated by dashed horizontal lines. If a particular $TaTi_2AlC_2$ configuration falls below all of these lines, the phase is expected to be more thermodynamically stable and thus will have a higher propensity to form. All four MAX phase unit cells fall within 8% of the ΔH_f threshold of TiC at –719.74 meV/atom.

6.7.2 Synthesis

Powders of TaC, TiC, Ti and Al of mesh size at least –250 (maximum particle size 63 μm – see Table 6.1 for further information), were purchased from Alpha Aesar (Ward Hill, MA, USA). Powder mixtures in the molar ratios in Table 6.2 were zirconia ball milled in plastic jars for 12 h to provide a homogenous mixture. The latter was then uniaxially cold pressed at 250 MPa into compact 1.27 cm diameter pellets of mass ~10 g. The pellets were loaded into a 82 × 31 × 18 mm Al_2O_3 boat, covered with an Al_2O_3 plate, and placed inside an Al_2O_3 tube furnace with an inert flowing Ar atmosphere. Additionally, pure Ti powder was placed in an adjacent crucible upstream to the pellet as a residual oxygen getter. The furnace was then heated to 1600 °C at a rate of 5 °C min^{-1} and held for 8 h, before cooling to room temperature at a similar rate to the heating.

For MXene synthesis, a small region of the solid sintered $(Ta_{0.38}Ti_{0.62})_3Al_{0.81}C_2$ MAX phase pellet was milled using a TiN–coated bit. The milled powder was then passed through a 400 mesh (particle size < 38 μm) sieve. One gram of as–sieved

MAX phase powder was then slowly added to a solution of 10 mL HCl (12M, Alfa Aesar, USA) and 1 g LiF (99.5%, 325 mesh, Alfa Aesar) at 20 °C and stirred for 12 h at 500 rpm. The resultant slurry was then transferred to a 50 mL centrifuge tube and deionised water was added to fill the remaining volume. It was then centrifuged at 3500 rpm for 60 s, with the resulting clear supernatant discarded. This washing procedure was repeated several times until the pH of the solution was ~7, at which point deionised water was added to the left–over sediment and the mixture sonicated under bubbling Ar flow for 1 h. Ice was added to the sonication bath to avoid oxidation. The solution was then centrifuged for 0.5 h at 3500 rpm and the supernatant was collected for further use. The sediments that are recovered after washing to pH 7 before sonication are referred to as multilayer, ML, powders. The MXene films obtained after vacuum filtering of the supernatant are referred to as delaminated MXene.

Table 6.1 – Details of source material used for synthesis. *As quoted by the manufacturer.

Material	Purity (wt.%)*	Average particle size* (μm)
TaC	99.5	44
TiC	99.5	2
Ti	99.5	15
Al	99.5	15

Table 6.2 – Mixing ratios for synthesis attempts of target compositions with varying Ta starting concentrations, along with various refined parameters with associated goodness of fit ($\chi2$) values obtained from Rietveld refinement.

Initial Ta at.%	Molar ratios				Composition (actual)	Wt.%	$\chi2$	Atom (Wyckoff)	z–coordinate	Occupancy			
										M^{I}		M^{II}	
	TaC	TiC	Ti	Al						Ta	Ti	Ta	Ti
5.0	0.15	1.85	1.0	1.1	$(Ta_{0.05}Ti_{0.95})_3AlC_2$	69.9(6)	2.58	C (4f) Ta,Ti (4f)	0.0774(4) 0.1303(1)	0.07(3)	0.9(1)	0.01(2)	0.99(7)
10.0	0.3	1.7	1.0	1.1	$(Ta_{0.09}Ti_{0.91})_3AlC_2$	35.0(4)	1.60	C (4f) Ta,Ti (4f)	0.0670(7) 0.1310(2)	0.087(2)	0.913(6)	0.104(2)	0.896(8)
20.0	0.6	1.4	1.0	1.1	$(Ta_{0.25}Ti_{0.75})_3Al_{0.77}C_2$	85.3(3)	1.72	C (4f) Ta,Ti (4f)	0.5764(7) 0.1299(1)	0.21(2)	0.79(7)	0.33(2)	0.67(7)
33.3	1.0	1.0	1.0	1.1	$(Ta_{0.38}Ti_{0.62})_3Al_{0.81}C_2$	87.9(2)	1.50	C (4f) Ta,Ti (4f)	0.5719(7) 0.1313(1)	0.340(6)	0.66(2)	0.466(7)	0.53(2)
50.0	1.5	0.5	1.0	1.1	$(Ta_{0.6}Ti_{0.4})_3AlC_2$	–	3.51	C (4f) Ta,Ti (4f)	0.575(5) 0.1323(6)	–	–	–	–

Table 6.3 – Key phase parameters, obtained from Rietveld (XRD) and SAED analysis, for $(Ta_{0.38}Ti_{0.62})_3Al_{0.81}C_2$ and $(Ta_{0.38}Ti_{0.62})_3C_2T_x$ MXene.

	a-lattice parameter (Å)		*c*-lattice parameter (Å)			Impurities	
Phase	XRD	SAED	XRD	SAED	Cell volume (Å^3)**	Phase	wt.%
β–$(Ta_{0.05}Ti_{0.95})_3AlC_2$	3.0901(3)	–	18.6005(5)	–	153.82(2)	$(Ta_{0.05}Ti_{0.95})C_x$† Al_2O_3 $TiAl_2$	26.4(3) 2.0(7) 1.7(5)
β–$(Ta_{0.09}Ti_{0.91})_3AlC_2$	3.0862(5)	–	18.584(2)	–	153.29(3)	$(Ta_{0.12}Ti_{0.88})C_x$† Al_2O_3 $TiAl_2$	52.5(3) 4.35(3) 8.20(5)
α–$(Ta_{0.25}Ti_{0.75})_3Al_{0.77}C_2$	3.0951(1)	–	18.5854(6)	–	154.189(8)	$(Ta_{0.24}Ti_{0.76})C_x$† Al_2O_3 $TiAl_2$	8.0(2) 2.20(4) 4.50(9)
α–$(Ta_{0.38}Ti_{0.62})_3Al_{0.81}C_2$	3.0981(1)	3.01(2)	18.6140(7)	18.59(2)	154.745(7)	$(Ta_{0.27}Ti_{0.73})C_x$† Al_2O_3	9.4(2) 2.64(1)
α–$(Ta_{0.6}Ti_{0.4})_3AlC_2$	3.108(1)	–	18.648(7)	–	156.0(1)	Fig. 6.8	–
$(Ta_{0.38}Ti_{0.62})_3C_2T_x$ (pristine)	–	3.14(3)*	–	11.8(1)*	100.3(2)	–	–
$(Ta_{0.38}Ti_{0.62})_3C_2T_x$ (ML)	–	–	19.7(1)	–	–	$(Ta_{0.27}Ti_{0.73})C_x$†	–
$(Ta_{0.38}Ti_{0.62})_3C_2T_x$ (delaminated)	–	2.97(3) 2.98(3)*	34.9(4)	–	266(4)	$(Ta_{0.27}Ti_{0.73})C_x$†	–

* From FFT. ** Using XRD values. † C occupancy not determined.

6.7.3 X–Ray Diffraction

For XRD characterisation, MAX phase samples milled to a powder using a TiN–coated bit and then crushed using an agate pestle and mortar. For ML MXene, the powder was scanned after air drying, while for delaminated MXene free standing vacuum filtered films were scanned. XRD scans were carried out using a Rigaku MiniFlex 300/600 diffractometer (Tokyo, Japan) with Cu–K_α radiation (40 kV, 15 mA) incident over a two–theta range of 5–75° for the MAX phases and 2–70° for MXenes, with a 0.02° step and a dwell time of 0.75 s. Additionally, a 1.25° 10 mm incident slit, a 1.25° 0.3 mm receiving slit, and two 5° Soller slits (incident and receiving) were in place. For the $Ti_3C_2T_z$ sample, XRD scans were performed on a PANalytical X'Pert Pro PW3050/60 (Malvern, UK) with a Cu–K_α source (40 kV, 40 mA) over a two–theta range of 5–70°, 0.033° step size and 1.2 s dwell time. A 2° 10 mm incident beam slit, automatic divergence slit for continuous 10 mm illumination length, and two 2.3° Soller slits (incident and receiving), were also in place.

Spectral phase identification for the MAX phases was performed using relaxed unit cells from computational calculations, as shown in Fig. 6.4, and known phases from the Inorganic Crystal Structure Database (FIZ Karlsruhe GmbH), using CrystalDiffract (CrystalMaker Software Ltd.). Where all major peaks were successfully identified using this method (samples with nominal initial Ta concentrations of 5, 10, 20 and 33.3 at.%.), quantitative phase analysis was performed using the Rietveld refinement method as implemented in the TOPAS software package (Bruker AXS GmbH) [324], [453]. The refined parameters included: five background parameters, scale factors, X and Y peak width profile parameters, lattice parameters, atomic positions, site occupancies for Ta, Ti and Al, and a single isotropic thermal displacement parameter for all atomic positions in each phase. The relevant Ta:Ti ratio, as obtained from SEM–EDS mapping, was fixed during refinement. For the MXene samples, basal peaks were identified *via* comparison with the respective MAX phase XRD data and XRD scans of $Ti_3C_2T_x$

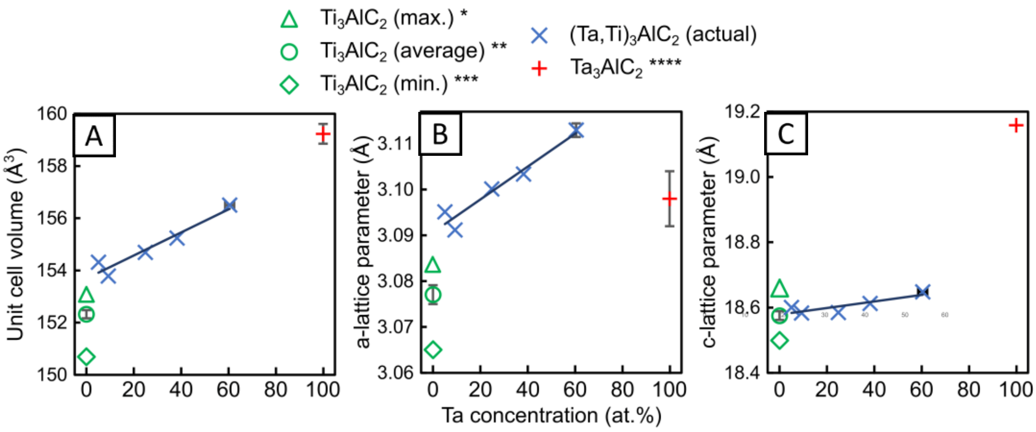

Fig. 6.6 – (A) The unit cell volumes, (B) *a*–lattice parameters, and (C) *c*–lattice parameters of Ti_3AlC_2 (green), $(Ta,Ti)_3AlC_2$ materials from this work (blue) and Ta_3AlC_2 (red). The *x*–axis for all plots is the Ta concentration, in at. %. * Bei et al. [448], ** [128], [162], [182], [278], [448], [472]–[474], *** Lane et al. [472], **** Etzkorn et al. [446].

MXene. For the sample with a starting Ta concentration of 50 at.%, the Pawley method was used in conjunction to the Rietveld method due to the presence of unidentified phases [449]. Two of the unverified structures 'X' and 'Y' in Fig. 6.7 are consistent with the $P6_3/mmc$ space group, with lattice parameters of $a = 3.041(1)$ Å, $c = 26.24(2)$ Å for X and $a = 2.716(1)$ Å, $c = 21.254(4)$ Å for Y. The formation of so many phases, none of which appeared to have a distinctly high phase fraction, is evidence that, beyond a certain Ta concentration in the Ti M–layer between 38 and 60 at.%, other MAX phases of 211, 413 or higher order stoichiometry have a higher thermodynamic propensity to form. Another possible culprit for the formation of this variety of higher order and ternary carbide phases is Al: either a deficit of Al in the starting mixture, as higher order MAX phases have higher ratios of MX– to A–layers, or the loss of Al from the newly formed matrix due to the sintering conditions, resulting in phase decomposition. Such behaviour has previously been reported in Ti_3SiC_2 MAX phase, where there is insufficient Si [454].

All samples analysed with Rietveld refinement contained varying concentrations of two common impurity phases. The first is an Fm–3m structure with lattice

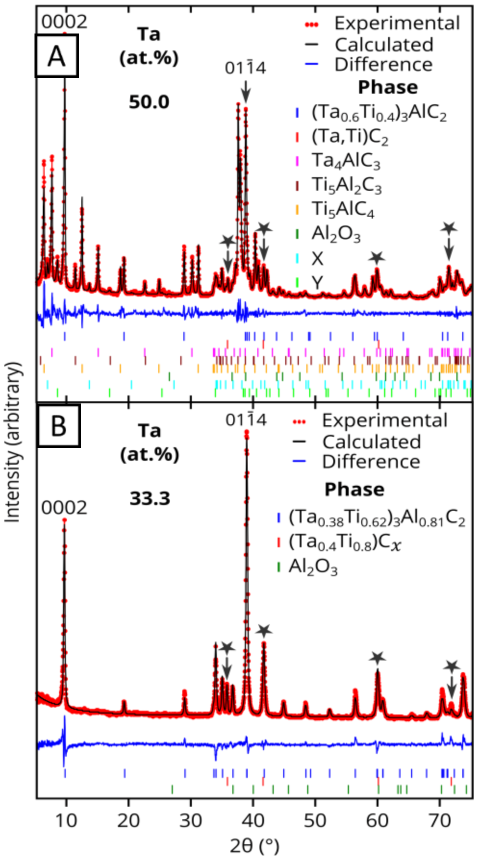

Fig. 6.7 – XRD scans (red spots), with overlaid refinement profiles in black and difference between scan and the refined profiles below in blue, of samples with initial M–layer Ta concentrations of (A) 50 at.% – with phases included in the Pawley refinement displayed on the right hand side; (B) 33.3 at.% – with phases included in the Rietveld refinement profile listed under 'Phase'. For both figures, the (0002) and (01$\bar{1}$4) peaks of the (Ta,Ti)$_3$AlC$_2$ phase have been labelled, with peaks representing (Ta,Ti)C$_2$ impurity identified by black stars.

parameters lying between those of (TaTi)C$_2$ and TiC, believed to be FCC (Ta,Ti)C$_x$ ($x \leq 2$) with relative Ta/Ti concentrations dependent on the starting composition. In the case of the sample with initial Ta = 10 at.%, this ternary carbide is actually the primary phase at 52.5(3) wt.%, whilst comprising < 10 wt.% in the two phases with high (> 85 wt.%) MAX phase concentration. Measures were employed to minimise the presence of these ternary carbides, such as ball–milling the initial powder mixture for 12 h to encourage uniform elemental distribution, as well as adding excess Al to account for loss from vaporisation during synthesis. However, smaller initial particle sizes may be necessary to further inhibit ternary formation by encouraging solid state diffusion. This is especially relevant for Ta, which has a

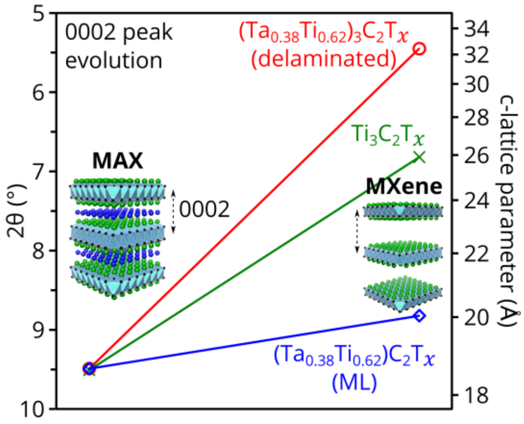

Fig. 6.8 – The (0002) basal peak (left axis) and corresponding *c*–lattice parameter (right axis) evolution from $(Ta_{0.38}Ti_{0.62})_3Al_{0.81}C_2$ as obtained from bulk XRD of delaminated $(Ta_{0.38}Ti_{0.62})_3C_2T_x$ (red), multilayer $(Ta_{0.38}Ti_{0.62})_3C_2T_x$ (blue), and $Ti_3C_2T_x$ partially delaminated with H_2O [452] (green).

melting point nearly 1.9 times greater than the furnace temperature employed (1600 °C). The second impurity present is Al_2O_3 which, for the apparatus used in this work, is expected. Despite the use of a Ti oxygen getter, the strongly negative formation enthalpy of Al_2O_3 (–3.44 eV atom^{-1} [455]) and small, but inevitable, presence of O_2 leads to preferential and rapid oxidation of exposed elemental Al in the pellet. Another more likely source of oxygen is the native oxide layers present on all metal and carbide particles. To mitigate this, synthesis under high vacuum conditions and/or pre–reducing the starting powders may be required. Additionally, small quantities of $TiAl_2$ (< 8.2 wt.%) were detected in XRD data of β–$(Ta_{0.05}Ti_{2.95})_3AlC_2$, β–$(Ta_{0.09}Ti_{0.91})_3AlC_2$ and α–$(Ta_{0.25}Ti_{0.75})_3Al_{0.77}C_2$.

The disparity between the Ti:Ta ratios in the starting powders and the primary MAX phase matrices can be explained by the presence of the cubic ternary carbide impurities with high Ti concentrations – i.e. $(Ta,Ti)C_x$ ($x \leq 2$). An example of these impurities can be seen in Fig. 6.9A. Analysis of several impurity particles suggests the Ti:Ta ratio, as well as varying between particles, appears to decrease from a maximum of ~3:1 at the centre, to around 1.4:1 in a thin shell surrounding the particle, before finally increasing to 1.62:1 in the main phase. Whilst the volume fraction of these impurities is low – < 10 wt.% according to XRD data (Table 6.3), due to the Ti:Ta ratio reaching almost 3.5:1 for the majority of the particle volume, the mean Ti:Ta ratio across large areas of the sample, including the primary MAX phase is ~2:1.

Despite the measures employed to minimise the presence of these impurity carbides, such as ball–milling the initial powder mixture for 12 h to encourage isotropic elemental distribution or adding excess Al to account for loss due to vaporisation during synthesis, smaller initial particle sizes may be necessary to further inhibit formation by encouraging solid state diffusion of elements with low diffusion rates, such as Ta.

6.7.4 Electron Microscopy

SEM analysis was performed using a FEI Quanta 650 FEG–ESEM operated at an accelerating voltage of 30 kV. The MAX phase samples were mechanically ground and polished to a 1 μm diamond finish prior to analysis. The ML MXene samples were prepared by pressing the powders on a carbon tape mounted on an aluminium stub. Both backscatter electron imaging and EDS quantitative elemental mapping were performed to identify the phases present and to measure the M^{I}:M^{II} ratios in the MAX phase and ternary carbide impurities (Fig. 6.9).

Electron transparent MAX phase lamellae were prepared for TEM analysis using the focused Ga^{+} ion beam *in–situ* lift–out method in an FEI Nova Nanolab 600 SEM [329]. For $(Ta_{0.38}Ti_{0.62})_3Al_{0.81}C_2$, atomic resolution HAADF–STEM images were obtained using a probe corrected FEI Titan G2 with an X–FEG source, operated at 200 kV, with lattice resolution EDS elemental mapping performed using the ChemiSTEM SuperX system on four different scan regions over two lamellae taken from different regions of the bulk sample, providing the range of Ti:Ta ratios reported in the main text. Quantification was performed *via* the standardless k–factor method and the spectrum images were binned for visual clarity. Binning values of 10 and 4 were used for the spatial and spectral axes respectively. All

STEM–EDS processing was performed in HyperSpy [361], with averaged profiles computed using the NumPy analysis package [362].

Table 6.4 – Normalised elemental concentrations, in at.%, calculated from SEM–EDS measurements of scan areas ‘A’ to ‘F’ as indicated in Fig. 6.9. Apparent MAX phase formulae derived from these measurements are also included.

Scan area	Ti	Ta	Ti/Ta	Al	C	Formula
A	30.5(3)	18.9(1)	1.61(6)	13.1(1)	38(1)	$Ta_{1.15}Ti_{1.85}Al_{0.80}C_{2.31}$
B	30.6(3)	18.8(2)	1.63(5)	13.6(5)	35(3)	$Ta_{1.14}Ti_{1.86}Al_{0.83}C_{2.13}$
C	31.8(9)	19.3(5)	1.7(1)	14.2(5)	35(3)	$Ta_{1.13}Ti_{1.87}Al_{0.83}C_{2.05}$
D	28.7(3)	17.9(2)	1.60(5)	12.6(1)	41(1)	$Ta_{1.15}Ti_{1.85}Al_{0.81}C_{2.64}$
E	31.1(7)	19.0(4)	1.6(1)	13.8(4)	36(2)	$Ta_{1.14}Ti_{1.86}Al_{0.83}C_{2.16}$
F	30.6(5)	19.4(3)	1.58(8)	13.4(3)	37(2)	$Ta_{1.16}Ti_{1.84}Al_{0.80}C_{2.22}$

Due to the HAADF detector geometry and sample thickness, the primary source of contrast in the HAADF micrographs is atomic mass (Z) variations. Atoms with a higher Z are more likely to scatter higher angle electrons than lighter ones and, therefore, an increase in HAADF intensity is indicative of an increase in average Z, which in this case refers to an increased Ta concentration (with a Z roughly 3.8 times that of Ti).

MXene TEM samples were prepared by drop–casting colloidally suspended MXene flakes onto a Cu grid with a holey C support film. The grid was then briefly dipped in isopropanol and dried on a hot plate at 80 °C before loading into the TEM. A JEOL ARM300CF STEM at the E02 beamline of the Electron Physical Sciences Imaging Centre (ePSIC) of Diamond Light Source, Ltd. was used for HAADF–STEM imaging 80 kV accelerating voltage, with convergence semi–angles of 32 mrad, and collection inner/outer semi–angle ranges of 68 / 206 mrad. For both the

MAX and MXene samples, SAED micrographs were obtained using an FEI Tecnai TF30 FEG–AEM microscope, operating at 300 kV.

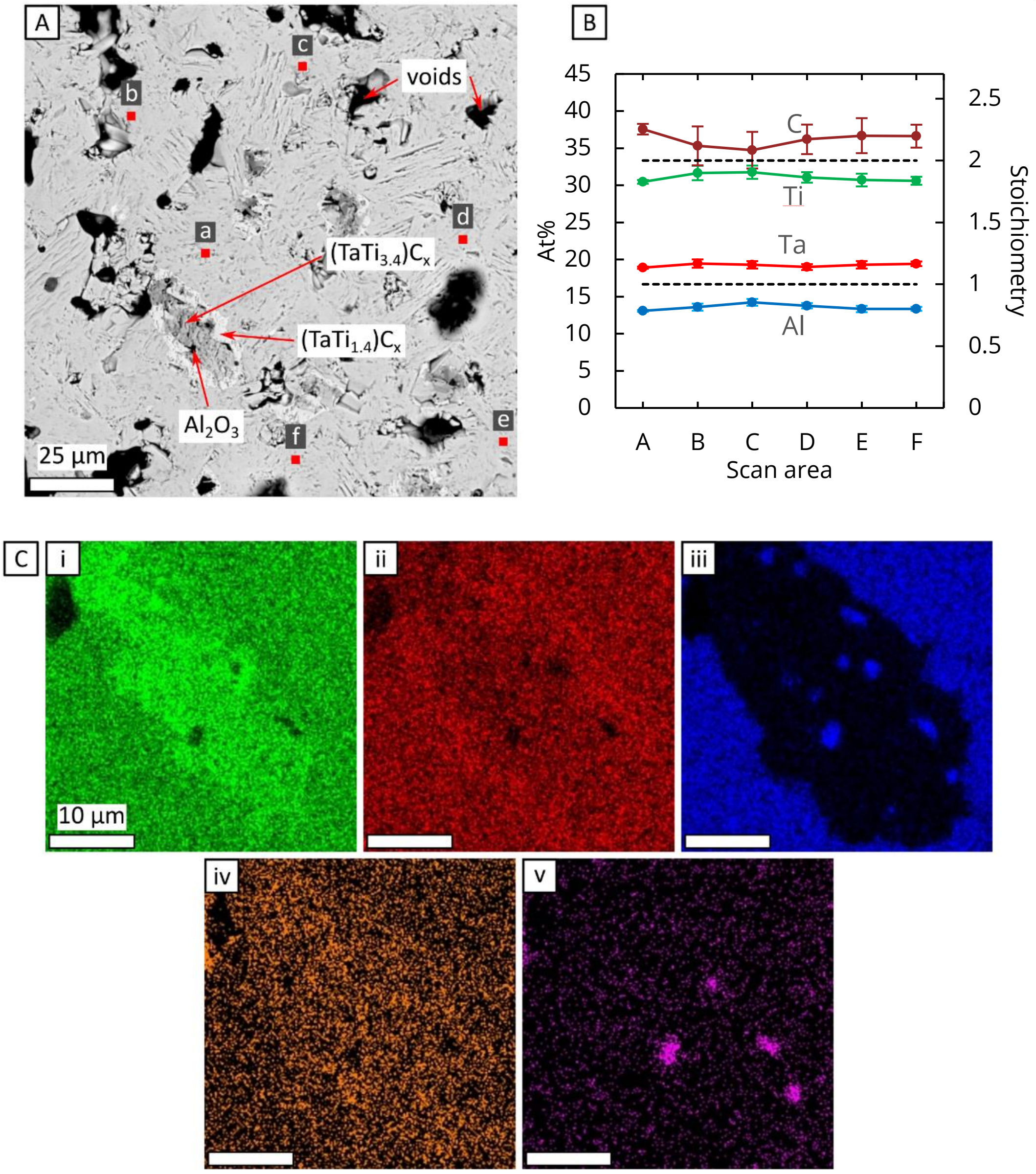

Fig. 6.9 – (A) Backscatter electron SEM micrograph of the surface of as–synthesised $(Ta_{0.38}Ti_{0.62})_3Al_{0.81}C_2$, with EDS scan regions ‘a’ to ‘f’ of the MAX phase identified by red squares, and a scan region with a typical impurity particle indicated by the red box. (B) Plot of SEM–EDS data from Table 6.4, with a MAX phase stoichiometry scale included on the right–hand y–axis. (C) X–ray count maps corresponding to the region in A for Ti (i), Ta (ii), Al (iii), C (iv) and O (v).

Despite the high MAX phase fractions in multiple samples – up to 87.9(2) wt.%, the main phase is itself neither dense nor homogenous. As expected from a pressure–less sintering method, evidence of voids can be seen in SEM micrographs, such as in Fig. 6.9a. It is possible that these defects exist due to Al failing to intercalate during sintering, or else where Al has been lost at the high temperature following formation, with subsequent decomposition of the HCP MAX phase into an FCC carbide – a process which is known to occur in other MAX phases at high temperatures (> 1000 °C) [186], [456].

Chapter 7: Manuscript 3 – ‘Irradiation tolerance of novel $(Ta_xTi_{1-x})_3AlC_2$ (x = 0, 0.25 or 0.32) MAX phases’

M. T. P. Rigby–Bell,[a] D. Lunt,[a] A. P. Wylie,[a] P. J. Barron,[a] S. M. Shubeita,[b] G. Harrison,[a] M. W. Barsoum,[c] P. Frankel,[a] and S. J. Haigh[a]

[a] Department of Materials, University of Manchester, Manchester, M1 3BB, UK.

[b] Dalton Cumbrian Facility, The University of Manchester, Moor Row, CA24 3HA, UK.

[c] Department of Materials Science & Engineering, Drexel University, Philadelphia, PA 19104, USA.

Supplementary information available (section 7.9): Thermal expansion characterisations, high–resolution digital image correlation analysis, crack formation analysis, tables of values.

7.1 Abstract

The MAX phases Ti_3AlC_2, $(Ta_{0.25}Ti_{0.75})_3Al_{0.77}C_2$, and $(Ta_{0.38}Ti_{0.62})_3Al_{0.81}C_2$, have been irradiated with 2 MeV protons at temperatures of ~141 °C, ~351 °C and ~658 °C, to doses of ~0.06 and ~0.12 dpa. Irradiation–induced crystallographic and microstructural evolutions have been characterised at the macro– and nanoscale using a combination of X–ray diffraction (XRD) and high–resolution digital image correlation (HRDIC). Anisotropic unit cell expansion in the *c*–axis and contraction in the *a*–axis were observed in all three materials following irradiation at the lower two temperatures, with anisotropic strains resulting in micro–cracking at grain boundaries and, to a lesser extent, through grains. At ~141 °C, Ti_3AlC_2 and $(Ta_{0.38}Ti_{0.62})_3Al_{0.81}C_2$ samples underwent significant exfoliation after doses of 1.04(2) dpa and 1.15(3) dpa at the Bragg peak, respectively. At ~350 °C and below, lattice parameter strain appeared to increase with irradiation dose, whilst at the highest temperature of ~650 °C, reduced lattice strains were displayed by the Ta–

containing phases compared with lower temperature irradiations, with Ti_3AlC_2 displaying no measurable lattice strain even at the highest dose, indicating a damage/recovery equilibrium. In general, Ti_3AlC_2 shows the highest tolerance to disorder compared to the Ta–containing phases. However, $(Ta_{0.25}Ti_{0.75})_3Al_{0.77}C_2$ displays a higher resistance to irradiation–induced exfoliation at ~141 °C than Ti_3AlC_2 and $(Ta_{0.38}Ti_{0.62})_3Al_{0.81}C_2$. Equally, both Ta–containing phases show reduced lattice strain after ~0.06 dpa and at ~141 °C compared to Ti_3AlC_2.

7.2 Introduction

The pathway to commercial thermonuclear fusion power is plagued with technological obstacles, with component material selection for future reactors of particular concern. Cyclic fusion neutron (14.1 MeV) radiation, thermal load (up to 10 MW m^{-2}, erosion and corrosion (few μm $year^{-1}$) resistant materials, capable of operating across a wide temperature range (up to 1500 μm) whilst minimising radioactive waste, are essential to the realisation of fusion as a safe, efficient and economically viable electricity production means. Notable advancements have been made recently in the development of materials for high heat flux and radiation damage resistant components in fusion, yet their readiness for industrial application is still notably low. Much of the research into plasma–facing component materials has focussed on tungsten and its associated alloys or composites, such as self–passivating W–Cr–Y alloys for use as the first wall armour in DEMO – a planned fusion power plant design [457]. Yet these alloys and other leading candidates were recently assessed at a Material Technology Readiness Level (MTRL) of 2–3 out of a possible 9, and where 8 is the minimum required for a material to be suitable for use in DEMO [458]. A serious issue with material development for fusion is the often prohibitively large volume of research required for qualification at high MTRLs, which inevitably takes decades to achieve, even on a global scale. The continual development of new and advanced materials is thus essential if fusion power is to be realised on an effective scale in the future.

The $M_{n+1}AX_n$, or ‘MAX’ phases, where generally ‘M’ is an early transition metal or lanthanide, ‘A’ is a group 12–15 element, X is either carbon or nitrogen and n is a positive integer, are a group of metallo–ceramic materials with unusual and often interesting properties. Due to their unique nanolaminated structure consisting of alternating ceramic ‘M_6X’ and metallic ‘A’ layers, MAX phases can exhibit an unusual mix of properties. They are elastically stiff (Young's modulus, $E > 300$ GPa), relatively soft (often < 10 GPa hardness), easily machinable, mechanical impact damage tolerant and have surprisingly high thermal conductivities (up to 60 W m^{-1} K^{-1}) [102], [103], [107], [172]. Additionally, several compositions have shown thermodynamic stability up to 1600 °C, corrosion resistance, radiation–induced amorphisation resistance up to 150 dpa, and thermal shock resistance up to 1400 °C [103], [185], [186], [240], [410].

As such, MAX phases have been proposed for a range of nuclear applications, including as coatings on accident tolerant fuel cladding and hard–facing material in fission reactors, and as structural materials in magnetic confinement fusion reactors [184], [209], [303], [399], [459]. The verdict on MAX phases as candidates for nuclear environment applications is still unclear, yet there are veins of research which have revealed promise. Select compositions such as Ti_3AlC_2 have shown a remarkable resistance to amorphisation under heavy ion and neutron irradiation, remaining crystalline up to 200 dpa at room temperature, despite profuse atomic disordering and subsequent phase transformation [240], [248]. Furthermore, it has been reported that certain MAX phases display suppression and even full reversibility of radiation damage at elevated temperatures both during and following irradiation [235], [265], [281].

However, MAX phases are known to exhibit anisotropic lattice instabilities, phase transformations and even phase decomposition, especially at high temperatures, during irradiation. This can lead to microcrack formation and even surface exfoliation under certain conditions [281], [286]. The formation and evolution of microcracks is of particular concern in MAX phases given the characteristic uniaxial grain structure which can encourage propagation, especially in textured specimens [398]. Mechanical failure during operation in a nuclear environment could be detrimental to reactor stability. Despite notable efforts in the literature, questions remain around the response of MAX phases to irradiation, particularly with regards to microstructural evolution and bulk failure modes, which must be addressed before they can be successfully implemented in demanding nuclear environments.

Many reported irradiations of MAX phases utilise heavy ions, due to the high displacement damage rates compared with nuclear fission test reactors [299]. However, there is growing evidence that protons may be used as alternatives to simulate neutron damage, despite the often significant differences in atomic displacement cascade size [251]. Large scale damage structures in Zr alloys and structural steels produced by protons are comparable to those produced in fission–relevant neutron spectra, especially in terms of elemental segregation and microstructural instabilities, with damage rates up to three orders of magnitude higher than for neutron irradiations [228], [232]. Additionally, the damage profile produced by protons is shallower before the Bragg peak (the region which receives the highest relative dose), compared with heavier ions. Combined with vastly increased penetration depth compared to heavy ions, this makes protons a reliable surrogate for simulating reactor–level neutron damage.

Ward *et al.* reported on the crystallographic evolution of Ti_3SiC_2 and Ti_3AlC_2 MAX phases following exposure to 1.5 MeV protons at 350 °C, to a dose of 0.1 dpa (1.438×10^{18} protons cm^{-2}) at 60 % of the Bragg peak and at a rate of 4.57×10^{-6} dpa s^{-1} [251]. A *c*–axis expansion and *a*–axis unit cell contraction were observed along with partial phase transformation to a face–centred–cubic impurity, consistent with previous heavy ion irradiations in the literature [211], [238], [269], [270], [275], [280], [283], [363], [243], [246], [250], [252], [257], [266]–[268]. Extensive microcracking was observed at grain boundaries, believed to be a result of the unit cell strain. These effects were more pronounced in Ti_3AlC_2, indicating a lower resistance to damage. However, despite these effects, high angle annular dark field scanning transmission electron microscopy (HAADF–STEM) analysis showed no loss of crystallinity in the nanolaminate MAX phase following irradiation, indicating a resistance to amorphisation.

In 2 MeV proton irradiations of Ti_3SiC_2 and Ti_3AlC_2 at 350–600 °C, lattice parameter changes appeared to follow an inverse linear trend with irradiation temperature, indicating a mechanism of thermally activated lattice recovery [281]. By extrapolating the data, the authors estimated the temperature at which lattice recovery would dominate during irradiation as ~685 °C and ~1050 °C for Ti_3SiC_2 and Ti_3AlC_2, respectively. Similar results have been reported for heavy ion and neutron irradiations of these and other MAX phases, such as Ti_2AlC [243], [252], [257], [266], [268], [270].

Despite the decreased lattice strains reported for neutron irradiation at higher irradiation temperatures, larger defect structures, such as basal plane dislocation loops, are still observed after moderate doses (> 1 dpa) [279]. Tallman *et al.* found that the dislocation loop sizes increases and the loop density decreases with increasing damage level and temperature (~735 to ~1085 °C ; 1.6–3.4 dpa) [257]. This differs from proton irradiation where no irradiation induced dislocation loops have been reported.

Ti_3AlC_2 samples have also been shown to fail *via* exfoliation of the target region during proton irradiation – with failure occurring near the Bragg peak depth at a dose of < 0.73 dpa at < 400 °C [281]. As this has not been observed at higher temperatures, it is thought that the exfoliation occurs due to a combination of radiation damage induced embrittlement and microcracking, and the accumulation of pressurised hydrogen, leading to blistering. Dose rate is also shown to be an important factor as Ti_3AlC_2 has been reported to be stable to higher damages, but only at lower dose rates (4.5×10^{-5} dpa s^{-1} compared to 1.8×10^{-4} dpa s^{-1}) [279]. Other heavy ion irradiations on Ti_3AlC_2 to significantly higher damage levels and dose rates have not observed any form of exfoliation, demonstrating the potential importance of precise irradiation conditions implantation profile [243], [270], [460].

In this work, we investigate the effect of Ta additions on the proton radiation tolerance of the Ti_3AlC_2 MAX phase, which has previously shown promise, due to its radiation tolerance at a range of temperatures [248], [277]. Three compositions are considered, with 0, 25 and 38 at.% Ta substitution into the Ti lattice site: Ti_3AlC_2, $(Ta_{0.25}Ti_{0.75})_3Al_{0.77}C_2$ and $(Ta_{0.38}Ti_{0.62})_3Al_{0.81}C_2$, for two target doses (~0.06 and ~0.12 dpa) and over a range of temperatures up to ~650 °C. Anisotropic lattice parameter evolution and bulk compositional changes are investigated using grazing incidence X–ray diffraction, with local microstrain and crack evolution assessed using a combination of scanning electron microscopy and high–resolution digital image correlation.

7.3 Experimental Methods

7.3.1 Material

$(Ta_{0.25}Ti_{0.75})_3Al_{0.77}C_2$ and $(Ta_{0.38}Ti_{0.62})_3Al_{0.81}C_2$ MAX phases, abbreviated going forward as 'Ta–25' and 'Ta–38', respectively, were synthesised *via* pressure–less sintering. Starting powders of TaC, TiC, Ti and Al from Alfa Aesar (Ward Hill, MA, USA), with mean particle sizes of less than 63 µm, were mixed in the desired molar ratios, with a 10 at.% Al excess to mitigate atmospheric loss during heating. Despite this precaution, the prepared Ta containing compositions still show a reduced Al content compared the parent Ti_3AlC_2 phase [461]. The mixture was then ZrO_2 ball milled in plastic jars for 12 h to provide a homogeneous blend, before being uniaxial cold pressed at 250 MPa. The resulting pellets were then sintered inside an 82 × 31 × 18 mm Al_2O_3 boat, covered with an Al_2O_3 plate, and placed inside an Al_2O_3 tube furnace with an inert flowing Ar atmosphere. Pure Ti powder was placed in an adjacent crucible upstream of the Ar flow to the pellet, as a residual oxygen getter.

The sintering was performed at 1600 °C, with a heating and cooling rate of 5 °C min^{-1} and an 8 h dwell at the maximum temperature. The resulting materials were 85.3(2) wt.% Ta–25, 8.0(2) wt.% $(Ta_{0.24}Ti_{0.76})C_x$, 4.50(9) wt.% $TiAl_2$, and 2.20(4) wt.% Al_2O_3, for Ta–25, and 87.96(2) wt.% Ta–38, 9.4(2) wt.% $(Ta_{0.27}Ti_{0.73})C_x$, 2.64(1) wt.% Al_2O_3 for Ta–38, according to refinements of X–ray diffraction (XRD) data combined with quantitative scanning electron microscopy energy dispersive X–ray spectroscopy (SEM–EDS) [461]. The mean MAX phase grain size (length × width) was 14.1(5) × 4.29(10) µm and 12.0(5) × 3.97(13) µm for Ta–25 and Ta–38, respectively, as estimated *via* measurements of apparent major/minor grain axes from SEM surface observations.

In an attempt to provide control data for the identical material without Ta additions, bulk Ti_3AlC_2 was obtained from Kanthal (Sandvik AB, Hallstahammar, Sweden). The material was synthesised *via* hot pressing of pre–reacted Ti_2AlC and TiC powders at 1400 °C, with a heating rate of 500 °C h^{-1}, for 4 h and under a uniaxial pressure of ~40 MPa. The resulting material was 95.1 wt.% Ti_3AlC_2, 4.1 wt.% TiC and 0.8 wt.% Al_2O_3, according to refinements of (XRD) data combined with quantitative SEM–EDS. The mean MAX phase grain size was 15(5) × 5(1) µm, estimated using a similar method as for Ta–25 and Ta–38 measurements.

The bulk densities of the as–synthesised materials were measured using the Archimedes method [314] and are listed in Table 7.3.

7.3.2 Proton Irradiation

Samples of Ti_3AlC_2, Ta–25 and Ta–38 were irradiated by 2 MeV protons to approximate doses of ~0.06 dpa and ~0.11 dpa at fixed temperatures of either ~141 °C, ~350 °C or ~650 °C. Irradiations were performed at the University of Manchester's Dalton Cumbrian Facility (DCF) using a 5 MeV tandem pelletron [364], operated at an average beam current of 10.4 µA. The protons were accelerated onto a stationary target containing bulk test samples. Bulk 7 × 3 × 1 mm

Table 7.1 – **Sample irradiation details:** including average irradiation temperature (T); depth of the Bragg peak (according to SRIM calculations); total fluence (f); and both dose and dose rate at 60% of the Bragg peak depth. The values marked '*' correspond to the irradiation period up to the surface exfoliation of the sample. The point of exfoliation has been estimated using thermal camera measurements, as a sharp increase in apparent temperature accompanies the loss of surface material and, therefore, a slight decrease in emissivity.

Material	T (°C)	Bragg depth (± 0.2 μm)	f ($\times 10^{18}$ H^+ cm^{-2})	Dose (dpa)	Dose rate ($\times 10^{-6}$ dpa s^{-1})
Ti_3AlC_2	141(8)	17.8	1.44(3)	0.0600(14)	4.41(10)
Ta–25	141(8)	19.6	1.44(3)	0.0558(13)	4.10(10)
Ta–38	141(8)	15.8	1.44(3)	0.0596(14)	4.37(10)
Ti_3AlC_2	141(8)	17.8	1.77(4)*	0.0736(17)*	5.33(13)*
Ta–25	141(8)	19.7	2.90(7)	0.112(3)	4.92(12)
Ta–38	141(8)	15.8	2.32(6)*	0.096(2)*	4.50(11)*
Ti_3AlC_2	349(7)	17.8	1.45(3)	0.0603(14)	5.31(13)
Ta–25	344(8)	19.7	1.45(3)	0.0561(13)	4.93(12)
Ta–38	354(8)	15.8	1.45(3)	0.0598(14)	5.27(12)
Ti_3AlC_2	367(7)	17.8	2.90(7)	0.121(3)	5.38(13)
Ta–25	347(8)	19.7	2.90(7)	0.112(3)	5.00(12)
Ta–38	346(7)	15.8	2.90(7)	0.120(3)	5.34(13)
Ti_3AlC_2	698(6)	17.8	1.45(3)	0.0605(14)	3.926(9)
Ta–25	646(4)	19.7	1.45(3)	0.0562(13)	3.650(9)
Ta–38	652(5)	15.8	1.45(3)	0.0600(14)	3.896(9)
Ti_3AlC_2	635(4)	17.8	2.89(7)	0.120(3)	4.84(11)
Ta–25	648(3)	19.7	2.89(7)	0.112(3)	4.50(11)
Ta–38	672(4)	15.8	2.89(7)	0.119(3)	4.80(11)

samples of Ti_3AlC_2, Ta–25 and Ta–38 were sectioned from as–synthesised pellets *via* electrical discharge machining, with the faces mechanically polished to a ¼ μm diamond finish. The rear faces of the samples were mounted on a steel backing plate, in contact with an inductive heating element, using a thin layer of silver paint

Table 7.2 – The atomic displacement values in eV of the elements used in SRIM calculations.

	m_r (amu)	E_d (eV)	Reference
Ta	180.95	90	[369]
Ti	47.867	30	[369]
Al	26.982	25	[369]
C	12.011	30	[368]

and with a thermocouple soldered to the rear of the central sample. A tantalum shim washer was fixed over the holder edges to prevent stray ions from activating the holder.

For ~141 °C irradiations, the thermocouple reading was used to track sample temperature variations, which were manually corrected *via* beam current adjustments, usually less than 0.5 µA. For irradiations at ~350 °C and ~650 °C, a thermal camera was instead used to monitor temperature variations, after calibration with the thermocouple at the start of the heating. The thermal camera provided higher reliability measurements, as it measures the irradiated sample surface, rather than the temperature at the rear, next to the heater. However, this camera only operates reliably above temperatures of ~150 °C and thus could not be used for the lower temperature setups. This introduces a potential source of error in the thermocouple readings from the room temperature irradiations, as these are likely lower than the actual surface value, due to beam heating of the irradiated surface and subsequent dissipation of heat as it is conducted through the 1 mm thickness of sample. The emissivities were measured as 0.29(3) for Ti_3AlC_2, 0.50(3) for Ta–25, and 0.41(2) for Ta–38.

Estimations of both atomic displacement damage and implanted ion density were performed using the Kinchin–Pease method [365] as implemented in the Monte Carlo software package Stopping and Range of Ions in Matter (SRIM) [366]. The "Ion Distribution and Quick Calculation of Damage" vacancy production method was employed for 1,000,000 simulated incident ions [367], [368]. The atomic

Table 7.3 – The theoretical and physical densities of the materials used in this work, along with their respective Bragg peak depths and damage levels after irradiation to 2.9×10^{18} H^+ cm^{-2} at a proton energy of 2 MeV.

Material	$\rho_{theoretical}$ (g/cm^3)	$\rho_{measured}$ (g/cm^3)	Bragg peak depth (µm)	Dose at Bragg peak (dpa)	60% of Bragg peak depth (µm)	Dose at 60% Bragg peak (dpa)
Ti_3AlC_2	4.30(3)	4.242(7)	29.6(2)	1.65(4)	17.8(2)	0.113(3)
Ta–25	6.12(1)	5.009(12)	27.2(2)	1.41(3)	16.3(2)	0.113(3)
Ta–38	7.28(1)	7.092(9)	25.6(2)	1.32(3)	15.4(2)	0.114(3)

displacement energies, with associated source references, used for each element and the densities for the materials considered are reported in Table 7.2 and Table 7.3, respectively.

The dose, in dpa, for each sample was calculated using the following relation:

$$\mathrm{dpa} = \frac{\mathrm{It}}{\mathrm{N_d Ae}}\left(\mathrm{V_{primary}} + \mathrm{V_{recoil}}\right) \qquad (7.1)$$

where I is the incident proton beam current, t is the irradiation time in seconds, N_d is the target material atomic number density, A is the irradiated area, e is the fundamental electron charge 1.602×10^{-19} C, $V_{primary}$ is the vacancies produced by primary collisions and V_{recoil} is the vacancies produced by recoils. Experimental fluctuations in beam current as well as ramp–up/ramp–down times, which affect the fluence, were taken into account during irradiations. Despite high–frequency beam current fluctuations during irradiation of up to ±5.7%, the propagated uncertainty of the damage, in dpa, received by the samples was only ±2.4% on average.

7.3.3 X–Ray Diffraction (XRD)

For all XRD characterisations, a Cu–K_α source was used, with X–rays incident on the samples over a 2θ range of 5–85°. The full list of experimental XRD parameters can be seen in Table 7.1. Prior to scanning as–irradiated samples, the surface was

Table 7.4 – XRD parameters.

Diffractometer	Bruker D8 Discover
Source	Cu–K$_\alpha$
Voltage (kV)	40
Current (mA)	40
Power (W)	1600
Detector	1D
Divergence slit length (mm)	16
Incident Soller slit opening (°)	None
Receiving Soller slit opening (°)	2.5
Receiving slit opening (°)	2.339
Length (mm)	18
2θ angular range (°)	5–85
2θ angular step (°)	0.02
Step dwell time (s)	4

gently polished with ¼ µm diamond paste to remove the gold pattern used for digital image correlation (discussed in the next section).

Quantitative phase and unit cell analysis of XRD profiles was performed using the software package TOPAS [323]. The Rietveld method was employed to refine calculated full profile to the experimental data, made possible by using the Newton–Raphson nonlinear least–squares minimisation routine [324]. The correlation between the calculated profile intensity I_c and the observed intensity I_o is defined by the objective function, χ^2. This is the sum of the individual squares of the weighted differences between I_o and I_c, written as:

$$\chi^2 = \sum \frac{1}{I_o}(I_o - I_c)^2 \qquad (7.2)$$

where I_c is given by:

$$I_c = S_f \sum_{i=j}^{N_{phases}} \frac{f_i}{V_j^2} \sum_{i=k}^{N_{peaks}} L_k \left|F_{k,j}\right|^2 S_j(2\theta_i - 2\theta_{k,j}) P_{k,j} A_j + I_b \qquad (7.3)$$

where S_f is the profile scale factor, N_{phases} is the number of phases present in the sample, f_i and V_j are the phase fraction and volume, respectively, N_{peaks} is the number of refined peaks, L_k is the Lorentz–polarisation factor, $|F_{k,j}|$ is the structure factor, θ_i is the peak position angle, $P_{k,j}$ is the preferred orientation, A_j is the peak area and I_b is the background profile intensity [320].

7.3.4 High–Resolution Digital Image Correlation (HRDIC)

The gold remodelling technique, adapted from [374] was utilised on ¼ µm polished surfaces of Ti_3AlC_2, Ta–25 and Ta–38. A ~20 nm thick gold layer was deposited using an Edwards S150B sputter coater. All samples were then placed on a steel hot plate at 350 °C and exposed to a partially enclosed steam atmosphere for 3 h to reform the gold layer. To prevent further pattern development during irradiations, a further heat treatment was performed for the samples prior to irradiation. This was done at 350 °C for 6 h, in the same environment on the hot plate as for the reforming, for room temperature and ~350 °C irradiations. For the ~650 °C irradiations, the samples were instead heat treated at 600 °C for 9 h in an argon furnace. For the majority of the samples, these heat treatments fully stabilised the speckle pattern, with no development of the speckle sizes seen after irradiation. The subsequent gold speckle pattern had a mean particle size of 45(13) nm, with a spacing of 32(10) nm. It should be noted that the initial gold layer thickness, quality, remodelling time, temperature and humidity all effect the size and structure of the resulting nanopattern [386]. As such, the parameters used in this work are not necessarily optimal for these materials, but nonetheless resulted in a fine, homogeneous pattern which allowed a localised strain resolution of ~350 nm.

Digital tracking of the individual gold nanofeatures before and after irradiation was enabled using SEM backscattered electron (BSE) detector imaging. Immersion mode BSE images were acquired using an FEI Magellan XHR 400L FEG–SEM, operated at 10 kV, a beam current of 0.8 nA, dwell time of 3 µs, working distance of ~5 mm and images captured using an insertable concentric BSE detector. For each sample, both before and after irradiation, an 8 × 8 image array was captured from the specimen centre using the Thermo Fisher Scientific MAPS software [390]. The individual 8–bit images had dimensions of 2048 × 1768 pixels and included up to a 20% overlap with adjacent regions. Mosaics consisting of the 64 individual images were stitched using ImageJ by applying a linear blend on overlapping identical regions [391], resulting in maps with dimensions ~12800 × 11050 pixels, or a 187.5 × 161.9 µm field of view. The mosaics of virgin and irradiated specimens were correlated using the commercial source software package DaVis 8.4.0 [392]. A sub–window size of 48 × 48 pixels with a 50% overlap was used equating to a spatial resolution of ~350 × 350 nm^2.

The DIC generates a full–field in–plane displacement map for each mosaic pair. The DIC analysis produces full–field in–plane displacement maps, $u(x_1, x_2, 0)$, on the plane x_1x_2 with normal x_3. The in–plane deformation is then calculated *via* differentiation of the displacement vectors using the displacement gradient tensor:

$$\frac{\partial u_i}{\partial x_j} = \begin{bmatrix} \frac{\partial u_1}{\partial x_1} & \frac{\partial u_2}{\partial x_1} \\ \frac{\partial u_1}{\partial x_2} & \frac{\partial u_1}{\partial x_2} \end{bmatrix} \tag{7.4}$$

To ensure consistency across displacement components and to reduce the impact of displacement uncertainty, second order central differences were used to compute the gradient. The effective shear strain, γ_{eff} – a convenient measure for representing slip shearing, was calculated using [393]:

$$\gamma_{\mathrm{eff}} = \sqrt{\left(\frac{\frac{\partial u_1}{\partial x_1} - \frac{\partial u_2}{\partial x_2}}{2}\right)^2 + \left(\frac{\frac{\partial u_1}{\partial x_2} + \frac{\partial u_2}{\partial x_1}}{2}\right)^2} \qquad (7.5)$$

The full HRDIC dataset for this work was processed using the DefDAP 0.92.3 Python library [395].

To supplement HRDIC characterisations, surface compositional analysis was performed using SEM energy dispersive X–ray spectroscopy (EDS). An FEI Quanta 650 FEG–SEM, equipped with an Oxford Instruments X–Max^{N} 50 EDS detector, was used for all scans, operated an accelerating voltage of 15 kV, a beam current of 10 nA and a working distance of 10 mm.

Finally, quantitative microcrack analysis of the samples both before and after irradiation was performed on the BSE micrographs used for HRDIC. A combination of image–based thresholding and particle tracking methods, as implemented in ImageJ [391], was used to estimate initial crack densities in the virgin material as well as the growth of pre–existing cracks and formation of independent cracks during irradiation.

7.4 Results

The average temperature and total dose received by each sample are outlined in Table 7.1. These include small variations due to unavoidable differences in experimental setup, including sample dimensions, material surface quality, surface contact with the holder, beam spill and current fluctuations, in addition to local microstructural anisotropies across the different materials. For brevity, the two target irradiation doses (0.06 and 0.12 dpa) delivered to each material will be referred to as ‘lower’ and ‘higher’. Equally, the three irradiation temperatures utilised will be referred to as ‘low’ (room temperature), ‘moderate’ (~350 °C) and ‘high’ (~650 °C). For example, the Ti_3AlC_2 sample irradiated to 0.0603(14) dpa at 349(7) °C will be referred to as the low dose, moderate temperature Ti_3AlC_2 sample. BSE images of the MAX phase samples (e.g., Fig. 7.10A–C) show their complex microstructure with a combination of XRD and EDS elemental mapping revealing the impurity phases in all samples. Our earlier work has shown that Ti_3AlC_2 is the purest with only TiC and Al_2O_3, with the Ta–based compositions containing (Ta,Ti)C, Al2O3 and amorphous $TiAl_2$ impurities.

7.4.1 HRDIC: Effect of Proton Dose

7.4.1.1 *Ti_3AlC_2*

As seen in Fig. 7.1–1 the lower dose, low irradiation temperature Ti_3AlC_2 sample displays significant anisotropic strain in the MAX phase grains (< 1%), increasing to ~2% in concentrated bands at grain boundaries. The values in and around TiC and Al_2O_3 impurity particles (indicated as the royal blue regions in Fig. 7.1E) are even higher, reaching compressive strains of up to 3% at grain boundaries, with little evidence of expansion. Significant microcrack formation is also observed (as represented in Fig. 7.4A), with an increase in number density of 12.8% across the sample surface, compared with the as–synthesised material, generally following grain boundaries but with some propagating through TiC and Al_2O_3 particles. Additionally, some pre–existing cracks display evidence of growth on the order of a few µm (~30%). No local strain data could be extracted for the higher dose Ti_3AlC_2 sample due to surface exfoliation during irradiation (for discussion, refer to section 7.5.2). As such, no dose effects could be deduced for this particular condition.

At the moderate irradiation temperature, the low dose Ti_3AlC_2 sample exhibits a largely homogeneous and low–magnitude strain distribution across both MAX phase and impurity grains, with effective strains of < 0.3%. There is a small degree of strain localisation at grain boundaries, reaching magnitudes of < 1% at high angle

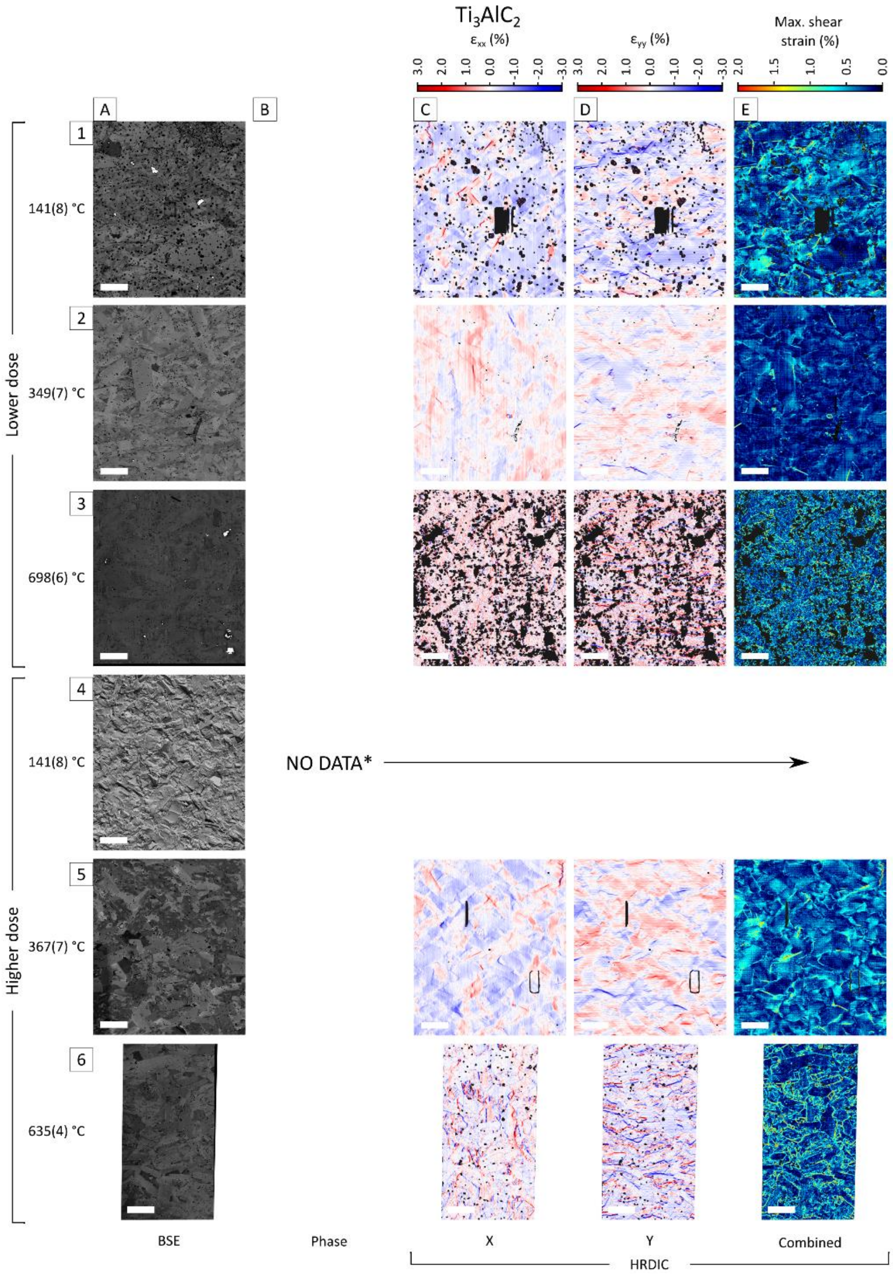

Fig. 7.1 – Local microstrain in Ti_3AlC_2: (A1–6) BSE micrographs of the central regions of the Ti_3AlC_2 samples following 2 MeV proton irradiation to ~0.06 dpa (lower dose, A1–3), and ~0.12 dpa (higher dose, A4–6). (B1–6) Corresponding phase maps for (A1–6) deduced from SEM–EDS. (C1–E6) HRDIC strain mapping for regions (A1–6) showing an ε_{xx} (horizontal) strain map (C1–6), an ε_{yy} (vertical) strain map (D1–6), and an effective shear strain, $\frac{1}{2}(\varepsilon_{xx}+\varepsilon_{yy})^2$, map (E1–6). Strain magnitudes, in %, are displayed as a colour map and range from –3.0% to 3.0% for ε_{xx} and ε_{yy}, and 0.0–2.0% for the effective shear strain. Voids are overlaid as black regions on D–O. All scale bars are 30 μm.

MAX phase boundaries. Additionally, extensive microcracking (34.6% increase from that in the virgin material) and growth of existing cracks are evident at grain boundaries, although this does not appear to be related to a particular phase. The behaviour of the higher dose sample is similar, but with homogeneous, anisotropic strains reaching $< 0.5\%$ in MAX phase grains and $< 1.3\%$ at grain boundaries, along with a higher degree of microcrack formation (57.5% compared to 34.6%). As with the lower dose, impurities display higher than average strains, with a gradient of increasing strain when approaching a grain–edge from the centre. The amorphous Ti–Al–C regions appear to show negligible strain, with slightly higher values in regions adjacent to crystalline phases with high strain concentrations. This indicates a passive response to irradiation, with strain dependant on the behaviour of surrounding phases.

The lower dose Ti_3AlC_2 sample irradiated at the highest temperature shows severe gold pattern damage, as with the Ta–25 and Ta–38 samples under similar conditions. Intact regions indicate strain is localised to bands surrounding MAX phase and TiC grains. The strain is anisotropic, reaching expansion maxima of up to 2%. Due to the pattern damage, no information on intragranular, amorphous phase or Al_2O_3–related strain could be extracted. The sample irradiated to the higher dose also experienced damage to the gold pattern, leaving an intact region covering ~50% of the sample. The most intense strain concentrations are again localised at MAX phase grain boundaries and at near–edge regions of TiC grains, but at higher concentrations and magnitudes up to 2% and 2.8%, respectively. Despite this, the intragranular strain in the MAX phase is considerably lower than that in the moderate irradiation temperature samples, with maxima of ~0.35%.

7.4.1.2 *Ta–25*

In the Ta–25 sample, irradiated at low temperature and to the lower dose, negligible strain is observed in the MAX phase grains. However, up to 0.75% shear strain is concentrated in grain boundary regions, which extends into the amorphous $TiAl_2$

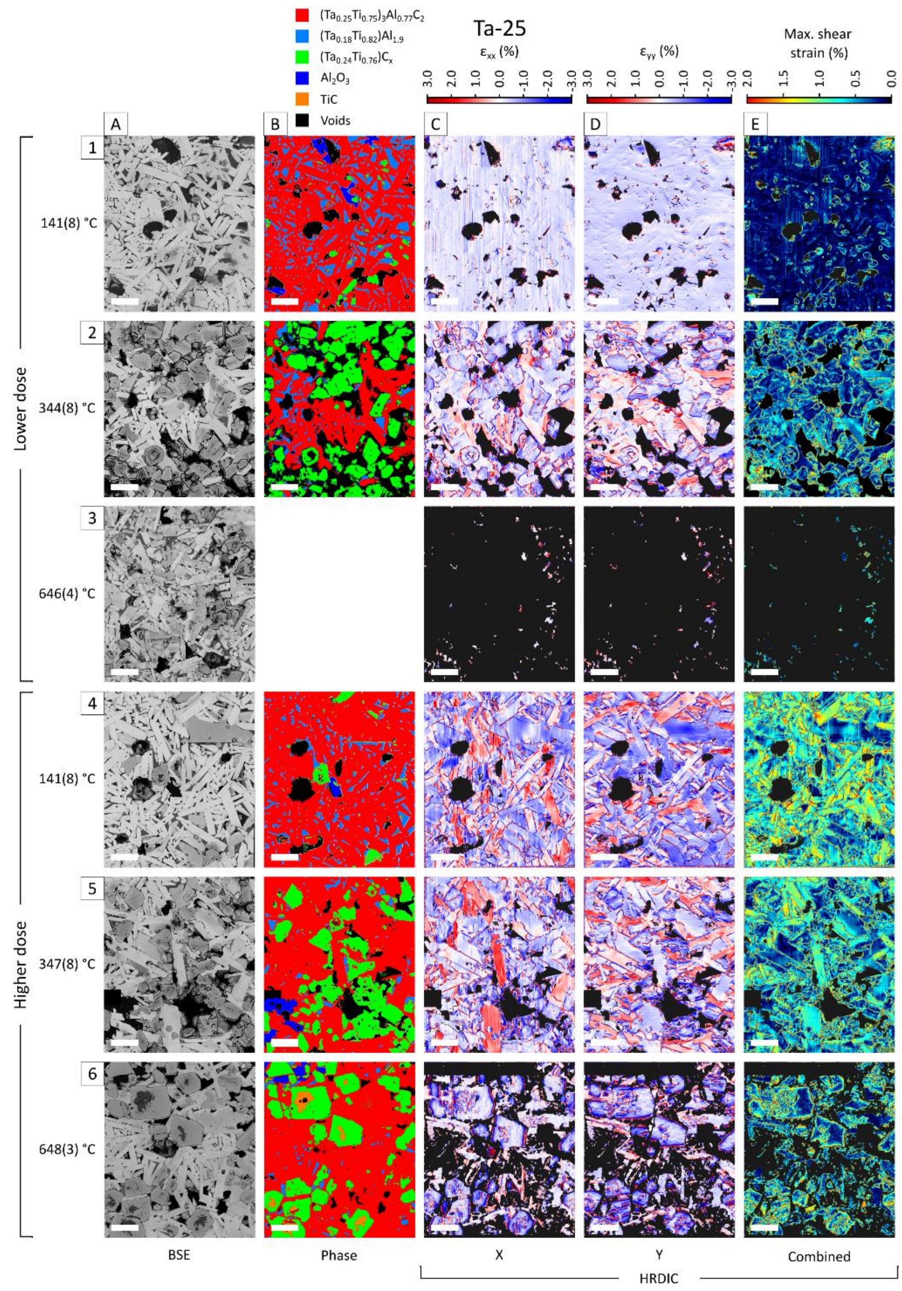

Fig. 7.2 – Local microstrain in Ta–25: (A1–6) BSE micrographs of the central regions of the Ta–25 samples following 2 MeV proton irradiation to ~0.06 dpa (lower dose, A1–3), and ~0.12 dpa (higher dose, A4–6). (B1–6) Corresponding phase maps for (A1–6) deduced from SEM–EDS. (C1–E6) HRDIC strain mapping for regions (A1–6) showing an ε_{xx} (horizontal) strain map (C1–6), an ε_{yy} (vertical) strain map (D1–6), and an effective shear strain, $\frac{1}{2}(\varepsilon_{xx}+\varepsilon_{yy})^2$, map (E1–6). Strain magnitudes, in %, are displayed as a colour map and range from –3.0% to 3.0% for ε_{xx} and ε_{yy}, and 0.0–2.0% for the effective shear strain. Voids are overlaid as black regions on D–O. All scale bars are 30 µm.

regions between some MAX phase grains (shown as light blue in the phase map in Fig. 7.2B1). The highest strain values of up to 1.6% appear to be concentrated at the grain boundaries of the MX impurity phase $(Ta_{0.24}Ti_{0.76})C_x$, seen as cyan–coloured loops on the HRDIC map in Fig. 7.2E1. The localisation of strain correlates with an increase in microcrack density (17.1%) in those regions. The regions of the lowest, and, incidentally, most homogeneous strain are generally the amorphous Ta–Ti–Al–C grains and Al_2O_3 particles, with maximum effective shear strains of 0.02%. Similar responses are seen in the higher dose sample, especially within grain boundary regions and impurities, but with a significant increase in magnitude – seen clearly in Fig. 7.2E2, in which grains are strongly highlighted by their respective strain distributions. High and relatively homogeneous strains of up to ~1.12% are observed in surrounding regions of MAX phase grains, including the amorphous $TiAl_2$ phase. As with the lower dose sample, MX impurity phase grains are surrounded by localised strain, but slightly higher in magnitude at up to 1.66%. However, unlike the lower dose sample – in which strain appears to be almost isotropic across all phases, in the higher dose sample a strong anisotropy is evident, as seen in Fig. 7.2C and D. The anisotropy consists of strain maxima of up to 3%, which is considerably larger than the *c*–axis strain observed with XRD measurements (~1.93%). Additionally, due to the elongated geometry and anisotropic strain distribution of the MAX phase grains, intense strain hotspots are observed where adjacent grains are aligned perpendicular to one another, i.e., high angle grain boundaries. Examples of this can be seen in Fig. 7.2E4, with hotspots visible as dark orange regions. Extensive microcrack formation is observed around hotspot regions and regions of high strain concentration surrounding grains, with an average microcrack density increase of 37.7% observed across the sample. Despite this, the microcracks appear to be generally < 5 μm in length. The lowest effective strains (~0.7%) in this sample are found in the amorphous Ta–Ti–Al–C regions but are still considerably higher than in the lower dose sample.

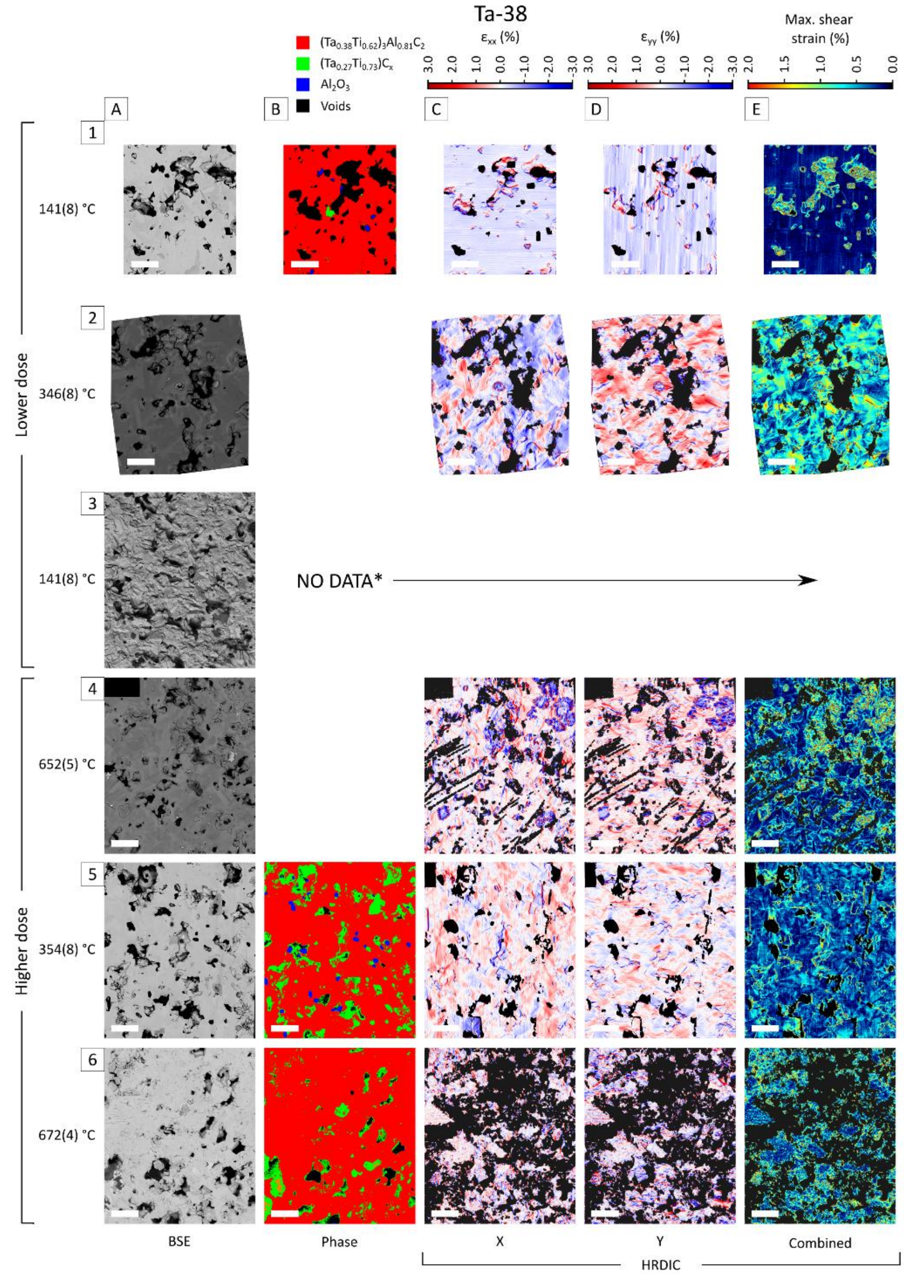

Fig. 7.3 – Local microstrain in Ta–38: (A1–6) BSE micrographs of the central regions of the Ta–38 samples following 2 MeV proton irradiation to ~0.06 dpa (lower dose, A1–3), and ~0.12 dpa (higher dose, A4–6). (B1–6) Corresponding phase maps for (A1–6) deduced from SEM–EDS. (C1–E6) HRDIC strain mapping for regions (A1–6) showing an ε_{xx} (horizontal) strain map (C1–6), an ε_{yy} (vertical) strain map (D1–6), and an effective shear strain, $\frac{1}{2}(\varepsilon_{xx}+\varepsilon_{yy})^2$, map (E1–6). Strain magnitudes, in %, are displayed as a colour map and range from –3.0% to 3.0% for ε_{xx} and ε_{yy}, and 0.0–2.0% for the effective shear strain. Voids are overlaid as black regions on D–O. All scale bars are 30 μm.

At the moderate irradiation temperature, the low dose Ta–25 sample displays the highest consistent strain of ~1.3% in grain boundary regions between MAX phase and MX impurities, as well as in the $TiAl_2$ amorphous phase between MAX phase grains. This strain is generally anisotropic and inhomogeneous, with compression and expansion on orthogonal axes but similar magnitudes. However, within the MX grains, the strain is relatively homogeneous and almost exclusively in compression, with magnitude ~0.25%. The MAX phase grains, as with the low temperature samples, display characteristic anisotropic strain, with compression in the long grain axis and expansion in the short axis, although the effective strain is generally lower than in the impurity phases, at ~0.15%. The amorphous Ta–Ti–Al–C regions display the lowest strains, in compression, of $< 0.1\%$. At the higher dose, similar behaviour is seen in all phases, yet to a significantly higher degree. The effective strain in MAX phase grains is ~1.3%, with hotspots up to 1.8% at high angle grain boundaries, whilst in MX grains compressive strain reaches 2.5%, with a higher concentration in the near–edge grain regions.

Following irradiation at the highest temperature, the gold nanopattern on the lower dose sample was largely destroyed. Therefore, no useful HRDIC data could be extracted from this sample. As this effect was only observed in select high temperature samples, it is presumed to be due to thermal evolution of the pattern rather than proton radiation damage. Interestingly, despite the similar irradiation temperature, the higher dose sample still had a partially intact pattern following irradiation, although only on the MX phase and a few select MAX phase grains. Although it is not clear why this is the case, it is assumed the adhesion of the gold speckles is related to the roughness of the surface in question, leading to a variation across both phase and grain orientation. From the limited data available, it appears that strain is localised in the grain near–edge and boundary regions of the MX phase, with a net compressive strain of ~1%. The effective strain in both MX and MAX phase grains appears to be considerably lower than in the samples irradiated at the moderate temperature, indicating enhanced recombination of point defects, leading to recovery, which is in–line with the XRD data.

7.4.1.3 *Ta–38*

In the lower dose, low temperature Ta–38 sample, strain is almost exclusively localised at impurity grain boundaries, including the MX and Al_2O_3 grains, with < 0.2% effective strain observed elsewhere. Equally, no strain is evident either in or adjacent to MAX phase grains. As the same material failed *via* exfoliation during the higher dose irradiation, reaching 0.096(2) dpa (~80% of the target dose), no HRDIC data could be obtained.

During the moderate temperature irradiation, the MAX phase grains in the lower dose sample show relatively homogeneous strain distributions of < 0.75%, with anisotropic expansion and contraction. At grain boundaries and where MAX phase grains are adjacent to MX grains, the strain is more pronounced at up to 1.3%. The highest strain magnitudes are again concentrated around MX grains, reaching 2% in places. At the same time, Al_2O_3 particles are almost devoid of strain, even at grain boundaries. At the higher dose, the strain distribution is remarkably similar to that in the lower dose sample, with significantly higher magnitudes and higher crack density increases (28.7% compared to 11.0%). In the MAX phase grains, contraction in the long grain axis and expansion in the short axis is evident, with maximum effective strains of up to 1.2%. In grain boundaries, the strain is more concentrated, with maxima of 1.8%.

At the highest irradiation temperature, as with the Ta–25 sample mentioned previously, a significant proportion of the gold pattern appears to have remodelled, as with the Ta–25 sample, leaving ~80% and ~30% of the pattern on the lower and higher dose samples, respectively. At the lower dose, high levels of compressive strain (< 2%) are localised towards the edge of MX impurity grains as with all other samples and conditions. Regions of expansion, although at a lower magnitude to the compression (< 1.5%), are observed in MX and MAX phase grain boundaries,

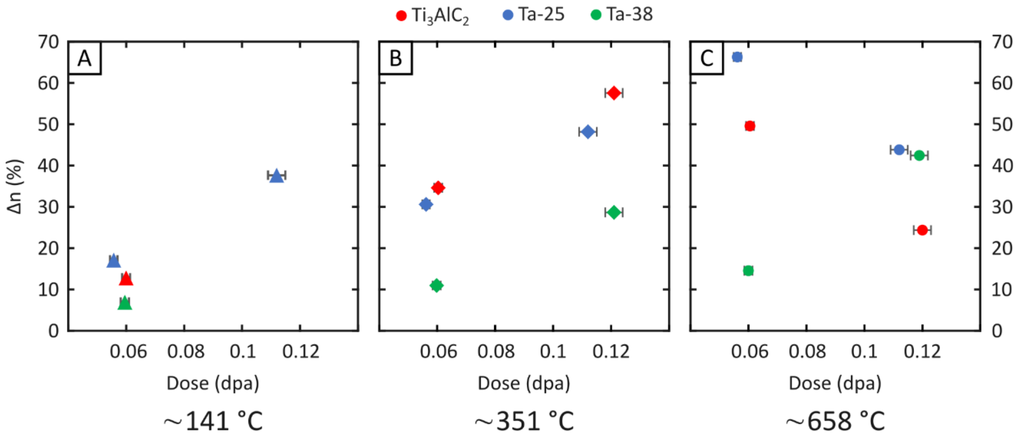

Fig. 7.4 – Microcrack formation: The percentage change in microcrack number density (Δn), relative to the virgin material surface, as a function of dose (dpa) for all irradiated specimens. Data from samples irradiated at ~141 °C, ~351 °C and ~658 °C are shown on separate plots, A–C, respectively. The relative uncertainties of Δn values are too small to be visible on the plots, so have been excluded. The Microcrack population values were obtained from the stitched BSE maps used for HRDIC analysis, *via* a combination of digital thresholding and visual inspection.

often fully surrounding the MX grains. Lower levels of strain, anisotropic but homogeneous, are seen in MAX phase grains, which is slightly more pronounced in grain boundaries – reaching ~0.7% away from MX impurities. At the higher dose, highly concentrated anisotropic strain fields are visible in MX impurities and between MAX phase and MX grains, reaching up to 3% of expansion in hotspots and in near–edge bands.

7.4.2 HRDIC: Effect of Irradiation Temperature

7.4.2.1 Ti_3AlC_2

Increasing the temperature from 141(8) °C to 349(7) °C appears to have the effect of reducing both the intragranular and grain boundary strain intensities significantly, although evidence of this can only be seen in the lower dose samples due to exfoliation of higher dose samples at the lowest temperature. However, the microcrack density increase following irradiation is significantly higher for the moderate temperature sample compared to the low temperature (34.6% and 12.8%, respectively). This is surprising considering the apparent reduction in irradiation induced lattice strain indicated by both the XRD and HRDIC data. This may be explained by the increased crack density in the virgin material of the moderate temperature sample, compared with that of the low temperature sample (3.5×10^{-2} μm^{-2} and 1.9×10^{-2} μm^{-2}, respectively). Interestingly, the presence of pre–existing cracks doesn't necessarily result in localised strain in that region. In fact, some notable grain boundary cracks of < 40 μm length, present in the virgin material, didn't grow even after the higher dose.

At the highest temperature, the intragranular strain in the MAX phase appears to have reduced significantly after both low and high dose, compared with the samples irradiated at the moderate temperature. In the higher dose sample, effective strain reaches ~0.25% in places, whereas in the lower dose sample it averages ~0.5%. Conversely, the localised strain at grain boundaries reaches < 1.13% at the highest temperature, but only ~1.05% in the moderate temperature sample. Additionally, highly concentrated grain boundary strain bands are significantly more widespread in the higher temperature sample, even when excluding cracked regions. This can be seen clearly in Fig. 7.1. This could be an indication of anisotropic recovery distributions, where grain boundaries act as defect sinks and thus experience higher strains than their respective grains.

7.4.2.2 *Ta–25*

The relationship between irradiation temperature and strain in the Ta–25 samples is more complex, as indicated by the XRD data. The lower dose samples show the opposite trend to that seen in Ti_3AlC_2, instead displaying increased intragranular and grain boundary strains at higher temperature. This is especially pronounced at MX impurity grain boundaries, which show high effective shear strains of < 1.3% in the low temperature sample, which increases to < 1.53% in the moderate temperature sample. The increase in magnitude is accompanied by an increased extent of strain, which affects over 50% of the moderate temperature sample grains, compared to less than 5% of grains in the low temperature sample. For the higher dose samples, homogeneous strain of high magnitude is observed at the lowest temperature – 1.1% on average and up to 1.83% at grain boundaries, in most MAX phase grains with hotspots near high angle grain boundaries. Less homogeneous but lower strain is seen in the MX (0.82%) and Al_2O_3 (0.1%) grains and amorphous regions (0.7%). When the temperature is increased, a lower extent of strain (0.99% average and 1.78% at grain boundaries) is observed, with slightly higher homogeneity across phases. The strain in MX grains is slightly lower (0.78%), and significantly lower in amorphous regions, at ~0.35%. The sample irradiated at the highest temperature has very few grains remaining with an intact gold pattern, the majority of which are either MX grains or amorphous regions. A decrease in strain magnitude (0.28%) and increase in homogeneity, compared with the lower temperature samples, is observed across all visible phases, but with increased grain boundary localisation. All visible MAX phase grains show anisotropic strain, but generally distributed homogeneously inside grains, with intense strain localisation at grain boundaries. The MX phase grains generally display a gradient of higher strain towards and at grain boundaries (< 1.85%), with significantly lower strain in central regions (< 0.2%).

7.4.2.3 *Ta–38*

For the Ta–38 samples, an increase in irradiation temperature follows a similar trend to Ti_3AlC_2, with the lower dose, low temperature sample an exception. Unlike for the low dose, low temperature Ti_3AlC_2 sample, negligible homogeneous and isotropic strain is observed in the MAX phase grains, with high intensity, homogeneous and anisotropic localised strain at MX grain boundaries and considerably decreased intragranular strain. As such, increasing the irradiation temperature appears to have the effect of increasing the strain in all phases, unlike for Ti_3AlC_2. It is possible that the unusually low strain values in the low temperature sample are due to radiation–induced amorphisation – something which has been shown to not occur in Ti_3AlC_2, even to very high doses (> 250 dpa). However, no evidence for this is seen in the XRD data, which suggests a negligible change in crystallinity in the bulk material following irradiation for all samples. At the highest irradiation temperature, lower strain is observed compared to the moderate temperature sample in all phases. The MAX phase intragranular strain is generally more homogeneous and anisotropic, with little variation in magnitude and direction between grains and a much lower effective strain. At grain boundaries, strain is localised as with the lower temperature samples, but at a considerably lower magnitude (0.8% compared to 0.99%). The localised effective strain in MX grain boundaries is as high as in other samples, but the intragranular strain is far less homogeneous.

For the higher dose samples, excluding the lowest irradiation temperature (due to exfoliation), the only reliable HRDIC data was extracted for the MAX phase grains, as the gold pattern was almost completely destroyed, leaving only a few MAX phase grain regions intact. Nonetheless, a significant decrease in the average strain is observed (0.32% compared with 0.92%), which is also significantly more homogeneous. At grain boundaries, the strain is more localised and intense, but again lower than in the moderate temperature sample (1.62% compared with 1.73%). It should also be noted that the high temperature, higher dose sample contained an unusually high microcrack density in the virgin material – 11.73×10^{-2} μm^{-2} compared to 3.7×10^{-2} μm^{-2} for the moderate temperature sample, which subsequently underwent a significantly higher relative increase (42.4% compared to 28.7%).

7.4.3 XRD

At the lowest irradiation temperature, the Ti_3AlC_2 sample irradiated to the lower dose underwent significant *c*–axis expansion – 0.45%, which is incidentally its highest value over the three temperatures. The expansion observed gradually decreases from 0.45% to 0.41%, in samples irradiated at the moderate and high temperatures, respectively. For the sample irradiated at the highest temperature,

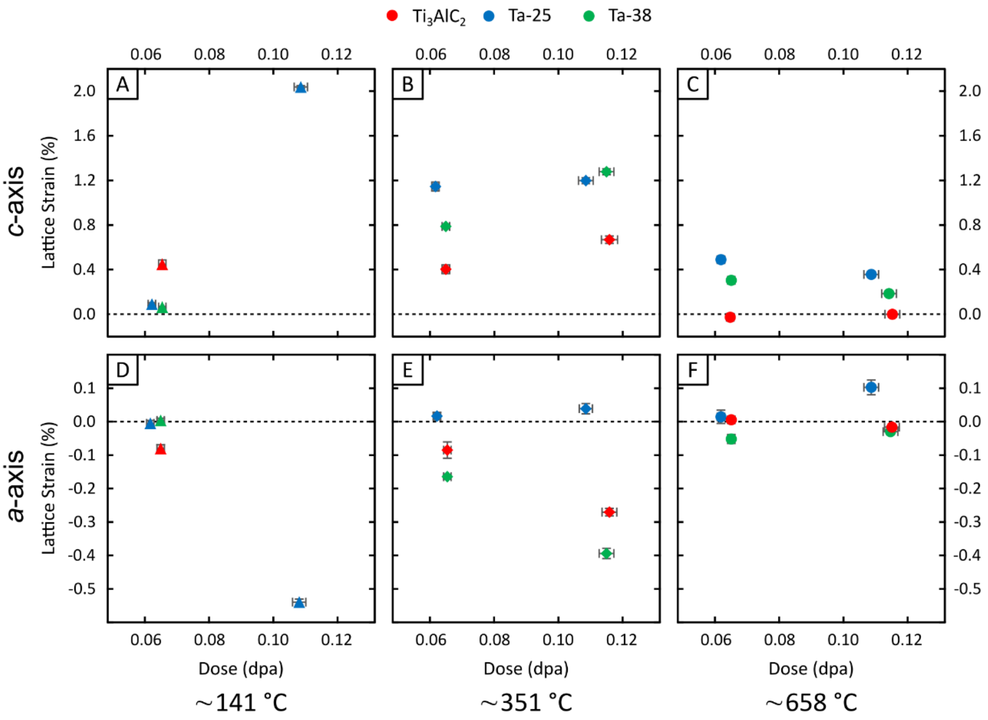

Fig. 7.5 – Anisotropic lattice–parameter evolution: Lattice strains (relative to the virgin material) are plotted as a function of dose (dpa), deduced from Rietveld refinement of GIXRD data from both before and after 2 MeV proton irradiation. The lattice strains in the *c*–axis are shown in the first row of tiles (A–C), with those in the *a*–axis shown in the second row of tiles (D–F). The three columns correspond to the three irradiation temperatures used – ~141 °C, ~351 °C and ~658 °C (A, D; B, E; and C, F, respectively). A dotted line is included on each plot to indicate 0% measured strain. In general, the lattice parameter changes are lower for the higher temperature irradiations, although the data is incomplete for the low temperature irradiations due to surface exfoliation of the Ti$_3$AlC$_2$ and Ta–38 samples after the higher dose (see section 7.5.2) for more details.

negligible *c*– and *a*–axis changes are observed, indicating a full thermally induced recovery from defects, in–line with observations made by Ward *et al*. [281].

Somewhat surprisingly, the lattice strains for both Ta–25 and Ta–38 at the lowest temperature are also almost negligible – 0.08% and 0.06%, respectively in the *c*–axis, and –0.01% and 0.00%, respectively in the *a*–axis. This contrasts with the 0.45% *c*–axis expansion and 0.08% *a*–axis contraction experienced by Ti$_3$AlC$_2$ under the same conditions but is in–line with the HRDIC data, in which little strain is observed for the Ta–based phases at the lowest irradiation temperature. This is perhaps an indication of a higher tolerance to irradiation at lower temperatures.

However, the notable differences in microstructure between the two Ta–containing phases and Ti_3AlC_2 complicate the understanding of this. It is expected that the addition of Ta in the M–layers will decrease the point defect production rate, due to the significantly higher threshold displacement energy of Ta compared with Ti (90 eV and 28 eV, respectively [368]). As such, it is possible that the defect production rate is below a critical recovery threshold at that temperature. In this scenario, the local heating from the proton beam may be enough to allow point defect recombination at a similar rate to production by knock–on damage. On the other hand, the increased porosity of the Ta–containing phases, 2.62% and 18.2% for Ta–38 and Ta–25, respectively, compared with 1.32% for Ti_3AlC_2, likely increase the number of Schottky defects produced. With vacancy mobility expected to be higher than that of interstitials, this would lead to a lattice disorder with a decreased concentration of M_A–A_M antisites, thus resulting in a less pronounced unit cell expansion. To emphasise this, the *a*–lattice parameter change at the lowest temperature is ~0.0% for both materials.

However, the trend is reversed at the moderate and high irradiation temperatures, where both Ta–based phases show significantly higher *c*–axis expansions than in Ti_3AlC_2. The highest – 1.14%, is experienced by Ta–25, in contrast to the 0.41% for Ti_3AlC_2. Equally, the *a*–axis contraction of Ta–38 is double that of Ti_3AlC_2 (0.16% vs 0.08%). As with Ti_3AlC_2, a degree of recovery from this expansion is seen in the high temperature irradiations. The reduction in *c*–axis strain experienced by all three materials from the moderate to high irradiation temperatures is similar (~0.5%), indicating similar rate of recovery and, therefore, point defect recombination rates. However, as the Ta–based phases display higher expansions at the moderate irradiation temperature, the similar recovery rates mean both compositions fall short of a full recovery at the highest temperature. Whilst the *c*–axis strain in Ti_3AlC_2 at the highest temperature goes to 0.0%, expansions of 0.5% and 0.32% are still observed for Ta–25 and Ta–38, respectively. For Ta–38, this behaviour is also reflected in a reduction of *a*–axis strain between the moderate and high temperatures, although at a slightly higher rate than for Ti_3AlC_2 (0.11% vs 0.07% change, respectively). Conversely, an entirely different regime of *a*–axis strain is displayed by Ta–25 at the same temperatures. Rather than a contraction, at the moderate and high temperature, the samples experience a slight *a*–axis expansion, with a 0.02% strain observed. Even considering the high relative uncertainty of this strain (0.019% at the high temperature), the values are far removed from those of Ta–38 and Ti_3AlC_2, indicating an alternative *a*–axis damage evolution pathway. For all three materials, a lattice parameter decrease of the detected MX impurity phase was observed. There is growing evidence in the literature that impurities in MAX phases such as TiC and Al_2O_3 act as defect sinks during irradiation, due to decreased mobility compared with the MAX phase. The diffusion of vacancies produced in neighbouring MAX phase grains, which is expected to be higher than that of interstitials, according to density functional theory (DFT) calculations [215], into TiC or (Ta,Ti)C could explain the observed lattice contraction.

At the higher dose, a similar trend for all three materials is observed – *c*–axis expansion and *a*–axis contraction, with decreasing magnitude as a function of temperature. However, unlike with the lower dose irradiations, this trend includes the lowest irradiation temperature, with a 2.03% *c*–axis strain experienced by Ta–25, falling rapidly and linearly with temperature to 0.36% at the highest temperature. Unfortunately, due to the Ti_3AlC_2 and Ta–38 samples undergoing mechanical exfoliation during irradiation at the lowest temperature, no relevant XRD data could be recorded and so it can only be speculated as to the lattice strains at this temperature. If a linear relationship between irradiation temperature and *c*–axis lattice is assumed, the *c*–axis strain of Ti_3AlC_2 and Ta–38 at the lowest temperature are estimated as 1.23% and 1.98%, respectively. If reliable, this indicates that, despite a higher lattice strain, the Ta–25 sample is more resistant to exfoliation under such conditions. However, it is important to emphasise that this behaviour may well be related to the microstructure, as opposed to the composition of the MAX phase. The Ta–25 sample contained a significantly higher porosity (18.2%) than either of the Ta–38 or Ti_3AlC_2 samples (2.62% and 1.32%, respectively). Voids and pores may act as accumulation sites for implanted hydrogen as it diffuses through the material. However, the free space they enclose will accommodate a limited volume of hydrogen gas before the pressure causes mechanical failure, encouraged by the presence and production of microcracks during irradiation. As the deposition of protons during irradiation occurs in a relatively small layer, with a full–width at half–maximum of 1.38 µm and 0.85 µm for Ta–38 and Ti_3AlC_2, respectively, the build–up of gas will likely be confined to a similarly small region. As an upper estimate, if all the implanted hydrogen is assumed to reside in voids, the pressure exerted by the gas in the implantation layer of Ta–25 will be ~22 times less than that in Ti_3AlC_2 and ~8 times less than that in Ta–38. This is also assuming the diffusion rate of trapped hydrogen in Ta–25 is similar to that in Ta–38 and Ti_3AlC_2. Of course, this is simply speculation given the limited data. To confirm the veracity of this scenario, the diffusion of hydrogen gas through all three materials at various temperatures would need to be assessed as a function of initial sample porosity.

If a similar extrapolation procedure is performed for the *a*–axis, contractions of 0.63% and 0.48% are predicted for Ta–38 and Ti_3AlC_2, respectively. This places the *a*–axis strains experienced by all three materials in a similar region at low temperature. However, the magnitudes are considerably higher than for the lower dose irradiations, indicating a lattice strain onset damage threshold between 0.06 dpa and 0.12 dpa, prior to which very little *a*–axis strain is exhibited.

As with the lower dose irradiations, the higher dose samples for both Ta–based phases experience significantly higher *c*–axis strains than Ti_3AlC_2, with apparently similar recovery rates. Once again, the *a*– and *c*–axis lattice strains of Ti_3AlC_2 at the highest irradiation temperature are significantly reduced, indicating a full recovery. This supports the idea proposed by Ward *et al.* that lattice strain recovery at a given temperature is a function of dose rate, with the total dose perhaps independent of lattice strain [281]. Whilst the Ta–based phases both exhibit significant lattice strain recovery in both the *a*– and *c*–axes, both materials have significant *c*–axis strain even after the high temperature irradiations – 0.36% and 0.19% for Ta–25 and Ta–38, respectively. Both of these final values are lower than the respective *c*–axis strains of the lower dose samples at the same temperature – 0.5% and 0.32%. As the dose rates were kept similar over both irradiations, this discrepancy could be due to a combination of individual temperature differences between irradiations and sample purity variations. For example, the Ta–38 sample temperatures for the lower and higher dose irradiations were 652(5) °C and 672(4) °C, respectively. Equally, the MAX phase purities for the Ta–25 samples varied between 91.9% and 58.6% for the lower and higher dose irradiations, respectively.

The *a*–axis strain exhibited by the Ta–25 sample appears to be entirely different to that of the Ta–38 and Ti_3AlC_2 samples, at the moderate and high temperatures – as with the lower dose sample. The only similarity with the other two materials is a relative decrease in *a*–axis contraction as a function of temperature. As with the lower dose irradiations, the moderate and high temperature irradiation Ta–25 samples display a somewhat unexpected *a*–axis expansion, this time with increased magnitudes of 0.04% and 0.11%, respectively. This contributes to an overall volume expansion far higher than the other two materials at all conditions studied (1.26% compared to 0.46% – the highest expansion observed for Ta–38). DFT calculations in the literature on the effect of various point defects on the lattice parameters of MAX phases have suggested C–Frenkel pairs can lead to a unit cell volume reduction [215], [216]. As such, it is possible that the production of C–Frenkel pairs dominates the damage evolution in Ta–25 at ~350 °C and ~650 °C, as opposed to M_A–A_M antisites.

7.4.3.1 *Secondary Phases*

Whilst Ti_3AlC_2 appears to exhibit reduced lattice strain in both *a*– and *c*–axes compared with the Ta–based phases under similar conditions, the corresponding MX impurity phases show the opposite behaviour. The TiC secondary phase in Ti_3AlC_2 experiences a strain of 1.25% at the moderate irradiation temperature and lower dose, whilst the Ti_3AlC_2 itself experiences only 0.41% and 0.08% strain in the *c*– and *a*–axes, respectively. Surprisingly, the strain observed in TiC in the higher dose sample, at the same temperature, falls to 0.29%, whilst the Ti_3AlC_2 follows the expected trend of increasing lattice strain with increasing dose. The TiC in the high temperature Ti_3AlC_2 sample appears to behave in a similar way to the MAX phase, with a very slight reduction in lattice strain from 0.6–0.54% (0.06%), which is well within the propagated uncertainty of ± 0.16% for those measurements. This is in–line with the hypothesis that a damage/recovery equilibrium has been achieved at 650 °C and ~$4.4(1) \times 10^{-6}$ dpa s^{-1}, at which the lattice strain is possibly independent of the dose. Evidence of this is also seen in all three MAX phase samples irradiated at the highest temperature, in which lattice strain reduces slightly in the higher dose samples, compared with the lower dose samples. This suggests that the annihilation rate of point defects is slightly higher than the dose rate, giving rise to gradual recovery over the longer time period (6.92 hours compared to 4.28 hours). On the other hand, the MX impurities in the Ta–phases at all conditions exhibit relatively minor lattice parameter expansions of < 0.1%. The sole exception to this is the $(Ta,Ti)C_x$ secondary phase in the Ta–25 lower dose, high temperature sample, which exhibits a lattice parameter contraction of 0.13%. Incidentally, this is the only clear example of lattice contraction in an MX impurity across all samples and conditions.

7.4.4 Exfoliation

Ward *et al.* observed a similar exfoliation of Ti_3AlC_2 at the Bragg peak, following 2 MeV proton irradiation to 0.73 dpa and at 350 °C. By extrapolating their data at higher temperatures, where exfoliation did not occur, the authors estimated the *c*–axis strain to be 1.2% at 350 °C. This is almost double the *c*–axis strain of 0.67% at 367(7) °C observed in the current work, indicating a more complex relationship

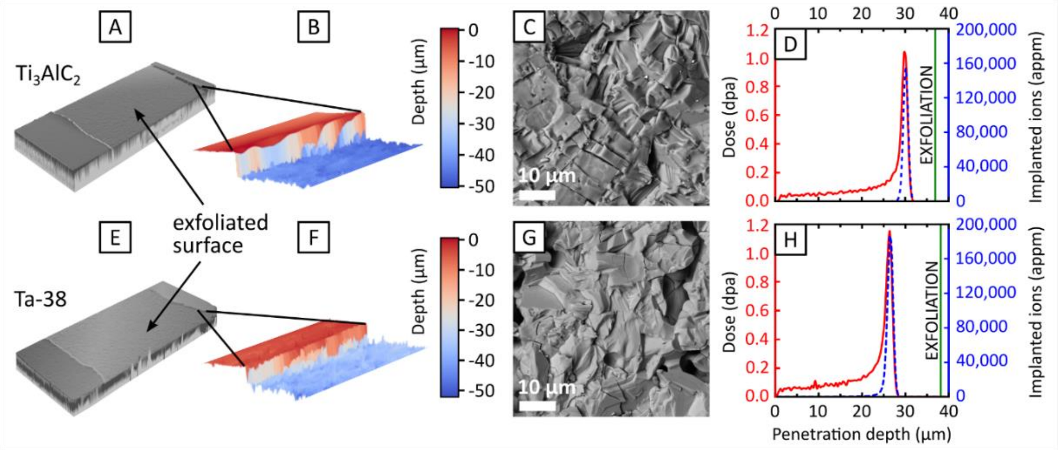

Fig. 7.6 – Surface exfoliation: 3D visualisations of the two samples, Ti_3AlC_2 (A) and Ta–38 (E), which underwent exfoliation during 2 MeV proton irradiation at ~141C. The exfoliated surface on each sample appears as an even depression, indicated by arrows with a respective edge region magnified in B and F, revealing sharp cliff–like interfaces between the undamaged and exfoliated surfaces – evidence of brittle fracture. The relative height in the edge regions (B, F) is represented by a red–blue colour map. A magnified region of the fracture surface is shown in BSE micrographs (C, G) of Ti_3AlC_2 and Ta–38, respectively, showing rough surfaces and a high density of microcracks in both samples. Finally, simulated dose (dpa) and ion implantation (appm) profiles are shown for each sample (D, H), with the depth of the exfoliated surface on each sample indicated by a vertical green line. Values were calculated using SRIM–2013 (for more details, see section 7.3.2). The exfoliation appears to have occurred at a considerably higher depth (> 20%) than the Bragg peak depth for both materials, with the largest difference seen in the Ta–38 sample (~12 um). Additionally, the Ta–38 sample received a higher dose before exfoliation than the Ti_3AlC_2 – 1.15(3) dpa compared to 1.04(2) dpa.

between irradiation temperature and lattice strain than the linear proportionality proposed by Ward *et al*. However, given the considerably lower dose rate used, it is not surprising that no exfoliation was observed at 367(7) °C in this work for any materials. The dose rate used in Ward *et al*.'s irradiations was 1.806×10^{-4} dpa s^{-1}, whilst in this work it was 0.053×10^{-4} dpa s^{-1}, providing support to their notion of dose–rate as a fundamental driver of exfoliation.

The surfaces exposed by exfoliation during irradiation show no evidence of ductile fracture mechanisms characteristic of MAX phases under mechanical strain, such as kink bands, planar deformation or delamination, as seen in Fig. 7.6C and G. An abundance of microcracks is visible on the exfoliated surfaces of both Ti_3AlC_2 and

Ta–38, propagating both around grain boundaries and cleaving through MAX phase grains. This indicates a brittle fracture failure mechanism, in which internal stress leads to the propagation of cracks through the sample. The fracture surfaces are remarkably consistent, with a height variation of < 3 μm in both cases and a surface roughness of 1.3(3) μm for Ti_3AlC_2 and 2.7(4) μm for Ta–38. This indicates a highly localised stress concentration along the plane parallel to the implantation layer from the irradiation. It would follow that the source of the stress is either the Bragg peak itself, which has a full–width half–maximum of 1.6(2) μm and 2.0(2) μm for Ti_3AlC_2 and Ta–38, respectively, or the implantation of hydrogen, which occurs in a 0.9(2) μm and 1.3(2) μm thin layer, respectively – according to SRIM calculations. However, the depths at which exfoliation appears to have occurred in Ti_3AlC_2 and Ta–38 – 37.12(19) μm and 38.1(1.2) μm, respectively, are considerably larger than the respective positions of the Bragg peak – 29.6(2) μm and 26.4(2) μm. The same is true for the peak of the implantation layer, which is expected to be within 0.1 μm of the Bragg peak in both cases. This difference is more pronounced for Ta–38 – at 12 μm, compared with the 7.42 μm for Ti_3AlC_2. The discrepancy may be explained by a combination of factors. The first is the uncertainty in the exfoliation surface position, which can be loosely defined as the resulting surface roughness. For Ta–38, this is 2.7(4) μm, which puts the potential difference between the Bragg peak and the exfoliation layer at < 10 μm. The second factor is the positions of the Bragg and implantation peaks. Whilst SRIM has been shown to accurately predict dislocation production in materials in the literature, the lack of any microstructural parameters, such as grain size or porosity, involved in the calculations open it to inaccuracies where porous materials are concerned. It is possible that, given the mean void size of 5.2(1) μm in Ta–38, the range of incident ions is considerably higher than for a homogeneous, dully dense material. Furthermore, the void size itself may be used to estimate the uncertainty in implantation peak position, which is unlikely to be confined to a region of 1.3(2) μm where voids of 5.2(1) μm size are uniformly distributed, which incidentally appears to be the case for both materials. This leads to the next observation – in

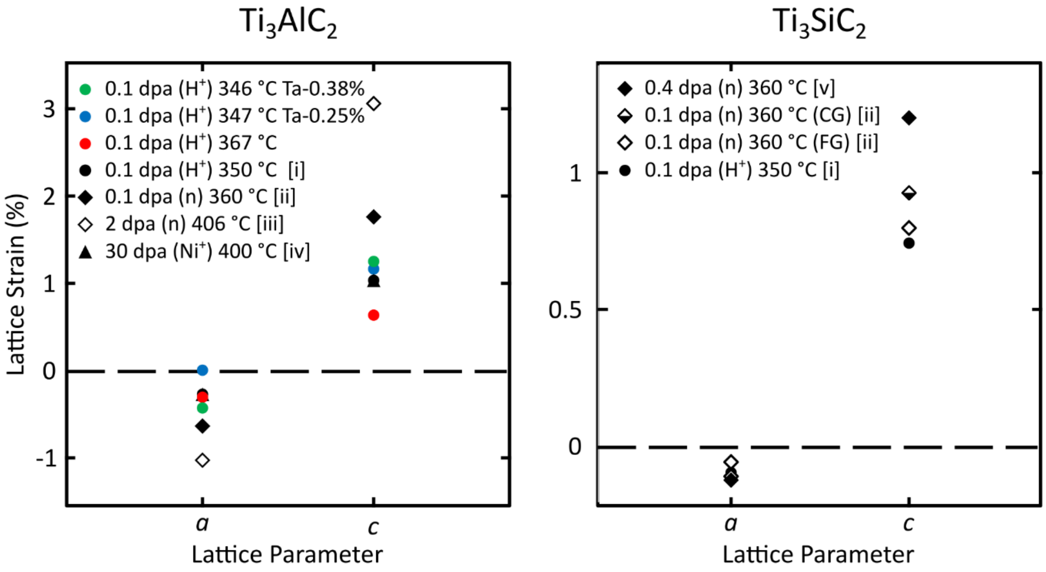

Fig. 7.7 – Comparisons of lattice instabilities in Ti_3SiC_2 and Ti_3AlC_2 reported in the literature, as well as from this work, following various irradiations. The references [i–v] are from [238], [251], [257], [266], [467], respectively.

addition to the variation in exfoliation depth and fracture surface roughness, which appears to be directly related to the initial microstructure of the respective material, the time of exfoliation varies between Ti_3AlC_2 and Ta–38. As such, the dose received by the samples before failure is different: 1.04(2) dpa at the Bragg peak for Ti_3AlC_2, and 1.15(3) dpa for Ta–38, whilst the Ta–25 sample, which did not fail during irradiation, received a dose of 1.48(3) dpa at the Bragg peak. The only evident correlations appear to be between relative sample porosity, average void size and the dose received before exfoliation – as relative porosity increases and average void size decreases, the irradiation dose received before exfoliation increases. Therefore, it would be unsurprising that as the Ta–25 sample has the highest relative porosity of 18.2(5)% and largest mean void size of 7.6(2) µm, it did not fail whilst the other two materials did.

However, to test this hypothesis, a systematic investigation into the effect of relative porosity and void size would be required for each material. The fact that Ta–25 in this work did not exfoliate at ~141 °C after the higher dose does not mean it will survive at either a further irradiation dose or increased dose rate. Nevertheless, this particular sample appears to be more resistant to proton irradiation induced exfoliation than both Ti_3AlC_2 and Ta–38 under the same conditions. The presence of voids may encourage the accumulation of hydrogen as opposed to isotropic diffusion, leading to instantaneous pressure centres.

7.4.5 Comparison of Materials

At the lowest irradiation temperature, a doubling of the dose in Ta–25 appears to lead to an increase in lattice strain of 1.95% (0.08–2.03%) in the *c*–axis, and 0.53% (0.01–0.54%) in the *a*–axis. This could be an indication of a threshold dose for lattice strain before which the microstructure can accommodate point defect production *via* the migration of defects to voids or impurities. It has been reported in the literature that impurities in MAX phases, such as binary carbides and/or Al_2O_3, often contain higher densities of black spot defects – thought to be interstitial clusters, and dislocations following irradiation [280], [399]. Defect migration calculations indicate lower threshold mobility energies of point defects along the MAX phase basal plane than in TiC and Al_2O_3. This could explain the increased damage exhibited by impurities and also the surprisingly low MAX phase lattice strain seen at low temperature in this work. If point defects are mobile in the MAX phase at ~141 °C and migrate faster than those in neighbouring impurity grains, then it follows that the impurities would have a higher defect density. Furthermore, if the defect density in impurities reaches a saturation threshold beyond which the matrix can no longer accommodate further point defects, then the resulting rapid build–up of defect concentration in the MAX phase would lead to the observed increase in lattice strain. A similar mechanism may be at play in grain boundaries and voids, in which a limited defect concentration can be accommodated, beyond which defects preferentially confine to the MAX phase structure. However, further experimental and simulation work on local defect concentrations and migration at the various conditions is required to investigate this.

For Ti_3AlC_2 and Ta–38, no dose effect at the lowest irradiation temperature can be assessed due to the irradiation induced exfoliation of the samples at the higher dose. However, this fact alone provides some insight into the varied response of Ta–Ti based MAX phases to proton irradiation. Whilst the Ta–25 shows an increased resistance to exfoliation at similar conditions, this may well be due to microstructural differences such as increased porosity, rather than fundamental composition. To test this, samples of Ta–25 with lower porosity must be investigated under comparable conditions. The fact that no exfoliation is observed at the lower dose is evidence that a dose effect, in addition to dose–rate, underpins the failure mechanism. Below a threshold dose rate at a given temperature and, therefore, hydrogen mobility, no exfoliation is expected to occur due to insufficient instantaneous internal pressure and a higher defect recombination rate than production. However, an increase in dose will result in higher anisotropic lattice strain, which will in turn cause microcrack formation and propagation. This is supported by the crack density increases seen in all samples following irradiation, which is significantly more pronounced at the higher dose than lower, as can be seen in Fig. 7.4. The resulting microstructural embrittlement, enhanced by the formation of copious point defects within the MAX phase lattice, which inhibit dislocation mobility, may then lead to mechanical failure by exfoliation – even at a dose–rate lower than the initial threshold.

At the moderate irradiation temperature, all three materials display a similar *c*–axis response to dose, although to varying degrees. The lower dose Ti_3AlC_2 and Ta–38 samples exhibit 0.41% and 0.79% *c*–axis expansions, respectively, which increase to 0.67% and 1.29% for the higher dose samples – a linear relationship between dose and *c*–axis strain for both materials. At the same time, the *a*–axis contractions show similar increases between the lower and higher dose samples for both materials – 0.08–0.27% for Ti_3AlC_2 compared with 0.16–0.39% for Ta–38. Ta–25 undergoes a *c*–axis strain of 1.14% and 1.20% after the lower and higher dose irradiations, respectively. This is a much smaller difference compared with Ti_3AlC_2

and Ta–38, which may be partially explained by the marginally lower doses received (0.11 compared to 0.12 dpa). However, slight *a*–axis expansions of 0.02% and 0.04% of the lower and higher dose samples, respectively, are observed in Ta–25. Additionally, no exfoliation was observed at the moderate temperature, indicating either a higher mobility of defects, dampening the lattice strain compared to at the low temperature, or an increased mobility of hydrogen implanted in the sample, which prevents the instantaneous accumulation of internal pressure. Therefore, it appears from this behaviour that Ta–25 is more resistant to irradiation–induced strain at ~350 °C than Ti_3AlC_2 and Ta–38, up to 0.112 dpa. Equally, Ta–25 is more resistant to irradiation–induced exfoliation at ~141C than Ti_3AlC_2 and Ta–38. Whether these differences are microstructure or crystallography–related, or a combination of the two, is unclear at this stage. However, there is evidence that Ta–25 undergoes crystallographic changes which lead to a different *a*–axis response to the other two materials – an expansion rather than the expected contraction under irradiation, characteristic of MAX phases in the literature.

At the highest irradiation temperature, the observed lattice strain response varies depending on the material. Ti_3AlC_2 appears, within error, to exhibit negligible *c*– and *a*–axis lattice strain after at both the lower and higher doses. This indicates a faster rate of defect annihilation is present than point defect production, due to increased defect mobility. This is also evidence that Ti_3AlC_2 is stable under 2 MeV proton irradiation between 635(4) °C and 698(6) °C – the irradiation temperatures achieved during 0.0605(14) and 0.120(3) dpa irradiations, for a dose rate of ~4.4(1) $\times 10^{-6}$ dpa s^{-1}. To test this, however, increased proton irradiation doses would need to be applied at a similar dose rate. On the other hand, the two Ta–based MAX phases both exhibit a reduction in *c*–axis lattice strain between the lower and higher dose levels. The magnitude of these strains are considerably higher for Ta–25 (0.5–0.36%) than for Ta–38 (0.32–0.19%), but neither material shows evidence of a full recovery – as seen with Ti_3AlC_2. For Ta–38, the *a*–axis undergoes a contraction at both the lower and higher dose, of 0.05 and 0.03%, respectively – in–line with the trend observed for the *c*–axis strain. However, Ta–25, which shows negligible *a*–axis strain after the lower dose irradiation, exhibits a significant expansion of 0.11% at the higher dose. This is similar to the response of Ta–25 at the moderate temperature, indicating a damage mechanism transition before ~350 °C which is also at play at ~650 °C.

DFT modelling in the literature, supported by TEM observations, suggests the most energetically favourable point defects in MAX phases are the M–A antisite (M_A:A_M) and, to a lesser extent, carbon Frenkel–pairs (V_C:C_i) [215], [217], [248], [256]. Both anisotropic lattice parameter changes and phase transformations, specifically to a cubic solid solution $(M_{n+1}A)X_n$ phase, in MAX phases under irradiation are thought to be due to the formation of M_A:A_M anti–sites and stacking faults, especially at low temperatures. Additionally, when the C_i–Frenkels reside either side of the A–layer, as in Ti_3AlC_2, modelling reproduces the lattice parameter changes seen by XRD after irradiation, suggesting MAX phases which promote C_i–Frenkel residency within the A–layer are preferable for enhanced stability under irradiation. This proposed mechanism supports previous suggestions of the structural stabilising by antisite defects, leading to amorphisation resistance even after high dose [256].

As such, it is assumed that the magnitude of the lattice strain is proportional to the number of stable point defects remaining after irradiation and the point defects are primarily M_A–A_M antisites. It follows that the materials which have experienced higher strains contain a higher density of M_A–A_M antisites, and, therefore, are more disordered. This would suggest that Ti_3AlC_2 is more resistant to disordering than the Ta–based phases at temperatures of ~350 °C and ~650 °C, whilst the opposite is true at ~141 °C.

7.5 Conclusions

The combination of XRD and HRDIC is a powerful route in the correlation of irradiation induced crystallographic instabilities in MAX phases. The primary benefit of HRDIC is it allows the elucidation of local strain distributions, where XRD provides a bulk average. In this work, bulk crystallographic, local microstructural strain distributions and microcrack formation levels have been assessed for three materials – Ti_3AlC_2 and novel $(Ta_{0.25}Ti_{0.75})_3Al_{0.77}C_2$ and $(Ta_{0.38}Ti_{0.62})_3Al_{0.81}C_2$ phases, following 2 MeV proton irradiation to either ~0.06 or ~0.11 dpa and at temperatures of ~141 °C, ~351 °C and ~658 °C. The XRD and HRDIC data are in good agreement, with the latter revealing a significantly higher granularity in the bulk radiation damage picture for MAX phases.

Across almost all samples and conditions, anisotropic strain is observed in the MAX phases following irradiation, with a *c*–lattice parameter expansion and *a*–lattice parameter contraction, which is significantly reduced at higher irradiation temperature. Whilst the strain is anisotropic across the vast majority of MAX phase grains, it is generally homogeneous inside grains. This is indicative of enhanced defect mobility and, therefore, recombination, which allows for instantaneous damage recovery at the dose rates involved in this work (~4–5 × 10^{-6} dpa s^{-1}). The highest effective shear strain levels are found in MX impurity (e.g., TiC) grain boundary regions and in high angle MAX phase grain boundary hotspots, where perpendicular grains are adjacent to one another. Additionally, MX grains display spatial strain gradients, with maxima at near edge and grain boundary regions and minima towards grain centres. Amorphous regions and Al_2O_3 exhibit the lowest strain levels, at points approaching 0%, even when adjacent to MX or MAX phase grains with > 2% shear strain. According to the HRDIC data, MX grains are almost exclusively in intragranular compression and grain boundary expansion, whilst the XRD data suggests the MX phase experiences expansion across almost all samples.

All three materials display higher crack formation rates with increased dose, with the exception of Ta–25 and Ti_3AlC_2 at the highest irradiation temperature, which display significant decreases in crack formation at the higher dose, possibly indicating a level of crack healing over the longer time period. Microcrack formation is more pronounced at grain boundaries and hotspots but pre–existing microcracks do not necessarily act as strain localisation sites. A higher pre–existing microcrack density does not correlate with a more pronounced increase in microcrack density following irradiation, suggesting the formation of microcracks is purely irradiation based and potentially unrelated to the integrity of the virgin microstructure.

An increase in dose increases both strain concentration in grain boundaries and homogeneity of strain inside grains, in addition to magnitudes across all phases. An increase in temperature reduces strain magnitudes across all phases but increases localisation of strain in grain boundaries and MX grains – indicating that these sites act as defect sinks.

Ta–25 experiences the highest strain levels relative to the other samples, and generally higher microcrack formation levels. Ta–38 displays lower strain levels than Ta–25, but still higher than Ti_3AlC_2, although it has generally the lowest microcrack formation levels across all conditions.

At temperatures below ~350 °C and at ~0.06 dpa, Ta–25 and Ta–38 are more resistant to proton irradiation induced disorder than Ti_3AlC_2. At temperatures above ~350 °C, Ti_3AlC_2 is the most resistant to lattice instabilities under proton irradiation. Between ~350 °C and ~650–700 °C, the lattice strain recovery rates appear to be similar for all three materials, reflected in both *a*–axis and *c*–axis strain reductions. The threshold recovery temperatures for the dose rates used are assumed to be between ~350 °C and ~650–700 °C for all materials, with a higher temperature threshold for Ta–25 and Ta–38, which still experience significant lattice strains at ~650 °C. Finally, despite significantly increased lattice instabilities under irradiation, Ta–25 appears to have a higher resistance to proton irradiation–induced surface exfoliation under the conditions studied.

Based on these results, all three materials appear to be promising candidates in high temperature, high irradiation environments, so long as the operational temperatures are kept above ~600 °C. At temperatures ~350 °C, Ti_3AlC_2 is more suitable than the Ta–based phases, whilst at ~141 °C, it is expected that both $(Ta_{0.25}Ti_{0.75})_3Al_{0.77}C_2$ and $(Ta_{0.38}Ti_{0.62})_3Al_{0.81}C_2$ perform better than Ti_3AlC_2, at least at irradiation doses.

Regardless, the doses in this study are objectively low in terms of nuclear materials applications and are therefore only relevant in assessing damage onset mechanisms, rather than predicting lifecycle performance. As such and especially regarding $(Ta_{0.25}Ti_{0.75})_3Al_{0.77}C_2$ and $(Ta_{0.38}Ti_{0.62})_3Al_{0.81}C_2$, for which no additional irradiation tolerance data currently exists, further work is required to assess the response of these phases to much higher dose levels, whilst tracking the local microstructural and crystallographic evolution.

7.6 Conflicts of Interest

There are no conflicts of interest to declare.

7.7 Acknowledgements

This work was supported by funding from the Engineering and Physical Sciences Research Council Fusion CDT programme and grants [EP/L01663X/1, EP/M010619/1, EP/S021531/1, EP/P009050/1]; Henry Royce Institute for Advanced Materials [EP/R00661X/1, EP/S019367/1, EP/P025021/1, EP/P025498/1]; and the Department of Materials XRD Facility.

7.8 Supplementary Information

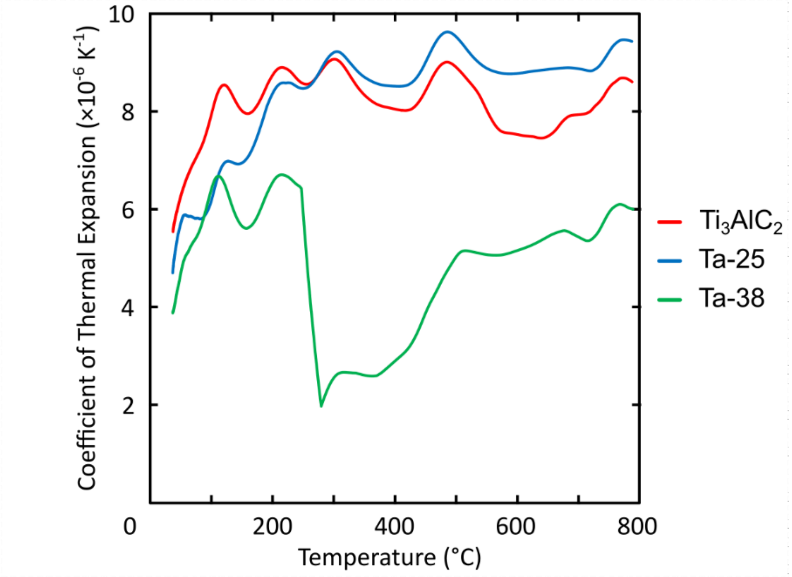

Fig. 7.8 – Thermal expansion of MAX phases: The coefficient of thermal expansion (CTE) for Ti_3AlC_2 (red), Ta–25 (blue), and Ta–38 (green) as a function of temperature, from room temperature to 800 °C. Expansion of a material represents a decrease in density, which leads to a reduced dose during irradiation. The change has increasing significance as the temperature of irradiation is increased. The values shown here are used to correct the material densities used in SRIM calculations, to provide a more accurate estimate of received dose.

Table 7.5 – Irradiation parameters for all samples: A selection of the key irradiation–related parameters, including irradiation temperature, dose, lattice parameters (before and after irradiation), and microcrack densities (before and after irradiation), for each sample.

Material	T (°C)	Dose (dpa)	Pristine	Irradiated	Change (%)	Pristine	Irradiated	Change (%)	n_0 ($\times10^{-2}$ μm^{-2})	n_i ($\times10^{-2}$ μm^{-2})	Δn (%)
Ti_3AlC_2	141(8)	0.0600(14)	18.552(5)	18.635(4)	0.45(3)	3.0713(3)	3.0688(2)	–0.081(12)	1.93	0.25	12.84
Ta–25	141(8)	0.0558(13)	18.572(2)	18.587(16)	0.081(14)	3.0924(2)	3.09219(18)	–0.007(9)	0.86	0.15	17.13
Ta–38	141(8)	0.0596(14)	18.6027(13)	18.6138(8)	0.060(8)	3.09604(16)	3.09614(7)	0.003(6)	1.76	0.12	6.93
Ti_3AlC_2	141(8)	0.0736(17)*	–	–	–	–	–	–	–	–	–
Ta–25	141(8)	0.112(3)	18.5685(19)	18.946(2)	2.033(15)	3.09315(19)	3.0765(2)	–0.538(9)	1.24	0.47	37.72
Ta–38	141(8)	0.096(2)*	–	–	–	–	–	–	–	–	–
Ti_3AlC_2	349(7)	0.0603(14)	18.553(7)	18.629(3)	0.41(4)	3.0719(7)	3.0693(2)	–0.08(2)	3.55	1.23	34.60
Ta–25	344(8)	0.0561(13)	18.563(2)	18.775(3)	1.142(19)	3.0935(3)	3.094(2)	0.016(12)	2.39	0.73	30.59
Ta–38	354(8)	0.0598(14)	18.5982(16)	18.7455(16)	0.792(12)	3.09555(17)	3.09045(16)	–0.165(8)	4.56	0.50	10.95
Ti_3AlC_2	367(7)	0.121(3)	18.554(4)	18.678(4)	0.67(3)	3.0721(2)	3.0638(2)	–0.270(9)	2.26	1.30	57.55
Ta–25	347(8)	0.112(3)	18.559(3)	18.781(3)	1.20(2)	3.093(3)	3.0942(3)	0.038(14)	2.17	1.05	48.20
Ta–38	346(8)	0.120(3)	18.590(4)	18.829(3)	1.29(3)	3.0945(3)	3.0823(3)	–0.394(14)	3.70	1.06	28.65
Ti_3AlC_2	698(6)	0.0605(14)	18.556(3)	18.551(4)	–0.03(3)	3.0732(2)	3.0734(2)	0.007(9)	3.72	1.84	49.52
Ta–25	646(4)	0.0562(13)	18.521(4)	18.613(3)	0.50(3)	3.0899(5)	3.0904(3)	0.016(19)	2.25	1.49	66.23
Ta–38	652(5)	0.0600(14)	18.581(3)	18.640(3)	0.32(2)	3.0951(3)	3.0936(3)	–0.048(14)	3.83	0.56	14.53
Ti_3AlC_2	635(4)	0.120(3)	18.555(4)	18.555(3)	0.00(3)	3.0729(2)	3.0725(2)	–0.013(9)	7.00	1.70	24.34
Ta–25	648(3)	0.112(3)	18.525(5)	18.5921(18)	0.36(3)	3.0877(7)	3.091(2)	0.11(2)	2.90	1.27	43.75
Ta–38	672(4)	0.119(3)	18.598(2)	18.6341(12)	0.194(13)	3.0954(2)	3.0946(13)	–0.026(8)	11.73	16.71	42.40

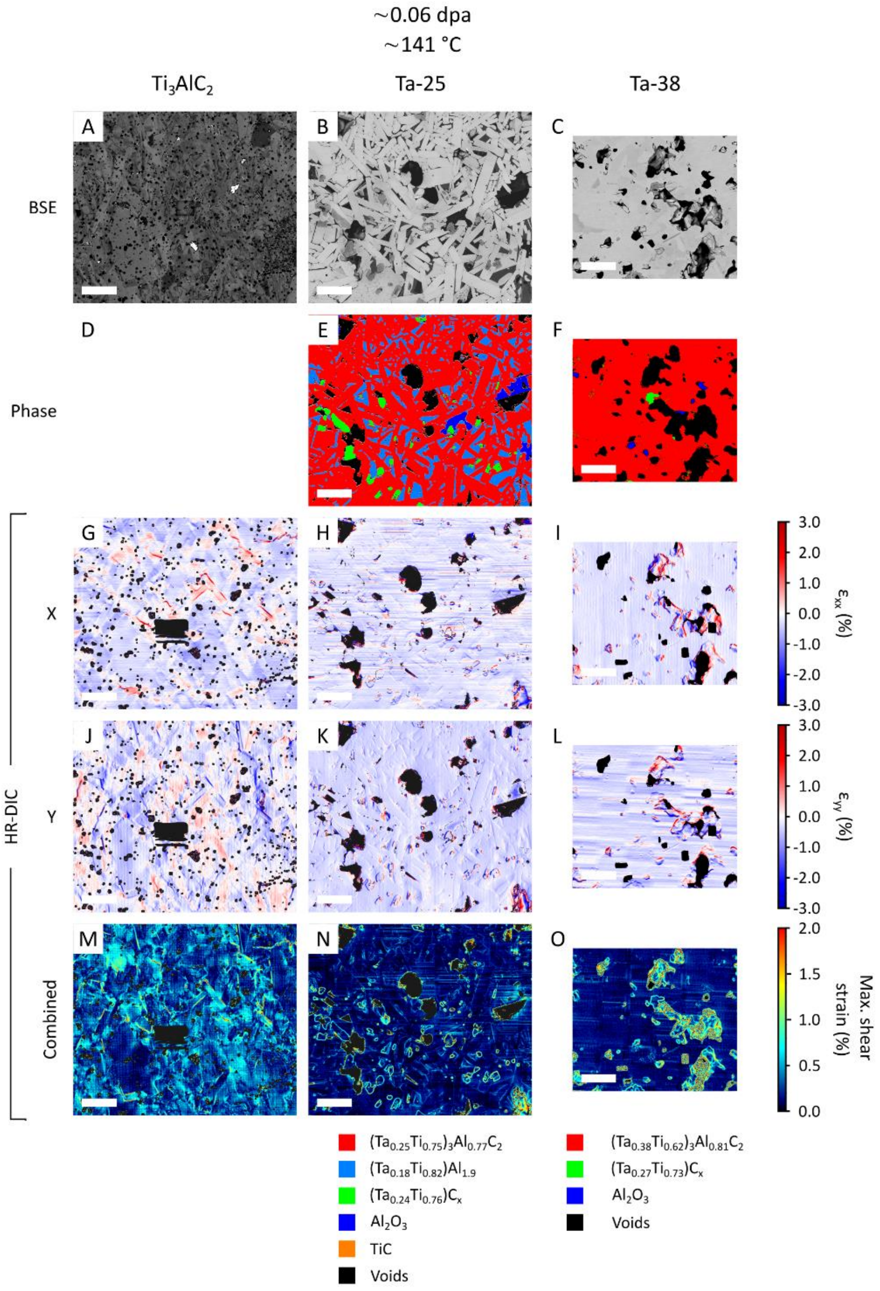

Fig. 7.9 – Irradiation–induced microstrain at low temperature after the lower dose irradiation: (A–C) BSE micrographs of the central regions of the samples. (D–F) Corresponding phase maps for (A–C) deduced from SEM–EDS. (G–O) HRDIC strain mapping for regions (A–C) showing an ε_{xx} (horizontal) strain map (G–I), an ε_{yy} (vertical) strain map (J–L), and an effective shear strain, $\frac{1}{2}(\varepsilon_{xx} + \varepsilon_{yy})^2$, map (M–O). Strain magnitudes, in %, are displayed as a colour map and range from –3.0–3.0% for ε_{xx} and ε_{yy}, and 0.0–2.0% for the effective shear strain. Voids are overlaid as black regions on D–O. All scale bars are 30 μm.

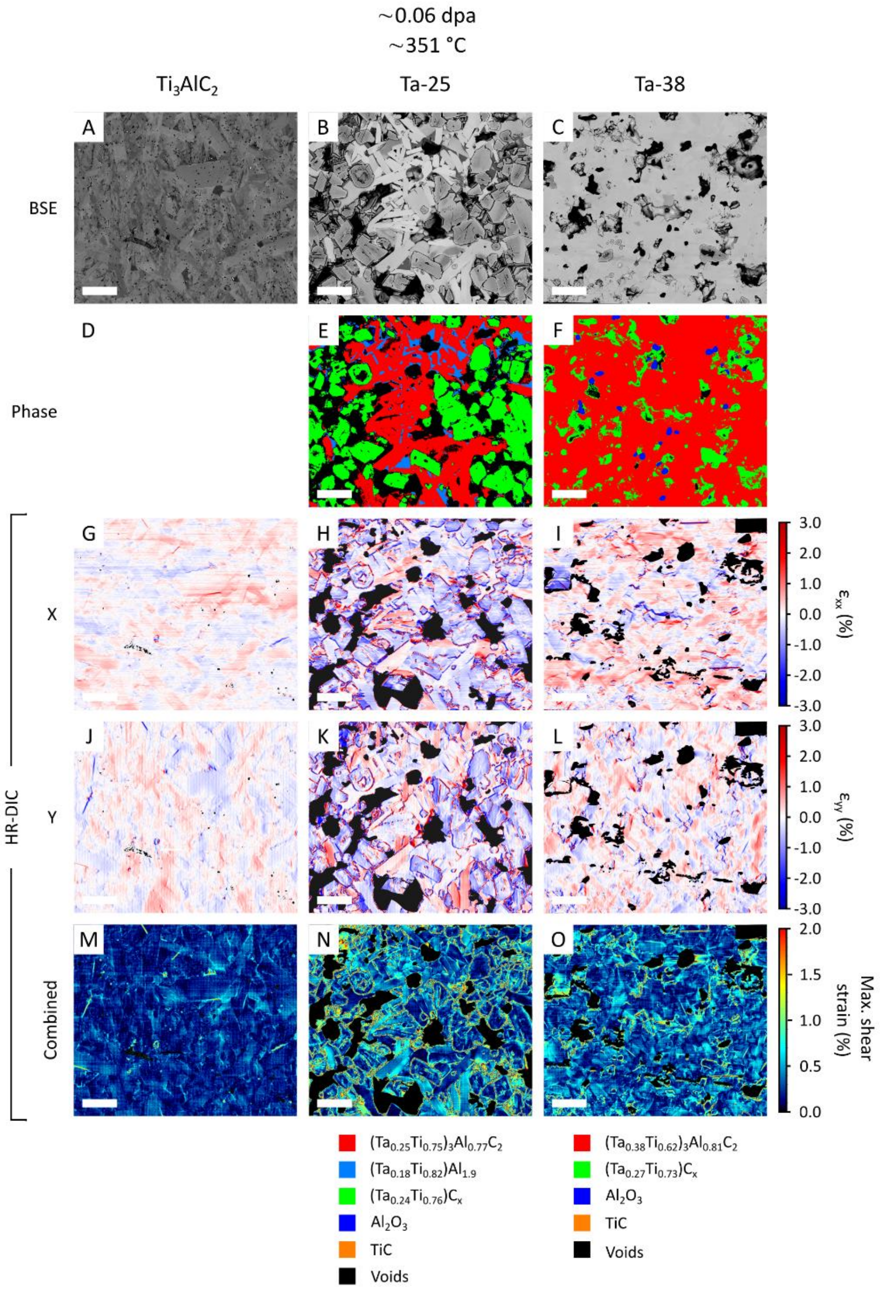

Fig. 7.10 – Irradiation–induced microstrain at moderate temperature after the lower dose irradiation: (A–C) BSE micrographs of the central regions of the samples. (D–F) Corresponding phase maps for (A–C) deduced from SEM–EDS. (G–O) HRDIC strain mapping for regions (A–C) showing an ε_{xx} (horizontal) strain map (G–I), an ε_{yy} (vertical) strain map (J–L), and an effective shear strain, $\frac{1}{2}(\varepsilon_{xx}+\varepsilon_{yy})^2$, map (M–O). Strain magnitudes, in %, are displayed as a colour map and range from –3.0–3.0% for ε_{xx} and ε_{yy}, and 0.0–2.0% for the effective shear strain. Voids are overlaid as black regions on D–O. All scale bars are 30 µm.

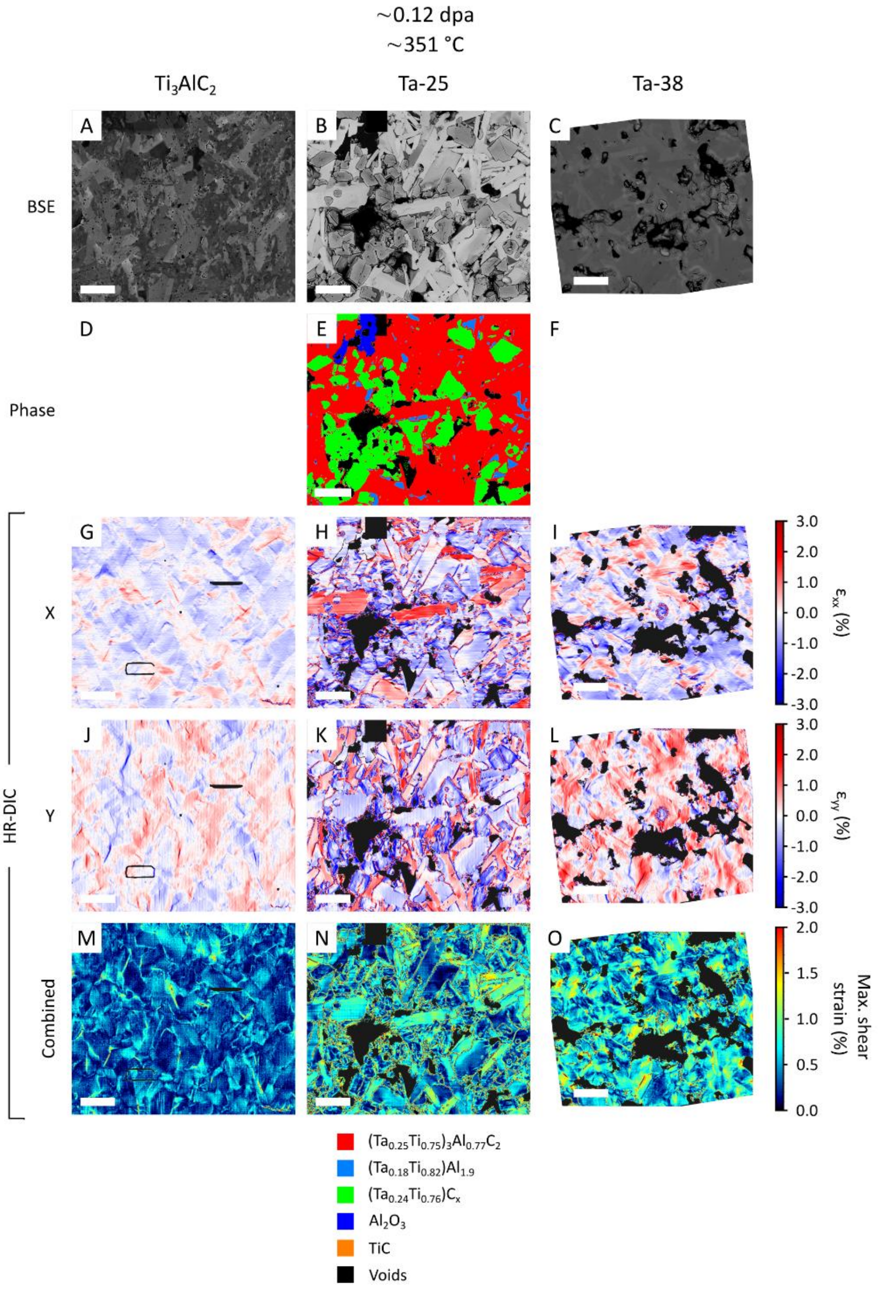

Fig. 7.11 – Irradiation–induced microstrain at moderate temperature after the higher dose irradiation: (A–C) BSE micrographs of the central regions of the samples. (D–F) Corresponding phase maps for (A–C) deduced from SEM–EDS. (G–O) HRDIC strain mapping for regions (A–C) showing an ε_{xx} (horizontal) strain map (G–I), an ε_{yy} (vertical) strain map (J–L), and an effective shear strain, $\frac{1}{2}(\varepsilon_{xx}+\varepsilon_{yy})^2$, map (M–O). Strain magnitudes, in %, are displayed as a colour map and range from –3.0–3.0% for ε_{xx} and ε_{yy}, and 0.0–2.0% for the effective shear strain. Voids are overlaid as black regions on D–O. All scale bars are 30 µm.

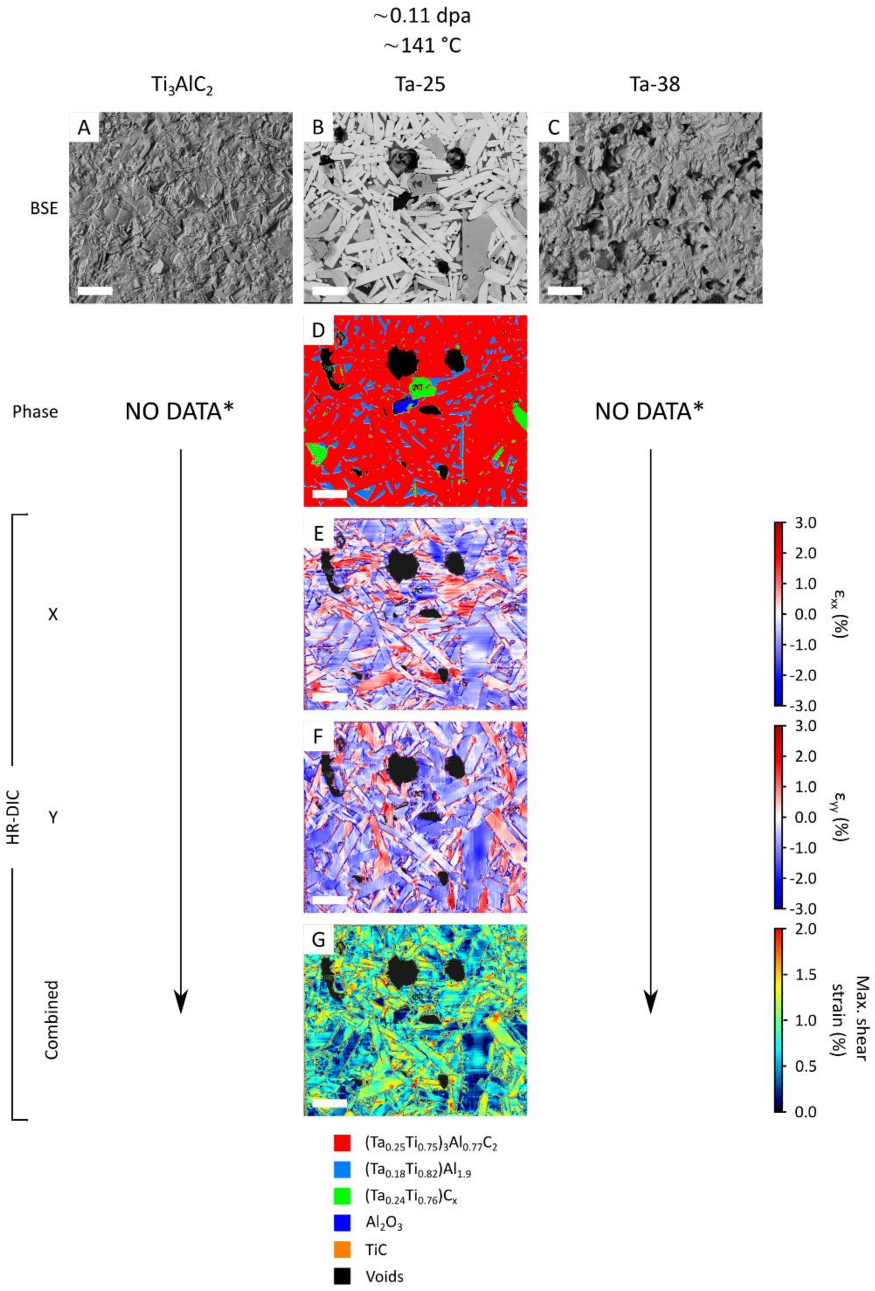

Fig. 7.12 – Irradiation–induced microstrain at low temperature after the higher dose irradiation: (A–C) BSE micrographs of the central regions of the samples. (D–F) Corresponding phase maps for (A–C) deduced from SEM–EDS. (G–O) HRDIC strain mapping for regions (A–C) showing an ε_{xx} (horizontal) strain map (G–I), an ε_{yy} (vertical) strain map (J–L), and an effective shear strain, $\frac{1}{2}(\varepsilon_{xx} + \varepsilon_{yy})^2$, map (M–O). Strain magnitudes, in %, are displayed as a colour map and range from –3.0–3.0% for ε_{xx} and ε_{yy}, and 0.0–2.0% for the effective shear strain. Voids are overlaid as black regions on D–O. All scale bars are 30 µm. For the Ti_3AlC_2 and Ta–38 samples (A and C), the micrographs are from the central region of the exfoliated fracture surface. Due to the loss of the gold patterned surface, no HRDIC data could be recorded for the samples that exfoliated.

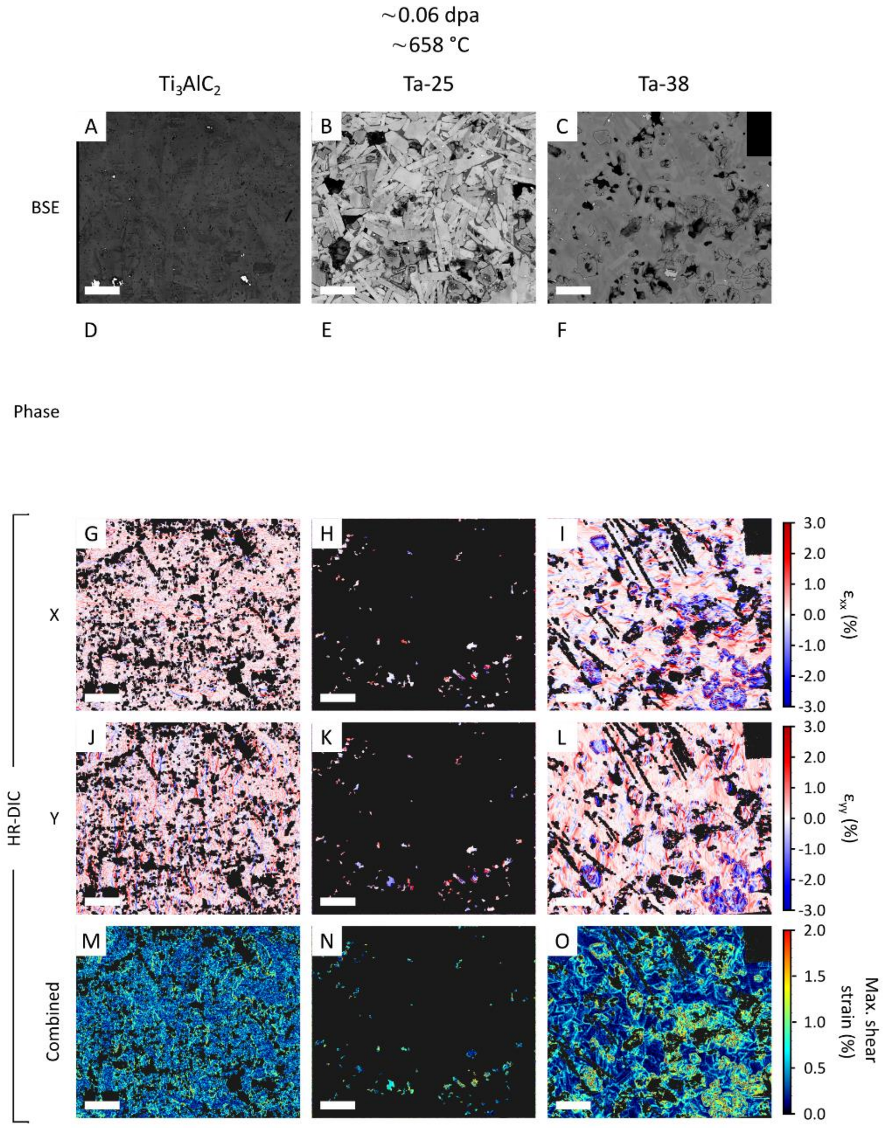

Fig. 7.13 – Irradiation–induced microstrain at high temperature after the lower dose irradiation: (A–C) BSE micrographs of the central regions of the samples. (D–F) Corresponding phase maps for (A–C) deduced from SEM–EDS. (G–O) HRDIC strain mapping for regions (A–C) showing an ε_{xx} (horizontal) strain map (G–I), an ε_{yy} (vertical) strain map (J–L), and an effective shear strain, $\frac{1}{2}(\varepsilon_{xx}+\varepsilon_{yy})^2$, map (M–O). Strain magnitudes, in %, are displayed as a colour map and range from –3.0–3.0% for ε_{xx} and ε_{yy}, and 0.0–2.0% for the effective shear strain. Voids are overlaid as black regions on D–O. All scale bars are 30 μm.

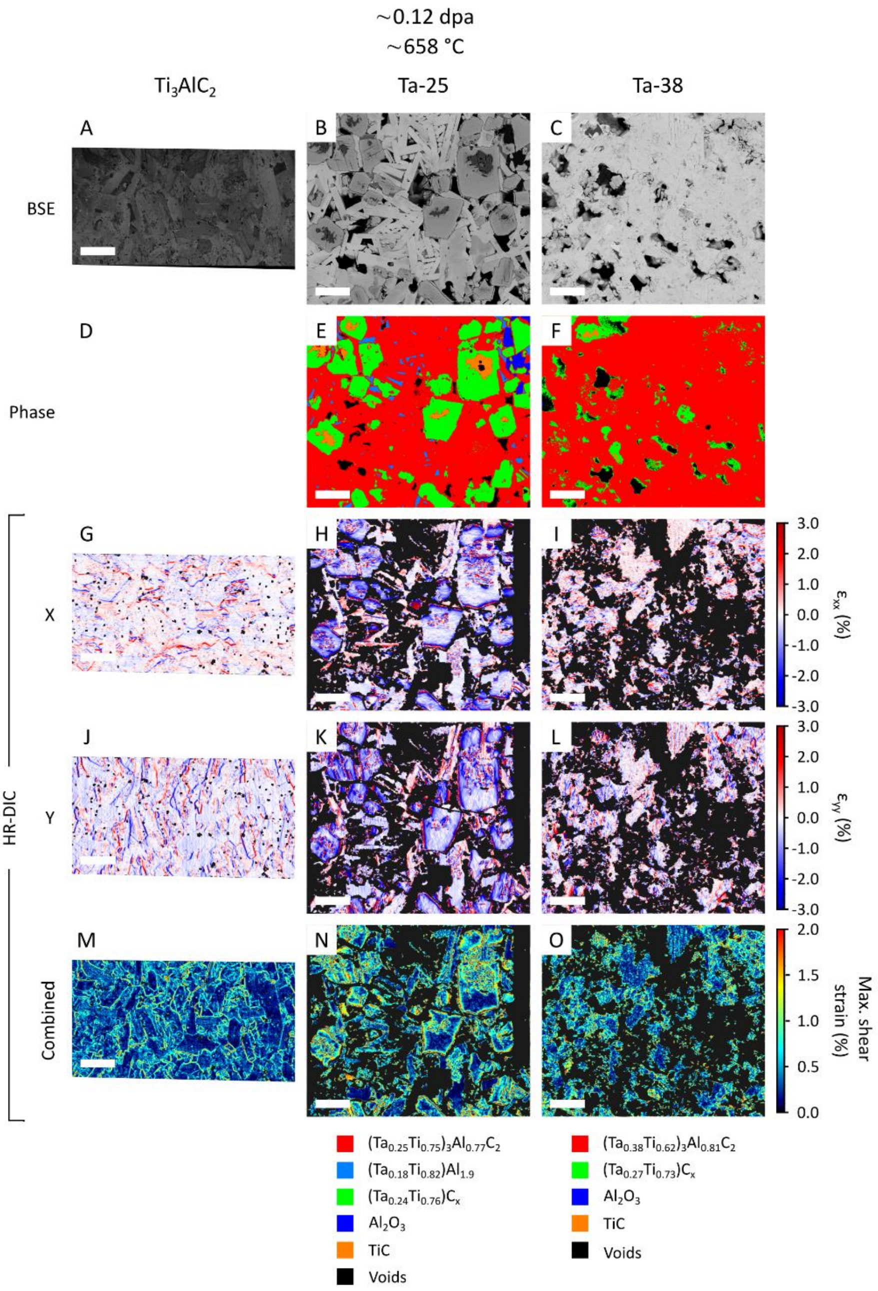

Fig. 7.14 – Irradiation–induced microstrain at high temperature after the higher dose irradiation: (A–C) BSE micrographs of the central regions of the samples. (D–F) Corresponding phase maps for (A–C) deduced from SEM–EDS. (G–O) HRDIC strain mapping for regions (A–C) showing an ε_{xx} (horizontal) strain map (G–I), an ε_{yy} (vertical) strain map (J–L), and an effective shear strain, $\frac{1}{2}(\varepsilon_{xx} + \varepsilon_{yy})^2$, map (M–O). Strain magnitudes, in %, are displayed as a colour map and range from –3.0–3.0% for ε_{xx} and ε_{yy}, and 0.0–2.0% for the effective shear strain. Voids are overlaid as black regions on D–O. All scale bars are 30 μm.

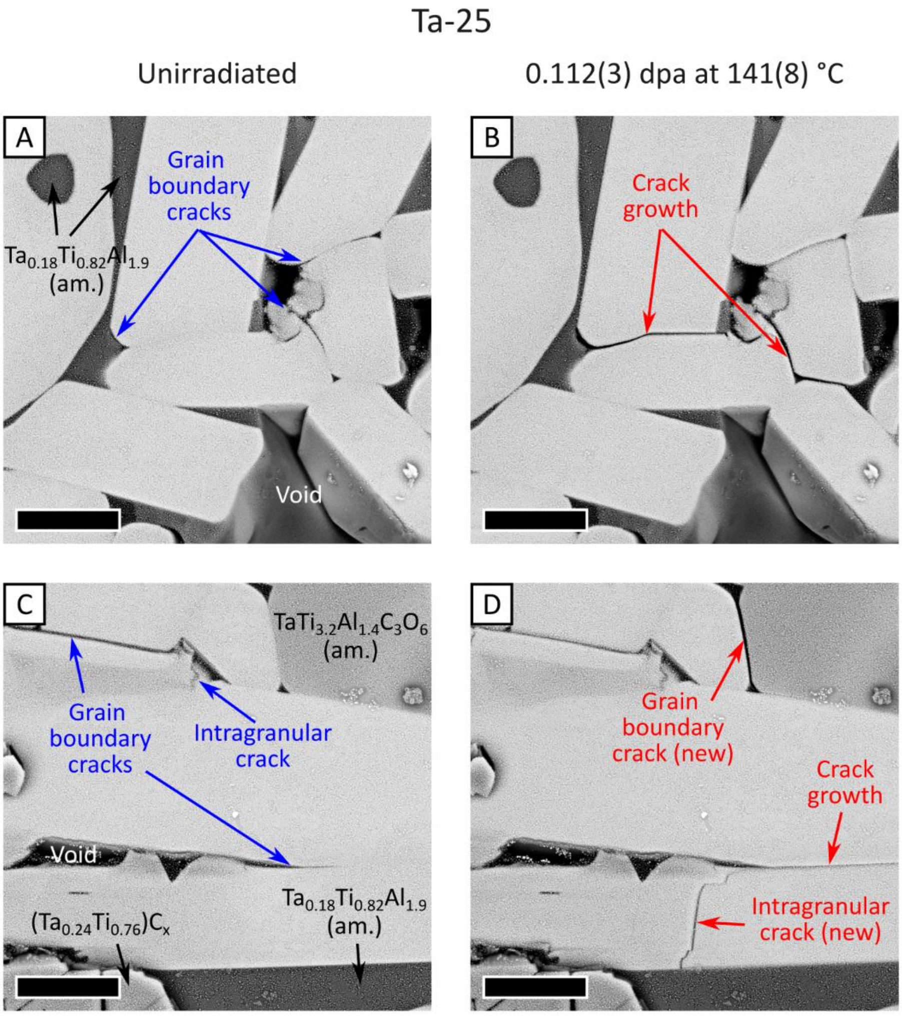

Fig. 7.15 – Formation and propagation of cracks in Ta–25: BSE–SEM micrographs of two separate regions on the surface of the higher dose, low temperature Ta–25 sample, both before (A, C) and after (B, D) irradiation to 0.112(3) dpa, displaying examples of the types of microcracks reported in Fig. 7.4. (A) Pre–existing microcracks at MAX phase grain boundaries are identified, which undergo irradiation–induced growth (B). (C) Pre–existing grain boundary cracks and a small intragranular crack are identified. (D) Following irradiation, the formation of new and independent microcracks is observed, both at grain boundaries and intragrain, in addition to the growth of a pre–existing grain boundary crack. In all samples the majority of microcracks, both pre–existing and irradiation–induced, are observed at grain boundaries. The few irradiation–induced intragranular cracks are generally located in MAX phase grains, with minimal crack formation observed in secondary phases. It is important to note that the data on pre–existing cracks was obtained from the samples following gold pattern remodelling for HRDIC (at up to 600 °C – see section 7.3.4 for details). Therefore, the effect of elevated temperature and subsequent cooling on the formation or evolution of microcracks has not been assessed. However, as the synthesis temperatures for all samples are > 1300 °C, it is assumed that this effect is negligible.

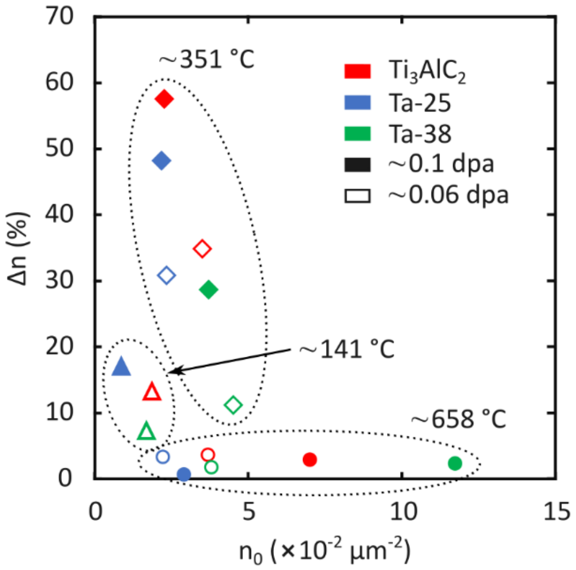

Fig. 7.16 – The correlation between pre–existing crack density (n_0) and subsequent change in crack density (Δn): A plot showing n_0 (*x*–axis) as a function of Δn (*y*–axis) for each irradiated sample, with the three materials Ti_3AlC_2, Ta–25 and Ta–38 colour coded in red, blue and green, respectively; the two target irradiation conditions 'lower dose' (~0.06 dpa) and 'higher dose' (~0.1 dpa) as empty and solid symbols, respectively; and the three irradiation temperatures ~141, ~351, and ~650 °C shown as triangles, diamonds and circles, respectively. The groups of points with a common irradiation temperature have been circled and labelled, highlighting the correlation dependence on irradiation temperature. For the low temperature irradiations, Δn appears to show a weak inverse proportionality with n_0, although the data is incomplete due to sample exfoliations. For the moderate temperature irradiations, Δn generally follows a steep decrease with increasing n_0, indicating an increased resistance to microcrack formation for samples with high levels of pre–existing cracks. This could be due to the pre–existing cracks acting as strain accommodation sites. As such, the level of irradiation–induced microcrack formation for more pristine samples is perhaps overestimated. For the high temperature irradiations, Δn is apparently independent of n_0, even at the unusually high pre–existing crack density found in the higher dose Ta–38 sample (11.73×10^{-2} µm^{-2}). At high temperatures, dislocation mobility and, therefore, plastic deformation is enhanced, suppressing crack formation. This would suggest that at ~650 °C microcrack formation is solely irradiation–induced, and not dependent on pre–existing microcrack density.

Chapter 8: Summary

The primary aim of this thesis is the demonstration of a rapid development workflow for novel MAX phases as candidates for high–heat flux and radiation–resistance applications in fusion devices. This has been established *via* a combination of high–throughput computational predictions, high–temperature powder synthesis, advanced X–ray, electron microscopy characterisations and digital correlation techniques, and high–temperature proton irradiations.

As such, the predicted thermodynamic stabilities, relative to elemental constituents, of 180 potential quaternary and quinary MAX phases have been calculated. The results of these calculations guided the synthesis and subsequent characterisation of novel $(Ta,Ti)_3AlC_2$ MAX phases and their derivative MXenes. Finally, two of these phases – $(Ta_{0.25}Ti_{0.75})_3Al_{0.77}C_2$ and $(Ta_{0.38}Ti_{0.62})_3Al_{0.81}C_2$, along with a reference Ti_3AlC_2 MAX phase, have been proton irradiated at temperatures up to ~650 °C to assess their tolerance to radiation damage.

8.1 Conclusions

8.1.1 Stability Predictions of Novel MAX Phases

Guided by an elemental down–selection, the formation enthalpies, relative to elemental constituents, have been calculated for 180 MAX phases in the $(M^{I}_{2/3},M^{II}_{1/3})_{n+1}(A^{I}_{x}A^{II}_{1-x})C_n$ system (M = Ti, V, Cr, Y, Ta, W; A = Al or Si; x = 0.5 or 1; and n = 2 or 3). The following can be concluded:

1. Phases with M^{I},M^{II} = Ti,Ta; Ti,V; and Ti,Y have the lowest formation enthalpies and are, therefore, the most likely to be thermodynamically stable.

2. With the exception of those containing W, compositions with a Si–based A–layer appear to be more stable than the Al–based phases.
3. Phases containing both W and Cr generally show the lowest propensity to form, with positive formation enthalpies for $Cr_2W(Al_{0.5}Si_{0.5})C_2$ (+79.75), Cr_2WAlC_2 (+83.77), Cr_2WSiC_2 (+157.72), W_2CrAlC_2 (+316.30), $W_2Cr(Al_{0.5}Si_{0.5})C_2$ (+460.37) and W_2CrSiC_2 (+965.00), with values in meV.
4. The 211 phases are expected to be more stable than their 312 counterparts.
5. The addition of Si to the Al–layer of the phases considered appears to increase the relative thermodynamic stability, indicating it may be possible to partially substitute Al for Si in stable MAX phases.
6. Whilst the full equilibrium simplex of competing phases for each composition has not been considered, atomic formation enthalpy calculations can provide guidance for synthesis trials of novel quaternary MAX phases, at a reduced computational cost.

8.1.2 Synthesis of Novel MAX Phases

New quaternary $(Ta_xTi_{1-x})_3AlC_2$ MAX phases, with x = 0.05, 0.1, 0.2, 0.33 and 0.5 have been synthesised and characterised. Incidentally:

1. Bulk and relatively phase pure $(Ta_{1-x}Ti_x)_3AlC_2$ MAX phases can be synthesised *via* high temperature, pressure–less sintering from a combination of elemental and binary carbide powders – TaC, TiC and Al.
2. An M–layer solid–solution is formed under these conditions, with a higher Ta concentration in the central M^{II} layers for all compositions.
3. The maximum Ta concentration in the Ti 312 M–layer is assumed to be between 38 and 60 at.%, based on the formation of several competing phases at higher initial Ta concentrations, and thus a significant reduction in phase purity.

4. The synthesis of solid solution Ta–Ti–based MXenes is possible *via* the chemical etching of $(Ta_{1-x}Ti_x)_3AlC_2$ MAX phases, with the synthesis pathway likely to be similar to the unalloyed $Ti_3C_2T_x$ MXene.
5. It is proposed that this approach can be used to synthesise a range of alloyed $(Ta,Ti)_3C_2T_x$ MXenes, with compositions that can be optimised for a wide range of potential applications.

8.1.3 Radiation Tolerance of Novel MAX Phases

Following irradiation by 2 MeV protons, to doses up to 0.12 dpa at 60% of the Bragg peak depth and temperatures up to ~650 °C, bulk crystallographic, local microstructural strain distributions, and microcrack formation have been assessed for three materials – Ti_3AlC_2, $(Ta_{0.25}Ti_{0.75})_3Al_{0.77}C_2$ (Ta–25), and $(Ta_{0.38}Ti_{0.62})_3Al_{0.81}C_2$ (Ta–38). The following was observed across all materials:

1. Whilst MAX phase lattice strains are anisotropic (*c*–axis expansion and *a*–axis contraction), microstrain is generally homogeneous across MAX phase grains. This is indicative of enhanced defect mobility and, therefore, recombination.
2. MX secondary phases display the highest local microstrain, with high concentrations in grain boundary regions and a gradient of increasing strain towards grain–edges from the centre.
3. Strain hotspots and subsequent cracking are evident at high angle MAX phase grain boundaries, suggesting textured compositions may be more suitable for irradiating environments.
4. Amorphous regions and Al_2O_3 impurities exhibit the lowest strain, at points approaching 0%, even when adjacent to MX or MAX phase grains with > 2% shear strain.
5. According to the HR–DIC data, MX grains are almost exclusively in intragranular compression and grain boundary expansion, whilst the XRD

data suggests the MX phase experiences expansion across almost all samples.

6. An increase in dose increases both strain concentration in grain boundaries and homogeneity of strain inside grains, in addition to magnitudes across all phases. An increase in temperature reduces strain magnitudes across all phases but increases localisation of strain in grain boundaries and MX grains – indicating that these sites act as defect sinks.
7. Microcrack formation is more pronounced at grain boundaries and hotspots but pre–existing microcracks do not necessarily act as strain localisation sites.

However, when comparing the response of the different materials, it was found that:

1. Ta–25 experiences the highest irradiation induced strain relative to the other samples, and generally a higher microcrack formation levels.
2. Ta–38 displays lower strain than Ta–25, but still higher than Ti_3AlC_2, although it has generally the lowest microcrack formation levels across all conditions. As such, it is perhaps more suited to structural applications in fusion than Ti_3AlC_2 or Ta–38.
3. The threshold recovery temperatures for the dose rates used are assumed to be between ~350 °C and ~650–700 °C for all materials, with a higher temperature threshold for Ta–25 and Ta–38, which still experience significant lattice strains at ~650 °C.
4. At temperatures below ~350 °C and at ~0.06 dpa, Ta–25 and Ta–38 are more resistant to proton irradiation induced disorder than Ti_3AlC_2. As such, Ti_3AlC_2 is potentially more suited to PFCs than the Ta–based phases.
5. The mechanism behind proton irradiation induced exfoliation is likely dependent on total dose, as well as dose rate and irradiation temperature.
6. Finally, despite significantly increased lattice instabilities under irradiation, Ta–25 appears to have a higher resistance to proton irradiation–induced surface exfoliation than Ta–38 and Ti_3AlC_2.

Based on these results, all three materials appear to be promising candidates in high temperature, high irradiation environments, so long as the operational temperatures are kept above ~600 °C. At ~350 °C, Ti_3AlC_2 is more suitable than the Ta–based phases, whilst at ~141 °C, it is expected that both $(Ta_{0.25}Ti_{0.75})_3Al_{0.77}C_2$ and $(Ta_{0.38}Ti_{0.62})_3Al_{0.81}C_2$ perform better than Ti_3AlC_2.

8.2 Further Work

Synthesis trials in this thesis focussed solely on the $(Ta,Ti)_3AlC_2$ system. However, other M^I/M^{II} pairs studied in Manuscript 1 produced formation enthalpies almost as low as the Ta–Ti phases, such as Ti–V and Ti–Y. Therefore, it would be sensible to investigate the synthesis of these phases, in addition to MAX phases with different n values (1, 3, 4, etc.), where possible.

The irradiation doses in this study are objectively low, in terms of nuclear materials applications, and are therefore only relevant in assessing damage onset mechanisms, rather than predicting operational or lifecycle performance. As such and especially regarding $(Ta_{0.25}Ti_{0.75})_3Al_{0.77}C_2$ and $(Ta_{0.38}Ti_{0.62})_3Al_{0.81}C_2$, for which no additional irradiation tolerance data currently exists, further work is required to assess the response of these phases to higher dose levels, whilst tracking the local microstructural and crystallographic evolution. A systematic ion irradiation campaign of $(Ta,Ti)_3AlC_2$ phases with similar phase purities and porosity, at a range of temperatures and to high doses (> 5 dpa), is required to fully assess the response to radiation damage.

That said, the presence of Al in the materials assessed is a problem for potential application to fusion environments, due to material activation. Therefore, future work must be performed to investigate the potential substitution of Al with Si in the A–layer, as well as assessing the effect of this substitution on the response to radiation damage. Incidentally, other low activation A–layer elements, such as Ga, may be produce phases with better responses to radiation damage than the Al–based phases studied here. As such, trials should focus on comparing the response of phases with alternate A–layer elements to irradiation.

These results, supported by recent observations in the literature, indicate that proton irradiation, especially at high dose rates, is not practical for high dose irradiation studies of MAX phases, due to the risk of surface blistering and exfoliation. In order to prevent exfoliation, the dose rate must be minimised, which results in longer irradiation times to reach a desired dose. As such, heavier ion irradiations, at the cost of a steeper damage profile and lower penetration, may be more suitable for simulating reactor–relevant neutron damage.

It is important to mention at this point that the work in this thesis represents only the first stages of a fusion–materials development workflow. Mechanical testing, thermal property analysis, microstructural optimisation, etc., are required to continue the development pathway. Nonetheless, the results presented here are a small but important step towards the development of suitable materials for the extreme environments encountered in fusion devices.

References

[1] Bloomberg New Energy Finance and B. N. E. Finance, *BNEF*, p. 6, Jun. 2017.

[2] BP, *BP Energy Outlook 2030, Stat. Rev. London Br. Pet.*, p. 81, 2020, [Online]. Available: https://www.bp.com/content/dam/bp/business–sites/en/global/corporate/pdfs/energy–economics/energy–outlook/bp–energy–outlook–2020.pdf

[3] J. Zarate, 2015. doi: http://dx.doi.org/10.1787/weo–2015–en.

[4] V. Masson–Delmotte, P. Zhai, A. Priani, S. L. Connors, C. Pean, and S. Berger, *Contrib. Work. Gr. I to Sixth Assess. Rep. Intergov. Panel Clim. Chang.*, 2021.

[5] L. Vinet and A. Zhedanov, *J. Phys. A Math. Theor.*, vol. 44, no. 8, pp. 1689–1699, Nov. 2011, doi: 10.1088/1751–8113/44/8/085201.

[6] H. Ritchie and M. Roser, *Our World in Data*. 2020. [Online]. Available: https://ourworldindata.org/co2–and–other–greenhouse–gas–emissions

[7] M. Z. Jacobson and M. A. Delucchi, *Energy Policy*, vol. 39, no. 3, pp. 1154–1169, 2011, doi: 10.1016/j.enpol.2010.11.040.

[8] M. Esteban and D. Leary, *Appl. Energy*, vol. 90, no. 1, pp. 128–136, 2012, doi: 10.1016/j.apenergy.2011.06.011.

[9] D. Clemente, P. Rosa–Santos, and F. Taveira–Pinto, *Renew. Sustain. Energy Rev.*, vol. 135, no. January 2020, p. 110162, 2021, doi: 10.1016/j.rser.2020.110162.

[10] E. Sugawara and H. Nikaido, vol. 58, no. 12. 2014. doi: 10.1128/AAC.03728–14.

[11] P. A. Owusu and S. Asumadu–Sarkodie, Cogent, 2016. doi: 10.1080/23311916.2016.1167990.

[12] A. M. Bradshaw, T. Hamacher, and U. Fischer, *Fusion Eng. Des.*, vol. 86, no. 9–11, pp. 2770–2773, 2011, doi: 10.1016/j.fusengdes.2010.11.040.

[13] RTE, 2018. [Online]. Available: https://www.rte–france.com/sites/default/files/apercu_energie_elec_2018_01_an.pdf

[14] I. E. A. (IEA), *Nucl. Power a Clean Energy Syst.*, 2019, doi: 10.1787/fc5f4b7e–en.

[15] M. S. D. I. L. Thomas, *Nature*, vol. 414, pp. 332–337, Nov. 2001.

[16] International Atomic Energy Agency (IAEA) and I. A. E. A. (IAEA), 1993. doi: 10.1016/0160–4120(93)90296–t.

[17] M. Braun and P. Volkholz, 2012. doi: 10.1051/jtsfen/2012nuc23.

[18] D. J. Ward, I. Cook, Y. Lechon, and R. Saez, *Fusion Eng. Des.*, vol. 75–79, no. SUPPL., pp. 1221–1227, 2005, doi: 10.1016/j.fusengdes.2005.06.160.

[19] E. E. Bloom, *J. Nucl. Mater.*, vol. 258–263, no. PART 1 A, pp. 7–17, 1998, doi: 10.1016/S0022–3115(98)00352–3.

[20] J. E. Phillips and C. E. Easterly, *Nucl. Saf.*, vol. 22, no. 5, pp. 612–626, 1981.

[21] G. Federici, W. Biel, M. R. Gilbert, R. Kemp, N. Taylor, and R. Wenninger, *Nucl. Fusion*, vol. 57, no. 9, 2017, doi: 10.1088/1741–4326/57/9/092002.

[22] H. Bolt *et al.*, *J. Nucl. Mater.*, vol. 329–333, no. 1–3 PART A, pp. 66–73, Aug. 2004, doi: 10.1016/j.jnucmat.2004.04.005.

[23] W. M. Nevins, *J. Fusion Energy*, vol. 17, no. 1, pp. 25–32, 1998, doi: 10.1023/A:1022513215080.

[24] L. L. Lucas and M. P. Unterweger, *J. Am. Chem. Soc.*, vol. 122, no. 50, pp. 12614–12614, 2000, doi: 10.1021/ja0048230.

[25] M. E. Sawan and M. A. Abdou,

Fusion Eng. Des., vol. 81, no. 8–14 PART B, pp. 1131–1144, 2006, doi: 10.1016/j.fusengdes.2005.07.035.

[26] A. R. Raffray *et al.*, *Nucl. Fusion*, vol. 54, no. 3, 2014, doi: 10.1088/0029–5515/54/3/033004.

[27] I. A. E. A. (IAEA), 2021. [Online]. Available: https://nucleus–new.iaea.org/sites/fusionportal/Pages/FusDIS.aspx

[28] M. Coleman *et al.*, *Fusion Eng. Des.*, vol. 109–111, no. 633053, pp. 1158–1162, 2016, doi: 10.1016/j.fusengdes.2015.12.063.

[29] R. J. Hawryluk, *Rev. Mod. Phys.*, vol. 70, no. 2, pp. 537–587, 1998, doi: 10.1103/revmodphys.70.537.

[30] G. Janeschitz *et al.*, *J. Nucl. Mater.*, vol. 220–222, pp. 73–88, Apr. 1995, doi: 10.1016/0022–3115(94)00447–1.

[31] F. Romanelli, *Efda*, pp. 1–75, 2012, doi: ISBN 978–3–00–040720–8.

[32] J. N. Brooks *et al.*, *Nucl. Fusion*, vol. 49, no. 3, 2009, doi: 10.1088/0029–5515/49/3/035007.

[33] T. Loarer *et al.*, *J. Nucl. Mater.*, vol. 438, no. SUPPL, 2013, doi: 10.1016/j.jnucmat.2013.01.017.

[34] S. Krat *et al.*, *Nucl. Mater. Energy*, vol. 11, pp. 20–24, Jan. 2017, doi: 10.1016/j.nme.2017.02.026.

[35] M. Keilhacker, *Phys. Fluids B*, vol. 2, no. 6, pp. 1291–1299, 1990, doi: 10.1063/1.859585.

[36] M. Abhangi *et al.*, *Nucl. Fusion*, vol. 53, no. 10, Oct. 2013.

[37] T. Tanno *et al.*, *Mater. Trans.*, vol. 49, no. 10, pp. 2259–2264, 2008, doi: 10.2320/matertrans.MAW200821.

[38] A. Xu *et al.*, *Acta Mater.*, vol. 87, pp. 121–127, 2015, doi: 10.1016/j.actamat.2014.12.049.

[39] A. Xu *et al.*, *Acta Mater.*, vol. 124, pp. 71–78, 2017, doi: 10.1016/j.actamat.2016.10.050.

[40] J. Matolich, H. Nahm, and J. Moteff, *Scr. Metall.*, vol. 8, no. 7, pp. 837–841, Jul. 1974, doi: 10.1016/0036–9748(74)90304–4.

[41] B. N. N. Singh and J. H. H. Evans, *J. Nucl. Mater.*, vol. 226, no. 3, pp. 277–285, Nov. 1995, doi: 10.1016/0022–3115(95)00121–2.

[42] P. M. Derlet, D. Nguyen–Manh, and S. L. Dudarev, *Phys. Rev. B*, vol. 76, no. 5, p. 054107, Aug. 2007, doi: 10.1103/PhysRevB.76.054107.

[43] J. W. Davis, V. R. Barabash, A. Makhankov, L. Plöchl, and K. T. Slattery, *J. Nucl. Mater.*, vol. 258–263, no. PART 1 A, pp. 308–312, Oct. 1998, doi: 10.1016/S0022–3115(98)00285–2.

[44] Y. Nemoto, A. Hasegawa, M. Satou, and K. Abe, *J. Nucl. Mater.*, vol. 283–287, no. PART II, pp. 1144–1147, Dec. 2000, doi: 10.1016/S0022–3115(00)00290–7.

[45] H. Bolt *et al.*, *J. Nucl. Mater.*, vol. 307–311, no. 1 SUPPL., pp. 43–52, Dec. 2002, doi: 10.1016/S0022–3115(02)01175–3.

[46] V. Barabash, G. Federici, J. Linke, and C. H. Wu, *J. Nucl. Mater.*, vol. 313–316, no. SUPPL., pp. 42–51, 2003, doi: 10.1016/S0022–3115(02)01330–2.

[47] G. Federici *et al.*, *J. Nucl. Mater.*, vol. 266, pp. 14–29, 1999, doi: 10.1016/S0022–3115(98)00876–9.

[48] U. Fischer, P. Batistoni, L. V. Boccaccini, L. Giancarli, S. Hermsmeyer, and Y. Poitevin, *Fusion Sci. Technol.*, vol. 47, no. 4, pp. 1052–1059, 2005, doi: 10.13182/FST05–A826.

[49] M. R. Gilbert and J. C. Sublet, *Nucl. Fusion*, vol. 51, no. 4, Apr. 2011, doi: 10.1088/0029–5515/51/4/043005.

[50] H. Nakamura, S. Sakurai, S. Suzuki, T. Hayashi, M. Enoeda, and K. Tobita, *Fusion Eng. Des.*, vol. 81, no. 8–14 PART B, pp. 1339–1345, 2006, doi: 10.1016/j.fusengdes.2005.10.009.

[51] D. Buchenauer, R. Kolasinski, M. Shimada, D. Donovan, D. Youchison, and B. Merrill, *Fusion Eng. Des.*, vol. 89, no. 7–8, pp. 1014–1018, 2014, doi: 10.1016/j.fusengdes.2014.03.009.

[52] N. Shinoda, Y. Yamauchi, Y. Nobuta, and T. Hino, *Fusion Eng. Des.*, vol. 89, no. 7–8, pp. 921–924, 2014, doi: 10.1016/j.fusengdes.2014.05.019.

[53] L. Batet, E. M. De Les Valls, L. A. Sedano, E. M. D. Les Valls, and L. A.

Sedano, *Fusion Eng. Des.*, vol. 89, no. 7–8, pp. 1158–1162, 2014, doi: 10.1016/j.fusengdes.2014.04.031.

[54] C. Li, X. Wu, C. Zhang, H. Ding, G. De Temmerman, and H. J. Van Der Meiden, *Fusion Eng. Des.*, vol. 89, no. 7–8, pp. 949–954, 2014, doi: 10.1016/j.fusengdes.2014.04.071.

[55] C. Shan *et al.*, *J. Nucl. Mater.*, vol. 191–194, pp. 221–225, 1992, doi: 10.1016/S0022–3115(09)80038–X.

[56] D. Levchuk, F. Koch, H. Maier, and H. Bolt, *J. Nucl. Mater.*, vol. 328, no. 2–3, pp. 103–106, 2004, doi: 10.1016/j.jnucmat.2004.03.008.

[57] T. Chikada, A. Suzuki, C. Adelhelm, T. Terai, and T. Muroga, *Nucl. Fusion*, vol. 51, no. 6, 2011, doi: 10.1088/0029–5515/51/6/063023.

[58] Z. Yao, J. Hao, C. Zhou, C. Shan, and J. Yu, *J. Nucl. Mater.*, vol. 283–287, no. PART II, pp. 1287–1291, 2000, doi: 10.1016/S0022–3115(00)00349–4.

[59] T. Chikada, A. Suzuki, and T. Terai, *Fusion Eng. Des.*, vol. 86, no. 9–11, pp. 2192–2195, 2011, doi: 10.1016/j.fusengdes.2011.01.036.

[60] E. Serra, P. J. Kelly, D. K. Ross, and R. D. Arnell, *J. Nucl. Mater.*, vol. 257, no. 2, pp. 194–198, 1998, doi: 10.1016/S0022–3115(98)00473–5.

[61] K. L. Wilson and M. I. Baskes, *J. Nucl. Mater.*, vol. 76–77, no. C, pp. 291–297, 1978, doi: 10.1016/0022–3115(78)90160–5.

[62] F. A. Garner *et al.*, *J. Nucl. Mater.*, vol. 356, no. 1–3, pp. 122–135, 2006, doi: 10.1016/j.jnucmat.2006.05.023.

[63] J. Roth *et al.*, *J. Nucl. Mater.*, vol. 390–391, no. 1, pp. 1–9, 2009, doi: 10.1016/j.jnucmat.2009.01.037.

[64] V. K. Alimov *et al.*, *J. Nucl. Mater.*, vol. 441, no. 1–3, pp. 280–285, 2013, doi: 10.1016/j.jnucmat.2013.06.005.

[65] S. J. Zinkle, A. Möslang, T. Muroga, and H. Tanigawa, *Nucl. Fusion*, vol. 53, no. 10, 2013, doi: 10.1088/0029–5515/53/10/104024.

[66] S. J. Zinkle, in *Comprehensive Nuclear Materials*, 1st ed., vol. 1, no. February, Elsevier Inc., 2012, pp. 65–98. doi: 10.1016/B978–0–08–056033–5.00003–3.

[67] R. E. Stoller, *J. Nucl. Mater.*, vol. 174, no. 2–3, pp. 289–310, 1990, doi: 10.1016/0022–3115(90)90242–F.

[68] D. Stork *et al.*, *J. Nucl. Mater.*, vol. 455, no. 1–3, pp. 277–291, 2014, doi: 10.1016/j.jnucmat.2014.06.014.

[69] N. Casal *et al.*, *J. Nucl. Mater.*, vol. 417, no. 1–3, pp. 1316–1320, Oct. 2011, doi: 10.1016/j.jnucmat.2011.01.092.

[70] A. K. Suri, N. Krishnamurthy, and I. S. Batra, *J. Phys. Conf. Ser.*, vol. 208, pp. 0–16, 2010, doi: 10.1088/1742–6596/208/1/012001.

[71] E. Gaganidze, C. Petersen, and J. Aktaa, *J. Nucl. Mater.*, vol. 386–388, no. C, pp. 349–352, 2009, doi: 10.1016/j.jnucmat.2008.12.131.

[72] B. S. S. Li and Y. Dai, *J. Nucl. Mater.*, vol. 450, no. 1–3, pp. 42–47, Jul. 2014, doi: 10.1016/j.jnucmat.2014.02.009.

[73] T. Zhang, C. Vieh, K. Wang, and Y. Dai, *J. Nucl. Mater.*, vol. 450, no. 1–3, pp. 48–53, 2014, doi: 10.1016/j.jnucmat.2013.12.007.

[74] S. J. Zenobia and G. L. Kulcinski, *Phys. Scr. T*, vol. T138, 2009, doi: 10.1088/0031–8949/2009/T138/014049.

[75] Y. Ueda *et al.*, *J. Nucl. Mater.*, vol. 442, no. 1–3 SUPPL.1, pp. S267–S272, 2013, doi: 10.1016/j.jnucmat.2012.10.023.

[76] A. Möslang *et al.*, *Nucl. Fusion*, vol. 45, no. 7, pp. 649–655, 2005, doi: 10.1088/0029–5515/45/7/013.

[77] M. R. Gilbert, J.–C. Sublet, and R. A. Forrest, *Ccfe–R(15)26*, no. December, pp. 1–696, 2015, [Online]. Available: http://www.ccfe.ac.uk/assets/documents/easy/CCFE–R(15)26.pdf

[78] F. Tavassoli, in *Procedia Engineering*, 2013, vol. 55, pp. 300–308. doi: 10.1016/j.proeng.2013.03.258.

[79] G. Federici, L. Boccaccini, F. Cismondi, M. Gasparotto, Y. Poitevin, and I. Ricapito, *Fusion Eng. Des.*, vol. 141, no. October 2018, pp. 30–42, 2019, doi: 10.1016/j.fusengdes.2019.01.141.

[80] M. Gorley *et al.*, *Fusion Eng. Des.*,

vol. 170, p. 112513, 2021, doi: 10.1016/j.fusengdes.2021.112513.

[81] D. Rapisarda *et al.*, .

[82] T. Nozawa *et al.*, *Nucl. Fusion*, vol. 61, no. 11, p. 116054, 2021, doi: 10.1088/1741–4326/ac269f.

[83] N. Mitchell *et al.*, *Supercond. Sci. Technol.*, vol. 34, no. 10, 2021, doi: 10.1088/1361–6668/ac0992.

[84] I. Smid, M. Akiba, G. Vieider, and L. Plöchl, *J. Nucl. Mater.*, vol. 258–263, no. PART 1 A, pp. 160–172, 1998, doi: 10.1016/S0022–3115(98)00358–4.

[85] J. Reiser, M. Rieth, B. Dafferner, and A. Hoffmann, *J. Nucl. Mater.*, vol. 442, no. 1–3 SUPPL.1, pp. S204–S207, 2013, doi: 10.1016/j.jnucmat.2012.10.037.

[86] A. Giannattasio, Z. Yao, E. Tarleton, and S. G. Roberts, *Philos. Mag.*, vol. 90, no. 30, pp. 3947–3959, 2010, doi: 10.1080/14786435.2010.502145.

[87] T. Leonhardt, *Jom*, vol. 61, no. 7, pp. 68–71, Jul. 2009, doi: 10.1007/s11837–009–0107–6.

[88] M. Fukuda, K. Yabuuchi, S. Nogami, A. Hasegawa, and T. Tanaka, *J. Nucl. Mater.*, vol. 455, no. 1–3, pp. 460–463, Dec. 2014, doi: 10.1016/j.jnucmat.2014.08.002.

[89] D. E. J. J. Armstrong, X. Yi, E. A. Marquis, and S. G. Roberts, *J. Nucl. Mater.*, vol. 432, no. 1–3, pp. 428–436, 2013, doi: 10.1016/j.jnucmat.2012.07.044.

[90] M. J. Baldwin and R. P. Doerner, *Nucl. Fusion*, vol. 48, no. 3, p. 35001, Jan. 2008, doi: 10.1088/0029–5515/48/3/035001.

[91] A. Khan, 2017.

[92] U. S. G. S. G. Survey, 2018.

[93] C. Linsmeier *et al.*, *Nucl. Fusion*, vol. 57, no. 9, p. 60pp, 2017, doi: 10.1088/1741–4326/aa6f71.

[94] M. Gasparotto *et al.*, *Fusion Eng. Des.*, vol. 66–68, pp. 129–137, 2003, doi: 10.1016/S0920–3796(03)00151–0.

[95] J. Stepanek, S. Entler, J. Syblik, L. Vesely, V. Dostal, and P. Zacha, *Fusion Eng. Des.*, vol. 166, no. April, p. 112287, 2021, doi: 10.1016/j.fusengdes.2021.112287.

[96] S. J. Zinkle and L. L. Snead, *Annu. Rev. Mater. Res.*, vol. 44, no. 1, pp. 241–267, 2014, doi: 10.1146/annurev–matsci–070813–113627.

[97] L. L. Snead, T. Nozawa, Y. Katoh, T.–S. S. Byun, S. Kondo, and D. A. Petti, *J. Nucl. Mater.*, vol. 371, no. 1–3, pp. 329–377, Sep. 2007, doi: 10.1016/j.jnucmat.2007.05.016.

[98] L. L. Snead, T. Nozawa, M. Ferraris, Y. Katoh, R. Shinavski, and M. Sawan, in *Journal of Nuclear Materials*, 2011, vol. 417, no. 1–3, pp. 330–339. doi: 10.1016/j.jnucmat.2011.03.005.

[99] A. Hasegawa, B. M. Oliver, S. Nogami, K. Abe, and R. H. Jones, *J. Nucl. Mater.*, vol. 283–287, no. PART II, pp. 811–815, 2000, doi: 10.1016/S0022–3115(00)00375–5.

[100] M. R. Gilbert, S. L. Dudarev, S. Zheng, L. W. Packer, and J. C. Sublet, *Nucl. Fusion*, vol. 52, no. 8, 2012, doi: 10.1088/0029–5515/52/8/083019.

[101] H. Nowotny, H. Boller, and O. Beckmann, *J. Solid State Chem.*, vol. 2, no. 3, pp. 462–471, Nov. 1970, doi: 10.1016/0022–4596(70)90105–2.

[102] M. W. Barsoum, Weinheim, Germany: Wiley–VCH Verlag GmbH & Co. KGaA, 2013. doi: 10.1002/9783527654581.

[103] M. W. Barsoum and T. El–Raghy, *Journal of the American Ceramic Society*, vol. 79, no. 7. pp. 1953–1956, 1996. doi: 10.1111/j.1151–2916.1996.tb08018.x.

[104] M. W. W. Barsoum and M. Radovic, in *Encyclopedia of Materials: Science and Technology*, vol. 2, Elsevier, 2004, pp. 1–16. doi: 10.1016/B0–08–043152–6/01931–8.

[105] L. Farber, I. Levin, M. W. Barsoum, T. El–Raghy, and T. Tzenov, *J. Appl. Phys.*, vol. 86, no. 5, pp. 2540–2543, 1999, doi: 10.1063/1.371089.

[106] M. W. Barsoum, T. El-Raghy, and L. U. J. T. Ogbuji, *J. Electrochem. Soc.*, vol. 144, no. 7, pp. 2508–2516, 1997, doi: 10.1149/1.1837846.

[107] T. Lapauw, A. K. Swarnakar, B. Tunca, K. Lambrinou, and J.

Vleugels, *Int. J. Refract. Met. Hard Mater.*, vol. 72, no. October 2017, pp. 51–55, 2018, doi: 10.1016/j.ijrmhm.2017.11.038.

[108] T. El–raghy, P. Blau, and M. W. Barsoum, pp. 125–130, 2000.

[109] J. C. C. Schuster, H. Nowotny, and C. Vaccaro, *J. Solid State Chem.*, vol. 32, no. 2, pp. 213–219, Apr. 1980, doi: 10.1016/0022–4596(80)90569–1.

[110] M. Sokol, V. Natu, S. Kota, and M. W. Barsoum, *Trends Chem.*, vol. 1, no. 2, pp. 210–223, 2019, doi: 10.1016/j.trechm.2019.02.016.

[111] M. Dahlqvist and J. Rosen, *Nanoscale*, vol. 12, no. 2, pp. 785–794, 2020, doi: 10.1039/c9nr08675g.

[112] M. Naguib *et al.*, *Mater. Res. Lett.*, vol. 2, no. 4, pp. 233–240, Oct. 2014, doi: 10.1080/21663831.2014.932858.

[113] J. Halim *et al.*, *J. Eur. Ceram. Soc.*, vol. 37, no. 1, pp. 15–21, 2017, doi: 10.1016/j.jeurceramsoc.2016.07.022.

[114] M. T. P. Rigby *et al.*, *RSC Adv.*, vol. 11, no. 5, pp. 3110–3114, 2021, doi: 10.1039/d0ra09761f.

[115] E. N. Caspi, P. Chartier, F. Porcher, F. Damay, and T. Cabioc'h, *Mater. Res. Lett.*, vol. 3, no. 2, pp. 100–106, 2015, doi: 10.1080/21663831.2014.975294.

[116] Z. Liu *et al.*, *Acta Mater.*, vol. 73, pp. 186–193, 2014, doi: 10.1016/j.actamat.2014.04.006.

[117] B. Anasori, J. Halim, J. Lu, C. A. Voigt, L. Hultman, and M. W. Barsoum, *Scr. Mater.*, vol. 101, pp. 5–7, 2015, doi: 10.1016/j.scriptamat.2014.12.024.

[118] Y. Zhou, F. Meng, and J. Zhang, *J. Am. Ceram. Soc.*, vol. 91, no. 4, pp. 1357–1360, 2008, doi: 10.1111/j.1551–2916.2008.02279.x.

[119] B. Anasori *et al.*, *J. Appl. Phys.*, vol. 118, no. 9, p. 094304, Sep. 2015, doi: 10.1063/1.4929640.

[120] M. Dahlqvist, B. Alling, and J. Rosén, *Phys. Rev. B – Condens. Matter Mater. Phys.*, vol. 81, no. 22, 2010, doi: 10.1103/PhysRevB.81.220102.

[121] Z. Liu, L. Zheng, L. Sun, Y. Qian, J. Wang, and M. Li, *J. Am. Ceram. Soc.*, vol. 97, no. 1, pp. 67–69, Jan. 2014, doi: 10.1111/jace.12731.

[122] T. Lapauw *et al.*, *Sci. Rep.*, vol. 8, no. 1, p. 12801, Dec. 2018, doi: 10.1038/s41598–018–31271–2.

[123] B. Tunca *et al.*, *Inorg. Chem.*, vol. 58, no. 10, pp. 6669–6683, 2019, doi: 10.1021/acs.inorgchem.9b00065.

[124] Q. Tao *et al.*, *Nat. Commun.*, vol. 8, pp. 1–7, 2017, doi: 10.1038/ncomms14949.

[125] Q. Tao *et al.*, *Chem. Mater.*, vol. 31, no. 7, pp. 2476–2485, Apr. 2019, doi: 10.1021/acs.chemmater.8b05298.

[126] Y. Li *et al.*, *Proc. Natl. Acad. Sci. U. S. A.*, vol. 117, no. 2, pp. 820–825, 2020, doi: 10.1073/pnas.1916256117.

[127] W. Bao *et al.*, *Scr. Mater.*, vol. 183, pp. 33–38, 2020, doi: 10.1016/j.scriptamat.2020.03.015.

[128] Y. C. Zhou, J. X. Chen, and J. Y. Wang, *Acta Mater.*, vol. 54, no. 5, pp. 1317–1322, 2006, doi: 10.1016/j.actamat.2005.10.057.

[129] T. Cabioch, P. Eklund, V. Mauchamp, M. Jaouen, and M. W. Barsoum, *J. Eur. Ceram. Soc.*, vol. 33, no. 4, pp. 897–904, 2013, doi: 10.1016/j.jeurceramsoc.2012.10.008.

[130] M. Dahlqvist, B. Alling, I. A. Abrikosov, and J. Rosén, *Phys. Rev. B – Condens. Matter Mater. Phys.*, vol. 81, no. 2, p. 024111, Jan. 2010, doi: 10.1103/PhysRevB.81.024111.

[131] J. Rosen, M. Dahlqvist, S. I. Simak, D. R. McKenzie, and M. M. M. M. Bilek, *Appl. Phys. Lett.*, vol. 97, no. 7, 2010, doi: 10.1063/1.3472280.

[132] R. Meshkian *et al.*, *Phys. Status Solidi – Rapid Res. Lett.*, vol. 9, no. 3, pp. 197–201, 2015, doi: 10.1002/pssr.201409543.

[133] Q. Z. Tao *et al.*, *Mater. Res. Lett.*, vol. 2, no. 4, pp. 192–198, 2014, doi: 10.1080/21663831.2014.909542.

[134] A. S. Ingason *et al.*, *Mater. Res. Lett.*, vol. 2, no. 2, pp. 89–93, 2017, doi: 10.1080/21663831.2013.865105.

[135] A. Mockute *et al.*, *Phys. Status Solidi – Rapid Res. Lett.*, vol. 8, no. 5, pp.

420–423, 2014, doi: 10.1002/pssr.201409087.

[136] M. Bugnet, M. Jaouen, V. Mauchamp, T. Cabioc'H, and G. Hug, *Phys. Rev. B – Condens. Matter Mater. Phys.*, vol. 90, no. 19, 2014, doi: 10.1103/PhysRevB.90.195116.

[137] F. L. Meng, Y. C. Zhou, and J. Y. Wang, *Scr. Mater.*, vol. 53, no. 12, pp. 1369–1372, 2005, doi: 10.1016/j.scriptamat.2005.08.030.

[138] M. W. Barsoum, M. Ali, and T. El–Raghy, *Metall. Mater. Trans. A Phys. Metall. Mater. Sci.*, vol. 31, no. 7, pp. 1857–1865, 2000, doi: 10.1007/s11661–006–0243–3.

[139] C. J. Rawn, M. W. Barsoum, T. El–Raghy, A. Procipio, C. M. Hoffmann, and C. R. Hubbard, *Mater. Res. Bull.*, vol. 35, no. 11, pp. 1785–1796, 2000, doi: 10.1016/S0025–5408(00)00383–4.

[140] P. Eklund *et al.*, *Acta Mater.*, vol. 55, no. 14, pp. 4723–4729, 2007, doi: 10.1016/j.actamat.2007.04.040.

[141] X. He, Y. Bai, C. Zhu, and M. W. Barsoum, *Acta Mater.*, vol. 59, no. 14, pp. 5523–5533, 2011, doi: 10.1016/j.actamat.2011.05.025.

[142] J. Wang, J. Wang, Y. Zhou, Z. Lin, and C. Hu, *Scr. Mater.*, vol. 58, no. 12, pp. 1043–1046, 2008, doi: 10.1016/j.scriptamat.2008.01.058.

[143] A. Guitton, A. Joulain, L. Thilly, and C. Tromas, *Philos. Mag.*, vol. 92, no. 36, pp. 4536–4546, 2012, doi: 10.1080/14786435.2012.715250.

[144] A. Murugaiah, M. W. Barsoum, S. R. Kalidindi, and T. Zhen, *J. Mater. Res.*, vol. 19, no. 7, pp. 2194–2203, 2004, doi: 10.1557/JMR.2004.0148.

[145] N. G. Jones *et al.*, *Acta Mater.*, vol. 69, pp. 149–161, 2014, doi: 10.1016/j.actamat.2014.01.045.

[146] M. F. Cover, M. M. M. M. Bilek, and D. R. McKenzie, *J. Phys. Condens. Matter*, vol. 23, no. 26, 2011, doi: 10.1088/0953–8984/23/26/268001.

[147] A. Guitton, A. Joulain, L. Thilly, and C. Tromas, *Sci. Rep.*, vol. 4, 2014, doi: 10.1038/srep06358.

[148] K. Gouriet *et al.*, *Philos. Mag.*, vol. 95, no. 23, pp. 2539–2552, 2015, doi: 10.1080/14786435.2015.1066938.

[149] L. Farber, M. W. Barsoum, A. Zavaliangos, T. El–Raghy, and I. Levin, *J. Am. Ceram. Soc.*, vol. 81, no. 6, pp. 1677–1681, Jan. 2005, doi: 10.1111/j.1151–2916.1998.tb02532.x.

[150] M. W. Barsoum, L. Farber, and T. El–Raghy, *Metall. Mater. Trans. A Phys. Metall. Mater. Sci.*, vol. 30, no. 7, pp. 1727–1738, 1999, doi: 10.1007/s11661–999–0172–z.

[151] R. Benitez *et al.*, *Acta Mater.*, vol. 189, pp. 154–165, 2020, doi: 10.1016/j.actamat.2020.02.057.

[152] A. G. Zhou and M. W. Barsoum, *J. Alloys Compd.*, vol. 498, no. 1, pp. 62–70, 2010, doi: 10.1016/j.jallcom.2010.03.099.

[153] R. L. L. Tsai and R. Raj, *Acta Metall.*, vol. 30, no. 6, pp. 1043–1058, Jun. 1982, doi: 10.1016/0001–6160(82)90001–3.

[154] A. I. Gusev, A. A. Rempel, and A. J. Magerl, vol. 47. Springer Science \& Business Media, 2013.

[155] T. El–Raghy, M. W. Barsoum, A. Zavaliangos, and S. R. Kalidindi, *J. Am. Ceram. Soc.*, vol. 82, no. 10, pp. 2855–2860, 1999, doi: 10.1111/j.1151–2916.1999.tb02167.x.

[156] H. O. Pierson, 1st ed. Noyes Publications, 1996.

[157] B. Poon, L. Ponson, J. Zhao, and G. Ravichandran, *J. Mech. Phys. Solids*, vol. 59, no. 10, pp. 2238–2257, 2011, doi: 10.1016/j.jmps.2011.03.012.

[158] G. Plummer *et al.*, *Mater. Today*, vol. 43, no. March, pp. 45–52, 2021, doi: 10.1016/j.mattod.2020.11.014.

[159] H. J. Rathod, T. Ouisse, M. Radovic, and A. Srivastava, *Sci. Adv.*, vol. 7, no. 33, pp. 1–10, 2021, doi: 10.1126/sciadv.abg2549.

[160] E. Broitman, *Tribol. Lett.*, vol. 65, no. 1, pp. 1–18, 2017, doi: 10.1007/s11249–016–0805–5.

[161] P. Eklund, Linköping University, 2007.

[162] X. H. Wang and Y. C. Zhou, *J. Mater. Sci. Technol.*, vol. 26, no. 5, pp. 385–416, 2010, doi: 10.1016/S1005–0302(10)60064–3.

[163] T. Lapauw *et al.*, *Inorg. Chem.*, vol.

55, no. 11, pp. 5445–5452, Jun. 2016, doi: 10.1021/acs.inorgchem.6b00484.

[164] H. Foratirad, H. Baharvandi, and M. G. Maraghe, *J. Eur. Ceram. Soc.*, vol. 37, no. 2, pp. 451–457, Feb. 2017, doi: 10.1016/j.jeurceramsoc.2016.09.004.

[165] M. W. Barsoum, *Prog. Solid State Chem.*, vol. 28, no. 1–4, pp. 201–281, Jan. 2000, doi: 10.1016/S0079–6786(00)00006–6.

[166] J. Zhang, L. Wang, W. Jiang, and L. Chen, *Mater. Sci. Eng. A*, vol. 487, no. 1–2, pp. 137–143, 2008, doi: 10.1016/j.msea.2007.12.004.

[167] D. Chen, X. Tian, H. Wang, and Z. Huang, *Int. J. Refract. Met. Hard Mater.*, vol. 47, pp. 102–107, 2014, doi: 10.1016/j.ijrmhm.2014.07.001.

[168] M. Sundberg, G. Malmqvist, A. Magnusson, and T. El–Raghy, *Ceram. Int.*, vol. 30, no. 7, pp. 1899–1904, Jan. 2004, doi: 10.1016/j.ceramint.2003.12.046.

[169] M. Zhang, W. Tian, P. Zhang, J. Ding, Y. Zhang, and Z. Sun, *Int. J. Miner. Metall. Mater.*, vol. 25, no. 7, pp. 810–816, Jul. 2018, doi: 10.1007/s12613–018–1629–0.

[170] B. S. Karpinos, V. M. Kulish, and T. O. Prikhna, *Strength Mater.*, vol. 52, no. 5, pp. 738–745, Sep. 2020, doi: 10.1007/s11223–020–00227–1.

[171] S. Gupta, D. Filimonov, V. Zaitsev, T. Palanisamy, T. El–Raghy, and M. W. Barsoum, *Wear*, vol. 267, no. 9–10, pp. 1490–1500, 2009, doi: 10.1016/j.wear.2009.03.021.

[172] M. W. Barsoum *et al.*, *J. Phys. Chem. Solids*, vol. 60, no. 4, pp. 429–439, 1999, doi: 10.1016/S0022–3697(98)00313–8.

[173] C. Y. Ho, R. W. Powell, and P. E. Liley, *J. Phys. Chem. Ref. Data*, vol. 1, no. 2, pp. 279–421, Apr. 1972, doi: 10.1063/1.3253100.

[174] M. W. Barsoum *et al.*, *Metall. Mater. Trans. A Phys. Metall. Mater. Sci.*, vol. 33, no. 9, pp. 2775–2779, 2002, doi: 10.1007/s11661–002–0262–7.

[175] J. D. Hettinger *et al.*, *Phys. Rev. B*, vol. 72, no. 11, p. 115120, Sep. 2005, doi: 10.1103/PhysRevB.72.115120.

[176] Y. H. Koh, H. W. Kim, H. E. Kim, and J. W. Halloran, *J. Eur. Ceram. Soc.*, vol. 24, no. 8, pp. 2339–2347, 2004, doi: 10.1016/S0955–2219(03)00644–7.

[177] E. H. Lutz, N. Claussen, and M. V Swain, *J. Am. Ceram. Soc.*, vol. 74, no. 1, pp. 11–18, 1991, doi: 10.1111/j.1151–2916.1991.tb07289.x.

[178] X. Q. You, T. Z. Si, N. Liu, P. P. Ren, Y. D. Xu, and J. P. Feng, *Ceram. Int.*, vol. 31, no. 1, pp. 33–38, 2005, doi: 10.1016/j.ceramint.2004.02.009.

[179] M. Aldridge and J. A. Yeomans, *J. Eur. Ceram. Soc.*, vol. 19, no. 9, pp. 1769–1775, 1999, doi: 10.1016/S0955–2219(98)00270–2.

[180] T. Hirano and K. Niihara, *Mater. Lett.*, vol. 26, no. 6, pp. 285–289, 1996, doi: 10.1016/0167–577X(96)80001–2.

[181] H. B. Zhang, Y. C. Zhou, Y. W. Bao, and M. S. Li, *J. Mater. Res.*, vol. 21, no. 9, pp. 2401–2407, 2006, doi: 10.1557/jmr.2006.0289.

[182] N. V. Tzenov and M. W. Barsoum, *J. Am. Ceram. Soc.*, vol. 83, no. 4, pp. 825–832, 2000, doi: 10.1111/j.1151–2916.2000.tb01281.x.

[183] A. Ganguly, T. Zhen, and M. W. Barsoum, *J. Alloys Compd.*, vol. 376, no. 1–2, pp. 287–295, 2004, doi: 10.1016/j.jallcom.2004.01.011.

[184] E. N. Hoffman, D. W. Vinson, R. L. Sindelar, D. J. Tallman, G. Kohse, and M. W. Barsoum, *Nucl. Eng. Des.*, vol. 244, pp. 17–24, 2012, doi: 10.1016/j.nucengdes.2011.12.009.

[185] I. M. Low, W. K. Pang, S. J. Kennedy, and R. I. Smith, *Ceram. Eng. Sci. Proc.*, vol. 31, no. 10, pp. 171–180, 2010, doi: 10.1002/9780470944103.ch17.

[186] W. K. Pang *et al.*, *J. Phys. Conf. Ser.*, vol. 251, no. 1, 2010, doi: 10.1088/1742–6596/251/1/012025.

[187] Z. Feng, P. Ke, Q. Huang, and A. Wang, *Surf. Coatings Technol.*, vol. 272, pp. 380–386, 2015, doi: 10.1016/j.surfcoat.2015.03.037.

[188] Y. Du, J. X. Liu, Y. Gu, X. G. Wang, F. Xu, and G. J. Zhang, *Ceram. Int.*,

vol. 43, no. 9, pp. 7166–7171, 2017, doi: 10.1016/j.ceramint.2017.02.153.

[189] Z. Lin, Y. Zhou, M. Li, and J. Wang, *Zeitschrift für Met.*, vol. 96, no. 3, pp. 291–296, Mar. 2005, doi: 10.3139/146.101033.

[190] M. T. Agne, M. Radovic, G. W. Bentzel, and M. W. Barsoum, *J. Alloys Compd.*, vol. 666, pp. 279–286, 2016, doi: 10.1016/j.jallcom.2016.01.050.

[191] T. Lapauw *et al.*, *J. Nucl. Mater.*, vol. 520, pp. 258–272, Jul. 2019, doi: 10.1016/j.jnucmat.2019.04.010.

[192] B. Tunca *et al.*, *Corros. Sci.*, vol. 171, p. 108704, Jul. 2020, doi: 10.1016/j.corsci.2020.108704.

[193] A. Heinzel, A. Weisenburger, and G. Müller, *J. Nucl. Mater.*, vol. 482, pp. 114–123, Dec. 2016, doi: 10.1016/j.jnucmat.2016.10.007.

[194] K. Ando, K. Furusawa, M. C. Chu, T. Hanagata, K. Tuji, and S. Sato, *J. Am. Ceram. Soc.*, vol. 84, no. 9, pp. 2073–2078, 2001, doi: 10.1111/j.1151–2916.2001.tb00960.x.

[195] K. Ando *et al.*, *J. Eur. Ceram. Soc.*, vol. 22, no. 8, pp. 1339–1346, 2002, doi: 10.1016/S0955–2219(01)00435–6.

[196] H. J. Yang, Y. T. Pei, J. C. Rao, and J. T. M. De Hosson, *J. Mater. Chem.*, vol. 22, no. 17, pp. 8304–8313, 2012, doi: 10.1039/c2jm16123k.

[197] F. Yao, K. Ando, M. C. Chu, and S. Sato, *J. Mater. Sci. Lett.*, vol. 19, no. 12, pp. 1081–1083, 2000, doi: 10.1023/A:1006715825737.

[198] T. K. GUPTA, *J. Am. Ceram. Soc.*, vol. 59, no. 5–6, pp. 259–262, 1976, doi: 10.1111/j.1151–2916.1976.tb10949.x.

[199] S. R. Choi and V. Tikare, *Scr. Metall. Mater.*, vol. 26, no. 8, pp. 1263–1268, Jan. 1992, doi: 10.1016/0956–716X(92)90574–X.

[200] P. Hrma, W. T. Han, and A. R. Cooper, *J. Non. Cryst. Solids*, vol. 102, no. 1–3, pp. 88–94, 1988, doi: 10.1016/0022–3093(88)90116–0.

[201] G. M. Song *et al.*, *Scr. Mater.*, vol. 58, no. 1, pp. 13–16, 2008, doi: 10.1016/j.scriptamat.2007.09.006.

[202] L. F. Marion *et al.*, in *Mechanical Properties and Performance of Engineering Ceramics and Composites IV*, vol. 3, Daytona Beach, 2009, pp. 189–198. doi: 10.1002/9780470584262.ch17.

[203] L. F. Marion and I. Monnet, *J. Nucl. Mater.*, vol. 433, no. 1–3, pp. 534–537, 2013, doi: 10.1016/j.jnucmat.2012.07.042.

[204] C. Sauder, A. Michaux, G. Loupias, P. Billaud, and J. Braun, *LWR Fuel Perform. Meet. Top Fuel 2013*, vol. 2, no. 2015, pp. 951–956, 2013.

[205] Z. Wang, S. Tsukimoto, M. Saito, and Y. Ikuhara, *Phys. Rev. B – Condens. Matter Mater. Phys.*, vol. 79, no. 4, pp. 1–10, 2009, doi: 10.1103/PhysRevB.79.045318.

[206] H. Dong, S. Li, Y. Teng, and W. Ma, *Mater. Sci. Eng. B Solid–State Mater. Adv. Technol.*, vol. 176, no. 1, pp. 60–64, 2011, doi: 10.1016/j.mseb.2010.09.002.

[207] Y. Katoh *et al.*, *J. Nucl. Mater.*, vol. 448, no. 1–3, pp. 497–511, 2014, doi: 10.1016/j.jnucmat.2013.10.002.

[208] J. Gonzalez–Julian, J. Llorente, M. Bram, M. Belmonte, and O. Guillon, *J. Eur. Ceram. Soc.*, vol. 37, no. 2, pp. 467–475, 2017, doi: 10.1016/j.jeurceramsoc.2016.09.029.

[209] F. Audubert, G. Abrivard, and C. Tallaron, *30th Int. Conf. Adv. Ceram. Compos.*, pp. 65–76, 2007, doi: 10.1002/9780470291344.ch8.

[210] GIF, 1993. doi: 10.1108/eb055690.

[211] J. C. Nappé *et al.*, *J. Nucl. Mater.*, vol. 385, no. 2, pp. 304–307, 2009, doi: 10.1016/j.jnucmat.2008.12.018.

[212] M. Utili, M. Agostini, G. Coccoluto, and E. Lorenzini, *Nucl. Eng. Des.*, vol. 241, no. 5, pp. 1295–1300, 2011, doi: 10.1016/j.nucengdes.2010.07.038.

[213] K. Lambrinou *et al.*, in *Ceramic Materials for Energy Applications V: A Collection of Papers Presented at the 39th International Conference on Advanced Ceramics and Composites*, 2015, pp. 19–34.

[214] A. Heinzel, G. Müller, and A. Weisenburger, *J. Nucl. Mater.*, vol. 392, no. 2, pp. 255–258, 2009, doi:

10.1016/j.jnucmat.2009.03.004.

[215] S. C. Middleburgh, G. R. Lumpkin, and D. Riley, *J. Am. Ceram. Soc.*, vol. 96, no. 10, pp. 3196–3201, 2013, doi: 10.1111/jace.12537.

[216] S. Zhao, J. Xue, Y. Wang, and Q. Huang, *J. Phys. Chem. Solids*, vol. 75, no. 3, pp. 384–390, 2014, doi: 10.1016/j.jpcs.2013.11.006.

[217] J. Xiao, T. Yang, C. Wang, J. Xue, and Y. Wang, *J. Am. Ceram. Soc.*, vol. 98, no. 4, pp. 1323–1331, 2015, doi: 10.1111/jace.13450.

[218] K. Suzuki, *J. Nucl. Mater.*, vol. 108–109, no. C, pp. 443–450, Jul. 1982, doi: 10.1016/0022–3115(82)90515–3.

[219] G. S. Was *et al.*, *Scr. Mater.*, vol. 88, pp. 33–36, 2014, doi: 10.1016/j.scriptamat.2014.06.003.

[220] J. Gan and G. . Was, *J. Nucl. Mater.*, vol. 297, no. 2, pp. 161–175, Aug. 2001, doi: 10.1016/S0022–3115(01)00615–8.

[221] M. . I. Luppo, C. Bailat, R. Schäublin, and M. Victoria, *J. Nucl. Mater.*, vol. 283–287, no. PART I, pp. 483–487, Dec. 2000, doi: 10.1016/S0022–3115(00)00370–6.

[222] S. A. A. Maloy, M. R. R. James, W. R. R. Johnson, T. S. S. Byun, K. Farrell, and M. B. B. Toloczko, *J. Nucl. Mater.*, vol. 318, no. SUPPL, pp. 283–291, May 2003, doi: 10.1016/S0022–3115(03)00087–4.

[223] S. A. Maloy, A. Zubelewicz, T. Romero, M. R. R. James, W. F. F. Sommer, and Y. Dai, *J. Nucl. Mater.*, vol. 343, no. 1–3, pp. 191–196, Aug. 2005, doi: 10.1016/j.jnucmat.2005.03.027.

[224] K. Mergia and N. Boukos, *J. Nucl. Mater.*, vol. 373, no. 1–3, pp. 1–8, 2008, doi: 10.1016/j.jnucmat.2007.03.267.

[225] G. Gupta, Z. Jiao, A. N. Ham, J. T. Busby, and G. S. Was, *J. Nucl. Mater.*, vol. 351, no. 1–3, pp. 162–173, 2006, doi: 10.1016/j.jnucmat.2006.02.028.

[226] B. H. Sencer, G. S. Was, M. Sagisaka, Y. Isobe, G. M. Bond, and F. A. Garner, *J. Nucl. Mater.*, vol. 323, no. 1, pp. 18–28, 2003, doi: 10.1016/j.jnucmat.2003.07.007.

[227] G. S. Was *et al.*, *J. Nucl. Mater.*, vol. 300, no. 2–3, pp. 198–216, 2002, doi: 10.1016/S0022–3115(01)00751–6.

[228] E. M. Francis *et al.*, *J. Nucl. Mater.*, vol. 454, no. 1, pp. 387–397, 2014, doi: 10.1016/j.jnucmat.2014.08.034.

[229] B. A. Loomis, *J. Nucl. Mater.*, vol. 141–143, no. PART 2, pp. 690–694, 1986, doi: 10.1016/0022–3115(86)90075–9.

[230] C. Abromeit, *J. Nucl. Mater.*, vol. 216, no. C, pp. 78–96, 1994, doi: 10.1016/0022–3115(94)90008–6.

[231] Y. Oya *et al.*, *Phys. Scr. T*, vol. T145, 2011, doi: 10.1088/0031–8949/2011/T145/014050.

[232] A. Harte *et al.*, *Acta Mater.*, vol. 130, pp. 69–82, 2017, doi: 10.1016/j.actamat.2017.03.024.

[233] R. Rayaprolu, S. Möller, C. Linsmeier, and S. Spellerberg, *Nucl. Mater. Energy*, vol. 9, pp. 29–35, 2016, doi: 10.1016/j.nme.2016.09.008.

[234] C. Wang *et al.*, *Nat. Commun.*, vol. 10, no. 1, pp. 1–9, 2019, doi: 10.1038/s41467–019–08588–1.

[235] D. Bowden *et al.*, *Acta Mater.*, vol. 183, pp. 24–35, Jan. 2020, doi: 10.1016/j.actamat.2019.10.049.

[236] M. Bugnet, V. Mauchamp, E. Oliviero, M. Jaouen, and T. Cabioc'h, *J. Nucl. Mater.*, vol. 441, no. 1–3, pp. 133–137, 2013, doi: 10.1016/j.jnucmat.2013.05.028.

[237] C. Wang *et al.*, *J. Am. Ceram. Soc.*, vol. 99, no. 5, pp. 1769–1777, 2016, doi: 10.1111/jace.14118.

[238] D. J. Tallman *et al.*, *Acta Mater.*, vol. 85, pp. 132–143, Feb. 2015, doi: 10.1016/j.actamat.2014.10.068.

[239] C. Wang *et al.*, *Acta Mater.*, vol. 98, pp. 197–205, 2015, doi: 10.1016/j.actamat.2015.07.043.

[240] C. Wang *et al.*, *Acta Mater.*, vol. 144, pp. 432–446, 2018, doi: 10.1016/j.actamat.2017.11.008.

[241] T. Yang *et al.*, *J. Nucl. Mater.*, vol. 513, pp. 120–128, 2019, doi: 10.1016/j.jnucmat.2018.11.004.

[242] M. Bugnet, T. Cabioc'h, V. Mauchamp, P. Guérin, M. Marteau, and M. Jaouen, *J. Mater. Sci.*, vol. 45,

no. 20, pp. 5547–5552, Oct. 2010, doi: 10.1007/s10853–010–4615–0.

[243] M. Le Flem *et al.*, *Int. J. Appl. Ceram. Technol.*, vol. 7, no. 6, pp. 766–775, 2010, doi: 10.1111/j.1744–7402.2010.02523.x.

[244] P. Song *et al.*, *Nucl. Instruments Methods Phys. Res. Sect. B Beam Interact. with Mater. Atoms*, vol. 326, pp. 332–336, 2014, doi: 10.1016/j.nimb.2013.10.046.

[245] K. R. Whittle *et al.*, *Acta Mater.*, vol. 58, no. 13, pp. 4362–4368, 2010, doi: 10.1016/j.actamat.2010.04.029.

[246] Q. Huang *et al.*, *J. Nucl. Mater.*, vol. 465, pp. 640–647, Oct. 2015, doi: 10.1016/j.jnucmat.2015.06.056.

[247] T. Yang *et al.*, *Acta Mater.*, vol. 65, pp. 351–359, 2014, doi: 10.1016/j.actamat.2013.11.002.

[248] C. Wang *et al.*, *Nat. Commun.*, vol. 10, no. 1, p. 622, Dec. 2019, doi: 10.1038/s41467–019–08588–1.

[249] C. Wang *et al.*, *J. Nucl. Mater.*, vol. 440, no. 1–3, pp. 606–611, 2013, doi: 10.1016/j.jnucmat.2013.04.070.

[250] M. K. Patel *et al.*, *Scr. Mater.*, vol. 77, pp. 1–4, 2014, doi: 10.1016/j.scriptamat.2013.12.010.

[251] J. Ward *et al.*, *J. Nucl. Mater.*, vol. 502, pp. 220–227, 2018, doi: 10.1016/j.jnucmat.2018.02.008.

[252] J. C. Nappé *et al.*, *J. Nucl. Mater.*, vol. 409, no. 1, pp. 53–61, 2011, doi: 10.1016/j.jnucmat.2010.12.235.

[253] L. Zhang *et al.*, *Appl. Surf. Sci.*, vol. 258, no. 17, pp. 6281–6287, Jun. 2012, doi: 10.1016/j.apsusc.2012.03.022.

[254] H. L. Heinisch, L. R. Greenwood, W. J. Weber, and R. E. Williford, *J. Nucl. Mater.*, vol. 327, no. 2–3, pp. 175–181, 2004, doi: 10.1016/j.jnucmat.2004.02.012.

[255] H. Zhang, J. J. Wang, J. J. Wang, Y. Zhou, S. Peng, and X. Long, *J. Nanomater.*, vol. 2013, no. 0001, 2013, doi: 10.1155/2013/831590.

[256] S. Zhao, J. Xue, Y. Wang, and Q. Huang, *J. Appl. Phys.*, vol. 115, no. 2, p. 023503, 2014, doi: 10.1063/1.4861384.

[257] D. J. Tallman *et al.*, *J. Nucl. Mater.*, vol. 468, pp. 194–206, 2016, doi: 10.1016/j.jnucmat.2015.10.030.

[258] N. I. Medvedeva, A. N. Enyashin, and A. L. Ivanovskii, *J. Struct. Chem.*, vol. 52, no. 4, pp. 785–802, 2011, doi: 10.1134/S0022476611040226.

[259] N. I. Medvedeva, D. L. Novikov, A. L. Ivanovsky, M. V. Kuznetsov, and A. J. Freeman, *Phys. Rev. B*, vol. 58, no. 24, pp. 16042–16050, Dec. 1998, doi: 10.1103/PhysRevB.58.16042.

[260] T. Liao, J. Wang, and Y. Zhou, *Scr. Mater.*, vol. 59, no. 8, pp. 854–857, Oct. 2008, doi: 10.1016/j.scriptamat.2008.06.044.

[261] Z. Zhang *et al.*, *J. Phys. Chem. C*, vol. 119, no. 29, pp. 16606–16613, 2015, doi: 10.1021/acs.jpcc.5b03249.

[262] Y. Bai, N. Srikanth, C. K. Chua, and K. Zhou, *Crit. Rev. Solid State Mater. Sci.*, vol. 44, no. 1, pp. 56–107, 2019, doi: 10.1080/10408436.2017.1370577.

[263] C. L. Tracy, M. Lang, F. Zhang, C. Trautmann, and R. C. Ewing, *Phys. Rev. B – Condens. Matter Mater. Phys.*, vol. 92, no. 17, p. 174101, Nov. 2015, doi: 10.1103/PhysRevB.92.174101.

[264] C. L. Tracy *et al.*, *Nucl. Instruments Methods Phys. Res. Sect. B Beam Interact. with Mater. Atoms*, vol. 326, pp. 169–173, May 2014, doi: 10.1016/j.nimb.2013.08.070.

[265] C. Wang, C. L. Tracy, and R. C. Ewing, *Appl. Phys. Rev.*, vol. 7, no. 4, p. 041311, Dec. 2020, doi: 10.1063/5.0019284.

[266] C. Ang, C. Silva, C. Shih, T. Koyanagi, Y. Katoh, and S. J. Zinkle, *Scr. Mater.*, vol. 114, pp. 74–78, 2016, doi: 10.1016/j.scriptamat.2015.11.008.

[267] Q. Huang *et al.*, *Acta Mater.*, vol. 110, pp. 1–7, 2016, doi: 10.1016/j.actamat.2016.03.021.

[268] C. Ang, S. Zinkle, C. Shih, C. Silva, N. Cetiner, and Y. Katoh, *J. Nucl. Mater.*, vol. 483, pp. 44–53, Jan. 2017, doi: 10.1016/j.jnucmat.2016.10.036.

[269] J. C. Nappé *et al.*, *J. Eur. Ceram. Soc.*, vol. 31, no. 8, pp. 1503–1511, 2011, doi:

10.1016/j.jeurceramsoc.2011.01.002.

[270] X. Liu *et al.*, *Nucl. Instruments Methods Phys. Res. Sect. B Beam Interact. with Mater. Atoms*, vol. 268, no. 5, pp. 506–512, 2010, doi: 10.1016/j.nimb.2009.11.017.

[271] D. W. Clark, S. J. Zinkle, M. K. Patel, and C. M. Parish, *Acta Mater.*, vol. 105, pp. 130–146, 2016, doi: 10.1016/j.actamat.2015.11.055.

[272] S. Liu, C. Wang, T. Yang, Y. Fang, Q. Huang, and Y. Wang, *Nucl. Instruments Methods Phys. Res. Sect. B Beam Interact. with Mater. Atoms*, vol. 406, pp. 662–669, 2017, doi: 10.1016/j.nimb.2017.01.040.

[273] B. Tunca, G. Greaves, J. A. Hinks, P. O. Å. Å. Persson, J. Vleugels, and K. Lambrinou, *Acta Mater.*, vol. 206, 2021, doi: 10.1016/j.actamat.2020.116606.

[274] H. Zhang, R. Su, I. Szlufarska, L. Shi, and H. Wen, *J. Eur. Ceram. Soc.*, vol. 41, no. 1, pp. 252–258, 2021, doi: 10.1016/j.jeurceramsoc.2020.08.015.

[275] J. G. Gigax *et al.*, *J. Nucl. Mater.*, vol. 523, pp. 26–32, 2019, doi: 10.1016/j.jnucmat.2019.05.021.

[276] A. Abdulkadhim *et al.*, *Surf. Coatings Technol.*, vol. 206, no. 4, pp. 599–603, Nov. 2011, doi: 10.1016/j.surfcoat.2011.06.003.

[277] T. Deng *et al.*, *Acta Mater.*, vol. 189, pp. 188–203, May 2020, doi: 10.1016/j.actamat.2020.03.008.

[278] T. Yang *et al.*, *Acta Mater.*, vol. 128, pp. 1–11, 2017, doi: 10.1016/j.actamat.2017.01.066.

[279] D. J. Tallman, L. He, J. Gan, E. N. Caspi, E. N. Hoffman, and M. W. Barsoum, *J. Nucl. Mater.*, vol. 484, pp. 120–134, 2017, doi: 10.1016/j.jnucmat.2016.11.016.

[280] M. A. Tunes, M. Imtyazuddin, C. Kainz, S. Pogatscher, and V. M. Vishnyakov, *Sci. Adv.*, vol. 7, no. 13, 2021, doi: 10.1126/sciadv.abf6771.

[281] J. Ward, D. Bowden, D. Stewart, M. W. Barsoum, P. Frankel, and M. Preuss, *Scr. Mater.*, vol. 165, pp. 98–102, 2019, doi: 10.1016/j.scriptamat.2019.02.022.

[282] L. X. Jia, Y. X. Wang, X. D. Ou, L. Q. Shi, and W. Ding, *Mater. Lett.*, vol. 83, pp. 23–26, 2012, doi: 10.1016/j.matlet.2012.05.093.

[283] H. F. Zhang *et al.*, *Acta Mater.*, vol. 97, pp. 50–57, 2015, doi: 10.1016/j.actamat.2015.07.015.

[284] Q. Song, P. Zhang, J. Zhuang, and X. J. Ning, *Comput. Mater. Sci.*, vol. 137, pp. 327–331, 2017, doi: 10.1016/j.commatsci.2017.06.004.

[285] Y. Xu *et al.*, *J. Chem. Phys.*, vol. 143, no. 11, 2015, doi: 10.1063/1.4931398.

[286] H. H. Shen *et al.*, *J. Nucl. Mater.*, vol. 485, pp. 262–272, 2017, doi: 10.1016/j.jnucmat.2016.12.022.

[287] S. Yang *et al.*, *RSC Adv.*, vol. 6, no. 64, pp. 59875–59881, 2016, doi: 10.1039/c6ra07082e.

[288] J. J. Liu *et al.*, *Phys. Chem. Chem. Phys.*, vol. 20, no. 27, pp. 18766–18774, 2018, doi: 10.1039/c8cp02082e.

[289] R. Su, H. Zhang, L. Shi, and H. Wen, *J. Eur. Ceram. Soc.*, vol. 39, no. 6, pp. 1993–2002, Jun. 2019, doi: 10.1016/j.jeurceramsoc.2019.01.056.

[290] J. Wang *et al.*, *Scr. Mater.*, vol. 137, pp. 13–17, 2017, doi: 10.1016/j.scriptamat.2017.05.003.

[291] H. Zhang, R. Su, L. Shi, D. J. O'Connor, and H. Wen, *Appl. Surf. Sci.*, vol. 434, pp. 1210–1216, Mar. 2018, doi: 10.1016/j.apsusc.2017.11.170.

[292] H. Zhang, R. Su, L. Shi, D. J. O'Connor, B. V. King, and E. H. Kisi, *J. Eur. Ceram. Soc.*, vol. 38, no. 4, pp. 1253–1264, 2018, doi: 10.1016/j.jeurceramsoc.2017.11.041.

[293] F. Wang, Q. Su, M. Nastasi, M. A. Kirk, M. Li, and B. Cui, *Ceram. Int.*, vol. 44, no. 12, pp. 14686–14692, 2018, doi: 10.1016/j.ceramint.2018.05.095.

[294] H. H. Qarra, K. M. Knowles, M. E. Vickers, S. Akhmadaliev, and K. Lambrinou, *J. Nucl. Mater.*, vol. 523, pp. 1–9, 2019, doi: 10.1016/j.jnucmat.2019.05.034.

[295] M. A. Tunes, R. W. Harrison, S. E. Donnelly, and P. D. Edmondson, *Acta Mater.*, vol. 169, pp. 237–247, 2019,

doi: 10.1016/j.actamat.2019.02.046.

[296] Q. Qi, G. J. Cheng, L. Q. Shi, D. J. O'Connor, B. V. King, and E. H. Kisi, *Acta Mater.*, vol. 66, pp. 317–325, Mar. 2014, doi: 10.1016/j.actamat.2013.11.019.

[297] H. Högberg *et al.*, *Surf. Coatings Technol.*, vol. 193, no. 1–3, pp. 6–10, Apr. 2005, doi: 10.1016/j.surfcoat.2004.08.174.

[298] P. Stoklasová, T. Grabec, K. Zoubková, P. Sedlák, S. Krátký, and H. Seiner, *Exp. Mech.*, vol. 61, no. 4, pp. 663–676, Apr. 2021, doi: 10.1007/s11340–021–00698–6.

[299] C. Wang, C. L. Tracy, and R. C. Ewing, *Appl. Phys. Rev.*, vol. 7, no. 4, p. 041311, Dec. 2020, doi: 10.1063/5.0019284.

[300] L. Hu, A. Kothalkar, M. O'Neil, I. Karaman, and M. Radovic, *Mater. Res. Lett.*, vol. 2, no. 3, pp. 124–130, 2014, doi: 10.1080/21663831.2013.873498.

[301] C. Tang *et al.*, *Surf. Coatings Technol.*, vol. 309, pp. 445–455, 2017, doi: 10.1016/j.surfcoat.2016.11.090.

[302] O. Berger, *Surf. Eng.*, vol. 36, no. 3, pp. 268–302, 2020, doi: 10.1080/02670844.2019.1611076.

[303] K. Lambrinou, T. Lapauw, B. Tunca, and J. Vleugels, in *Ceramic Engineering and Science Proceedings*, vol. 37, no. 7, 2017, pp. 223–233. doi: 10.1002/9781119321811.ch21.

[304] C. Hu, Y. Sakka, T. Nishimura, S. Guo, S. Grasso, and H. Tanaka, *Sci. Technol. Adv. Mater.*, vol. 12, no. 4, p. 44603, 2011, doi: 10.1088/1468–6996/12/4/044603.

[305] J. Coburn *et al.*, *Nucl. Mater. Energy*, vol. 19, pp. 316–323, 2019, doi: 10.1016/j.nme.2019.02.036.

[306] B. N. Nguyen, C. H. Henager, and R. J. Kurtz, *J. Nucl. Mater.*, vol. 495, pp. 504–515, 2017, doi: 10.1016/j.jnucmat.2017.09.011.

[307] J. Coburn and M. Bourham, *Fusion Sci. Technol.*, vol. 72, no. 4, pp. 692–698, 2017, doi: 10.1080/15361055.2017.1352426.

[308] J. D. Coburn *et al.*, *Fusion Sci. Technol.*, vol. 75, no. 7, pp. 621–635, 2019, doi: 10.1080/15361055.2019.1623570.

[309] W. Jeitschko, H. Nowotny, and F. Benesovsky, *Monatshefte f�r Chemie*, vol. 94, no. 4, pp. 672–676, 1963, doi: 10.1007/BF00913068.

[310] W. Jeitschko, H. Nowotny, and F. Benesovsky, *Monatshefte für Chemie und verwandte Teile anderer Wissenschaften*, vol. 94, no. 6, pp. 1201–1205, Nov. 1963, doi: 10.1007/BF00905711.

[311] A. Zhou and X. K. Qian, in *Advances in science and technology of Mn+1AXn phases*, Woodhead Publishing Limited, 2012, pp. 1–19. doi: 10.1016/B978–1–84569–991–8.50001–1.

[312] N. Atazadeh *et al.*, *Int. J. Refract. Met. Hard Mater.*, vol. 61, pp. 67–78, 2016, doi: 10.1016/j.ijrmhm.2016.08.003.

[313] L. Chlubny and J. Lis, in *Ceramic Transactions*, vol. 234, D. Zhu, H. T. Lin, Y. Zhou, T. Hwang, M. Halbig, and S. Mathur, Eds. 2012, pp. 65–70. doi: 10.1002/9781118491867.ch8.

[314] P. Mohazzab, *J. Appl. Math. Phys.*, vol. 05, no. 04, pp. 836–843, 2017, doi: 10.4236/jamp.2017.54073.

[315] P. W. H. Bragg and W. L. Bragg, *Proc. R. Soc. London. Ser. A, Contain. Pap. a Math. Phys. Character*, vol. 88, no. 605, pp. 428–438, Jul. 1913, doi: 10.1098/rspa.1913.0040.

[316] E. Atkins, vol. 29, no. 12. 1978. doi: 10.1088/0031–9112/29/12/034.

[317] C. Tang *et al.*, *J. Vac. Sci. Technol. A*, vol. 38, no. 1, p. 013401, 2020, doi: 10.1116/1.5131544.

[318] J. Etzkorn, M. Ade, D. Kotzott, M. Kleczek, and H. Hillebrecht, *J. Solid State Chem.*, vol. 182, no. 5, pp. 995–1002, 2009, doi: 10.1016/j.jssc.2009.01.003.

[319] T. Novoselova, S. Malinov, W. Sha, and A. Zhecheva, *Mater. Sci. Eng. A*, vol. 371, no. 1–2, pp. 103–112, 2004, doi: 10.1016/j.msea.2003.12.015.

[320] A. A. Coelho, *J. Appl. Crystallogr.*, vol. 33, no. 3 II, pp. 899–908, 2000, doi: 10.1107/S002188980000248X.

[321] G. Ribárik, B. Jóni, and T. Ungár, *Crystals*, vol. 10, no. 7, p. 623, Jan. 2020, doi: 10.3390/cryst10070623.

[322] B. L. Henke, E. M. Gullikson, and J. C. Davis, *At. Data Nucl. Data Tables*, vol. 54, no. 2, pp. 181–342, 1993.

[323] B. AXS, 2017.

[324] H. M. Rietveld, *J. Appl. Crystallogr.*, vol. 2, no. 2, pp. 65–71, 1969, doi: 10.1107/s0021889869006558.

[325] B. H. Toby, *Powder Diffr.*, vol. 21, no. 1, pp. 67–70, 2006, doi: 10.1154/1.2179804.

[326] J. Trincavelli, S. Limandri, and R. Bonetto, *Spectrochim. Acta – Part B At. Spectrosc.*, vol. 101, pp. 76–85, 2014, doi: 10.1016/j.sab.2014.07.016.

[327] D. E. Newbury and N. W. M. Ritchie, *Scanning*, vol. 35, no. 3, pp. 141–168, Jan. 2013, doi: 10.1002/sca.21041.

[328] N. W. M. Ritchie, D. E. Newbury, and J. M. Davis, *Microsc. Microanal.*, vol. 18, no. 4, pp. 892–904, Jan. 2012, doi: 10.1017/S1431927612001109.

[329] F. A. Stevie *et al.*, *Surf. Interface Anal.*, vol. 31, no. 5, pp. 345–351, 2001, doi: 10.1002/sia.1063.

[330] A. B. Yankovich *et al.*, *Nat. Commun.*, vol. 5, no. 1, p. 4155, Sep. 2014, doi: 10.1038/ncomms5155.

[331] T. Akashi *et al.*, *Appl. Phys. Lett.*, vol. 106, no. 7, p. 074101, Feb. 2015, doi: 10.1063/1.4908175.

[332] E. Yücelen, I. Lazić, and E. G. T. Bosch, *Sci. Rep.*, vol. 8, no. 1, p. 2676, Dec. 2018, doi: 10.1038/s41598–018–20377–2.

[333] Rayleigh, *London, Edinburgh, Dublin Philos. Mag. J. Sci.*, vol. 8, no. 49, pp. 261–274, Jan. 1879, doi: 10.1080/14786447908639684.

[334] J. I. Goldstein *et al.*, vol. 25, no. 4. Springer, 2017. doi: 10.1017/s1551929517000578.

[335] R. F. F. Egerton, *Microsc. Res. Tech.*, vol. 75, no. 11, pp. 1550–1556, Nov. 2012, doi: 10.1002/jemt.22099.

[336] R. F. F. Egerton, *Ultramicroscopy*, vol. 127, pp. 100–108, Apr. 2013, doi: 10.1016/j.ultramic.2012.07.006.

[337] J. M. Cowley, Oxford University Press, 1992.

[338] J. M. Cowley and P. M. Fields, *Acta Crystallogr. Sect. A*, vol. 35, no. 1, pp. 28–37, Jan. 1979, doi: 10.1107/S0567739479000061.

[339] R. F. Egerton, Boston, MA: Springer US, 2005. doi: 10.1007/b136495.

[340] R. Erni, M. D. Rossell, C. Kisielowski, and U. Dahmen, *Phys. Rev. Lett.*, vol. 102, no. 9, p. 096101, Mar. 2009, doi: 10.1103/PhysRevLett.102.096101.

[341] P. D. D. Nellist and S. J. J. Pennycook, 2000, pp. 147–203. doi: 10.1016/S1076–5670(00)80013–0.

[342] D. B. Williams and C. B. Carter, Boston, MA: Springer US, 2009. doi: 10.1007/978–0–387–76501–3.

[343] C. Hetherington, *Mater. Today*, vol. 7, no. 12, pp. 50–55, Dec. 2004, doi: 10.1016/S1369–7021(04)00571–1.

[344] P. Lu, E. Romero, S. Lee, J. L. MacManus–Driscoll, and Q. Jia, *Microsc. Microanal.*, vol. 20, no. 6, pp. 1782–1790, Dec. 2014, doi: 10.1017/S1431927614013245.

[345] A. J. D'Alfonso, B. Freitag, D. Klenov, and L. J. Allen, *Phys. Rev. B*, vol. 81, no. 10, p. 100101, Mar. 2010, doi: 10.1103/PhysRevB.81.100101.

[346] L. Keeney, C. Downing, M. Schmidt, M. E. Pemble, V. Nicolosi, and R. W. Whatmore, *Sci. Rep.*, vol. 7, no. 1, p. 1737, Dec. 2017, doi: 10.1038/s41598–017–01902–1.

[347] I. P. Jones, London: Institute of Materials, 1992.

[348] H. S. von Harrach *et al.*, *Microsc. Microanal.*, vol. 15, no. S2, pp. 208–209, Jul. 2009, doi: 10.1017/S1431927609094288.

[349] Y. H. LI, Z. CHEN, and M. H. LORETTO, *J. Microsc.*, vol. 170, no. 3, pp. 259–264, Jun. 1993, doi: 10.1111/j.1365–2818.1993.tb03349.x.

[350] G. Cliff and G. W. Lorimer, *J. Microsc.*, vol. 103, no. 2, pp. 203–207, Mar. 1975, doi: 10.1111/j.1365–2818.1975.tb03895.x.

[351] M. WATANABE and D. B. WILLIAMS, *J. Microsc.*, vol. 221, no. 2, pp. 89–109, Feb. 2006, doi: 10.1111/j.1365–2818.2006.01549.x.

[352] J. E. Wood, D. B. Williams, and J. I. Goldstein, *J. Microsc.*, vol. 133, no. 3, pp. 255–274, Mar. 1984, doi: 10.1111/j.1365–2818.1984.tb00490.x.

[353] M. Li *et al.*, *J. Am. Chem. Soc.*, vol. 141, no. 11, pp. 4730–4737, 2019, doi: 10.1021/jacs.9b00574.

[354] T. Lapauw *et al.*, *J. Eur. Ceram. Soc.*, vol. 36, pp. 943–947, 2016.

[355] M. Dahlqvist, J. Lu, R. Meshkian, Q. Tao, L. Hultman, and J. Rosen, *Sci. Adv.*, vol. 3, no. 7, p. e1700642, 2017, doi: 10.1126/sciadv.1700642.

[356] B. Manoun, S. K. Saxena, T. El–Raghy, and M. W. Barsoum, *Appl. Phys. Lett.*, vol. 88, no. 20, pp. 86–89, 2006, doi: 10.1063/1.2202387.

[357] Z. Lin, M. Zhuo, Y. Zhou, M. Li, and J. Wang, *J. Am. Ceram. Soc.*, vol. 89, no. 12, pp. 3765–3769, 2006, doi: 10.1111/j.1551–2916.2006.01303.x.

[358] Z. Lin, M. Li, and Y. Zhou, *J. Mater. Sci. Technol.*, vol. 23, no. 2, pp. 145–165, 2007.

[359] R. Meshkian, Q. Tao, M. Dahlqvist, J. Lu, L. Hultman, and J. Rosen, *Acta Mater.*, vol. 125, pp. 476–480, Feb. 2017, doi: 10.1016/j.actamat.2016.12.008.

[360] M. Griseri *et al.*, *J. Eur. Ceram. Soc.*, vol. 40, no. 5, pp. 1829–1838, 2020, doi: 10.1016/j.jeurceramsoc.2019.12.052.

[361] F. de la Peña *et al.*, Zenodo, Aug. 2020. doi: 10.5281/zenodo.3973513.

[362] S. Van Der Walt, S. C. Colbert, G. Varoquaux, S. Van Der Walt, S. C. Colbert, and G. Varoquaux, *Comput. Sci. Eng.*, vol. 13, no. 2, pp. 22–30, Mar. 2011, doi: 10.1109/MCSE.2011.37.

[363] S. Liu *et al.*, *Nucl. Instruments Methods Phys. Res. Sect. B Beam Interact. with Mater. Atoms*, vol. 435, no. August 2017, pp. 50–55, 2018, doi: 10.1016/j.nimb.2017.10.006.

[364] P. T. Wady *et al.*, *Nucl. Instruments Methods Phys. Res. Sect. A Accel. Spectrometers, Detect. Assoc. Equip.*, vol. 806, pp. 109–116, 2015, doi: 10.1016/j.nima.2015.09.088.

[365] G. H. Kinchin and R. S. Pease, *Reports Prog. Phys.*, vol. 18, no. 1, p. 301, Jan. 1955, doi: 10.1088/0034–4885/18/1/301.

[366] J. F. Ziegler, M. D. Ziegler, and J. P. Biersack, *Nucl. Instruments Methods Phys. Res. Sect. B Beam Interact. with Mater. Atoms*, vol. 268, no. 11–12, pp. 1818–1823, 2010, doi: 10.1016/j.nimb.2010.02.091.

[367] R. E. Stoller, M. B. Toloczko, G. S. Was, A. G. Certain, S. Dwaraknath, and F. A. Garner, *Nucl. Instruments Methods Phys. Res. Sect. B Beam Interact. with Mater. Atoms*, vol. 310, pp. 75–80, 2013, doi: 10.1016/j.nimb.2013.05.008.

[368] S. Agarwal, Y. Lin, C. Li, R. E. Stoller, and S. J. Zinkle, *Nucl. Instruments Methods Phys. Res. Sect. B Beam Interact. with Mater. Atoms*, vol. 503, no. December 2020, pp. 11–29, Sep. 2021, doi: 10.1016/j.nimb.2021.06.018.

[369] D. C. Irradiation, *ASTM Int. E521 – 16*, vol. 96, no. 2009, pp. 1–21, 2009, doi: https://doi.org/10.1520/E0521–16.

[370] J. QUINTA DA FONSECA, P. M. MUMMERY, and P. J. WITHERS, *J. Microsc.*, vol. 218, no. 1, pp. 9–21, Apr. 2005, doi: 10.1111/j.1365–2818.2005.01461.x.

[371] M. F. Ashby, *Philos. Mag. A J. Theor. Exp. Appl. Phys.*, vol. 21, no. 170, pp. 399–424, Feb. 1970, doi: 10.1080/14786437008238426.

[372] H. Jin, W.–Y. Lu, and J. Korellis, *J. Strain Anal. Eng. Des.*, vol. 43, no. 8, pp. 719–728, Aug. 2008, doi: 10.1243/03093247JSA412.

[373] H. A. A. A. Padilla, J. Lambros, A. J. J. J. Beaudoin, and I. M. M. M. Robertson, *Int. J. Solids Struct.*, vol. 49, no. 1, pp. 18–31, Jan. 2012, doi: 10.1016/j.ijsolstr.2011.09.001.

[374] F. Di Gioacchino, J. Quinta da Fonseca, F. Di Gioacchino, and J. Q. da Fonseca, *Exp. Mech.*, vol. 53, no. 5, pp. 743–754, Jun. 2013, doi: 10.1007/s11340–012–9685–2.

[375] T. Zhang, J. Jiang, B. A. Shollock, T. Ben Britton, and F. P. E. Dunne, *Mater. Sci. Eng. A*, vol. 641, pp. 328–339, Aug. 2015, doi:

10.1016/j.msea.2015.06.070.

[376] E. Héripré *et al.*, *Int. J. Plast.*, vol. 23, no. 9, pp. 1512–1539, Sep. 2007, doi: 10.1016/j.ijplas.2007.01.009.

[377] J. Carroll, W. Abuzaid, J. Lambros, and H. Sehitoglu, *Rev. Sci. Instrum.*, vol. 81, no. 8, p. 083703, Aug. 2010, doi: 10.1063/1.3474902.

[378] M. D. D. McMurtrey, G. S. S. Was, B. Cui, I. Robertson, L. Smith, and D. Farkas, *Int. J. Plast.*, vol. 56, pp. 219–231, May 2014, doi: 10.1016/j.ijplas.2014.01.001.

[379] M. P. Echlin, J. C. Stinville, V. M. Miller, W. C. Lenthe, and T. M. Pollock, *Acta Mater.*, vol. 114, pp. 164–175, Aug. 2016, doi: 10.1016/j.actamat.2016.04.057.

[380] G. Martin, C. W. Sinclair, and R. A. Lebensohn, *Mater. Sci. Eng. A*, vol. 603, pp. 37–51, May 2014, doi: 10.1016/j.msea.2014.01.102.

[381] J. C. C. Stinville, N. Vanderesse, F. Bridier, P. Bocher, and T. M. M. Pollock, *Acta Mater.*, vol. 98, pp. 29–42, Oct. 2015, doi: 10.1016/j.actamat.2015.07.016.

[382] X. Guo, J. Liang, Z. Xiao, and B. Cao, *Optik (Stuttg).*, vol. 125, no. 18, pp. 5316–5322, Sep. 2014, doi: 10.1016/j.ijleo.2014.06.067.

[383] A. D. Smith *et al.*, *Sci. Rep.*, vol. 10, no. 1, pp. 1–11, 2020, doi: 10.1038/s41598–020–62241–2.

[384] A. Orozco–Caballero, D. Lunt, J. D. Robson, J. Quinta da Fonseca, and J. Q. da Fonseca, *Acta Mater.*, vol. 133, pp. 367–379, 2017, doi: 10.1016/j.actamat.2017.05.040.

[385] R. Thomas *et al.*, *Materialia*, vol. 5, no. September 2018, p. 100248, 2019, doi: 10.1016/j.mtla.2019.100248.

[386] Y. L. L. Dong and B. Pan, *Exp. Mech.*, vol. 57, no. 8, pp. 1161–1181, Oct. 2017, doi: 10.1007/s11340–017–0283–1.

[387] C. Efstathiou, H. Sehitoglu, and J. Lambros, *Int. J. Plast.*, vol. 26, no. 1, pp. 93–106, Jan. 2010, doi: 10.1016/j.ijplas.2009.04.006.

[388] P. D. D. Littlewood and A. J. J. Wilkinson, *Int. J. Fatigue*, vol. 43, pp. 111–119, Oct. 2012, doi: 10.1016/j.ijfatigue.2012.03.001.

[389] K. Kozak, M. M. Bućko, L. Chlubny, J. Lis, G. Antou, and T. Chotard, *Mater. Sci. Eng. A*, vol. 743, no. August 2018, pp. 114–122, 2019, doi: 10.1016/j.msea.2018.11.063.

[390] T. F. Scientific, [Online]. Available: https://www.thermofisher.com/uk/en/home/electron–microscopy/products/software–em–3d–vis/maps–software.html

[391] J. Schindelin *et al.*, *Nat. Methods*, vol. 9, no. 7, pp. 676–682, Jul. 2012, doi: 10.1038/nmeth.2019.

[392] LaVision, Göttingen, 2010. [Online]. Available: https://www.lavision.de

[393] F. Di Gioacchino, J. Q. Da Fonseca, F. Di Gioacchino, and J. Quinta Da Fonseca, *Int. J. Plast.*, vol. 74, pp. 92–109, Nov. 2015, doi: 10.1016/j.ijplas.2015.05.012.

[394] G. E. Dieter, Toronto: McGraw–Hill Book Company, Inc., 1986.

[395] M. D. Atkinson, R. Thomas, A. Harte, P. Crowther, and J. Q. da Fonseca, 2020. doi: 10.5281/zenodo.3784775.

[396] M. Abdou *et al.*, *Fusion Eng. Des.*, vol. 100, pp. 2–43, 2015, doi: 10.1016/j.fusengdes.2015.07.021.

[397] J. W. Coenen *et al.*, *Phys. Scr.*, vol. 2016, no. T167, 2016, doi: 10.1088/0031–8949/2016/T167/014002.

[398] M. W. Barsoum and M. Radovic, *Annu. Rev. Mater. Res.*, vol. 41, no. 1, pp. 195–227, 2011, doi: 10.1146/annurev–matsci–062910–100448.

[399] D. J. Tallman, Drexel University, 2015.

[400] X. H. Wang and Y. C. Zhou, *Oxid. Met.*, vol. 59, no. 3–4, pp. 303–320, 2003, doi: 10.1023/A:1023092027697.

[401] M. A. Ali *et al.*, *J. Alloys Compd.*, vol. 743, pp. 146–154, Apr. 2018, doi: 10.1016/j.jallcom.2018.01.396.

[402] L. Shang, D. Music, M. T. Baben, and J. M. Schneider, *J. Phys. D. Appl. Phys.*, vol. 47, no. 6, p. 065308, Feb. 2014, doi: 10.1088/0022–3727/47/6/065308.

[403] J. Emmerlich *et al.*, *Acta Mater.*, vol.

55, no. 4, pp. 1479–1488, 2007, doi: 10.1016/j.actamat.2006.10.010.

[404] H. B. Zhang, Y. W. Bao, and Y. C. Zhou, *J. Mater. Sci. Technol.*, vol. 25, no. 1, pp. 1–38, 2009.

[405] NDA, [Online]. Available: https://ukinventory.nda.gov.uk/about–radioactive–waste/what–is–radioactivity/what–are–the–main–waste–categories/

[406] D. Gleisberg, vol. 3. 1992. doi: 10.1007/978–3–540–47108–0_4.

[407] P. F. Schmit *et al.*, *Phys. Rev. Lett.*, vol. 113, no. 15, Oct. 2014, doi: 10.1103/PhysRevLett.113.155004.

[408] O. Berger, C. Leyens, S. Heinze, R. Boucher, and M. Ruhnow, *Thin Solid Films*, vol. 580, pp. 6–11, 2015, doi: 10.1016/j.tsf.2015.03.008.

[409] R. Boucher, O. Berger, and C. Leyens, *Surf. Eng.*, vol. 32, no. 3, pp. 172–177, 2016, doi: 10.1179/1743294415Y.0000000103.

[410] J. Ward *et al.*, *Corros. Sci.*, vol. 139, pp. 444–453, Jul. 2018, doi: 10.1016/j.corsci.2018.04.034.

[411] M. Sokol, J. Yang, H. Keshavan, and M. W. Barsoum, *J. Eur. Ceram. Soc.*, vol. 39, no. 4, pp. 878–882, 2019, doi: 10.1016/j.jeurceramsoc.2018.10.019.

[412] A. Shamsipoor, M. Farvizi, M. Razavi, A. Keyvani, and B. Mousavi, *Oxid. Met.*, vol. 95, no. 1–2, pp. 1–21, 2021, doi: 10.1007/s11085–020–10008–5.

[413] M. Khazaei, V. Wang, C. Sevik, A. Ranjbar, M. Arai, and S. Yunoki, *Phys. Rev. Mater.*, vol. 2, no. 7, pp. 1–12, 2018, doi: 10.1103/PhysRevMaterials.2.074002.

[414] A. Mockuté, no. 1573. 2014. doi: 10.3384/diss.diva–104829.

[415] M. Radovic and M. W. Barsoum, *Am. Ceram. Soc. Bull.*, vol. 92, no. 3, pp. 20–27, 2013.

[416] C. Racault, F. Langlais, and C. Bernard, *J. Mater. Sci.*, vol. 29, no. 19, pp. 5023–5040, 1994, doi: 10.1007/BF01151093.

[417] M. Dahlqvist, A. Petruhins, J. Lu, L. Hultman, and J. Rosen, *ACS Nano*, vol. 12, no. 8, pp. 7761–7770, 2018, doi: 10.1021/acsnano.8b01774.

[418] R. Meshkian *et al.*, *Adv. Mater.*, vol. 30, no. 21, p. 1706409, May 2018, doi: 10.1002/adma.201706409.

[419] M. Dahlqvist and J. Rosen, *Phys. Chem. Chem. Phys.*, vol. 17, no. 47, pp. 31810–31821, 2015, doi: 10.1039/c5cp06021d.

[420] G. Kresse and J. Furthmüller, *Phys. Rev. B – Condens. Matter Mater. Phys.*, vol. 54, no. 16, pp. 11169–11186, 1996, doi: 10.1103/PhysRevB.54.11169.

[421] G. Kresse and J. Furthmüller, *Comput. Mater. Sci.*, vol. 6, no. 1, pp. 15–50, 1996, doi: 10.1016/0927–0256(96)00008–0.

[422] F. Han, *Probl. Solid State Phys. with Solut.*, vol. 50, no. 24, pp. 391–396, 2011, doi: 10.1142/9789814365031_0023.

[423] J. P. Perdew and Y. Wang, *Phys. Rev. B*, vol. 45, no. 23, pp. 13244–13249, 1992, doi: 10.1103/PhysRevB.45.13244.

[424] J. P. Perdew, K. Burke, and M. Ernzerhof, *Phys. Rev. Lett.*, vol. 77, no. 18, pp. 3865–3868, 1996, doi: 10.1103/PhysRevLett.77.3865.

[425] D. Joubert, *Phys. Rev. B – Condens. Matter Mater. Phys.*, vol. 59, no. 3, pp. 1758–1775, 1999, doi: 10.1103/PhysRevB.59.1758.

[426] H. J. Monkhorst and J. D. Pack, *Phys. Rev. B*, vol. 13, no. 12, pp. 5188–5192, 1976, doi: 10.1103/PhysRevB.13.5188.

[427] A. University *et al.*, 2019. https://www.supercomputing.wales (accessed Aug. 13, 2019).

[428] G. Leaver, 2019. http://ri.itservices.manchester.ac.uk/csf3/ (accessed Aug. 13, 2019).

[429] J. Lu, A. Thore, R. Meshkian, Q. Tao, L. Hultman, and J. Rosen, *Cryst. Growth Des.*, vol. 17, no. 11, pp. 5704–5711, 2017, doi: 10.1021/acs.cgd.7b00642.

[430] M. Naguib, V. N. Mochalin, M. W. Barsoum, and Y. Gogotsi, *Adv. Mater.*, vol. 26, no. 7, pp. 992–1005, 2014, doi: 10.1002/adma.201304138.

[431] M. Naguib *et al.*, *ACS Nano*, vol. 6, no. 2, pp. 1322–1331, 2012, doi: 10.1021/nn204153h.

[432] C. Shi, M. Beidaghi, M. Naguib, O. Mashtalir, Y. Gogotsi, and S. J. L. L. Billinge, *Phys. Rev. Lett.*, vol. 112, no. 12, pp. 1–5, 2013, doi: 10.1103/PhysRevLett.112.125501.

[433] J. Ran, G. Gao, F. T. Li, T. Y. Ma, A. Du, and S. Z. Qiao, *Nat. Commun.*, vol. 8, no. 13907, pp. 1–10, 2017, doi: 10.1038/ncomms13907.

[434] H. Lin, X. Wang, L. Yu, Y. Chen, and J. Shi, *Nano Lett.*, vol. 17, no. 1, pp. 384–391, 2017, doi: 10.1021/acs.nanolett.6b04339.

[435] B. Anasori, M. R. Lukatskaya, and Y. Gogotsi, *Nat. Rev. Mater.*, vol. 2, no. 2, 2017, doi: 10.1038/natrevmats.2016.98.

[436] X. Zhang, Z. Zhang, and Z. Zhou, *J. Energy Chem.*, vol. 27, no. 1, pp. 73–85, 2018, doi: 10.1016/j.jechem.2017.08.004.

[437] Z. Ling *et al.*, *Proc. Natl. Acad. Sci. U. S. A.*, vol. 111, no. 47, pp. 16676–16681, 2014, doi: 10.1073/pnas.1414215111.

[438] R. Wang, S. Wang, Y. Zhang, D. Jin, X. Tao, and L. Zhang, *J. Mater. Chem. A*, vol. 6, no. 3, pp. 1017–1027, 2018, doi: 10.1039/c7ta09153b.

[439] L. Lorencova *et al.*, *Electrochim. Acta*, vol. 235, pp. 471–479, 2017, doi: 10.1016/j.electacta.2017.03.073.

[440] Q. Peng *et al.*, *J. Am. Chem. Soc.*, vol. 136, no. 11, pp. 4113–4116, 2014, doi: 10.1021/ja500506k.

[441] F. Shahzad *et al.*, *Science (80–.).*, vol. 353, no. 6304, pp. 1137–1140, 2016, doi: 10.1126/science.aag2421.

[442] X. Zhang *et al.*, *RSC Adv.*, vol. 5, no. 4, pp. 2762–2767, 2015, doi: 10.1039/c4ra13800g.

[443] W. Yang *et al.*, *Adv. Mater.*, vol. 31, no. 37, pp. 1–8, 2019, doi: 10.1002/adma.201902725.

[444] J. Orangi, F. Hamade, V. A. Davis, and M. Beidaghi, *ACS Nano*, vol. 14, no. 1, pp. 640–650, 2020, doi: 10.1021/acsnano.9b07325.

[445] S. Sridharan and H. Nowotny, *Int. J. Mater. Res.*, vol. 74, no. 7, pp. 468–472, Jul. 1983, doi: 10.1515/ijmr–1983–740711.

[446] J. Etzkorn, M. Ade, and H. Hillebrecht, *Inorg. Chem.*, vol. 46, no. 4, pp. 1410–1418, 2007, doi: 10.1021/ic062231y.

[447] J. C. Slater, *J. Chem. Phys.*, vol. 41, no. 10, pp. 3199–3204, 1964, doi: 10.1063/1.1725697.

[448] G. P. Bei, V. Gauthier–Brunet, C. Tromas, and S. Dubois, *J. Am. Ceram. Soc.*, vol. 95, no. 1, pp. 102–107, 2012, doi: 10.1111/j.1551–2916.2011.04846.x.

[449] G. S. Pawley, *J. Appl. Crystallogr.*, vol. 14, no. 6, pp. 357–361, Dec. 1981, doi: 10.1107/s0021889881009618.

[450] E. N. Caspi, P. Chartier, F. Porcher, F. Damay, and T. Cabioc'h, *Mater. Res. Lett.*, vol. 3, no. 2, pp. 100–106, 2015, doi: 10.1080/21663831.2014.975294.

[451] M. Ghidiu, M. R. Lukatskaya, M. Q. Zhao, Y. Gogotsi, and M. W. Barsoum, *Nature*, vol. 516, no. 7529, pp. 78–81, 2015, doi: 10.1038/nature13970.

[452] L. Verger, V. Natu, M. Carey, and M. W. Barsoum, *Trends Chem.*, vol. 1, no. 7, pp. 656–669, 2019, doi: 10.1016/j.trechm.2019.04.006.

[453] A. A. Coelho, *J. Appl. Crystallogr.*, vol. 51, no. 1, pp. 210–218, Feb. 2018, doi: 10.1107/S1600576718000183.

[454] M. Griseri *et al.*, *J. Eur. Ceram. Soc.*, vol. 39, no. 10, pp. 2973–2981, 2019, doi: 10.1016/j.jeurceramsoc.2019.04.021 .

[455] A. Jain *et al.*, *APL Mater.*, vol. 1, no. 1, 2013, doi: 10.1063/1.4812323.

[456] I. M. Low and W. K. Pang, *Key Eng. Mater.*, vol. 617, no. May 2015, pp. 153–158, 2014, doi: 10.4028/www.scientific.net/KEM.617.153.

[457] G. Federici *et al.*, *Fusion Eng. Des.*, vol. 136, no. April, pp. 729–741, 2018, doi: 10.1016/j.fusengdes.2018.04.001.

[458] M. Richardson *et al.*, *J. Nucl. Mater.*, vol. 550, p. 152906, 2021, doi:

10.1016/j.jnucmat.2021.152906.

[459] K. Lambrinou, T. Lapauw, and J. Vleugels, *MatISSE/JPNM Work.*, pp. 1–32, 2015, [Online]. Available: http://www.fp7–matisse.eu/wp–content/uploads/2015/12/MatISSE–2015–MAX–Phases–Lambrinou.pdf

[460] J. Gubicza, IGI Global, 2014. doi: 10.4018/978–1–4666–5852–3.

[461] M. T. P. Rigby–Bell *et al.*, *RSC Adv.*, vol. 11, no. 5, pp. 3110–3114, 2021, doi: 10.1039/D0RA09761F.

[462] R. Pampin and P. J. Karditsas, *Fusion Eng. Des.*, vol. 81, no. 8–14 PART B, pp. 1231–1237, 2006, doi: 10.1016/j.fusengdes.2005.09.054.

[463] M. R. Gilbert, S. Zheng, R. Kemp, L. W. Packer, S. L. Dudarev, and J.–C. Sublet, *Fusion Sci. Technol.*, vol. 66, no. 1, pp. 9–17, Aug. 2014, doi: 10.13182/FST13–751.

[464] J. Knaster, A. Moeslang, and T. Muroga, *Nat. Phys.*, vol. 12, no. 5, pp. 424–434, May 2016, doi: 10.1038/nphys3735.

[465] S. . J. Zinkle and N. . M. Ghoniem, *Fusion Eng. Des.*, vol. 51–52, pp. 55–71, Nov. 2000, doi: 10.1016/S0920–3796(00)00320–3.

[466] GIF, 2015. doi: 10.1787/9789264237216–en.

[467] D. W. Clark, The University of Tennessee, Tennessee, 2015. doi: 10.1017/CBO9781107415324.004.

[468] X. M. Liu, M. Le Flem, J. L. Béchade, and I. Monnet, *J. Nucl. Mater.*, vol. 401, no. 1–3, pp. 149–153, 2010, doi: 10.1016/j.jnucmat.2010.04.015.

[469] R. Kumar, M. M. Lucas, C. Lampadaris, L. Austin, and B. Kosar, 2018. doi: 10.13140/RG.2.2.11708.74882.

[470] J. H. Ward, 2018.

[471] D. J. Kelly, 2019.

[472] N. J. Lane, S. C. Vogel, E. N. E. N. Caspi, and M. W. Barsoum, *J. Appl. Phys.*, vol. 113, no. 18, p. 183519, May 2013, doi: 10.1063/1.4803700.

[473] M. A. Pietzka and J. C. Schuster, *J. Phase Equilibria*, vol. 15, no. 4, pp. 392–400, 1994, doi: 10.1007/BF02647559.

[474] N. J. Lane, M. Naguib, J. Lu, L. Hultman, and M. W. Barsoum, *J. Eur. Ceram. Soc.*, vol. 32, no. 12, pp. 3485–3491, Sep. 2012, doi: 10.1016/j.jeurceramsoc.2012.03.035.